

Atomic-layer-deposited surface passivation schemes for silicon solar cells

Citation for published version (APA):

van de Loo, B. W. H. (2017). *Atomic-layer-deposited surface passivation schemes for silicon solar cells*. [Phd Thesis 1 (Research TU/e / Graduation TU/e), Applied Physics and Science Education]. Technische Universiteit Eindhoven.

Document status and date:

Published: 15/03/2017

Document Version:

Publisher's PDF, also known as Version of Record (includes final page, issue and volume numbers)

Please check the document version of this publication:

- A submitted manuscript is the version of the article upon submission and before peer-review. There can be important differences between the submitted version and the official published version of record. People interested in the research are advised to contact the author for the final version of the publication, or visit the DOI to the publisher's website.
- The final author version and the galley proof are versions of the publication after peer review.
- The final published version features the final layout of the paper including the volume, issue and page numbers.

[Link to publication](#)

General rights

Copyright and moral rights for the publications made accessible in the public portal are retained by the authors and/or other copyright owners and it is a condition of accessing publications that users recognise and abide by the legal requirements associated with these rights.

- Users may download and print one copy of any publication from the public portal for the purpose of private study or research.
- You may not further distribute the material or use it for any profit-making activity or commercial gain
- You may freely distribute the URL identifying the publication in the public portal.

If the publication is distributed under the terms of Article 25fa of the Dutch Copyright Act, indicated by the "Taverne" license above, please follow below link for the End User Agreement:

www.tue.nl/taverne

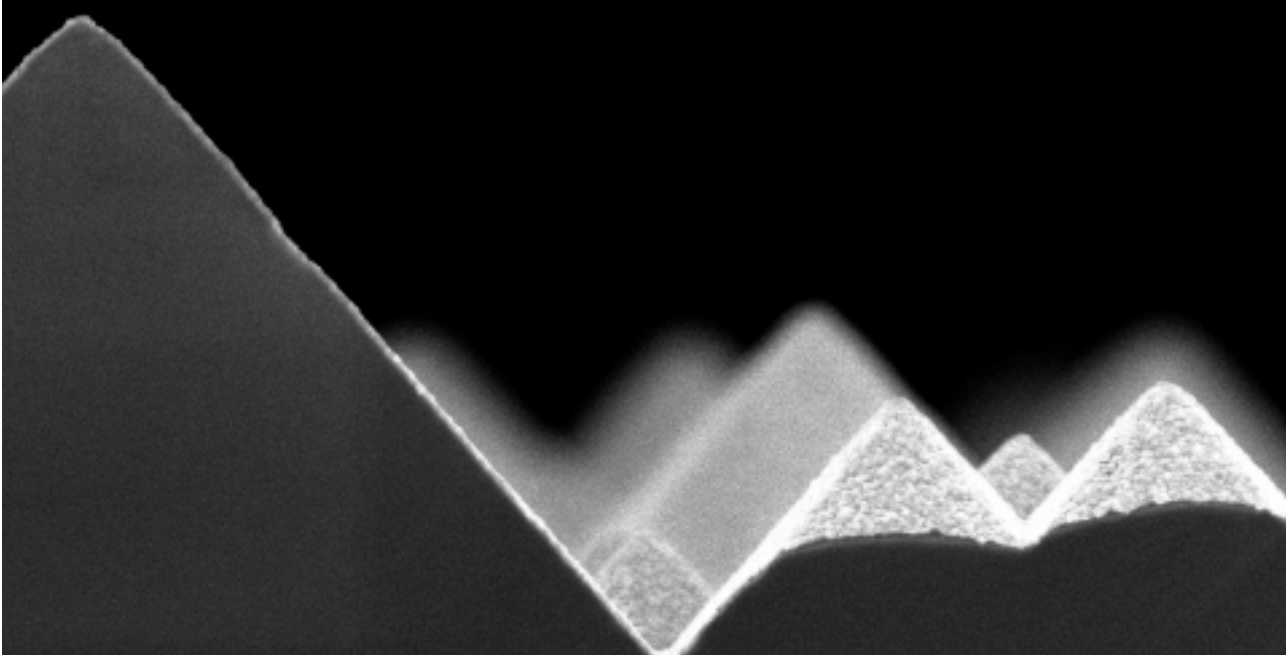
Take down policy

If you believe that this document breaches copyright please contact us at:

openaccess@tue.nl

providing details and we will investigate your claim.

Atomic-Layer-Deposited Surface Passivation Schemes for Silicon Solar Cells



Bas van de Loo

Atomic-Layer-Deposited Surface Passivation Schemes for Silicon Solar Cells

PROEFSCHRIFT

ter verkrijging van de graad van doctor aan de Technische Universiteit Eindhoven, op gezag van de rector magnificus prof.dr.ir. F.P.T. Baaijens, voor een commissie aangewezen door het College voor Promoties, in het openbaar te verdedigen op woensdag 15 maart 2017 om 16:00 uur

door

Bas Wim Hans van de Loo

geboren te 's-Hertogenbosch

Dit proefschrift is goedgekeurd door de promotoren en de samenstelling van de promotiecommissie is als volgt:

voorzitter:	prof.dr.ir. G.M.W. Kroesen
1 ^e promotor:	prof.dr.ir. W.M.M. Kessels
2 ^e promotor:	prof.dr. A.W. Weeber (TUD)
leden:	Prof.Dr. S.H. Christiansen (Freie Universität Berlin)
	Prof.Dr. S.W. Glunz (Albert-Ludwigs-Universität Freiburg)
	prof.dr. G.H. Gelinck
	prof.dr. A. Fiore
adviseur:	dr.ir. E.H.A. Granneman (Levitech B.V.)

Het onderzoek of ontwerp dat in dit proefschrift wordt beschreven is uitgevoerd in overeenstemming met de TU/e Gedragscode Wetenschapsbeoefening.

FUNDING INFORMATION

This research was financially supported by the ADEM Innovation Lab and the Top Sector Alliance for Knowledge and Innovation (TKI) of the Dutch Ministry of Economic Affairs through the programs *DutchNess*, *Nchanted*, *Antilope*, *Advanced Nanolayers 1 & 2*, *Compass*, and *IBChampion*.

Cover: Scanning electron microscopy image of 75-nm amorphous/crystalline $\text{In}_2\text{O}_3:\text{H}$ prepared by atomic layer deposition on random-pyramid textured Si.

This thesis is printed and bound by Ipskamp Printing, Enschede

A catalogue record is available from the Eindhoven University of Technology Library

ISBN: 978-90-386-4229-1

CONTENTS

Chapter 1: General Introduction	1
1.1 Crystalline silicon photovoltaics	1
1.2 High-efficiency <i>n</i> -type c-Si solar cells	3
1.3 Research framework, goals and outline	6
Chapter 2: Atomic Layer Deposition for High-Efficiency c-Si Solar Cells	13
2.1 Introduction to high-efficiency crystalline silicon solar cells	14
2.2 Nanolayers for surface passivation of Si homojunction solar cells	20
2.3 Transparent conductive oxides for Si heterojunction solar cells	44
2.4 Prospects for ALD in passivating contacts	57
2.5 Conclusions & Outlook	68
Chapter 3: Boron-Doped Silicon Surfaces from B₂H₆ Passivated by ALD Al₂O₃ for Solar Cells	81
3.1 Introduction	82
3.2 Experimental	84
3.3 Results	87
3.4 Conclusions	94
Chapter 4: ‘Zero-charge’ SiO₂/Al₂O₃ Stacks for the Simultaneous Passivation of <i>n</i>⁺- and <i>p</i>⁺- Doped Silicon Surfaces by Atomic Layer Deposition	97
4.1 Introduction	98
4.2 Experimental	100
4.3 Results	102
4.4 Conclusions	110
Addendum: Integration of ALD SiO ₂ /Al ₂ O ₃ stacks in industrial solar cells	114
Chapter 5: Understanding and Reducing Charge-Carrier Recombination at Highly Doped Crystalline Silicon Surfaces	117
5.1 Introduction	118
5.2 Theoretical evaluation of recombination at the high doped surface	120
5.3 Empirical evaluation of recombination at the highly doped surface	123
5.4 Reducing recombination at boron doped surfaces	125
5.5 Conclusions	128
Appendix A	131
Appendix B	132

Chapter 6: Surface Passivation of Phosphorus-Doped Black Si by Atomic Layer Deposited SiO₂/Al₂O₃ Stacks	133
6.1 Introduction	134
6.2 Experimental details	135
6.3 Results	137
6.4 Conclusions	141
Chapter 7: Quantification of <i>pn</i>-junction Recombination in Interdigitated-Back Contact Crystalline Silicon Solar Cells	143
7.1 Introduction	144
7.2 Experimental details	147
7.3 Results	149
7.4 Discussion: mechanisms of <i>pn</i> -junction recombination	154
7.5 Conclusions	156
Chapter 8: Silicon Surface Passivation by Transparent Conductive ZnO	163
8.1 Introduction	164
8.2 Experimental details	165
8.3 Results	167
8.4 Conclusions	175
Chapter 9: Conclusions & Outlook	179
9.1 Conclusions	179
9.2 Outlook: further opportunities for c-Si photovoltaics	183
Summary	187
Contributions of the author	189
List of publications	190
Acknowledgements	194
Curriculum Vitae	196

CHAPTER 1

General Introduction

1.1 Crystalline silicon photovoltaics

After their invention by Bell Laboratories in 1954,[1] crystalline silicon (c-Si) solar cells have steadily been improved from the initial conversion efficiencies of ~6 % up to 25%¹ in 1998.[2,3] Since then, efficiencies >25% have been demonstrated by several institutes and companies,[3–8] and the current record efficiency of 26.33% is in proximity to the projected upper limit for single-junction c-Si photovoltaics (PV) of 29.4%.[10] In addition to the increase in record efficiency of c-Si solar cells by >1% absolute in the last two decades, the field of c-Si photovoltaics has seen a tremendous progress. Innovations in terms of cell design and in high-volume manufacturing allowed PV prices to reach grid parity already at several places in the world and enabled the large-scale breakthrough of PV.[11,12] Despite the established record conversion efficiencies >25%, most cost-effective commercially available PV modules to date currently (October 2016) comprise solar cells with an efficiency of 19 – 21%.

To bridge the efficiency gap between lab-scale and industrially produced solar cells, cost-effective and scalable processing of high-efficiency solar cells is a prerequisite. The importance of a high energy conversion efficiency can easily be pointed out when looking at the balance of system costs, which include all costs which are not related to the PV module itself, such as installation, cabling, and inverter costs. For the domestic use of PV electricity, such costs are already about 50% of the total system cost². [13] Increasing the efficiency of PV brings down the relative costs of the area-related balance of system expenses, such as labor and cabling costs.

Surface passivation by atomic layer deposition of Al₂O₃

One of the key innovations which is currently being implemented in industry to increase the efficiency of c-Si solar cells, is *surface passivation* by aluminum oxide (Al₂O₃), see

¹ Under present standard test conditions (STC)

² For rooftop systems of 10-100 kWp in Germany in the first quartile of 2015

Fig. 1. This material gained significant attention after publications by Agostinelli *et al.*[14] and Hoex *et al.*[15] in 2006. In these publications, it has been shown that a thin film of Al_2O_3 , prepared by *atomic layer deposition* (ALD, see Fig. 2) on the c-Si surface could be used to reduce the density and effectiveness of defects at the c-Si surface. These defects induce recombination of electron and holes, which are formed in the c-Si through the absorption of light. The decrease in this recombination at the surface by *surface passivation*, allows for higher operating voltages and hence higher solar cell efficiencies.

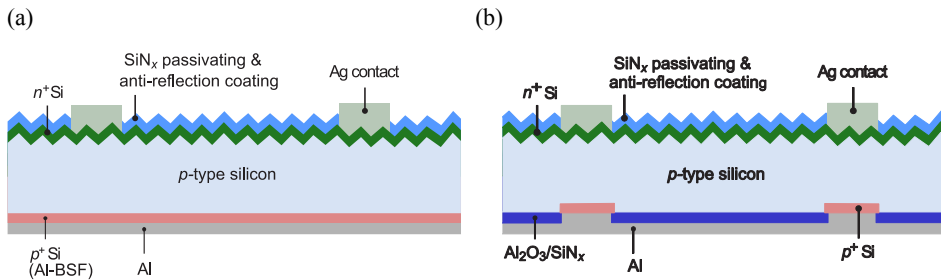


Figure 1 Schematic representations of (a) the Al back surface field (Al-BSF) cell and (b) the passivated emitter and rear cell (PERC) concepts. Both concepts are based on *p*-type crystalline Si as light-absorbing material. To reach a higher efficiency than the Al-BSF cell, in the PERC configuration the rear c-Si surface is passivated by an $\text{Al}_2\text{O}_3/\text{SiN}_x$ thin film stack. This passivation stack is later locally opened to make the hole-selective contacts. For both cell concepts, the highly doped n^+ Si region at the front is formed through the diffusion of phosphorus into a textured Si front surface, which makes the silver front contacts selective for the extraction of electrons. A SiN_x layer serves as anti-reflection and passivation coating. The p^+ Si at the rear side of both cells is formed by alloying (screen-printed) Al with the c-Si base. In this way, a hole-selective contact is formed.

Soon after these publications, significantly improved solar cell efficiencies were demonstrated when using ALD Al_2O_3 . [16,17] Due to this finding, atomic layer deposition has now entered the PV manufacturing industry as a high-throughput deposition technique, as will be extensively discussed in Chapter 2. Furthermore, surface passivation by Al_2O_3 (not necessarily deposited by ALD) is enabling the shift from the ‘*Aluminum back-surface field*’ (Al-BSF), which is the mainstream industrial solar cell architecture, to the ‘*passivated emitter and rear cell*’ (PERC) concept, [18] resulting in an approximate efficiency increase of about 1% absolute. In parallel to this ongoing shift in mainstream industrial solar cell concept, many more c-Si solar cell technologies are being developed at a rapid pace. A prominent example is the development of solar cells based on *n*-type Si as absorber material, as will be discussed in detail in the next section. Key in this overall development remains the focus on cost-effective and scalable processing, while at the

same time higher conversion efficiencies are still being targeted. In the remainder of the introduction, first the current status and challenges of n -type Si solar cells will be discussed, which play a prominent role in this dissertation, before outlining the goals of this thesis.

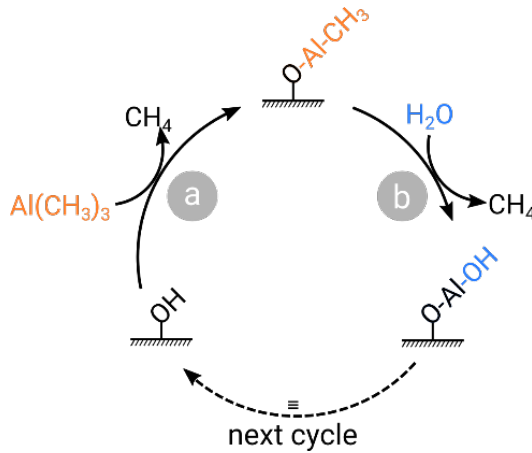


Figure 2 Schematic display of the surface reactions which are taking place during atomic layer deposition (ALD) of Al_2O_3 . In ALD, a surface is successively exposed to precursor gases (here H_2O and $\text{Al}(\text{CH}_3)_3$), which react with the surface in a self-limiting way (steps a and b). By the consecutive exposure of the surface to the precursors in a cyclic fashion, a thin film is grown. In this example, ~ 1 Å of Al_2O_3 is deposited during one ALD ‘cycle’. As the surface reactions taking place during ALD are self-limiting, films or film stacks can be grown with an Ångström-level control in thickness, a high uniformity over large areas and conformally over non-planar geometries. To prevent parasitic reactions between the different precursors used in the ALD reaction steps, the precursors are separated either in time (referred to as *temporal* ALD) or in space (termed *spatial* ALD).

1.2 High-efficiency n -type c-Si solar cells

In the search for even higher solar cell efficiencies than offered by PERC, also solar cells based on monocrystalline n -type Si are being developed to pave their way to industrialization. Monocrystalline, n -type Si, generally induces less recombination than multicrystalline p -type Si, and therefore has a higher efficiency potential. In particular, n -type Si is less sensitive than p -type Si to transition metal contaminants and it does not suffer from light-induced degradation (LID) due to the formation of boron-oxygen defects.[19] Nonetheless, the use of n -type Si as base material typically requires a redesign of the solar cell layout. Figure 3 shows the cell architectures of two upcoming industrial high-efficiency homojunction n -type Si solar cells.

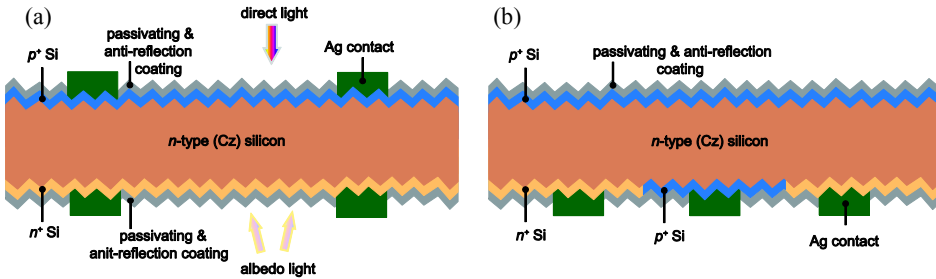


Figure 3 Schematics of the current layout of (a) a bifacial solar cell concept capable of capturing light from both sides and (b) an interdigitated-back contact (IBC) cell concept, which does not suffer from shading losses induced by metal at the front side. Both cell concepts are based on high-quality, Czochralski-grown n -type Si. The highly doped p^+ and n^+ Si regions are formed through in-diffusion of boron and phosphorus atoms, respectively. The p - and n -type highly doped regions make the contacting (screen-printed) silver electrodes selective for the extraction of holes or electrons and serve as lateral transport pathways for holes and electrons, respectively. Note that several other IBC architectures comprise an n^+ Si region at the front surface. Both sides of the cells comprise a random-pyramid texture and an anti-reflection and passivating coating to enhance the light absorption and to reduce surface recombination losses.

The n -type solar cells of Fig. 3 are in particular of industrial interest as they use similar process steps as conventional p -type Si solar cells (e.g., a phosphorus diffusion, deposition of a SiN_x anti-reflection coating, screen printing of metal, contact firing), making the production process more easily adoptable by photovoltaic industries.

Despite the promising aspects of n -type Si solar cells, a number of technological and scientific challenges have to be addressed to achieve high efficiencies while remaining cost-competitive; for instance, insensitivity of cell efficiencies to variations in resistivity of the n -type Si base, an independent control of diffused n^+ and p^+ Si doping profiles, a minimal consumption of silver paste, a reduced recombination at both surfaces, reduced recombination at the contacts (in particular at the p^+ Si side), etc. . To get an idea about the most stringent limitations on the efficiency of a typical industrial n -type cell concept at the start of this PhD project, an overview of the efficiency loss factors of ‘ n -Pasha’ solar cells (see Fig. 3a) at the year 2013 is provided in Table 1. As is clear, *extrinsic recombination* imposed the largest loss factor for the n -Pasha solar cells. The extrinsic recombination of electrons and holes is mediated by the presence of defects or high doping levels and takes place in the c -Si bulk, the surface, the doped regions, and at the metal contacts.

Table 1 Break-down of loss mechanisms in ‘*n-Pasha*’ solar cells, at the start of this Ph.D. project, adapted from Janssen *et al.* [20].

Loss mechanism	J_{sc} (mA·cm⁻²)	V_{oc} (V)	FF	η (%)	$\Delta\eta$ (% abs.)
<i>Intrinsic recombination</i>	46.0	0.745	0.85	29.3	
<i>Metal reflection</i>	41.6	0.743	0.85	27.0	-2.2
<i>Other optical losses</i>	40.0	0.741	0.85	25.3	-1.7
<i>Extrinsic recombination</i>	39.1	0.651	0.81	20.9	-4.4
<i>Ohmic dissipation</i>	39.1	0.651	0.78	19.8	-1.1

As was mentioned before, recombination through surface defects can be reduced through passivation. Although various passivation materials exist, emerging solar cell designs and the search for higher conversion efficiencies impose increasingly stringent demands on surface passivation. For instance, in the cells of Fig. 3, a highly doped *p*-type Si front surface should be passivated. In IBC solar cells, highly doped *p*- and *n*-type Si surfaces (in brief, p^+ and n^+ Si) are adjacent and preferably passivated simultaneously by the same passivation material. Novel light trapping schemes, such as black-Si textures, especially require a high-quality of surface passivation due to their large surface area. Adding to the complexity of surface passivation, subsequent solar cell processing can also significantly influence the passivation quality, such as the deposition of an anti-reflection coating and high temperature process steps such as the ‘firing’ of metal contacts.

Also the metal contacts and highly doped regions in diffused-junction c-Si solar cells induce significant recombination losses. For this reason, significant research attention is currently devoted to solar cells with Si heterojunction (SHJ) contacts. SHJs do not require a highly doped region and are formed by a material which is deposited *on* the crystalline Si surface. Therefore, passivation of defects at the c-Si surface is an essential function of SHJ contacts, which is why they are also referred to as *passivating contacts*. The most prominent SHJs are the intrinsic and doped hydrogenated amorphous silicon (a-Si:H) layers, which exhibit outstanding passivation and contact properties.[5][9] Nonetheless, the sensitive a-Si:H layers cannot withstand temperatures above 200 °C, and therefore require a complete redesign of the solar cell architecture and manufacturing processes. Recently, doped polycrystalline Si (poly-Si) emerged as an alternative passivating contact material.[7,21] Poly-Si is compatible with the metal firing steps employed to contact the screen printed solar cells used in the cells of Fig. 3.[22] Unfortunately, the low transparency of poly-Si based passivating contacts generally limits their application to the rear side of the solar cell.

1.3 Research framework, goals and outline

The work presented in this dissertation took place in the Plasma and Materials Processing (PMP) group at the Eindhoven University of Technology (TU/e) in the Netherlands. Although most of this research was carried out at the TU/e, the TU/e was also engaged in several consortia working on photovoltaics, supported by the *Top Sector Alliance for Knowledge and Innovation* (TKI) programs¹ and *ADEM Innovation Lab* of the Dutch ministry of Economic Affairs. In addition to the TU/e, the consortia encompass research institutes, including the Energy Research Centre of the Netherlands (ECN) and Delft University of Technology, as well as PV equipment manufacturers, such as ASM International, Besi, Eurotron, Levitech, Meyer Burger, and Tempres Systems.

Within the framework of the TKI collaborations, the research was in particular focused on the development of industrially viable, high-efficiency solar cells based on *n*-type c-Si as absorber material. Specifically, the *n-Pasha* and the *Mercury* cell concepts were developed. *n-Pasha* is a bifacial solar cell concept, capable of capturing light from both the front and rear sides, and is currently in production at e.g., Yingli Solar under the brand name *Panda*. *Mercury* is a relatively new interdigitated back-contacted (IBC) concept which was developed in recent years.

Companies such as Levitech and ASM International develop ALD reactors which are equipped for high-volume manufacturing of passivation layers in the PV industry. The PMP group has extensive experience with the characterization and preparation of thin functional films, especially by (plasma-assisted) atomic layer deposition and chemical vapor deposition (CVD). Furthermore, the group has played a pioneering role in the passivation of c-Si surfaces by ALD Al₂O₃ in the past.[23–25]

Although the main working principles of surface passivation by ALD Al₂O₃ were already demonstrated in previous work, the development of the abovementioned solar cells based on *n*-type Si revealed numerous remaining scientific questions or technological challenges. In Fig. 4, an overview of the topics addressed in this dissertation is given.

¹The projects *Advanced Nanolayers 1&2*, *Antilope*, *Compass*, *DutchNess*, *IBChampion* and *Nchanted*

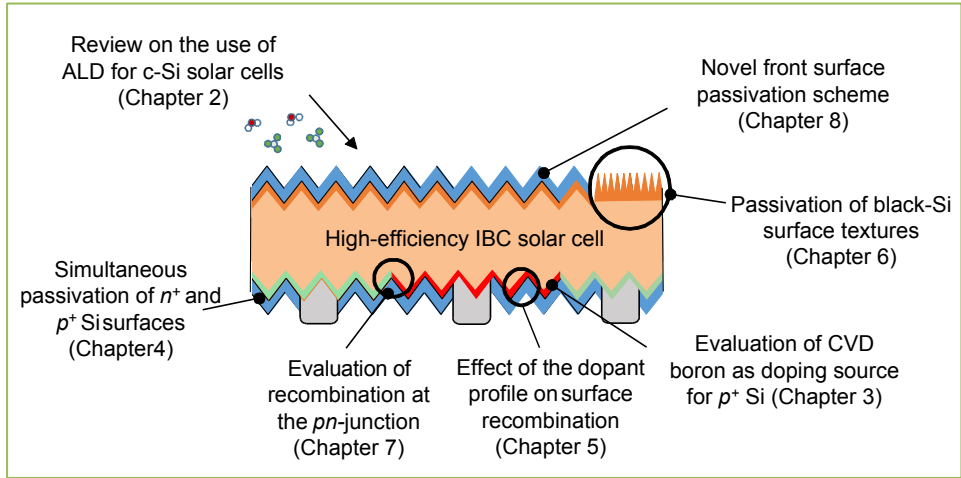


Figure 4 Schematic representation of an interdigitated-back contact solar cell and the focus areas which are investigated in the chapters of this dissertation.

First, in Chapter 2, a full review on the current and future role of ALD for c-Si photovoltaics is presented. This includes the physical principles and current status of surface passivation by Al_2O_3 and other materials. Besides for the deposition of surface passivation layers, it is shown that ALD is suitable for the preparation of many more functional layers for c-Si photovoltaics, such as transparent conductive oxides and carrier-selective contacts. The work presented in this chapter is part of a book on ALD for energy conversion applications, edited by J. Bachmann.

The next chapters of this dissertation deal with the passivation of highly doped surfaces, which is of importance for the solar cells that are developed in the aforementioned consortium. As will become clear in this dissertation, surface recombination depends significantly on the preparation method and dopant distribution of the highly doped regions.

For instance, an alternative boron doping process was developed at Delft University of Technology. This process used, instead of the commonly used BBr_3 as a boron source gas, a pure boron layer on the c-Si surface as diffusion source to form p^+ -type Si. This pure boron layer was deposited by chemical vapor deposition, making the approach radically different from standard tube diffusions. The application of this alternative doping method for c-Si photovoltaics is investigated Chapter 3.

For highly n -type doped surfaces, it was found that passivation by Al_2O_3 was not an ideal match due to its negative fixed charge density.[26] At the same time, the IBC cell architecture demanded a high level of surface passivation of n^+ as well as p^+ Si surfaces,

preferably by a single surface passivation scheme. Earlier work in the PMP group by Dingemans and Terlinden *et al.* [27–29] revealed that the fixed charge density of Al_2O_3 could be controlled by the insertion of an ALD SiO_2 interlayer between the c-Si and Al_2O_3 with a precisely tuned thickness. Moreover, Bordihn *et al.* pioneered the use of an ALD $\text{SiO}_2/\text{Al}_2\text{O}_3$ passivation scheme on both sides of PERC solar cells. [25] In Chapter 4, it will be shown that ALD $\text{SiO}_2/\text{Al}_2\text{O}_3$ stacks are well capable of providing surface passivation to n^+ Si surfaces, as well as to n^+ and p^+ Si surfaces simultaneously. The ALD stacks were scaled up at ASM's high-throughput ALD batch reactors after modifications of the ALD SiO_2 process (the batch reactors required an ALD process based on ozone rather than O_2 plasma as oxidant). Ultimately, the stacks were tested in 6" n -type bifacial and IBC solar cells.

The optimization of the highly doped regions and surface passivation schemes is an intricate task. Despite results in throughout literature showing the outstanding passivation of highly boron-doped surfaces by Al_2O_3 (e.g., Refs. [17],[30]), no apparent gains in solar cell efficiency for n -Pasha cells were obtained when using ALD Al_2O_3 instead of SiN_x yet. Moreover, the testing of the available passivation materials (see e.g., Ref. [31] for such a comparison) after modifications of the doping profile is a time-consuming task. Highly doped regions fulfil many requirements in solar cells. Chapter 4 focusses on the passivation of highly doped surfaces by various industrially relevant surface passivation schemes. The focus lies on the effective decoupling of the other functions -and the profile-of the highly doped regions from surface recombination, to provide guidelines for further optimizations.

Black Si nanotextures were being (further) developed several places, including at Delft University of Technology [32,33] Despite its excellent optical properties, the recombination in such nanotextures remains a bottleneck for a large-scale implementation in c-Si solar cells. Therefore, the knowledge gained in Chapters 3–5 on the topic of surface passivation of highly doped regions was used in Chapter 6, which addresses the recombination of lowly- as well as highly doped black-Si textures. For instance, the ALD $\text{SiO}_2/\text{Al}_2\text{O}_3$ passivation stacks presented in Chapter 4 are used for the surface passivation of n^+ -type black Si front surface textures in Chapter 6.

The passivation of uniform highly doped n^+ and p^+ Si surfaces was studied in earlier Chapters. Nonetheless, at the rear side of IBC cells, the situation becomes radically more complex. There, the n^+ and p^+ Si regions are interdigitated and form pn -junctions. During the development of IBC cells, clues were found for the presence of a significant efficiency loss channel, possibly near the pn -junction, which was not under control yet. To resolve

and understand this issue, dedicated experiments were set up, of which the results and insights are presented in Chapter 7.

At last, in Chapter 8, a novel surface passivation scheme is presented. Recently, novel passivating contacts have been gaining significant attention in the c-Si PV community, to overcome strong recombination which is often associated with the presence of highly doped regions in homojunction solar cells. Nonetheless, a transparent passivating contact which is not based on a-Si:H is lacking. Several co-workers in the PMP group [34–36] as well as researchers from many other groups [37–40] have been investigating the use of metal oxides as transparent passivating contacts. The knowledge gained on surface passivation in this dissertation work ultimately led to the discovery of surface passivation by ZnO films. The ZnO films are of great interest as transparent passivating electron contacts. Moreover, the methods to achieve surface passivation by ZnO, which are discussed in Chapter 8, can also be of use in the development of other passivating contacts.

To conclude this section, the expertise of the project partners in terms of solar cells and their processing (doping, texturing, etc.) combined with the expertise of the PMP group on the topic of surface passivation and ALD has formed the basis of several fruitful collaborations during this PhD project. As a result, some of the (published) chapters in this dissertation (i.e., Chapter 3, 6 and 7) have been written in collaboration with project partners. Note that, even though many research questions in this dissertation work originate from the development of bifacial and IBC solar cell concepts, the findings presented in this dissertation are more universally applicable.

References

1. Chapin, D.M., Fuller, C.S., and Pearson, G.L. (1954) A New Silicon *p-n* Junction Photocell for Converting Solar Radiation into Electrical Power. *J. Appl. Phys.*, **25** (5), 676.
2. Zhao, J., Wang, A., Green, M. A., and Ferrazza, F. (1998) 19.8% efficient “honeycomb” textured multicrystalline and 24.4% monocrystalline silicon solar cells. *Appl. Phys. Lett.*, **73** (14), 1991.
3. Green, M.A., Emery, K., Hishikawa, Y., *et al.* (2014) Solar cell efficiency tables (version 44). *Prog. Photovoltaics Res. Appl.*, **22** (7), 701–710.
4. Cousins, P.J., Smith, D.D., Luan, H.-C., *et al.* (2010) Generation 3: Improved performance at lower cost. *35th IEEE Photovolt. Spec. Conf.*, 275–278.
5. Yamaguchi, T., Ichihashi, Y., Mishima, T., *et al.* (2014) Achievement of More Than 25 % Conversion Heterojunction Solar Cell. **4** (6), 1433–1435.
6. Smith, D.D., Cousins, P., Westerberg, S., *et al.* (2014) Toward the Practical Limits of Silicon Solar Cells. *IEEE J. Photovoltaics*, **4** (6), 1465–1469.
7. Glunz, S.W., Feldmann, F., Richter, A., *et al.* (2015) The Irresistible Charm of a Simple Current Flow Pattern – 25 % With a Solar Cell Featuring a Full-Area Back Contact. *Proc. 31st EU-PVSEC Hambg.*, 259–263.

8. Adachi, D., Hernández, J.L., and Yamamoto, K. (2015) Impact of carrier recombination on fill factor for large area heterojunction crystalline silicon solar cell with 25.1% efficiency. *Appl. Phys. Lett.*, **107** (23), 233506.
9. “World ’s Highest Conversion Efficiency of 26.33% Achieved in a Crystalline Silicon Solar Cell - A World First in a Practical Cell Size” September 14, 2016, NEDO, Kaneka Corporation.
10. Richter, A., Hermle, M., and Glunz, S.W. (2013) Reassessment of the limiting efficiency for crystalline silicon solar cells. *IEEE J. Photovoltaics*, **3** (4), 1184–1191.
11. Roselund, C. (2016) Residential solar has passed grid parity in 20 states already. *PV-magazine*.
12. Kenning, T. (2015) “Paradigm change” in Indian power sector as solar bids reach grid parity. *PV-Tech*.
13. (2015) Photovoltaics Report, Fraunhofer ISE. *Freiburg, Novemb. 17*.
14. Agostinelli, G., Delabie, A., Vitanov, P., *et al.* (2006) Very low surface recombination velocities on *p*-type silicon wafers passivated with a dielectric with fixed negative charge. *Sol. Energy Mater. Sol. Cells*, **90** (18–19), 3438–3443.
15. Hoex, B., Heil, S.B.S., Langereis, E., *et al.* (2006) Ultralow surface recombination of c-Si substrates passivated by plasma-assisted atomic layer deposited Al₂O₃. *Appl. Phys. Lett.*, **89** (4), 42112.
16. Schmidt, J., Merkle, A., Brendel, R., *et al.* (2008) Surface passivation of high-efficiency silicon solar cells by atomic-layer-deposited Al₂O₃. *Prog. Photovoltaics Res. Appl.*, **16** (6), 461–466.
17. Benick, J., Hoex, B., van de Sanden, M.C.M., *et al.* (2008) High efficiency *n*-type Si solar cells on Al₂O₃-passivated boron emitters. *Appl. Phys. Lett.*, **92** (25), 253504.
18. Chunduri, S.K., and Schmela, M. (2016) PERC Solar Cell Technology 201: Background, Status and Outlook. *Taiyang news*.
19. Macdonald, D., and Geerligs, L.J. (2004) Recombination activity of interstitial iron and other transition metal point defects in *p*- and *n*-type crystalline silicon. *Appl. Phys. Lett.*, **85** (18), 4061.
20. Janssen, G.J.M., Gutjahr, A., Burgers, A.R., *et al.* (2013) Power loss analysis of n-Pasha cells validated by 2D simulations. *proc. 28th EU-PVSEC Paris*, 1755.
21. Feldmann, F., Simon, M., Bivour, M., *et al.* (2014) Efficient carrier-selective *p*- and *n*-contacts for Si solar cells. *Sol. Energy Mater. Sol. Cells*, **131**, 100–104.
22. Stodolny, M.K., Lenes, M., Wu, Y., *et al.* (2016) *n*-Type polysilicon passivating contact for industrial bifacial *n*-type solar cells. *Sol. Energy Mater. Sol. Cells*, **158**, 24–28.
23. Hoex, B. (2008) Ph.D. Thesis “Functional thin films for high-efficiency solar cells”, Eindhoven University of Technology.
24. Dingemans, G. (2011) Ph.D. thesis “Nanolayer surface passivation schemes for silicon solar cells”, Eindhoven University of Technology.
25. Bordihn, S. (2014) Ph.D. Thesis “Surface passivation by Al₂O₃-based film stacks for Si Solar Cells”, Eindhoven University of Technology.
26. Hoex, B., van de Sanden, M.C.M., Schmidt, J., *et al.* (2012) Surface passivation of phosphorus-diffused *n*⁺-type emitters by plasma-assisted atomic-layer deposited Al₂O₃. *Phys. status solidi - Rapid Res. Lett.*, **6** (1), 4–6.
27. Dingemans, G., Terlinden, N.M., Verheijen, M.A., *et al.* (2011) Controlling the fixed charge and passivation properties of Si(100)/Al₂O₃ interfaces using ultrathin SiO₂ interlayers synthesized by atomic layer deposition. *J. Appl. Phys.*, **110** (9), 93715.
28. Terlinden, N.M., Dingemans, G., Vandalon, V., *et al.* (2014) Influence of the SiO₂ interlayer thickness on the density and polarity of charges in Si/SiO₂/Al₂O₃ stacks as studied by optical second-harmonic generation. *J. Appl. Phys.*, **115** (3), 33708.

29. Dingemans, G., van Helvoirt, C.A.A., Pierreux, D., *et al.* (2012) Plasma-Assisted ALD for the Conformal Deposition of SiO₂: Process, Material and Electronic Properties. *J. Electrochem. Soc.*, **159** (3), H277–H285.
30. Hoex, B., Schmidt, J., Bock, R., *et al.* (2007) Excellent passivation of highly doped *p*-type Si surfaces by the negative-charge-dielectric Al₂O₃. *Appl. Phys. Lett.*, **91** (11), 112107.
31. Saynova, D.S., Romijn, I.G., Cesar, I., *et al.* (2013) Dielectric Passivation Schemes for High Efficiency *n*-Type c-Si Solar Cells. *Proc. 28th EU-PVSEC*, 1188–1193.
32. Ingenito, A., Isabella, O., and Zeman, M. (2014) Experimental Demonstration of $4n^2$ Classical Absorption Limit in Nanotextured Ultrathin Solar Cells with Dielectric Omnidirectional Back Reflector. *ACS Photonics*, **1** (3), 270–278.
33. Ingenito, A., Isabella, O., and Zeman, M. (2015) Nano-cones on micro-pyramids: modulated surface textures for maximal spectral response and high-efficiency solar cells. *Prog. Photovoltaics Res. Appl.*, **20** (1).
34. Smit, S., Garcia-Alonso, D., Bordihn, S., *et al.* (2014) Metal-oxide-based hole-selective tunneling contacts for crystalline silicon solar cells. *Sol. Energy Mater. Sol. Cells*, **120**, 376–382.
35. Macco, B., Vos, M.F.J., Thissen, N.F.W., *et al.* (2015) Low-temperature atomic layer deposition of MoO_x for silicon heterojunction solar cells. *Phys. status solidi - Rapid Res. Lett.*, **9** (7), 393–396.
36. Melskens, J., van de Loo, B.W.H., Macco, B., *et al.* (2015) Concepts and prospects of passivating contacts for crystalline silicon solar cells. *IEEE 42nd Photovolt. Spec. Conf.*, (June), 1–6.
37. Battaglia, C., Yin, X., Zheng, M., *et al.* (2014) Hole selective MoO_x contact for silicon solar cells Hole selective MoO_x contact for silicon solar cells. *Nano Lett.*, **14** (2), 967–71.
38. Avasthi, S., McClain, W.E., Man, G., *et al.* (2013) Hole-blocking titanium-oxide/silicon heterojunction and its application to photovoltaics. *Appl. Phys. Lett.*, **102** (20), 203901.
39. Young, D.L., Nemeth, W., Grover, S., *et al.* (2014) Carrier-selective, passivated contacts for high efficiency silicon solar cells based on transparent conducting oxides. *IEEE 40th Photovolt. Spec. Conf.*, 1–5.
40. Yang, X., Zheng, P., Bi, Q., and Weber, K. (2016) Silicon heterojunction solar cells with electron selective TiO_x contact. *Sol. Energy Mater. Sol. Cells*, **150**, 32–38.

CHAPTER 2

Atomic Layer Deposition for High-Efficiency Crystalline Silicon Solar Cells*

Preface In this Chapter, an overview is provided of the current and potential role of atomic layer deposition (ALD) within crystalline silicon (c-Si) photovoltaics. More specifically, in the Section 2.1, c-Si solar cell concepts will be introduced. Potential applications of ALD to advance these solar cells are outlined. In Section 2.2, ALD surface passivation schemes and the recent introduction of ALD Al₂O₃-based passivation layers into the photovoltaic industry will be reviewed. In this section, also novel experimental results will be included. Section 2.3 treats atomic-layer-deposited transparent conductive oxides, which find their application in silicon heterojunction solar cells. Section 2.4 discusses the use of ALD in the upcoming field of passivating contacts. The potential processing simplicity and effectiveness of such passivating contacts will be illustrated.

* Published as: *B. Macco,¹ B. W. H. van de Loo,¹ and W. M. M. Kessels, as a chapter in "Atomic layer deposition in energy conversion applications" by Julien Bachman, Wiley, 2017 (¹Both authors contributed equally.)*

2.1 Introduction to high-efficiency crystalline silicon solar cells

In the year 2015, crystalline silicon (Si) solar cells are being mass-produced at a typical rate of 43 GWp/year, and they dominate the photovoltaic (PV) market with a share of >90%.[1] The success of Si solar cells over other solar cell technologies lies in their ever improving cost-effectiveness, high efficiency and proven stability. In fact, the Si solar cells themselves are not even the main contributor to the total cost of solar electricity anymore.[1] Because of this, higher conversion efficiencies have become the main driver for a further cost reduction of solar electricity.

As is the case for most semiconductor devices, also for Si solar cells the electronic quality of the surfaces is becoming more important. Therefore, a precise engineering of interfaces is key in achieving optimal device performance and consequently higher conversion efficiencies. For instance, by reducing the interface defect density of Si by a thin passivation layer of Al₂O₃, the efficiency of Si solar cells could significantly be enhanced. It was for this particular application that the potential of atomic layer deposition (ALD) for Si solar cells was for the first time revealed in 2004.[2] Due to the development of novel high-throughput ALD reactors, ALD of Al₂O₃ has since then even found its way to the high-volume manufacturing (HVM) of Si solar cells. Today, Al₂O₃ nanolayers prepared by ALD can contribute to a ~1% absolute increase in conversion efficiency of commercial *p*-type solar cells and they are incorporated in *n*-type laboratory solar cells with record efficiencies of >25%.[3]

In a broader context, the success of ALD Al₂O₃ also triggered the exploration of ALD for the preparation of other functional layers for a variety of other solar cell concepts. For example ALD is used for the deposition of transparent conductive oxides (TCOs). TCOs should be simultaneously transparent and conductive, and therefore should have a high electron mobility. It turns out that ALD is well suited for the deposition of such films, as is for instance evident from ALD TCOs with record-high electron mobilities of 138 cm²V⁻¹s⁻¹.[4]

This chapter will illustrate that ALD is in fact an enabler of novel high-efficiency Si solar cells, owing to its (unique) merits such as a high material quality, precise thickness control and the ability to prepare film stacks in a well-controlled way. In the remainder of this section, a brief overview of the field of Si solar cells is given, where for each concept the present and potential role of ALD is discussed.

In short, a solar cell can deliver power when excess electrons and holes, created by the absorption of light in the semiconductor, are extracted separately by electrodes. To enable this, the two types of electrodes should be made selective for the extraction of only electrons or holes. Commonly, Si solar cells are classified by the type of junction which is formed in the creation of such *carrier selective contacts*. Based on such classification, in Fig. 1, a concise overview of the most common Si solar cell concepts is given. Note that each individual concept will be discussed in more detail below.

The first class of solar cells (which is industrially by far the most used) is based on *homojunctions*, which are formed by doping separate regions of the Si, making them highly *n*- or *p*-type doped (also referred to as n^+ or p^+ Si). In this way, the metal electrode which contacts the n^+ or p^+ Si is made selective for the extraction of either electrons or holes, respectively.

Heterojunctions, which are junctions between Si and other materials, are also used to achieve such charge-carrier selectivity. Interestingly, for these types of cells, i.e., whether involving homojunctions, heterojunctions, or a combination of both, record conversion efficiencies over 25% have been demonstrated on a lab scale.[3,5–8] Although such efficiencies are already close to the predicted fundamental limit of 29.4% for Si solar cells,[9] research efforts are still ongoing to attain more cost-effective approaches for the high-volume manufacturing of such cells in industry.

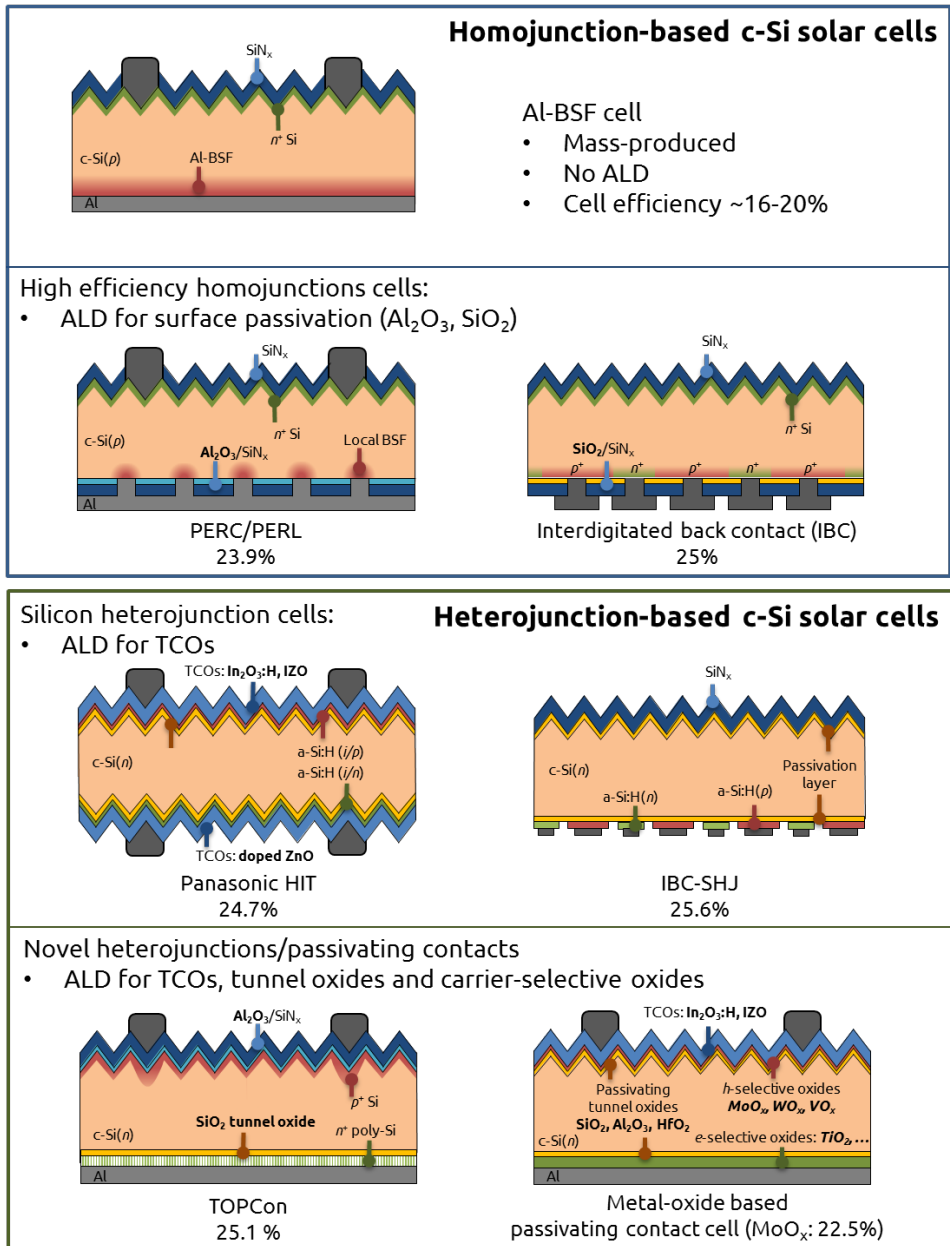
ALD for Si homojunction solar cells

The current workhorse of the PV industry is the aluminium back-surface field (Al-BSF) solar cell which is based on *p*-type Si (see Fig. 1). It typically yields moderate conversion efficiencies of 16 – 20% and can be manufactured very cost-effectively. On the front side, an n^+ Si region is present (conventionally termed an ‘emitter’), which makes the front contacts selective for the extraction of electrons. Moreover, the n^+ Si also serves as lateral conduction pathway for electrons to the front contact grid. In between the metal contacts, hydrogenated amorphous silicon nitride, a-SiN_x:H (also referred to as SiN_x) is typically present as anti-reflection coating (ARC). Additionally, the SiN_x reduces electron-hole recombination at the Si surface and bulk, which is referred to as *surface passivation*. The latter is vital to achieve a high open-circuit voltage, V_{oc} , and hence a high solar cell efficiency. At the full back side of the Al-BSF solar cell, Al is screen-printed and subsequently partially alloyed with the Si by a high-temperature “firing” step at about 800 °C. In this way, Al contacts Al-doped (p^+ -type) Si, and a hole-selective contact is formed. In the Al-BSF concept, generally no layers are prepared by ALD.

A more advanced concept, which is still industrial but allows for higher conversion efficiencies, is the so-called passivated emitter and rear contact (PERC) solar cell. Instead of using Al over the full area (as is the case for the Al-BSF cell), it uses *local* Al contacts at the rear side. In this way, the Si surface in between the contacts can be passivated by a thin film or stack of thin films, which reduces charge-carrier recombination and in this way enhances the conversion efficiency. In the last decade, ALD of Al₂O₃ has been proven to be very successful for the passivation of this lowly doped *p*-type Si back surface, and this application even paved the way for ALD for implementation in solar cell manufacturing.

Besides reducing charge-carrier recombination at the Si back surface, the recombination via defects in the Si bulk should also be minimized to attain high conversion efficiencies. For instance, rather than the low-cost multicrystalline Si, which has also defects at its grain boundaries, more expensive monocrystalline Si wafers can be used. Also *n*-type Si wafers can be used instead of the conventionally used *p*-type Si wafers, as they generally have a higher bulk material quality due to e.g., the absence of boron-oxygen defects and reduced sensitivity for most common transition metal impurities. Therefore, *n*-type cell concepts compete with (*p*-type) PERC concepts for a spot in the high-efficiency segment. Most solar cells based on *n*-type Si require *p*-type doping of the full Si front surface (such a cell is not shown in Fig. 1). For a long time, this approach was considered to be challenging, in part due to a lack of a suitable passivation scheme for *p*⁺ Si. Also for the passivation of these *p*⁺ Si surfaces, Al₂O₃ prepared by ALD resulted in a breakthrough, yielding solar cell conversion efficiencies of up to 23.2% at that time.[10]

Finally, even higher efficiencies can in principle be obtained by using interdigitated back-contact (IBC) cell concepts,[6] albeit at the price of requiring more processing steps. In IBC concepts, the electron- as well as the hole-selective contacts are localized at the rear side to avoid parasitic absorption and reflection by front metallization. Also for IBC solar cells, ALD layers are being investigated, for instance to passivate defects at the *n*⁺ or *p*⁺ Si surfaces at the back side of the solar cell simultaneously.[11]



ALD for Si heterojunction solar cells

A radically different solar cell design, which has successfully been developed by Panasonic (formerly Sanyo), is the heterojunction with intrinsic thin layer (HITTM), [12] generally referred to as the silicon heterojunction (SHJ) concept. Here, intrinsic and doped hydrogenated amorphous Si (a-Si:H) layers are used for the passivation of the Si surfaces and to achieve selectivity for the extraction of charge carriers, respectively. For conventional Si homojunction solar cells, the lateral conduction of excess charge carriers towards the metal grid takes place via the highly doped and conductive regions. However, in SHJ cells, the conductivity in the highly doped regions is low (i.e., the thickness of the highly doped regions is 5 – 10 nm), which is why TCOs are used on both sides of the SHJ cell.

TCOs prepared by ALD can fulfil the stringent requirements set by the SHJ cells in terms of processing (e.g., a low deposition temperature <200°C, and *soft* deposition) as well as in material quality (e.g., high conductivity and transparency and a suitable work function). Despite its high potential, ALD is not yet implemented in HVM for this application. Nonetheless, the deposition of TCOs in an industrial ALD reactors has already been achieved. [13]

The discrepancy between the maximal efficiency for conventional SHJ cells (25.1% [14]) and the fundamental limit of Si solar cells (i.e., 29.4% [9]) is partially attributed to the parasitic absorption or reflection by the front a-Si:H layers and the TCO. This can be overcome in several ways. For instance, by using an IBC-SHJ concept, no front TCO is required and the a-Si:H layers are only used at the back side. In this way, the world record efficiency for silicon solar cells of 26.33% has been achieved by Kaneka. [15] It is not disclosed at this moment whether ALD is used in this concept.

Novel passivating contacts and ALD

Due to the limit in processing temperature which can be a challenge for HVM and due to parasitic absorption of a-Si:H based heterojunction cells, research efforts are also targeting other types of materials that make the electrodes carrier-selective. These are generally referred to as *passivating contacts*.

For example, a novel passivating contact approach is the tunnel oxide passivated contact (TOPCon). It has excellent thermal stability and so far has reached a conversion efficiency of 25.1%. [3] TOPCon is in fact a *hybrid* cell design, as on the front a classical homojunction is formed, which is passivated by Al₂O₃, whereas at the full back side a highly doped (partially) crystalline Si, so-called poly-Si, passivating contact forms a

heterojunction. The contact is made selective to extract either electrons or holes by the choice of dopant. Moreover, a very thin, passivating tunnel oxide at the interface between Si and the partially crystalline Si is key in achieving the high conversion efficiencies.[16] Conceivably, the precise thickness control offered by ALD can play a key role in studying and optimizing the often encountered trade-off between surface passivation and contact resistivity in passivating contacts.

Interestingly, there is also increasing interest in novel heterojunctions based on metal-oxides as passivating contacts. Preferably, they are fully transparent, in contrast to partially crystalline Si and a-Si:H. If such a passivating contact can be used on the full area of the solar cell, they could yield a significant process simplification. Metal oxides of interest include for example MoO_x ,[17] WO_x ,[18] NiO_x ,[19] and TiO_x ,[20] for which ALD processes readily exist and are also being explored.[21] Also well-defined stacks of metal oxides or other materials can be used, which provide surface passivation, carrier selectivity as well as lateral conduction.[22,23] Potentially, such stacks could find their way into novel silicon solar cell concepts, allowing for very high conversion efficiencies in combination with cost-effective manufacturing.

Outline of this chapter

The chapter is organized as follows. In section 2.2, the role of ALD in preparing passivation layers for homojunction Si solar cells is discussed. Special attention is given to the physics of surface passivation, the surface passivation by ALD Al_2O_3 , ALD as a high-throughput deposition technique in the PV industry and recent developments in the field of passivation layers prepared by ALD. Section 2.3 focusses on TCOs prepared by ALD for use in heterojunction Si solar cells, such as doped ZnO and In_2O_3 films. Therefore, the physics of TCOs and the specific requirements of TCOs for SHJ cells are briefly discussed first. Finally, in section 2.4, novel passivating contacts based on metal oxides are considered. Various unique aspects of ALD, such as the ability to prepare precisely tailored stacks play an important role here.

2.2 Nanolayers for surface passivation of Si homojunction solar cells

In this section, the status-quo and opportunities for ALD passivation layers for Si homojunction solar cells are discussed. First, the physical mechanisms of surface recombination and the basics of surface passivation are discussed. Next, an overview of ALD Al_2O_3 , which is widely used for the passivation of p and p^+ -type surfaces, is given. Moreover, also the requirements for deposition techniques in the high-volume manufacturing of silicon solar cells in industry are discussed together with novel high-throughput ALD reactors. In Section 2.2.4 further opportunities and recent developments in the field of ALD for the passivation of Si are outlined. Examples include ALD layers for the passivation of n^+ Si, the passivation of surfaces with demanding topologies and recent developments of novel, alternative passivation layers prepared by ALD.

2.2.1 Basics of surface passivation

The physics of surface recombination

By the absorption of light in Si, excess electrons and holes are generated (see Fig. 2), with densities Δn and Δp , respectively, which increases their respective densities n and p from their equilibrium values n_0 and p_0 to $n=n_0+\Delta n$ and $p=p_0+\Delta p$. After generation, the excess charge carriers thermalize very rapidly (i.e., in $\sim 10^{-12}$ s) to the temperature of the Si lattice, T . Rather than by a single Fermi energy level, E_F , which is used to describe semiconductors in the dark, under illumination the distributions of electrons and holes can be described by their own quasi-Fermi energies, E_{Fn} and E_{Fp} . Also here, the carrier densities are still given by the energetic distance of the quasi Fermi level to the conduction and valence band, respectively. For Boltzmann statistics, the pn product is given by;

$$pn = (p_0 + \Delta p)(n_0 + \Delta n) = n_i^2 \exp\left(\frac{E_{Fn} - E_{Fp}}{kT}\right) \quad (2.2.1)$$

With n_i the intrinsic carrier density and k the Boltzmann constant. The free energy per electron hole pair is $E_{fn} - E_{fp}$, and corresponds to the implied voltage iV_{oc} in the cell, i.e., $E_{Fn} - E_{Fp} = q \cdot iV_{oc}$, with q the elementary charge.

The quasi-Fermi level splitting induced by the generation of charge carriers is also the driver of processes which tend to restore thermodynamic equilibrium. In such processes excess charge carriers recombine and their associated free energy is lost. To a certain

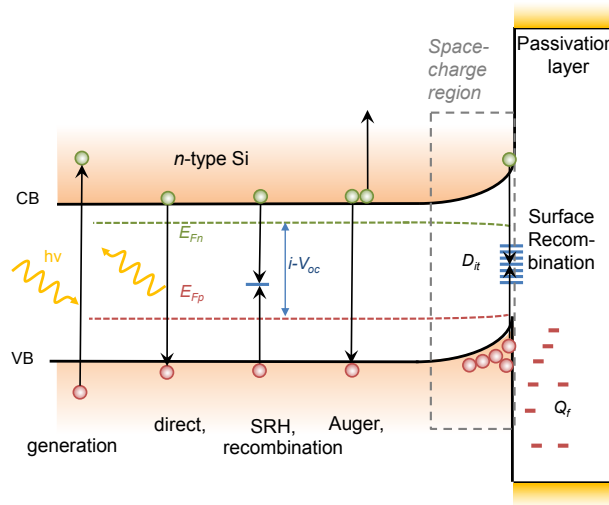


Figure 2 Schematic band diagram of the passivated silicon surface, indicating the generation of excess carriers by the absorption of light and the recombination thereof, which can take place either directly, via a third carrier (in the Auger process) or via defect states (SRH recombination). At the surface, a high density of interface (defect) states D_{it} exists. A passivation layer reduces the D_{it} , and (in this example) reduces the electron concentration at the surface via a negative fixed charge density Q_f , which induces a space-charge region and upwards band-bending. The quasi-Fermi level for electrons E_{Fn} and holes E_{Fp} , the valence band (VB) and conduction band (CB) of Si and the implied open-circuit voltage iV_{oc} are indicated.

extent this recombination is unavoidable, because of intrinsic channels, which are direct (radiative) and Auger recombination. In these processes, the energy is transferred to a photon and/or phonons or a third carrier, respectively. Also recombination via extrinsic lattice defects or impurities which form states in the band gap of Si can take place, a pathway which is named after Shockley, Read, and Hall (SRH) who formulated the theory describing this kind of recombination. In particular at the surface, as the silicon lattice terminates, a high density of Si dangling bonds is natively present, which form defect levels (e.g., P_{b0} defects) and therefore induce strong SRH recombination.

The recombination rate of charge carriers at the surface U_s (with units $\text{cm}^{-2}\text{s}^{-1}$) can be described via the extended SRH formalism, which considers a continuum of defects throughout the band gap of Si, with energy-dependent density, $D_{it}(E)$;

$$U_s = \left(p_s n_s - n_{i,eff,s}^2 \right) \int_{E_g} \frac{dE}{\frac{n_s + n_1(E)}{S_{p0}(E)} + \frac{p_s + p_1(E)}{S_{n0}(E)}} \quad (2.2.2)$$

with $S_{n0}(E) = v_t D_{it}(E) \sigma_n(E)$ and $S_{p0}(E) = v_t D_{it}(E) \sigma_p(E)$. In these expressions, v_t is the thermal velocity, $n_{i,eff,s}$ the *effective* intrinsic carrier concentration at the surface (taking into account band gap narrowing and Fermi-Dirac statistics), n_s and p_s the electron and hole concentrations at the surface, $\sigma_n(E)$ and $\sigma_p(E)$ the (energy-dependent) hole or electron capture cross sections respectively, which are directly related to the physical processes of carrier capture by the defect states. The SRH densities n_1 and p_1 , given by

$$n_1 = N_C \exp\left(-\frac{E_C - E_t}{kT}\right), \quad p_1 = N_V \exp\left(-\frac{E_t - E_V}{kT}\right),$$

determine the effectiveness of the defects as recombination sites, where E_t the energy level of the defect and N_C and N_V the effective density of states of the conduction and valence band, respectively. In particular defects near the center of the band gap of Si are most effective as recombination sites. Also when the capture rate of electrons by a defect equals the capture rate of holes, i.e., when the following condition is satisfied;

$$\sigma_p \times p_s \approx \sigma_n \times n_s \quad (2.2.3)$$

the defect is most effective as a recombination site.

Even though U_s is the main physical parameter which should be minimized, it is experimentally not directly accessible. For this reason, other figures of merit are usually used to assess the surface recombination (see table 1), such as the effective minority carrier lifetime τ or the implied open circuit voltage iV_{oc} , which are both ideally as high as possible. However, of both these parameters also include the influence of other recombination processes, such as those in the bulk of Si. To quantify only the surface recombination, the effective surface recombination velocity S_{eff} or surface saturation current density J_{0s} can be evaluated.[24,25] The latter parameter J_{0s} (with units $A \cdot cm^{-2}$) offers the advantage that it (for flat quasi-Fermi levels) directly translates to the open-circuit voltage V_{oc} of the solar cell via:

$$V_{oc} = \frac{nkT}{q} \ln\left(\frac{J_{sc}}{J_{0s} + J_{0,other}} + 1\right) \quad (2.2.4)$$

with n the ideality factor, J_{sc} the short-circuit current density and $J_{0,others}$ a parameter accounting for all other recombination pathways, such as in the Si bulk. Due to the large surface-to-volume ratio in Si solar cells, the surface can be the dominant recombination source. With current trends toward thinner or higher quality Si wafers, bulk recombination is further reduced, making surface recombination even more important.

Table 1 A selection of commonly used parameters to assess surface passivation quality. Some parameters not only account for recombination at the surface, but also encompass recombination in the highly doped region (HDR), in the Si bulk or in the space-charge region (SCR) induced in the Si by the passivation scheme. The parameters are evaluated with respect to their average carrier densities in the Si bulk (n, p), the densities at the surface (n_s, p_s), the edge of the SCR (n_d, p_d), or the base side of the HDR (n_w, p_w). They can be assessed by photoconductance (PC), photoluminescence (PL), current-voltage (J - V) or Suns- V_{oc} measurements.

Parameter	Symbol	Encompasses recombination in or at the	Assessed by	Definition
Effective minority carrier lifetime	τ_{eff}	Bulk, HDR, SCR, surface	PC, PL	$\tau_{eff} \equiv \frac{\Delta n}{U_{(total)}}$
Surface recombination velocity (SRV)	S	Surface	Inaccessible (in most cases)	$S \equiv \frac{U_s}{\Delta n_s}$
Effective surface recombination velocity	S_{eff}	Surface, SCR	PC, PL	$S_{eff} \equiv \frac{U_s}{\Delta n_d}$
Implied open-circuit voltage	iV_{oc}	Bulk, HDR, SCR, surface	PC, PL	$iV_{oc} \equiv \frac{kT}{q} \ln \left(\frac{np}{n_i^2} \right)$
Surface saturation current density	J_{0s}	Surface	PC, PL	$J_{0s} \equiv qU_s \left(\frac{p_s n_s}{n_{i,eff,s}^2} - 1 \right)^{-1}$
“Emitter” Saturation current density	J_{0e}, J_0	HDR, SCR, surface	PC, PL, J-V, Suns- V_{oc}	$J_{0e} \equiv qU_{HDR,surface} \times \left(\frac{p_w n_w}{n_{i,eff,w}^2} - 1 \right)^{-1}$

Surface passivation in practice

To minimize surface recombination, several strategies can be used. First of all, the D_{it} which is natively present can be reduced by orders of magnitude by several approaches, which is referred to as *chemical passivation*. Chemical passivation can be obtained by depositing a thin film on the silicon surface, which binds to the Si dangling bonds. Moreover, (atomic) hydrogen released from the passivation scheme or forming gas in a

post deposition anneal (PDA) can subsequently passivate remaining defects. The most prominent examples of materials used for surface passivation of solar cells include thermally grown SiO₂, plasma-enhanced chemical vapor deposited (PECVD) SiN_x, PECVD a-Si:H and ALD Al₂O₃. [26,27] Naturally, to achieve chemical passivation, the passivation layers should also exhibit a low density of states at energy levels which are relevant for charge carrier-recombination in Si. For this reason, materials with a wide band gap and low impurity content are most successful. Metals on the contrary, have a large and continuous distribution of states and therefore act as catalyst for carrier recombination when brought in contact with Si.

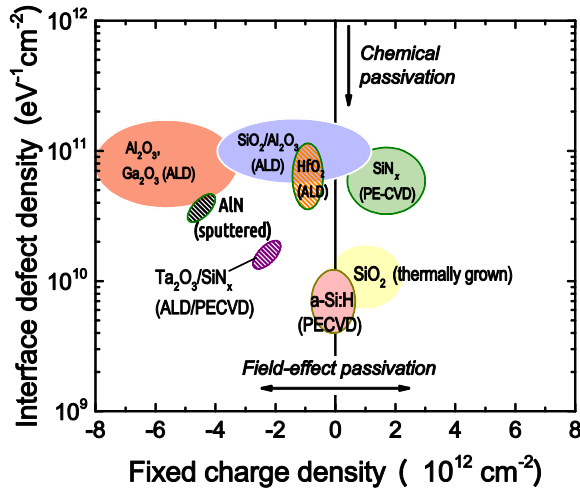


Figure 3 Schematic overview of typical interface defect densities and fixed charge densities of passivation schemes, adapted from Cuevas *et al.*, [28] Note that the actual interface properties might strongly depend on the processing conditions of the passivation layer.

Another strategy to reduce surface recombination is the suppression of either the electron or hole concentration at the surface (see equation 2.2.2). Such suppression can be achieved via band bending in the Si, for instance by a fixed charge density Q_f in the passivation layer, and is commonly known as *field-effect passivation*. Thermally-grown SiO₂ natively possesses a slight positive $Q_f \sim 10^{11} \text{ cm}^{-2}$, SiN_x a strong positive Q_f (typically $\sim 3 \cdot 10^{12} \text{ cm}^{-2}$) whereas ALD Al₂O₃ films typically exhibit a strong negative Q_f ($\sim 10^{12} - 10^{13} \text{ cm}^{-2}$). [29] In Fig. 3, a schematic overview of interface properties of various passivation schemes is given.

Naturally, the carrier densities at the Si surface are, besides band bending, also largely dictated by the (local) *doping level* of the silicon N_s . The polarity of the fixed charge density in the dielectric is of importance when passivating doped surfaces, as the Q_f can either further reduce or increase the minority carrier density, and in this way has a strong influence on the surface recombination. For instance for heavily p -type doped surfaces (p^+ Si), electrons are the minority carriers. The passivation scheme for such surface therefore ideally has a negative Q_f to reduce the electron concentration even further. For n^+ Si surfaces on the other hand, electrons are the *majority* carriers and their density is not reduced significantly by a negative Q_f . Therefore, the negative Q_f typically increases the minority carrier density at n^+ Si surfaces, which increases surface recombination.

To further illustrate the effect of the doping level and fixed charge density on the surface recombination, in Fig. 4 the SRH is evaluated for a fixed level of chemical passivation. Interestingly, for very high doping levels (i.e., $N_s > 10^{20} \text{ cm}^{-3}$), the density and polarity of fixed charges in the range evaluated here have virtually no influence on the surface recombination, which is low in all cases. For lower N_s (i.e., in the range of $\sim 10^{20} \text{ cm}^{-3}$ or lower) the condition where the SRH recombination is the strongest (equation 2.2.3) is met, but only when a passivation layer with the ‘wrong’ charge polarity is used. Explicitly put, a high J_{0s} arises for a negative Q_f on n^+ -type Si or for positive Q_f on p^+ Si surfaces. Finally, for lower N_s (i.e., $N_s < 10^{18} \text{ cm}^{-3}$), the passivation quality is excellent, even in case of a ‘wrong’ charge polarity. In that case, the band bending induced by the fixed charge density brings the Si surface into inversion. Even though in that case the surface can be very well passivated, inversion layers are still undesirable in most solar cells. It is shown that they can form parasitic shunt pathways and possibly induce SRH recombination in the depletion region which is formed near the surface, having an adverse impact on the efficiency of solar cells.[30,31]

In summary, it can be stated that for passivation schemes a low D_{it} is always preferred, whereas in general the ideal Q_f depends on the surface doping concentration of the Si. Methods to control the Q_f of ALD passivation schemes will be discussed in section 2.2.4. Finally, it should be noted that in case of very strong surface recombination, such as for poorly passivated surfaces or when metal is contacting Si, the surface recombination rate becomes limited by the transport of excess charge-carriers towards the surface. In this case, the presence of a highly doped (p^+ or n^+ Si) region can significantly reduce the transport of excess carriers towards the surface and in this way reduce recombination. Well-known examples are the p^+ Si and n^+ Si regions of Si homojunction solar cells (see

Fig. 1), which ‘shield’ the metal contacts and make them selective for the extraction of only one charge carrier type. For well-passivated surfaces on the other hand, the transport of minority carriers through the highly doped region is generally not limiting or affecting the surface recombination rate. Then, the highly doped region is called *transparent*.

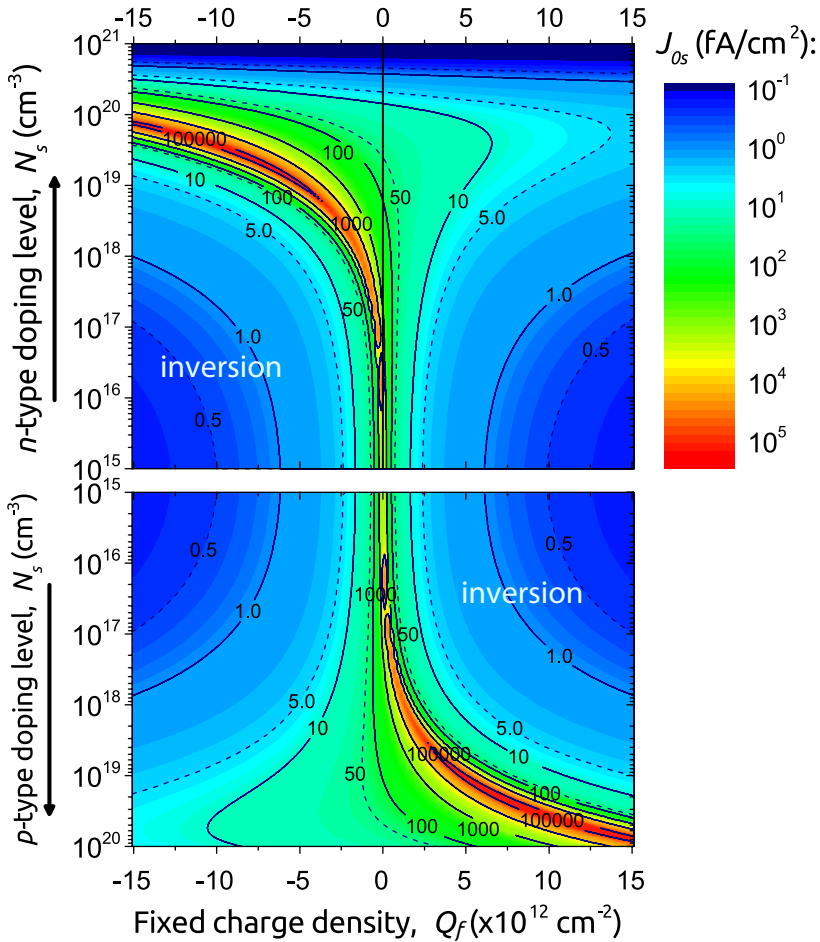


Figure 4 The effects of the fixed charge density and the surface doping concentration on the surface saturation current density for a fixed level of chemical passivation. The results are evaluated using equation (2.2.2) for a single defect, with $S_{n0} = S_{p0} = 5000$ cm/s. The carrier densities are derived from the Girisch algorithm,[32] using Fermi-Dirac statistics, $n_i = 9.65 \cdot 10^9$ cm⁻³,[33] a base injection level of $\Delta n = 1 \cdot 10^{15}$ cm⁻³ and base doping level of $N_{base} = 1 \cdot 10^{15}$ cm⁻³. For the band gap narrowing of *n*- and *p*- type Si, the empirical models of Yan and Cuevas are used.[34,35]

Compatibility of passivation schemes with Si homojunction solar cells

For implementation in Si solar cell manufacturing, passivation schemes should meet many requirements, both from a device and processing perspective. From an optical point of view, a high transparency to the solar spectrum is necessary when passivating the front or (for bifacial cells, which capture light from both sides) the rear surface. Moreover, a suitable refractive index n of ~ 2 at 2 eV is preferred for anti-reflection purposes, although sometimes the passivation scheme can be combined with a separate ARC. In contrast, a low refractive index is preferred when acting as dielectric mirror on the back side of the solar cell.

As solar cells and PV modules are designed to last for decades, also a long-term stability of the passivation scheme is required. Passivation schemes can in particular suffer from light- or potential- induced degradation (LID or PID, respectively). An ultra-high-temperature stability (i.e., up to 800°C for some seconds) is required when screen- or stencil-printed metal fingers are “fired” through the passivation layer and ARC to contact the Si. In contrast, when the contacts are made at low temperatures by electro-plating, this requirement is redundant. However in the latter process, a pinhole-free thin film with a low leakage current is necessary to prevent undesired “ghost” plating of metal

Finally, the implementation in solar cells can also put (technological) requirements on the processing of passivation schemes. For instance a large area uniformity is desired, with solar cell dimensions $156 \times 156 \text{ mm}^2$ being the industrial standard. Moreover, a low-temperature process for the preparation of the passivation layer is preferred, not only from a cost-perspective, but also because high temperatures (for instance used for thermal oxidation) can cause severe degradation of the Si bulk quality,[36] in particular for multicrystalline Si. In addition to passivation of its surface, for multicrystalline Si also the passivation of dislocations by hydrogen can be required.

2.2.2 Surface passivation by ALD Al_2O_3

The passivation of p -type Si and heavily doped p^+ -type Si surfaces is very relevant for many high-efficiency solar cell concepts. Nonetheless, historically, before the introduction of ALD Al_2O_3 , the passivation of such p -type Si surfaces was challenging. Thermal oxidation of Si yields excellent levels of chemical passivation with a very low positive Q_f , but its passivation of boron-doped surfaces is not stable over time.[37] Besides, thermal oxidation depletes the boron-doping near the surface, and its high temperature processing can have an adverse impact on the bulk lifetime.[36,38] SiN_x on the other hand, although

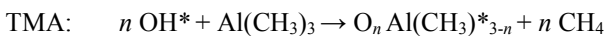
very well suited as passivation layer for n^+ Si and as ARC, is undesirable for the passivation of p -type Si surfaces due to its positive Q_f .

The first results on Si surface passivation for solar cells by Al_2O_3 were reported in 1980s by Hezel and Jaeger.[39,40] In this case the Al_2O_3 was prepared by CVD (pyrolysis). Nonetheless, the broad recognition of Al_2O_3 as an outstanding surface passivation layer was yet to come. It was not until 2006, before this was realized. This time, it was reported by Agostinelli *et al.*,[27] and Hoex *et al.*,[41] that Al_2O_3 provides excellent passivation on p -type Si surfaces. In these cases, the Al_2O_3 was prepared by ALD using trimethylaluminium (TMA) and H_2O or O_2 plasma as precursors. The excellent levels of surface passivation offered by the Al_2O_3 films were attributed to a combination of excellent chemical and field-effect passivation. In particular, ALD Al_2O_3 provides a very low D_{it} of $<10^{11} \text{ cm}^{-2}$, while it distinctively exhibits a large *negative* Q_f of 10^{12} – 10^{13} cm^{-2} . [29] Such interface properties were already reported in the first ALD Al_2O_3 experiments using TMA and H_2O in 1989.[42] Due to its negative Q_f , Al_2O_3 is the ideal match for the passivation of p - and p^+ Si surfaces.[43]

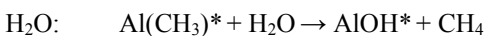
Shortly after its (re-)discovery, the first solar cells with ALD Al_2O_3 demonstrated high efficiencies, for instance PERC and PERL cells of 20.6%, [44] and 23.2% [10] efficiency, respectively. Due to these advantages, ALD of Al_2O_3 has now found its way into solar cell manufacturing, as will be extensively discussed in section 2.2.3. Moreover, the full potential of Al_2O_3 has likely not yet been reached, as is evident from e.g., recent results where Si solar cells with Al_2O_3 passivation layers demonstrated conversion efficiencies over 25%. [3] For an extensive overview on the topic of surface passivation by Al_2O_3 , the reader is referred to Dingemans and Kessels [29]. Here, some key aspects related to surface passivation by ALD Al_2O_3 will be outlined.

ALD of Al_2O_3 for passivation

The most commonly applied and widely-studied ALD process for Al_2O_3 is based on TMA as metal-organic precursor with either H_2O , O_3 or O_2 plasma as co-reactant. The first half-cycle can be described by the following reaction of the surface species (*) for $n=1,2$ [45]:



After a purge step, the second ALD half-cycle takes place, which in the case of thermal ALD can be described by the following ligand-exchange reaction:



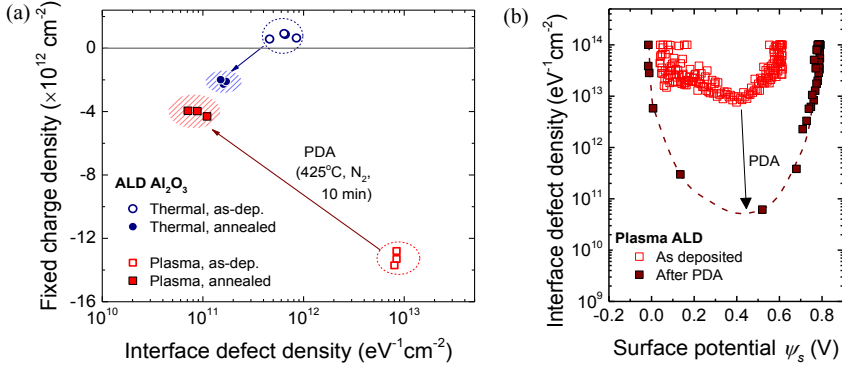
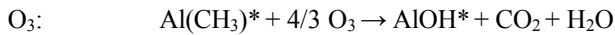
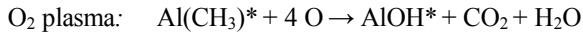


Figure 5 Interface properties as determined by corona oxide characterization of semiconductors (COCOS) of *n*-type Si (100) passivated by Al_2O_3 films prepared by plasma (i.e., using O_2 plasma) or thermal ALD (i.e., using H_2O) in as-deposited state and after post-deposition anneal at 425°C in N_2 ambient. (a) After annealing, the D_{it} is significantly reduced for both deposition methods. (b) The D_{it} of the Si/ Al_2O_3 interface is particularly reduced near mid-gap. N. Nandakumar of National University of Singapore is acknowledged for the COCOS measurements.

As a sufficient thermal budget is required for the latter to take place, alternatively highly-reactive species are often used in so-called energy-enhanced ALD processes, such as O_3 or O_2 plasma when working at lower temperatures. Possible combustion-like reaction pathways are:



The resulting Al_2O_3 films are amorphous, with a high optical band gap of ~ 6.4 eV. The latter makes Al_2O_3 films very suitable for application at the front surface of solar cells. Depending on the synthesis method, Al_2O_3 has a refractive index of ~ 1.55 – 1.65 at 2 eV which is too low for application as an ideal ARC, for which reason it is therefore often capped by SiN_x .

In the as-deposited state, the passivation quality provided by Al_2O_3 strongly depends on the oxidant chosen during the ALD process (see Fig. 5). When using water or ozone as oxidant, the passivation can be reasonable (i.e., resulting in a $D_{it} < 10^{12} \text{ eV}^{-1} \text{ cm}^{-2}$) in the as-deposited state. However, for plasma-assisted ALD, the passivation is initially very poor. In fact, the surface is de-passivated as a result of plasma damage, in particular due to vacuum ultraviolet radiation which is emitted in the plasma-step.[46,47] The D_{it} of as-

deposited ALD Al_2O_3 films can be strongly reduced by a short PDA at temperatures between 400 – 450 °C, with comparable results for an anneal in forming gas (N_2/H_2) or N_2 ambient.[48] In actual Si solar cell processing, a dedicated PDA is often redundant because of the high temperatures used in the subsequent processing steps, such as the deposition of SiN_x or contact firing steps.

Hydrogenation of interface defects

Before the deposition of Al_2O_3 , commonly the SiO_2 which is natively present at the Si surface, is removed by dipping the Si in diluted hydrofluoric acid (HF). Nevertheless, after ALD the Si/ Al_2O_3 interface is in fact a Si/ SiO_2 / Al_2O_3 interface, as is commonly observed by e.g., transmission electron microscopy (TEM) (see Fig. 6).[41,49]

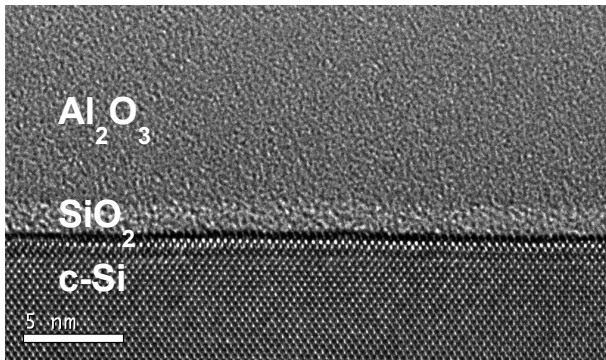


Figure 6 High-resolution TEM image of the annealed Al_2O_3 layer prepared by plasma ALD on Si, showing the amorphous character of the Al_2O_3 layer. The SiO_2 interface layer has a thickness of 1.5 nm.

The remaining defects at the Si/ SiO_2 interface are effectively passivated by hydrogen which is released from the Al_2O_3 during subsequent PDA. Evidence for this hydrogenation was found experimentally by the deposition of deuterated Al_2O_3 , where deuterium present in the Al_2O_3 film diffused during PDA to the Si/ SiO_2 interface.[50] The activation energy for the interface hydrogenation does not depend on the amount of hydrogen which is incorporated in the Al_2O_3 films, but the rate of hydrogenation does.[51] Therefore, the hydrogenation of interface defects is to some extent dependent on the amount of hydrogen present in the Al_2O_3 film and on its microstructure.[52] The best passivation properties are found for dense and hydrogen-containing Al_2O_3 films, such as for ALD Al_2O_3 films deposited at ~200 °C.

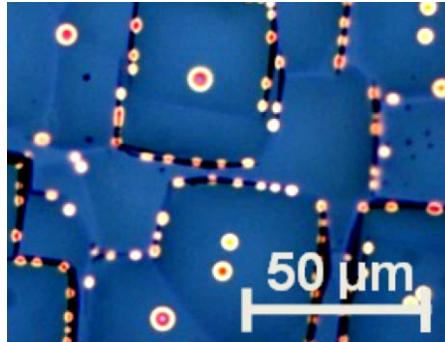


Figure 7 Optical microscopy image of blisters formed in an $\text{Al}_2\text{O}_3/\text{SiN}_x$ film after firing at $850\text{ }^\circ\text{C}$. The film stack passivates a Si surface with a random pyramid texture. Adapted from Bordihn *et al.*,[53]

Interestingly, Al_2O_3 can also be used to passivate defects when it is not deposited directly onto the Si surface. For instance, the passivation of Si by materials such as HfO_2 , TiO_2 , or deposited SiO_2 layers, could be strongly improved after capping by Al_2O_3 with a subsequent PDA.[50,54–56] In fact, for SiO_2 , it has even been shown that the Al_2O_3 capping layer can even be removed after PDA, without compromising the improved passivation properties.[29,50] Nonetheless, capping by Al_2O_3 not only ensures the hydrogenation of interface defects during a PDA, but can also improve the long-term and high-temperature stability of the surface passivation stack.[50,57] Recently, it was reported that ALD Al_2O_3 even is an excellent source of hydrogenation to improve the passivation of poly-Si contacts, such as used in the TOPCon approach (see introduction).[58]

Finally, it has to be noted that although that the hydrogenation provided by the Al_2O_3 is preferred for passivation, the hydrogen can also lead to some adverse effects in solar cell manufacturing. For instance, a rapid increase in temperature (such as when contacts are “fired” through the dielectric) can induce blistering of the Al_2O_3 film (see Fig. 7).[59] Most likely hydrogen released from the Al_2O_3 at higher temperatures builds up under the Al_2O_3 film, which acts as a diffusion barrier, eventually causing a local delamination.[59,60] In actual solar cell processing, the formation of blisters can be avoided by slowly releasing hydrogen using a more gradual increase in temperature during subsequent process steps. Furthermore, the formation of blisters can be avoided by using thin Al_2O_3 films (i.e., less than 10 nm in thickness).[60] Interestingly, solar cell concepts exist where the blisters in the Al_2O_3 film are used to advantage, to form local point contacts to the Si.[61]

Interface engineering by Al₂O₃

From a scientific as well as from a processing perspective, it is interesting to see the effect of Al₂O₃ thickness on the surface passivation quality. The best passivation results are found for Al₂O₃ thicknesses >5 nm for plasma ALD,[62] and >10 nm for thermal ALD.[29] For very thin Al₂O₃ layers, the level of chemical passivation achieved after PDA starts to deteriorate, which likely can be attributed due to a lack of interface hydrogenation during PDA.[62]

Interestingly, it has been demonstrated that the fixed charge density of Al₂O₃ however is located in very close vicinity of the Si–Al₂O₃ interface, i.e., within the first 2 nm of the Al₂O₃.[62] The latter is very relevant for Si solar cell processing. SiN_x is conventionally used as an ARC due to its suitable refractive index (tunable between 1.9 – 2.7), but when deposited directly on Si it is not an ideal match for *p*-type or *p*⁺-type Si due to its positive Q_f . By using Al₂O₃ as thin interlayer in Al₂O₃/SiN_x stacks, the total Q_f of the stacks becomes negative.[63] Therefore, Al₂O₃/SiN_x stacks are an ideal match for the passivation of the front *p*⁺-type surfaces. The fact that very thin Al₂O₃ layers can be used, makes ALD a viable technique for high-volume manufacturing (HVM). It has to be stressed however, that for ultrathin Al₂O₃ layers (i.e., <10 nm) in Al₂O₃/SiN_x stacks, the interface properties such as Q_f and D_{it} are strongly dependent on the thickness of the Al₂O₃ film, the process conditions during film growth and subsequent firing or annealing conditions.[63]

Influence of the surface conditions on the passivation properties

It is common that the interface properties of passivation schemes are significantly dependent on the Si surface conditions, such as the doping level, crystallographic termination and the surface topology.[64,65] Such aspects have also been investigated for ALD Al₂O₃.

For highly doped *p*⁺ Si surfaces with a wide range of surface doping concentrations, very low J_0 values are reported regardless of the oxidant used during ALD.[66–69] In fact, Al₂O₃ passivates the *p*⁺ Si surface so effectively, that Auger recombination within the highly doped region is often the dominant recombination mechanism and the principal contributor to the measured J_0 .[67,70,71] Recently, it has even been shown by Black *et al.*, that the interface parameters Q_f and S_{n0} for boron-doped Si surfaces passivated by Al₂O₃ prepared by thermal ALD are in fact *independent* of the surface doping concentration, at least up to $N_s \leq 3 \cdot 10^{19} \text{ cm}^{-3}$.[69] Nonetheless, care must still be taken when passivating *p*⁺ Si, as in some cases a boron-rich layer (which is a boron-Si compound) can be formed on the Si surface during boron-diffusion, which can inhibit the

surface passivation by ALD Al_2O_3 . [67,72] Overall, as stated before, ALD Al_2O_3 is very effective for the passivation of p - and p^+ -Si surfaces, virtually independent of the surface doping concentration.

For highly doped n^+ Si surfaces, the level of passivation provided by ALD Al_2O_3 is in many cases found to be compromised due to its negative Q_f [73–75] as could be expected on the basis of Fig. 4. This holds in particular for surface doping levels in the range of 10^{18} - 10^{20} cm^{-3} . Although on lowly doped n -type Si surfaces, excellent passivation results by Al_2O_3 are achieved, here the negative Q_f leads to inversion, which is generally undesirable in solar cells. Therefore, also (novel) ALD-based schemes are successfully being explored for the passivation of n - and n^+ -type Si surfaces, as will be discussed further in section 2.2.4.

Besides the doping level, the passivation of Si surfaces can strongly depend on other surface conditions, such as the crystallographic orientation and cleaning procedure. For ALD Al_2O_3 however, dedicated studies so far revealed marginal differences in the passivation of Si (100) and (111) surfaces. [71] On the other hand, the surface cleaning influences to the final passivation properties of Al_2O_3 and should therefore be considered. [76]

2.2.3 ALD in solar cell manufacturing

Requirements for manufacturing in the PV industry

The success of ALD Al_2O_3 as a passivation layer on a lab-scale was the incentive for the development of high-throughput ALD reactors, specifically designed for the photovoltaic industry. Even though high-throughput ALD reactors were readily used for manufacturing in the integrated-circuit (IC) industry, the demands set by the IC and PV industry are markedly different (see table 2). Whereas the requirements in terms of e.g., particle generation and film uniformity are relaxed for the PV industry compared to the IC industry, the former is rigorously more demanding in terms of throughput and costs. The production lines for crystalline Si solar cells are typically designed for a throughput of up to 1 wafer/s, whereas the costs for e.g., the deposition of Al_2O_3 are (depending on cell design) only allowed to be 0.03-0.05 \$/wafer in order to remain cost-effective.

Table 2 Comparison of typical film and equipment requirements by the integrated-circuit (IC) and photovoltaic (PV) industries. Adapted from Granneman *et al.*, [77]

	<i>IC industry</i>	<i>PV industry</i>
# process steps per device	200-400	15-20
Film uniformity (%)	>99	>96
Particle generation	Important	Irrelevant
Metal (Fe) contamination (cm⁻²)	<10 ¹⁰	<10 ¹²
Cost-of-ownership (\$/wafer)	3-10	0.03-0.05
Equipment Cost (M\$)	2-5	0.5-2.5
Equipment Throughput (wafers/hr)	10-50	1000-3000
Equipment Uptime	>95%	>95%
Wafer breakage	1:50,000	1:1000

For the deposition of thin films, ALD is competing with physical vapour deposition (PVD), plasma-enhanced (PE) and atmospheric pressure (AP) chemical vapour deposition (CVD) and spray pyrolysis. In general, to compete with the abovementioned deposition techniques, ALD processes should offer additional advantages. For instance, they should be low-cost and preferably provide benefits in terms of spatial uniformity and solar cell efficiency.

For a high yield of the ALD process, efficient precursor consumption and low-temperature processing would aid in attaining a low cost-of-ownership. Apart from an optimized reactor design, another way to ensure an efficient precursor usage and optimized throughput is to minimize precursor dosing until the ALD half-reactions are at the onset of saturation. As long as the quality and homogeneity of the deposited films are still acceptable, this might be a valid approach. In addition, also “solar grade” precursors can be used. These precursors are less pure and hence are lower cost.[78,79]

When ALD films can be used on both sides of the solar cells (see e.g., in the next section), or when stringent requirements are set on the composition, uniformity and thickness of the films or film stacks, such as for passivating contacts, ALD in particular might become the deposition method of choice.

High-throughput ALD reactors

Two distinct ALD methods are being used for high-volume manufacturing in the PV industry, i.e., *temporal* and *spatial* ALD, which differ in the way the precursors are delivered to the solar cells (see Fig. 8).

With *temporal* ALD, the precursor and co-reactant dosing are separated *in time* by purge or pump steps. Using temporal ALD, which is the most common form of ALD in research and development, a sufficiently high throughput for the PV industry can be achieved by placing many wafers (typically 500-1000 wafers) simultaneously in a batch reactor. As the wafers are placed back-to-back, parasitic deposition on the other side of the wafers (*wrap-around*) is ideally avoided. As ALD uniquely is a surface limited deposition method, homogeneous films can in principle be obtained on all wafers. Generally, in batch reactors the purge, precursor and reactant dosing times must be longer compared to single-wafer ALD tools, due to the very large surface areas which are exposed. Therefore, in batch ALD it is often preferred to use O_3 rather than H_2O as co-reactant due to its higher reactivity and because it allows for shorter purge times.

In *spatial* ALD (S-ALD), the precursor and co-reactant dosing steps are separated not *in time*, as is the case for temporal ALD, but *in space*. The wafers can float on N_2 bearings through S-ALD reactors, and move through separated precursor and co-reactant zones (see Fig. 8), which are separated from each other by nitrogen gas bearings at (sub-) atmospheric

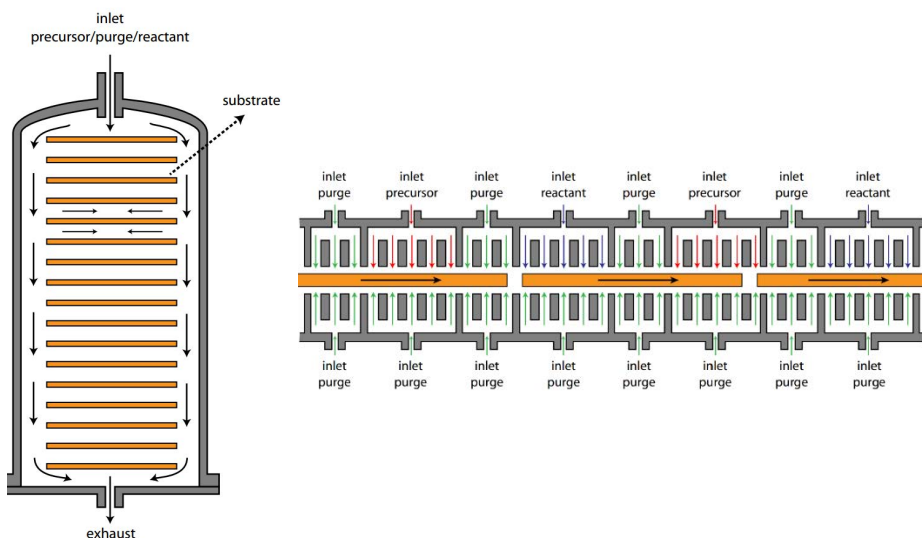


Figure 8 Schematic representation of batch ALD (left) and spatial ALD (right), adapted from references [80,81].

pressures. In this way, the lengthy purge times which are otherwise required to separate the precursor and reactant gases are avoided. As only the wafers encounter the spatially separated precursors, the ALD half-reactions take only place at the surface of the wafer, and (ideally) not on the reactor walls. The spatial ALD concept is particularly interesting for *in-line* processing and can, because of the absence of purge steps, operate at atmospheric pressure. Moreover, in principle no pumps or fast switching valves are required. In table 3, a selection of industrial aspects of temporal and spatial ALD are compared.

Table 3 Comparison of industrial aspects for temporal and spatial ALD.

	<i>Temporal ALD</i>	<i>Spatial ALD</i>
Processing:	Batch	In-line
Pressure:	~1 Torr	Atmospheric or lower
Single side deposition by:	back-to-back wafer stacking	Precursor injection from one side of the wafer
Double side deposition	Viable (no back-to-back stacking, half the throughput)	Viable (when precursor injection from both sides of the wafer)
Companies for Si PV:	ASM, Beneq	Levitech, SoLayTec
Deposition on walls:	Yes	No
Limit on throughput:	Purge and dose times	Surface reaction kinetics, wafer handling
Deposition of stacks:	Flexible	Possible
Turn-around-time for ~nm films:	Long (~0.5-1 hour)	Short (<1 min)

ALD Al₂O₃ in PV industry

Besides ALD, also other synthesis methods of Al₂O₃ are suitable for the passivation of Si surfaces, such as PECVD or AP-CVD and sputtering.[40,69,82–84] In the PV industry, PECVD is in particular competing with ALD as a deposition method for Al₂O₃, as PECVD reactors are already installed in most production lines for the deposition of SiN_x, whereas ALD is a relatively new technique in the field of PV manufacturing. Nonetheless, as was discussed in the section 2.2.3, even very thin, homogeneous, films of Al₂O₃ of less than 2 nm in thickness could be sufficient for solar cells to benefit from its negative Q_f when combined with a SiN_x ARC or a SiO₂ dielectric mirror. The fact that very thin Al₂O₃ layers can be used, makes ALD in particular interesting for HVM. The very thin films required for passivation enables a significant lower TMA usage for ALD (<4 mg/wafer) compared to CVD methods (9-15 mg/wafer), saving considerably on operation costs.[85] More importantly, in direct comparisons, the best passivation properties of Al₂O₃ are often achieved when it is prepared by ALD.[69,86]

For instance, Schmidt *et al.*, [86] compared in 2010 the Si surface passivation provided by single layers of Al_2O_3 prepared by sputtering, PECVD, spatial ALD and temporal ALD. In Fig. 9, a selection of results is given. ALD, with plasma ALD in particular, yielded the highest passivation performance before as well as after a high-temperature firing step. Importantly, the found differences in surface passivation quality translated well to differences in conversion efficiency of PERC solar cells, ranging from 20.1% for solar cells where the Al_2O_3 was prepared by sputtering, to 21.4% for solar cells where it was deposited by ALD and subsequently was capped by PECVD SiO_2 . [86] Note that research activities on the passivation by Al_2O_3 by various passivation methods are still ongoing. For Al_2O_3 films prepared by sputtering for instance, the absence of hydrogen or the presence of sputter damage affected the surface passivation. [29] Indeed, the preparation of Al_2O_3 films by sputtering has since 2010 been significantly improved when using a hydrogen-containing ambient. [87] Also Al_2O_3 films prepared by PECVD have shown considerably improved results $\sin\Omega_e$ then. [88]

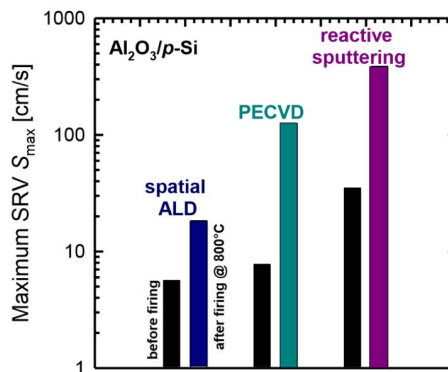


Figure 9 Comparison between the passivation quality in terms of upper limit of S_{eff} or SRV (where a low S_{eff} is preferred) of Al_2O_3 passivation layers prepared by spatial ALD, PECVD and sputtering, before and after firing at 800 °C. Adapted from Schmidt *et al.*, [86]

Currently, both spatial and temporal ALD systems are being piloted in the PV industry for the HVM of thin Al_2O_3 layers. To date, no high-throughput reactors capable of plasma ALD have been developed for the Si PV industry yet. Very similar results in passivation are reported on lowly doped Si surfaces for spatial as well as temporal ALD of Al_2O_3 when combined with SiN_x capping layers, [29,77] even in direct comparison. [86] Also, no significant differences in passivation quality by both deposition methods are found for either n^+ or p^+ Si surfaces, which is indicative of the robustness of ALD as a deposition

method.[89] However, as will become clear in the following sections, the different reactor designs each have their own distinct advantages in terms of the preparation of doped films and stacks, and in terms of processing complexity. In the end, cost-of-ownership and yield considerations are expected to play a decisive role in the final choice of reactor type or deposition method for the HVM in the PV industry.

2.2.4 New developments for ALD passivation schemes

With the passivation of p -type and p^+ Si surfaces by ALD being fully established, research incentives are currently also targeting the passivation of n^+ Si surfaces by ALD. Moreover, ALD passivation layers are being explored to enable novel light trapping schemes that otherwise suffer from a high surface recombination, such as “black Si” texturing. Finally, other new passivation materials prepared by ALD are also being found, and ALD-based passivation schemes are being further tuned using doping or the fabrication of stacks. In this section, these recent developments in the field of surface passivation by ALD are outlined.

ALD stacks for the passivation of n^+ Si or n^+ and p^+ Si surfaces

The passivation of n^+ Si surfaces is very relevant for many high-efficiency solar cell designs (see Fig. 1). Unfortunately, as was mentioned in the previous sections, the negative Q_f makes Al_2O_3 less than ideal for this application. Additionally, for e.g., IBC solar cells, n^+ and p^+ Si regions are adjacent and preferably passivated simultaneously. By using passivation schemes without a significant Q_f , but with a high level of chemical passivation (i.e., a low D_{it}), effects associated with a ‘wrong’ charge polarity, such as depletion region recombination or parasitic shunting can ideally be avoided on both surface types. In such a “zero-charge” approach, rather than relying on field-effect passivation by a fixed charge, the high doping levels at the n^+ and p^+ Si surfaces could ensure the local reduction of the minority charge carrier density.[11] Finally, the simultaneous passivation of n^+ and p^+ Si surfaces by ALD could also be of interest from an (industrial) perspective, as it could allow for the simultaneous passivation of both sides of solar cells in a single ALD run. Fortunately, the negative Q_f of Al_2O_3 -based layers can be tuned in several ways.

First, the Q_f of Al_2O_3 single layers is reduced using higher deposition temperatures (i.e., ~300-500 °C), although this approach comes at the expense of reduced chemical passivation.[90,91] Furthermore, the fixed charge density of Al_2O_3 was found to be reduced by capping it with (PECVD) SiN_x in combination with a subsequent high-

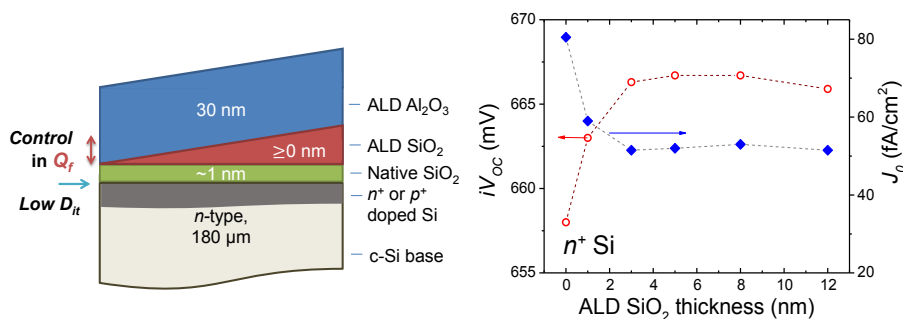


Figure 10 Schematic display of the SiO₂/Al₂O₃ passivation scheme (left). Passivation results obtained using SiO₂/Al₂O₃ stacks on an n⁺ Si surface (having an active surface doping concentration $N_s = 2 \cdot 10^{20} \text{ cm}^{-3}$) on a symmetrical lifetime sample (right), adapted from van de Loo *et al.*, [11]

temperature (>800 °C) firing step.[74] Richter *et al.*, demonstrated that such Al₂O₃/SiN_x stack is well capable of passivating n⁺ surfaces with a wide range of surface doping concentrations ($\sim 10^{18}$ – $2 \cdot 10^{20} \text{ cm}^{-3}$).[74] Nonetheless, in this stack, a negative Q_f of $\sim 1.9 \times 10^{12} \text{ cm}^{-2}$ is still present,[63] which is not ideal for implementation in solar cells due to inversion or depletion region effects.

Alternatively, ALD SiO₂/Al₂O₃ or HfO₂/Al₂O₃ stacks prepared at 200 °C (e.g., using Hf(NMeEt)₄ and H₂O for HfO₂, and SiH₂(NEt₂)₂ and O₂ plasma for SiO₂) can be used as passivation schemes with tunable Q_f . [54,57,92] The Al₂O₃ capping layer in these stacks ensures the hydrogenation of the Si-SiO₂ or Si-HfO₂ interface during annealing, resulting in excellent levels of chemical passivation, with D_{it} values $< 10^{11} \text{ cm}^{-2}$. [54,57] The very thin (i.e., 2–4 nm) SiO₂ or HfO₂ interlayer in its turn prevents the formation of a negative Q_f in the Al₂O₃. [54,57,92] For thicker SiO₂ interlayers (>4 nm), the overall charge polarity of SiO₂/Al₂O₃ stacks even becomes positive, (depending on the preparation method of SiO₂) as the SiO₂ layer contains a very low positive Q_f in the bulk. [57,92,93] Overall, the ‘digital’ thickness control and the excellent homogeneity of the interlayers provided by ALD enables a precise control of Q_f in SiO₂/Al₂O₃ and HfO₂/Al₂O₃ stacks. [11,54,57] Recently, it was demonstrated that ALD SiO₂/Al₂O₃ stacks outperform the passivation of n⁺ Si surfaces provided by single layers of Al₂O₃ or by fired Al₂O₃/SiN_x stacks. [11]

As mentioned, the possibility to passivate n⁺ Si with an ALD-based passivation scheme opens up new opportunities for ALD reactors in HVM. For S-ALD, Al₂O₃ can be deposited on p⁺ Si, whereas simultaneously SiO₂/Al₂O₃ stacks could be deposited on n⁺ Si

side of the solar cell using the bottom side of the spatial ALD reactor. For batch ALD, both sides of solar cells could be passivated in a single deposition run. In fact, $\text{SiO}_2/\text{Al}_2\text{O}_3$ stacks have already successfully been scaled up in industrial batch ALD reactors.[11]

ALD for the passivation of surfaces with demanding topologies

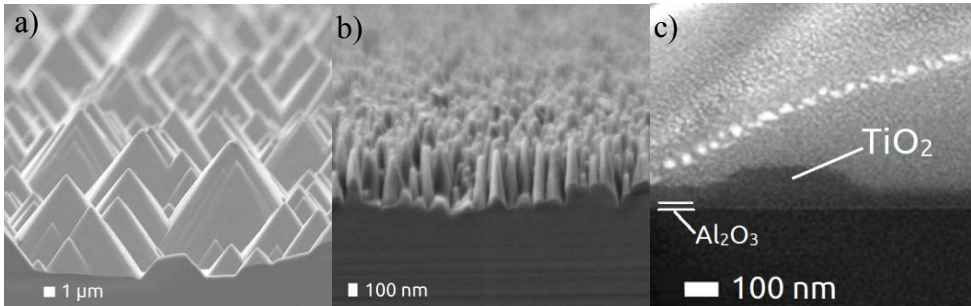


Figure 11 SEM images of different approaches which are used to enhance the light absorption in Si solar cells. In (a) the current industrial standard method for monocrystalline Si is used, where random-pyramids are created by wet-chemical etching of the Si. On the RP-textured surface, subsequently the passivation layer and ARC are deposited. In (b) a “black Si” texture is shown which is formed by reactive ion etching and subsequently is passivated by a 30-nm Al_2O_3 film prepared by plasma ALD (the authors would like to acknowledge A. Ingenito from Delft University of Technology for the black Si synthesis). (c) A cross-section of a TiO_2 resonator, adapted from Spinelli *et al.*, [94] The TiO_2 is deposited by electron beam evaporation on a 30 nm Al_2O_3 film prepared by plasma ALD, which provides the surface passivation.

Most high-efficiency solar cells have, at least at the front surface, a random-pyramid (RP) texture (created by wet-chemical etching) in combination with an ARC, to ensure good light trapping and correspondingly a high short-circuit current density (see Fig. 11a). The random-pyramid texture typically results in an increase of roughly ~ 1.7 in surface recombination for Al_2O_3 -based passivation schemes compared to planar surfaces, which can be attributed to the increase in surface area. Alternatively, the front surface can be etched by reactive ions, which creates a very rough surface topology, referred to as “black silicon” (see Fig. 11b). Black Si exhibits excellent light coupling properties, even without ARC.[95–97] Compared to RP-textured Si, black Si shows particularly a high absorption in the short-wavelength range. Moreover, its absorption is less dependent on the angle of incidence compared to RP-textured Si.[97]

Despite of these benefits, the surface area of the black Si surface is significantly increased compared to planar substrates, typically by a factor in the range of 7-14.[98,99]

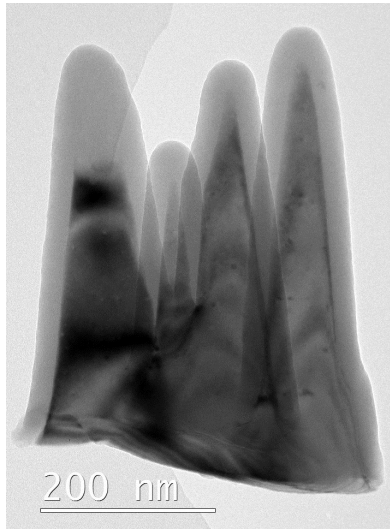


Figure 12 Bright-Field TEM image of black-Si pillars of figure 11b. A conformal Al₂O₃ layer of 30 nm thickness is deposited by plasma ALD.

This strong increase in surface area puts stringent requirements on the passivation quality of the black Si surface. For a long time, solar cells with black Si texture only achieved efficiencies <18.2%. Only recently, it has been reported on IBC cells comprising black Si with an conversion efficiency of 22.1%. [97] In this case, the black Si surface was passivated by Al₂O₃ deposited by thermal ALD. [97]

Conceivably, a full coverage of Al₂O₃ films over the pillars of the black-Si (see e.g., the TEM results in Fig. 12), is crucial for the surface passivation, making ALD an ideal candidate. Moreover, it is commonly observed that the recombination rate of charge carriers at the black Si surfaces is much lower than what would be expected on the basis of the large surface area. [98–101] An important reason for this observation is that the field-effect passivation is markedly more effective for black Si textures than for planar or random-pyramid textured surfaces. [98,101] More specifically, the fixed charge density in the passivation layer can bring the needles of the black Si texture almost completely into inversion or accumulation, and in this way effectively suppresses the surface recombination. Finally, for application in solar cells, more heavily-doped black Si surfaces textures are also relevant. Whereas first results for Al₂O₃ on *p*⁺ doped black Si are promising, [102] for *n*⁺ doped black-Si surfaces, the SiO₂/Al₂O₃ or HfO₂/Al₂O₃ ALD stacks discussed in the previous section could be interesting candidates.

Besides black Si, ALD Al_2O_3 films also have been used for the surface passivation of other textures with an even more demanding surface topology, such as Si-nanowires or hierarchical textures.[96,103] For such topologies, multiple precursor dosing steps are even used during ALD to ensure a good conformality of the film over the nanostructure.[96] Interestingly, light-trapping approach have also been developed, in which *flat* Si surfaces could be used.[94] In this approach, the flat surface was passivated by ALD Al_2O_3 . On top of the passivation layer, nano-sized TiO_2 resonators are deposited, which enhance the light trapping in the Si (see Fig. 11c).[94]

This approach not only makes the texturing of the surface and the use of an ARC redundant, they moreover do not adversely affect the surface passivation provided by the ALD Al_2O_3 films and are therefore very promising for application in solar cells.

Novel ALD-based passivation schemes

After the tremendous success of ALD Al_2O_3 , the surface passivation properties of various other materials prepared by ALD has also been explored, including TiO_2 , Ta_2O_5 , and Ga_2O_3 . A selection of passivation results and corresponding interface properties for these materials is given in table 4. Recently, Cuevas and co-workers identified Ga_2O_3 [104] and Ta_2O_5 [105] prepared by ALD (the latter in combination with PECVD SiN_x capping layer) as materials which provide excellent surface passivation. Although outstanding surface passivation results have been demonstrated, these materials do not yet offer apparent benefits in terms of processing complexity, cost or passivation quality compared to e.g., Al_2O_3 films or $\text{SiO}_2/\text{Al}_2\text{O}_3$ stacks. Nonetheless, these novel materials might become very useful in the emerging field of passivating contacts, as will be discussed in section 2.4.

Other passivation materials can be interesting because of their refractive index of ~ 2 at 2 eV, which makes them also suitable as ARCs. TiO_2 was for instance traditionally used before SiN_x as ARC in Si solar cells, although it was gradually being replaced by SiN_x due to the poor passivation quality of the former. However, Liao *et al.*,[106] recently demonstrated excellent surface passivation by TiO_2 using thermal ALD using TiCl_4 and H_2O as precursors. The passivation of TiO_2 could be achieved after a PDA in combination with a subsequent light-soaking step.[106] Interestingly, recently ALD TiO_2 has been used in PERC cells as combined ARC and passivating layer of p^+ Si, with the efficiency of 20.4% being close to a reference cell of 21.3 % which uses a stack of $\text{Al}_2\text{O}_3/\text{SiN}_x$. [107] Finally, TiO_2 is also suitable as (a part of) a passivating electron contact, with first solar cell results achieving already 20.5%. [108]

Besides the deposition of single layers, ALD is also well-suited to prepare stacks or doped films in a well-controlled way. This ability can potentially be used to carefully fine-tune the electrical or optical properties of the passivation layer or scheme. For instance, using materials with different refractive indices, it is possible to make double-layered or graded ARCs, or Bragg mirrors to enhance light trapping in solar cells. A passivation scheme prepared by ALD which is also suitable as ARC could be a stack of $\text{Al}_2\text{O}_3/\text{ZnO}$, where even improvements in passivation properties were found after capping the Al_2O_3 by ZnO . [23] The interface properties such as D_{it} and Q_f of ALD Al_2O_3 or SiO_2 layers could also be improved by using doping. [109, 110] For instance, it was found that Al_2O_3 doped with TiO_2 has a slightly more negative Q_f compared to single layers of Al_2O_3 . [109]

Finally, ALD also offers the possibility to make nanolaminates or alloys, which potentially also could be used to improve the passivation properties and can even add new functionalities to it. For example, it has been reported that ALD $\text{TiO}_2\text{-Al}_2\text{O}_3$ nanolaminates have an increased conductivity compared to a single layer of Al_2O_3 , albeit at the price of a reduced passivation quality. [110] Moreover, $\text{Al}_2\text{O}_3\text{-TiO}_2$ nanolaminates are successfully used to enhance the damp-heat stability of the surface passivation scheme, as they act as

Table 4. Selection of optimal surface passivation conditions provided by several materials prepared by ALD. The SiN_x layers which are sometimes used as capping layer are prepared by PECVD. Note that S_{eff} depends on the doping level of the bulk. [25] Therefore, only S_{eff} data based on polished, float-zone, *n*-type Si wafers with a base resistivity of 1-5 $\Omega\cdot\text{cm}$ are included here. For each process, the substrate temperature T_{dep} and growth-per-cycle (GPC) are indicated.

Material or stack	Metal precursor	Co-reactant	T_{dep} (°C)	GPC (Å)	PDA (°C, ambient)	D_{it} (10^{11} eV^{-1} cm^{-2})	Q_f (10^{12} cm^{-2})	S_{eff} (cm s^{-1})	Ref
Al_2O_3	AlMe_3	plasma	200	1.1	450, N_2	0.8	-5.6	2.8	[46]
	AlMe_3	O_3	200	0.9	400, N_2	1.0	-3.4	6.0	[46]
	AlMe_3	H_2O	200	1.1	350, N_2	0.4	-1.3	4.0	[46]
SiO_2	$\text{SiH}_2(\text{NEt})_2$	plasma	200	1.2	400, N_2	10	0.6-0.8	25*	[55]
$\text{SiO}_2/\text{Al}_2\text{O}_3$	$\text{SiH}_2(\text{NEt})_2$	plasma	200	1.2	400, N_2	1	-5.8,+0.6	3	[55]
$\text{HfO}_2/\text{Al}_2\text{O}_3$	$\text{Hf}(\text{NMeEt})_4$	H_2O	150	1.1	350, N_2/H_2	<1	-(4-1)	<1	[93]
Ta_2O_5	$\text{Ta}_2(\text{OEt})_{10}$	H_2O	250	0.3	no	n.a.	-1.8	~467	[105]
$\text{Ta}_2\text{O}_5/\text{SiN}_x$	$\text{Ta}_2(\text{OEt})_{10}$	H_2O	250	0.3	no	n.a.	-1.0	3.2	[105]
TiO_2	TiCl_4	H_2O	100	0.6	200-250, N_2, \dagger	n.a.	n.a.	2.8	[106]
Ga_2O_3	GaMe_3	O_3	250	0.2	350, H_2/Ar	n.a.	n.a.	6.5	[104]

n.a. = not available; * = unstable in time, † = after light soaking

a moisture barrier layer.[111] Al_2O_3 - TiO_2 ‘alloys’ also have been explored (deposited using an Al_2O_3 : TiO_2 ALD cycle ratio of 1:1), resulting in a slight improvement in surface passivation.[112] Overall, it has been demonstrated that the precise control in film growth and film composition offered by ALD opens up numerous possibilities to further develop ALD-based passivation schemes.

2.3 Transparent conductive oxides for Si heterojunction solar cells

In this section, the role of ALD in preparing both ZnO- and In_2O_3 -based TCOs for SHJ solar cells is reviewed. First, the basics of TCOs and important aspects with respect to implementation in SHJ solar cells will be reviewed. From this it follows that the upcoming high-mobility In_2O_3 -based TCOs are especially promising for use on the front side of the solar cell due to their excellent conductivity and transparency. Consequently, these TCOs have played a key role in achieving the recent record efficiencies for SHJ cells. ZnO-based TCOs are mostly promising as a low-cost alternative at the rear side of the solar cell, since the optoelectronic requirements at the rear side are less stringent whereas the work function of ZnO is also more suited for the electron-collecting side.

ALD processes of both ZnO- and In_2O_3 -based TCOs will be discussed. In the subsection on ALD of doped ZnO-based films ($\text{ZnO}:X$, $X=\text{Al}$, B , Ga , ...), the high control over the doping level offered by the use of dopant supercycles is discussed.[113,114] The challenge of dopant clustering which is inherent to the supercycle approach is addressed, together with several strategies to mitigate this clustering. For (doped) In_2O_3 , an overview of existing ALD processes is given, with special attention to the ALD process of high-mobility H-doped In_2O_3 , given the very promising properties it can provide. Finally, recent developments in the HVM of ALD TCOs, with a focus on (doped) ZnO, is briefly touched upon.

2.3.1 Basics of TCOs in SHJ solar cells

Lateral conductivity

The first requirement of a TCO is that it should have a low resistivity in order to prevent excessive Ohmic losses during lateral charge transport to the metal grid. The resistivity ρ is determined by the carrier density N_e and the mobility μ_e of the charge carriers by $\rho = (N_e \mu_e e)^{-1}$, in which e is the elementary charge. A typical sheet resistance for the front

TCO with a thickness of 75 nm is $\sim 40 \Omega/\square$, which translates to a resistivity of 0.3 m Ω -cm.[115] Note that the TCO should preferably also serve as an antireflection coating to maximize the incoupling of light, which more or less fixes the thickness to 75 nm given that TCOs typically have a refractive index of around 2. In Fig. 13, the dashed isolines of constant resistivity show the typical N_e ($>1 \cdot 10^{20} \text{ cm}^{-3}$) and μ_e values that are needed to achieve such resistivity values.

TCOs typically have a high band gap of $\sim 3 \text{ eV}$ and therefore a very low intrinsic carrier density N_e . Nonetheless, thin films of In_2O_3 and ZnO are often unintentionally n -type doped by the presence of doubly charged oxygen vacancies (V_o^{2+}) and singly charged H^+ , which leads to a typical N_e up to a level of $\sim 10^{19} \text{ cm}^{-3}$ or higher. In order to achieve a sufficiently low resistivity, TCOs are often intentionally further n -type doped by other elements such as Sn for In_2O_3 and Al, Ga and B for ZnO to increase N_e to the order of 10^{20} – 10^{21} cm^{-3} .

The carrier mobility μ_e is limited by the scattering of charge carriers. An intrinsic, unavoidable scattering process is phonon scattering. Depending on the quality of the (typically) polycrystalline TCO, also extrinsic scattering processes can be significant, for example on crystallographic defects such as grain boundaries and other impurities. Nonetheless, typically the dominant scattering process for carrier density values in the range of interest ($>1 \cdot 10^{20} \text{ cm}^{-3}$) is the Coulombic scattering that arises from the introduction of ionized dopants, known as ionized impurity scattering (IIS). For homogeneously dispersed ionized dopants, the mobility limit due to IIS, μ_{ii} , can be calculated by:[116]

$$\mu_{ii} = \frac{3(\varepsilon_r \varepsilon_0)^2 h^3 N_e}{Z^2 m^{*2} e^3 N_i F_{ii}^{np}(\xi_0)} \quad (2.3.1)$$

In this equation, h is Planck's constant, ε_0 and ε_r are the vacuum and relative permittivity, respectively, and m^* the effective electron mass. Z is the charge state of the ionized impurity and N_i the concentration of ionized impurities. $F_{ii}^{np}(\xi_0)$ is the screening function for IIS in a degenerate semiconductor which depends on the carrier density through the factor $\xi_0 = (3\pi^2)^{1/3} \varepsilon_r \varepsilon_0 h^2 N_e^{1/3} / m^* e^2$. [116] For N_e values $>1 \cdot 10^{20} \text{ cm}^{-3}$, IIS limits the mobility of ZnO to approximately $<50 \text{ cm}^2/\text{Vs}$ and that of In_2O_3 to $<150 \text{ cm}^2/\text{Vs}$. [117,118] In this respect, In_2O_3 is at a clear advantage, which is mostly caused by a lower effective mass of

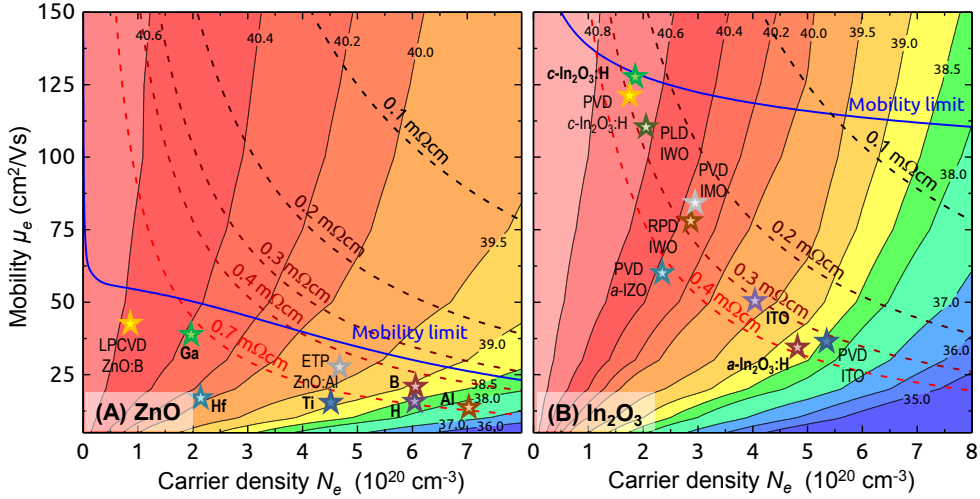


Figure 13 Contour plots of the simulated J_{sc} (in mA/cm^2) of SHJ solar cells featuring a ZnO-based (a) or In_2O_3 -based (b) TCO as a function of carrier density and mobility. Dashed lines are isolines of constant resistivity. The simulated cell structure consists of a textured wafer with 5 nm of intrinsic a-Si:H, 10 nm of p -type a-Si:H and 75 nm of TCO on the front side of the solar cell. Photon currents were simulated using OPAL2[119] and the optical constants of In_2O_3 and ZnO were taken from ellipsometry measurements.[114,120] In order to calculate the effect of free-carrier absorption for varying carrier density and mobility, the contribution of the Drude oscillator ϵ_{Drude} to the modeled dielectric function was varied accordingly. The interband absorption was assumed to remain constant, together with a constant m^* of $0.23m_e$ for In_2O_3 and $0.4m_e$ for ZnO, respectively. The thick solid line is the mobility limit as a function of the carrier density. For ZnO, this was calculated using the Masetti model[121] with the most recent parameters of Ellmer *et al.*,[122] The mobility limit for In_2O_3 was calculated using the mobility limits due to both phonon and ionized impurity scattering.[116,120] For ZnO, literature values (found in table 5) of ALD films with various dopant atoms are displayed, as well as ZnO:B made by low-pressure CVD and ZnO:Al by expanding thermal plasma CVD.[123] For In_2O_3 , values for amorphous ($a\text{-In}_2\text{O}_3\text{:H}$) and crystallized indium oxide($c\text{-In}_2\text{O}_3\text{:H}$) (prepared by ALD[120]), ITO[114], IMO[124] and amorphous IZO[125] (prepared by sputtering) and IWO (prepared by reactive plasma deposition (RPD)[126] and pulsed laser deposition (PLD)[127]) are shown. ALD processes are denoted in bold.[128]

the electrons of $\sim 0.2\text{-}0.3 m_e$ as compared to $\sim 0.4\text{-}0.5 m_e$ for ZnO. The limits of the carrier mobility as a function of carrier density in ZnO- and In_2O_3 -based TCOs, which for high carrier densities is mainly caused by IIS, are shown in Fig. 13 by the blue solid lines.

Transparency

Besides having a low resistivity, TCOs should provide excellent transparency for the photon energy range of interest for solar cells ($\sim 1.12 - 3.5$ eV). Due to their high band gap ($E_g > 3$ eV), ZnO and In_2O_3 are in principle very transparent up to that photon energy, as can be seen by the spectral absorption coefficient of nominally-undoped ZnO in Fig. 14(a). Above the band gap of ~ 3 eV, a strong increase in optical absorption in the ZnO is observed as expected. For higher doping, the onset of absorption shifts to higher photon energies, which corresponds to an increase in optical band gap. This effect is known as the Burstein-Moss (BM) shift: As can be seen in Fig. 14(b), the Fermi level E_F of ZnO is close to the conduction band since it is (almost) degenerate by the unintentional doping. By increased doping of the TCO, the Fermi level is raised further into the conduction band. This leads to an increase of the optical band gap, since the occupied states in the bottom of the conduction band are unavailable for optical transitions from the top of the valence band. In this respect, high doping of the TCO is beneficial since the transparency is extended to higher photon energies. This advantage is however relatively small, since very few photons are present in the solar spectrum at these high photon energies, as can be seen in Fig. 14(a).

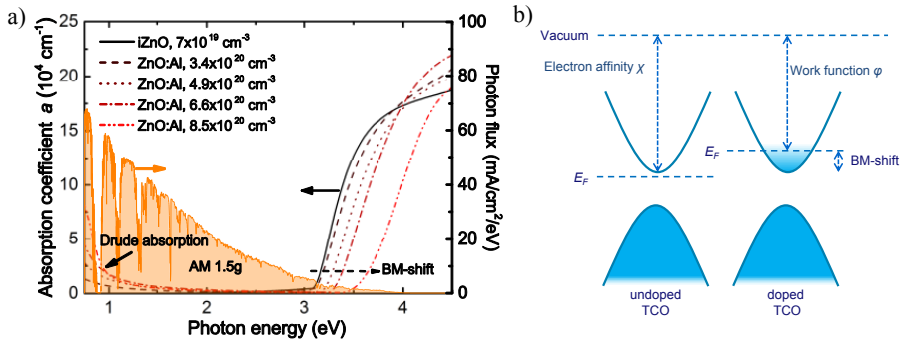


Figure 14 (a) Absorption coefficient of Al-doped ZnO layers of varying carrier density prepared by thermal ALD at 200 °C using DEZ and DMAI as Zn and Al source, respectively. The increasing Drude contribution and Burstein-Moss (BM) shift with doping level are indicated. (b) Schematic band diagram of an unintentionally doped TCO (left) and an intentionally doped TCO (right). The electron affinity χ denotes the energetic distance from the conduction band edge to the vacuum level, whereas the work function ϕ is the distance from the Fermi level E_F to the vacuum.

The free carriers generated by doping lead to increased free carrier absorption (FCA) at low photon energies due to an increase in Drude absorption, as can be seen in Fig. 14(a). This is a very detrimental effect, since the solar spectrum contains the most photons at low

photon energy. Additionally, this increased Drude contribution reduces the refractive index n at low photon energies, leading to enhanced free carrier reflection (FCR) due to a refractive index mismatch. The Drude contribution to the complex dielectric function ϵ_{Drude} is determined by the plasma frequency ω_p and the scatter frequency ω_τ :[129]

$$\epsilon_{Drude}(\omega) = -\frac{\omega_p^2}{\omega^2 + i\omega\omega_\tau}, \quad \omega_p^2 = \frac{e^2 N_e}{\epsilon_0 m^*}, \quad \omega_\tau = \frac{e}{m^* \mu_e} \quad (2.3.2)$$

where ω_p denotes the onset frequency of the Drude contribution, whereas the damping term ω_τ determines the broadening around the onset frequency. From these equations, it can be seen that a high mobility is advantageous in two ways. First, it reduces the required N_e for a low resistivity and thereby it reduces ω_p . At the same time a high mobility (or low ω_τ) reduces the Drude contribution above the plasma frequency because of a reduced broadening.

The effect of the Drude contribution on the J_{sc} of a SHJ solar cell due to FCA and FCR is shown for both ZnO and In₂O₃-based TCOs in the simulated contour plots of Fig. 13. The figure shows that a high μ_e and low N_e are key to achieving a high J_{sc} . On the other hand, both a high μ_e and N_e are desirable for a low resistivity. In this respect, the higher mobility limit of In₂O₃ compared to ZnO allows for higher J_{sc} as well as lower resistivity values. Nonetheless, the contour plot shows a lower sensitivity of the J_{sc} for N_e and μ_e in the case of ZnO in comparison to In₂O₃. This is mostly due to the higher effective electron mass in ZnO, which leads to a lower ω_p and ω_τ for a given N_e and μ_e , respectively.

For comparison, a selection of carrier density and mobility values taken from literature reports (which will be discussed in the next section) are shown in Fig. 13, in which the bold-faced labels denote ALD processes. The ZnO-based processes show mobility values well below the mobility limit, which indicates that scattering processes related to material quality (e.g., grain boundary and neutral impurity scattering) play an important role. Nonetheless, ALD is at least on par with other deposition methods, especially since the reported films deposited by expanding thermal plasma (ETP) and low pressure CVD (LPCVD) were much thicker (>500 nm).

For the In₂O₃-based processes, it can be seen that various high-mobility TCOs have appeared that greatly outperform sputtered ITO. In particular, crystallized In₂O₃:H (*c*-In₂O₃:H) is very promising because of the low resistivity (<0.3 mΩ·cm) and very high J_{sc} due to a μ_e which is very close to the mobility limit. This material was initially developed by sputtering[130], but recently also an ALD process has been developed as will be discussed later.[4,120] Nonetheless, it has proven to be difficult to make a good metal-TCO contact for this material and the H-doped material is less stable at operating

conditions, which however can be remedied by the use of bilayers.[131]-[132] Recently also sputtered amorphous Zn-doped indium oxide (IZO) has gained interest, as it combines a relatively high μ_e (~ 60 cm²/Vs) with good metal-TCO contact properties and stability.[132]-[125] Also Mo-doped In₂O₃ (IMO) and W-doped In₂O₃ (IWO) are high-mobility TCOs, and SHJ solar cells based on the latter TCO in combination with copper metallization have reached efficiencies exceeding 22%.[126]

Compatibility with SHJ solar cells

It is required that the produced TCO and the processing thereof is compatible with the SHJ solar cell design and processing. The restrictions in terms of TCO processing are mostly dictated by the ultrathin intrinsic and doped a-Si:H layers. Especially the *p*-type doped a-Si:H layer is very temperature sensitive, and this puts an upper limit on the processing temperature of 200 °C.[115] Additionally, these ultrathin layers are prone to plasma-induced damage. For example, sputter deposition of TCOs leads to plasma-induced damage of the underlying a-Si:H films, thereby reducing the level of surface passivation.[114,133] Although post-deposition annealing can (partially) recover this damage, the microstructure of the a-Si:H layers is irreversibly altered.[133]

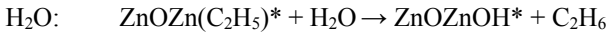
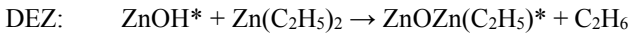
In addition to the considerations above, also the work function ϕ of the TCO is of importance. The front TCO contacting the a-Si:H(*p*) layer preferably has a ϕ equal or exceeding the ϕ of the a-Si:H(*p*) layer (~ 5.3 eV), whereas the rear TCO contacting the a-Si:H(*n*) layer preferably has a ϕ equal or below the ϕ of the a-Si:H(*n*) layer (~ 4.2 eV).[134] A mismatch in ϕ leads to a Schottky contact between the doped a-Si:H/TCO layer, and the associated depletion region can extend into the Si wafer and reduce the band bending, thereby seriously affecting the fill factor and even the open circuit voltage.[135,136] Although this effect can be mitigated by increasing the thickness and doping level of a-Si:H layers, this comes at the expense of enhanced parasitic light absorption and defect density in especially the a-Si:H(*p*) layer.[134]-[137] As can be seen in the schematic of Fig. 14(b), the ϕ of a degenerate TCO is determined by the electron affinity χ and the doping level through the Burstein-Moss shift, $\chi - \Delta E_{BM} = \phi$ (ignoring band gap narrowing).[138] Therefore, control over the work function of the TCO through its doping level is of importance for the optimization of the doped a-Si:H/TCO contact.[114,134]-[137] Since the electron affinity χ of ZnO (~ 4.4 eV) is lower than that of In₂O₃ (~ 5.0 eV), ZnO seems more suited to contact the a-Si:H(*n*) layer whereas lowly doped In₂O₃ is more suited for the front a-Si:H(*p*) layer.[138]

Together with the less stringent requirements on transparency at the rear side of the cell, ZnO-based TCOs are therefore more likely to be an effective low-cost alternative for indium-based TCOs at this side of the cell.[139] In fact, it has been recently shown that doped ZnO can replace the rear ITO without conversion efficiency loss.[139]

2.3.2 ALD of transparent conductive oxides

ALD of doped ZnO

The by far most studied ALD process for ZnO is the process based on diethyl zinc (DEZ, ZnEt₂) and water, which yields high growth rates (typically >1.5 Å/cycle) at temperatures <200 °C.[140] The process can be described by the following reaction:[141]



Unintentionally doped ZnO made by ALD can have an electron density up to $\sim 10^{19} \text{ cm}^{-3}$ due to the presence of oxygen vacancies and/or H dopants. Nonetheless, the resistivity of ZnO is typically in the high $10^{-3} \Omega\cdot\text{cm}$ regime, which necessitates cationic doping in order to reach the (low) $10^{-4} \Omega\cdot\text{cm}$ regime required for SHJ solar cell applications.

The most prevalent approach for doping of ZnO is by Al using TMA, although other dopant precursors and atoms such as B, Ga, Ti, Hf and even H have gained significant interest over the last years. An overview of low temperature ALD processes of doped ZnO can be found in table 5.

Table 5. Selection of reported low-temperature ALD processes of doped ZnO using DEZ as the Zn source.

Dopant	Doping precursor	T_{dep} (°C)	Doping level (at. %)	N_e (10^{20} cm^{-3})	μ_e (cm^2/Vs)	ρ ($\text{m}\Omega\cdot\text{cm}$)	Ref
Al	AlMe ₃	200	1.9	1.4	14.3	3.1	[142]
	AlMe ₃ [#]	170	-	4.3	7	2.1	[143]
	AlMe ₃ [*]	200	7	8	-	-	[144]
	AlMe ₂ (O ⁱ Pr)	250	4.6	10	6	1.1	[145]
	AlMe ₂ (O ^t Pr)	200	-	0.7-7	13.4-15.6	0.7-6.7	[114]
B	B(O ⁱ Pr) ₃	150-240	1.6	<3	<12	2.2-3.5	[146]
	B ₂ H ₆	150	-	~6	~20	0.64	[147]
Ti	Ti(OCHMe ₂) ₄	200	1.6	2.9	20.4	1.05	[148]
	-	-	-	4.5	15	0.9	[149]
Ga	GaMe ₃	210	-	~2	25-40	0.8	[150]
Hf	Hf(NMeEt) ₄	220	1.7	2.1	17	1.6	[151]
H	H ₂ plasma	200	-	6	15	0.7	[152]

[#] This process uses dehydroxylation to decrease the amount of TMA deposited.

^{*} This process uses functionalization by alkyl alcohols to decrease the amount of TMA deposited.

The introduction of dopants in the ZnO matrix is most commonly achieved using so-called ALD supercycles. The principle of an ALD supercycle is shown in Fig. 15. In such an ALD supercycle, an integer number n of ZnO cycles is followed by one dopant cycle. By repeating such supercycles, a structure as is shown in Fig. 16(a) is obtained, in which the dopants lie in distinct planes. This is distinctly different from CVD and PVD methods in which the dopants are randomly incorporated into the lattice. The *vertical* spacing of dopants can be accurately controlled by the number of ZnO cycles between the dopant (e.g., Al₂O₃) steps, i.e., the cycle ratio n . Therefore, using such a supercycle approach, the carrier density can be controlled with great accuracy by the cycle ratio n , as shown in Fig. 4(b).

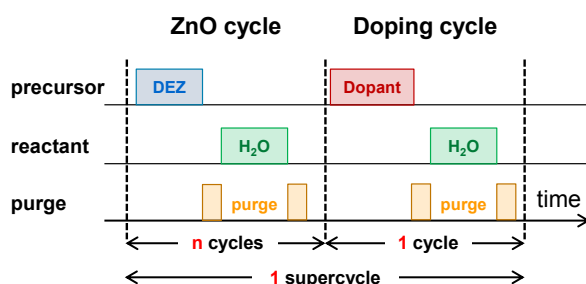


Figure 15 Schematic representation of the ALD supercycle principle. In ALD supercycles used for doping of ZnO, n cycles of the ZnO ALD process are followed by 1 cycle of a process containing a dopant element (Al, B, Ga, ...). This supercycle is repeated until the desired film thickness is reached. Adapted from Knoops *et al.*,[45]

For a proper control of the *vertical* spacing of the dopants, it is important to be aware of deviations from steady-state ALD behavior that can occur when switching ALD processes in the supercycle approach. For example, a reduction in growth rate has been observed for ZnO after either a doping step using TMA or a DMAI, which only recovers after ~ 4 ZnO cycles.[145,153] This reduction has been attributed to the coexistence of AlOH* and ZnOH* surface species after the Al₂O₃ step, which leads to proton transfer from the AlOH* group to the relatively basic ZnOH* group, resulting in a reduced density of surface OH groups.[145] Additionally, for the case of TMA it has been observed that ZnO can etched during the TMA exposure step by the following reaction:



Such abovementioned effects show that the growth per super cycle (GPSC) can vary from what would be expected from linear addition of the growth rates of the comprising ALD cycles.

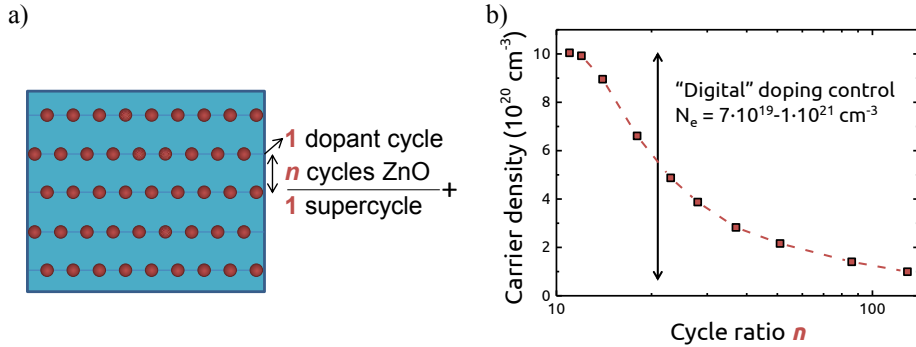


Figure 16 (a) Schematic representation of the superstructure obtained when using ALD supercycles. The cycle ratio n controls the *vertical* spacing of the dopants. (b) Demonstration of the accurate control over the carrier density in ZnO that is possible using the supercycle approach. The used process employs DMAI as dopant precursor and DEZ as Zn precursor, at a deposition temperature of 200 °C.

The presented supercycle approach inherently results in planes of high dopant density in the superstructure, which potentially leads to clustering of dopants. Such clustering can have several detrimental effects. First, clustering leads to a reduced doping efficiency, which enhances neutral impurity scattering by inactive dopants and limits the maximum achievable doping level. Secondly, the dopant cycle can interrupt the grain growth of the ZnO, thereby enhancing grain boundary scattering.[113]

Finally, for a given dopant density, ionized impurity scattering is minimized when the dopants are isotropically distributed. Therefore, besides control over the *vertical* spacing, also control over the *lateral* spacing of dopants is highly desired for optimization of doped ZnO layers. Several approaches have been proposed in literature to reduce this dopant clustering by reducing the number of dopant atoms deposited per cycle. Wu *et al.*, have shown that by replacing TMA as dopant precursor by a bulkier precursor, such as DMAI, the lateral distance between Al atoms can be increased due to enhanced steric hindrance, as is schematically shown in Fig. 17.[145] Because of the decrease in Al atoms deposited per dopant cycle from $\sim 1.1 \text{ at/nm}^2$ to $\sim 0.3 \text{ at/nm}^2$, the percentage of Al atoms in the film that are active as dopant, i.e., the doping efficiency, increases from $\sim 10\%$ to almost 60% .[145] Due to this, a maximum carrier density level up to 10^{21} cm^{-3} could be achieved, as opposed to a maximum of $\sim 4 \cdot 10^{20} \text{ cm}^{-3}$ for TMA.

Besides the use of steric hindrance, the amount of Al deposited in the dopant step can also be reduced by reducing the amount of hydroxyl sites available for TMA chemisorption. A rather simple approach was used by Park *et al.*, who prolonged the

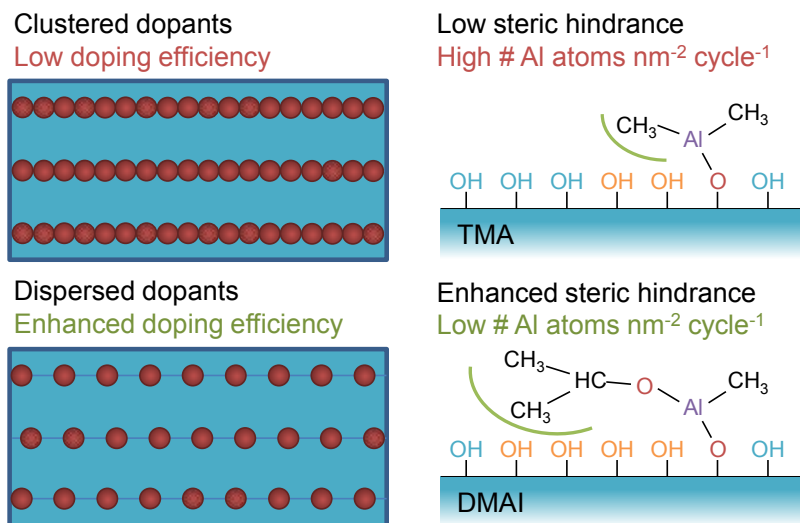


Figure 17 Schematic of the correlation between dopant clustering and doping efficiency. One approach for reduced dopant clustering is the use of dopant precursors with bulky ligands that lead to steric hindrance, as is shown for TMA and DMAI in the figure.

purge time after the water dose in order to reduce the amount of hydroxyl groups via dehydroxylation reactions.[143] Another approach is to dose the TMA immediately after the last DEZ dose, i.e., to omit the H₂O dose. Since less hydroxyl sites are available for TMA chemisorption, the Al incorporation is reduced and the doping efficiency is enhanced.[153]

Finally, functionalization of the surface by exposure to alkyl alcohols prior to TMA exposure can be used to reduce the amount of sites available for chemisorption of TMA. The alkoxide or alkoxyate surface groups that are formed are subsequently removed during the oxidant step.[144]

Beyond Al doping: Doping by B, Ti, Ga, Hf and H

Although Al doping has been the by far most studied dopant for ZnO, other dopant atoms such as B, Ti, Ga, Hf and even H have gained significant interest as well. Boron-doping of ZnO, well known in the field of low-pressure CVD, has been demonstrated using both B₂H₆ and triisopropyl borate (B(OⁱPr)₃, or TIB) as B-precursors. Using B₂H₆, Sang *et al.*, reported on ZnO:B with a promisingly low resistivity of 0.64 mΩ·cm obtained at a low deposition temperature of 150 °C (See table 5).[147] Also the carrier mobility, 20 cm²/Vs,

was quite respectable. Despite these promising results, few further reports on the use of B_2H_6 as ALD dopant can be found in literature. This could very well be due to the high toxicity of B_2H_6 in conjunction with its extremely high vapor pressure, which renders controlled dosing difficult.[146] Recently, $B(O^iPr)_3$ has emerged as a promising alternative B-precursor. At a deposition temperature of 200 °C a low resistivity of 0.9 $m\Omega\cdot cm$ could be achieved. Like in the case of DMAI, the $B(O^iPr)_3$ precursor benefits from its bulky ligands in reducing the amount of B dopants deposited per cycle.[146]

As can be seen from table 5, also the use of Ti and Ga as dopant has been shown to enable resistivity values $<1 m\Omega\cdot cm$. Interestingly, Thomas *et al.*, have demonstrated that it is also possible to dope ZnO with H by interleaving ZnO cycles by H_2 plasma treatments.[152] In this way, a resistivity of 0.7 $m\Omega\cdot cm$ was achieved at a reasonably high mobility of 15 cm^2/Vs .

To conclude this section on doped ZnO, several groups have shown that resistivity values well below 1 $m\Omega\cdot cm$ can be achieved at low temperatures (≤ 200 °C). Key to achieving efficient doping is reduction of dopant clustering through the use of innovative approaches to reduce the number of dopant atoms deposited per cycle. Even though values typical for conventional sputtered ITO ($\sim 0.4 m\Omega\cdot cm$) cannot be reached, considerations regarding cost and material availability could make doped ZnO an effective alternative to ITO, especially at the rear side of a SHJ solar cell.

ALD of In_2O_3

Although historically Sn-doped In_2O_3 (ITO) has been the most widely used TCO for SHJ solar cells, relatively less literature on ALD of In_2O_3 -based TCOs seems to be available compared to ZnO. In table 6, a brief overview of ALD processes of (doped) In_2O_3 is shown.

In 1995 Asikainen *et al.*, demonstrated ALD of both In_2O_3 and ITO using a halide $InCl_3$ precursor, and achieved a very low resistivity of 0.25 $m\Omega\cdot cm$ by Sn-doping.[154] However, the process featured a low GPC of 0.2 Å and required a high deposition temperature of 500 °C. At lower temperatures, the use of $In(acac)_3$, $In[(^iPrN)_2CN(CH_2Me)]_3$, $InMe_3$, DMLDMin, $In(TMHD)_3$ and $InCp$ have been reported. $In(acac)_3$ and $In[(^iPrN)_2CN(CH_2Me)]_3$ have a somewhat higher GPC, but the optoelectronic properties have so far not been reported. $InMe_3$ and H_2O can yield a reasonable resistivity ($\sim 3 m\Omega\cdot cm$) at an intermediate temperature (200-250 °C) and a GPC of ~ 0.39 Å.

In 2006, Elam *et al.*, demonstrated an ALD process for In₂O₃ based on indium cyclopentadienyl (InCp) and ozone at temperatures 200–450 °C.[155] Promisingly, a high GPC of 1.3–2.0 Å was achieved and a very low resistivity of 0.3 mΩ·cm was reached at 275 °C by Sn-doping using TDMASn and H₂O₂. A few years later, Libera *et al.*, showed that although H₂O and O₂ by themselves do not yield growth in combination with InCp, a combination of H₂O and O₂ as oxidants yields a high GPC (1.0–1.6 Å) at very low deposition temperatures (100–250 °C).[156] They proposed that both oxidants are needed for growth since they serve different roles, i.e., H₂O eliminates the Cp ligand and O₂ oxidizes the surface In from oxidation state +1 to +3. Moreover, a low resistivity of 0.34 mΩ·cm was achieved for an amorphous film at 100 °C. The highest mobility value of 111 cm²/Vs was achieved at 140 °C, which is around the amorphous-polycrystalline growth transition temperature.

Table 6 Selection of reported ALD processes for (doped) In₂O₃.

Dopant	Precursors	T_{dep} (°C)	N_e (10 ²⁰ cm ⁻³)	μ_e (cm ² /Vs)	ρ (mΩ·cm)	GPC (Å)	Ref
-	InCl ₃ , H ₂ O	500	0.25	72	3	0.2	[154]
Sn	InCl ₃ , SnCl ₂ , H ₂ O	500	5.2	47	0.25	0.2	[154]
-	In(acac) ₃ , H ₂ O	160-255	-	-	30-6×10 ⁴	0.15-0.25	[157]
-	In[(ⁱ PrN) ₂ CN(CH ₂ Me)] ₃ , H ₂ O	230-300	-	-	-	0.45	[158]
-	InMe ₃ , H ₂ O	200-250	0.27	84	2.8	~0.39	[159]
-	DMLDMIn, H ₂ O	300	0.75	28.7	1.6	0.6	[160]
-	In(Me ₃ HD) ₃ , O ₂ plasma	100-400	-	-	2.5-18	0.14	[161]
-	InCp, O ₃	200-450	-	-	16	1.3-2.0	[155]
Sn	InCp, O ₃ , TDMASn, H ₂ O ₂	275	4	50	0.3	1.1–1.7	[162]
7H?	InCp, H ₂ O+O ₂	100-250	0.8-4.5	38-111	0.34-2.5	1.0-1.6	[156]
H*	InCp, H ₂ O+O ₂	100	1.8	138	0.27	1.2	[4,120]

*The films were post-crystallized at 150-200 °C

Macco *et al.*, have demonstrated that the ALD process of Libera *et al.*, using InCp and a combination of O₂ and H₂O actually unintentionally yields H-doped In₂O₃ (In₂O₃:H), where an amorphous film deposited at 100 °C has a H content of 4.2 at. %.[4] By low temperature post-deposition annealing at 150-200 °C, solid phase crystallization of the film occurs, which yields a low resistivity of 0.27 mΩ·cm at a record-high electron mobility of ~138 cm²/Vs and a relatively low carrier density of 1.8·10²⁰ cm⁻³. This combination leads to negligible free carrier absorption in the photon energy range relevant for SHJ solar cells.[4] In fact, the quality of crystallized layers is such that only phonon

and ionized impurity scattering processes play a role, meaning that the mobility is at its fundamental limit, as can also be seen in Fig. 13 (b).[120] The excellent optoelectronic properties in combination with the low temperature processing and high growth rate make this process very interesting for SHJ solar cell applications. To the authors' knowledge, there are currently no ALD processes reported for IZO, IMO and IWO, which is a clear opportunity for further development.

2.3.3 High volume manufacturing of ALD TCOs

Although ALD is not yet used in industry for the preparation of TCOs for SHJ solar cells, the ALD approach can potentially offer some key benefits over the most-commonly used sputtering method. First, due to the absence of harsh plasma conditions during ALD, plasma damage (e.g., during sputtering) to the substrate is avoided. Therefore, recent studies have focused on the use of ALD as a “soft deposition” method to deposit TCOs in SHJ solar cells and have demonstrated improved passivation.[114,163] Additionally, as shown in the section on ALD of doped ZnO, ALD allows for a high level of control over the doping level of the TCO and thereby its work function. This greatly facilitates the optimization of the doped a-Si:H/TCO contact by varying the doping level and potentially even the doping profile.[114,134][137]

Moreover, after the recent introduction of high-throughput ALD reactors for HVM of Al₂O₃ in the PV industry, also the deposition of (doped) ZnO by such reactors, most notably spatial ALD (S-ALD), is being explored.[164,165][81,166][167] As can be seen in table 7, S-ALD processes have been reported that combine high deposition rates exceeding 1 nm/s with rather good material properties. In particular, Ellinger *et al.*, showed that a very low resistivity (<0.5 mΩ·cm) can be obtained at high growth rates (~1.5 nm/s), on par with typical growth rates obtained with sputtering, at an intermediate deposition temperature (250 °C).

Table 7. Selection of reported S-ALD results of both intrinsic and doped ZnO using DEZ as the Zn source.

Dopant	Doping source	GPC (nm)	T_{dep} (°C)	N_e (10^{20} cm^{-3})	μ_e (cm^2/Vs)	ρ ($\text{m}\Omega\cdot\text{cm}$)	Ref
-	-	0.6	200			$1-2 \times 10^5$	[13,168]
-	-	~1	75-250	0.2-0.7	14-30	4-150	[167]
Al	TMA	0.2	200	5	6	2	[169]
Al	DMAI	~1.5	250	-	-	0.46	[170]
In	InMe ₃	0.1	200	6	3	3	[171]
Ga	GaMe ₃	0.4	250			2	[172]

A key difference between temporal and spatial ALD of doped TCOs is that in spatial ALD, the dopants can, apart from using the supercycle approach, also be introduced by *premixing* or by *co-injection* with the other precursor, due to a homogeneous delivery of the precursor to the substrate. In such approaches, both precursors compete for reactive surface sites. As a result, the amount of dopant incorporation depends for example on the partial pressures of both precursors and can even depend on exposure times.[169] One might thus say that some level of control which is typical for the supercycle approach is lost when switching to premixed or co-injected precursors. Nonetheless, the good material properties that have been reported and the ability to even successfully deposit other multicomponent oxides such as InGaZnO demonstrate that this is not necessarily a drawback for the industrial application of precursor mixing or co-injection in S-ALD.[173]

2.4 Prospects for ALD in passivating contacts

In this section, the upcoming field of passivating contacts and the possible role of ALD therein will be discussed. First, the basic principles and requirements of passivating contacts and some of its concepts will be outlined. Subsequently, examples of passivating tunnel and carrier-selective oxides and the use of ALD for preparing such oxides will be reviewed.

2.4.1 Basics of passivating contacts

A passivating contact is typically a stack of thin films on the Si absorber, which passivates the Si surface and simultaneously acts as a selective membrane for either holes or electrons. Examples include the traditional silicon heterojunction cell and the TOPCon concept, as discussed in the introduction.

How to make a passivating contact

To briefly illustrate the working principle and the merits of passivating contacts, schematic band diagrams of example strategies to produce carrier-selective contacts are shown in Fig. 18. All diagrams consider the Si under illumination, which leads to excess charge carriers. Since in a metal (or TCO) there can be no quasi-Fermi level splitting, the two quasi-Fermi levels must converge at the contact. Since a gradient in a Fermi level represents a force, this leads to a current of both electrons (J_n) and holes (J_p) towards the metal:

$$J_n = en\mu_n \nabla E_{Fn}, \quad J_p = ep\mu_p \nabla E_{Fp} \quad (2.4.1)$$

In these equations, μ_n and μ_p are the electron and hole mobility. Also note that all these quantities in principle depend on the spatial coordinate x .

In order for a contact to be *selective*, the region or film(s) in between the Si and metal contact must, besides providing passivation, induce a strong *asymmetry* in the electron and hole currents to the metal contact. In order to understand how this asymmetry can be achieved, one should realize that equations 2.4.1 are basically Ohm's law for electrons and holes.[174] If the conductivity for a charge carrier is high (i.e., a high product of mobility and carrier concentration), there will be a low gradient in quasi-Fermi level towards the contact for a given current (i.e., little voltage drop). Therefore, in the case of a passivating contact, the quasi-Fermi level of the carrier that is to be extracted should be as flat as possible (i.e., low resistance), whereas the other quasi-Fermi level should show a high degree of bending (i.e., high resistance). This is markedly different from an ideal passivation layer on Si where both quasi-Fermi levels are flat (high resistance to both carriers), and a Si/metal contact, in which case in principle both quasi-Fermi levels will bend (low resistance to both carriers).

In Fig. 18(a), the conventional method for making an electron-selective contact ($J_n \gg J_p$) is shown, i.e., by heavily doping the Si. The selectivity for electrons arises from the high resistance for holes in the heavily doped n^+ Si region. Note that the holes actually experience a strong force towards the metal, as seen by the strong gradient of the Fermi level, E_{Fp} . Nevertheless, the hole current J_p in this region is very low since the large energetic distance between the valence band and E_{Fp} ensures a low density of holes p and hence a high resistance for holes. Although contacts based on such homojunctions can be very selective, the V_{oc} of such devices is typically limited by Auger recombination occurring in the highly doped region. This drawback is avoided by using passivating contacts, examples of which are depicted in Fig. 18 (b-d).

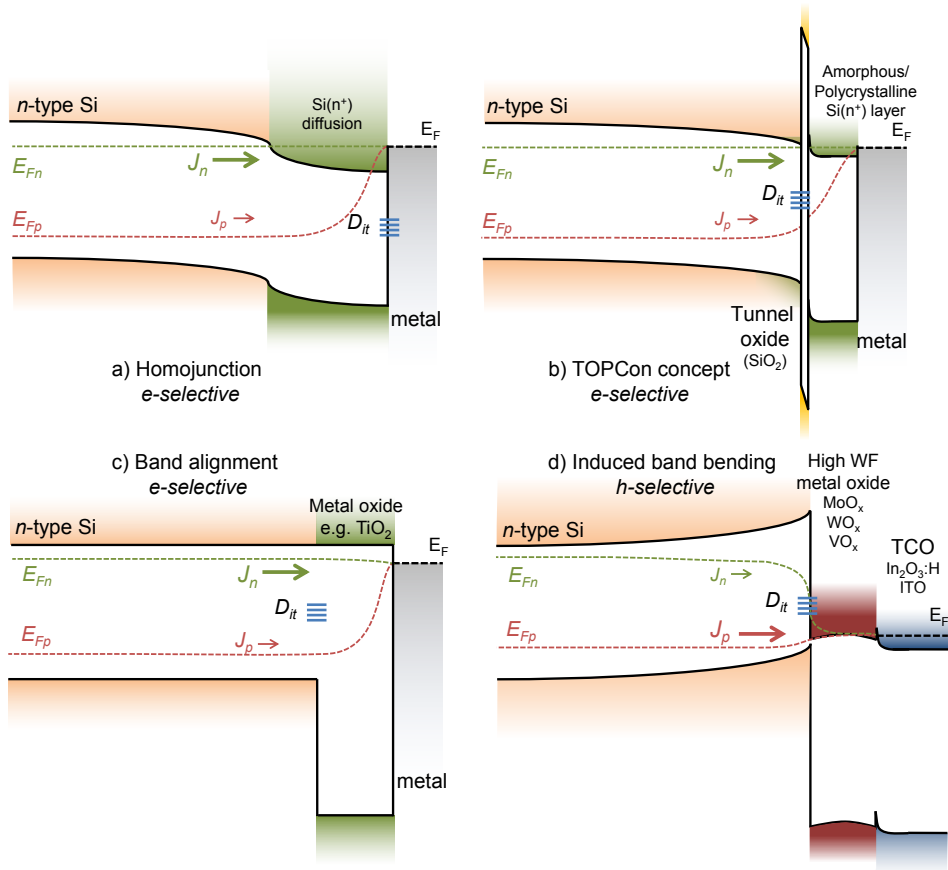


Figure 18 Schematic band diagrams of various approaches for making carrier selective contacts. All band diagrams refer to the situation under illumination and are not drawn to scale. (a) A conventional electron-selective contact made by n^+ -type doping. (b) An electron-selective contact made by the TOPCon concept, consisting of a tunnel oxide and a thin (partially) crystalline n^+ -Si film. (c) An electron-selective contact which is realized through *band-alignment* of the Si with a metal oxide film. (d) A hole-selective contact which is realized through *induced band-bending* by a high work function metal oxide film. Often concepts (c) and (d) also employ separate ultrathin passivation layers, but these were not drawn for simplicity.

In Fig. 18 (b) the TOPCon concept is shown. Here, the n^+ doping of the (partially) crystalline Si layer provides selectivity to extract electrons in a fashion quite similar to the doped region of (a). A very thin SiO₂ tunnel oxide of ~ 1.4 Å, typically prepared by a nitric acid oxidation step (NAOS), provides chemical passivation and acts as a diffusion barrier

for dopants. Note that the typical thickness of the doped Si layer (few tens of nanometers) is much less than a typical conventional doped region ($\sim 0.5 \mu\text{m}$) in homojunction cells and thus leads to much less Auger recombination.

In Fig. 18 (c), an electron-selective contact is formed by *band-alignment*: A wide band gap material is deposited on Si, with little (or ideally no) conduction band offset. In this way, the hole current J_p is greatly reduced by the large valence band offset. Again, the strong gradient in E_{Fp} shows that the holes experience a strong force towards the metal, but the large energetic distance between the valence band and E_{Fp} ensures a low density of holes p in the metal oxide film and thereby a low hole current J_p . Note that for simplicity it is here assumed here that no band bending occurs (i.e., no fixed charge and equal work functions of the n -type Si and the metal oxide film are assumed).

In Fig. 18 (d), a hole-selective contact is formed by *induced band-bending*: In this example, the high work function ($> \sim 5.5 \text{ eV}$) of a metal oxide (such as MoO_x , WO_x or VO_x), induces a strong upward band bending at the n -type Si surface leading to inversion. Hereas the band bending reduces the electron concentration at the surface, the band bending facilitates a high hole current J_p to the metal.

In Fig. 19 an overview is given of the band offsets with Si of (a selection of) oxides that are of interest for the formation of a passivating contact. It should be noted that these values can vary considerably depending on the exact processing conditions, and the values are therefore indicative. Ta_2O_5 , TiO_2 and strontium titanate (STO) are of interest as electron-selective contact due to their small conduction band offset. Likewise, NiO is of interest as a hole-selective contact due to its small conduction band offset,[19,175] whereas MoO_3 and WO_3 form hole-selective contacts by induced band-bending.[176][18]

For simplicity, separate passivation layers were not shown in the band diagrams in Fig. 18. Nonetheless, since the oxides used for selectivity generally do not offer (excellent) passivation, many passivating contact schemes employ a-Si:H or ultrathin ($< 2 \text{ nm}$) tunnel oxide layers such as Al_2O_3 and SiO_2 in the between the Si and the carrier-selective layer for interface passivation.[†]

[†] Besides providing interface passivation, these layers are also thought to aid in selectivity: If for example a-Si:H is added in between the Si and high WF metal oxide of figure 18(d), most of the drop in E_{Fn} will occur in the a-Si:H instead of in the Si. Since the mobility in a-Si:H is orders of magnitudes lower than in Si, this will lead to a reduced J_n towards the metal contact, according to equation 2.4.1.

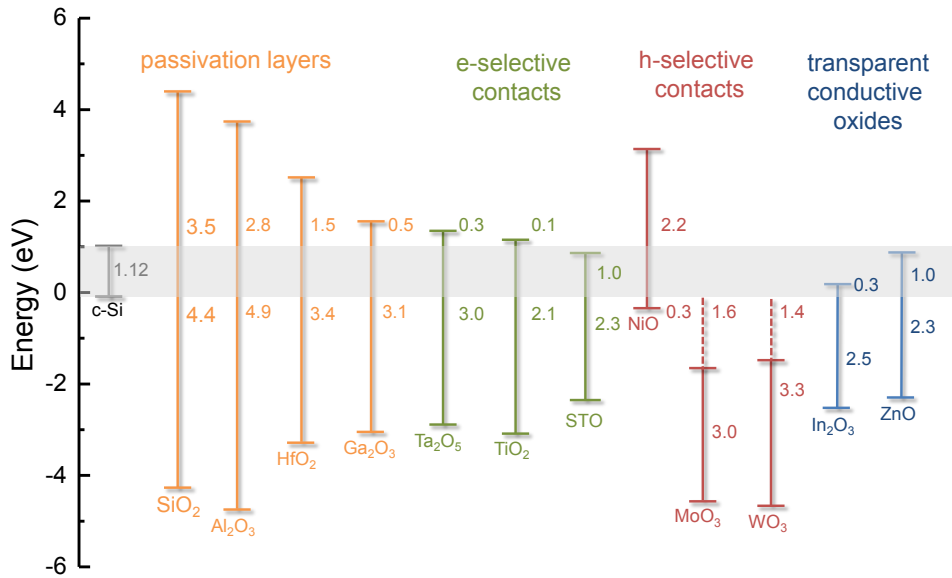


Figure 19 Schematic of the band offsets of a selection of oxides with Si. Offsets are denoted in eV. Adapted from references [177] and [178].

In Fig. 19, also typically used oxide passivation layers are shown. As discussed in section 2.2, such oxides should have a low interface defect density D_{it} , whereas the presence of a fixed charge density Q_f can be either beneficial or detrimental to the passivation quality depending on the doping of the wafer. When applied to passivating contacts, additional requirements for such layers come into play. Since the oxides should allow for tunneling, the D_{it} should be low even for ultrathin (<2 nm) layers. The presence of fixed charge is also of importance, as the band bending induced by fixed charge can affect the selectivity, analogous to the case of Fig. 18(d). For example, the high negative fixed charge of Al₂O₃ makes Al₂O₃ more suited for hole-selective contacts rather than electron-selective contacts. Finally, the band offsets with Si play a role as well since tunnel probabilities are inversely and exponentially proportional to the band offsets. For example, for SiO₂ the asymmetry in the valence band (4.4 eV) and conduction band (3.5 eV) offset makes it such that electrons tunnel much easier than holes.[179] Therefore, asymmetry in the band offsets can also aid in selectivity.

Requirements of a passivating contact

To assess the potential of various passivating contact schemes, it is instructive to discuss the two main figures of merit of a passivating contact:

- The contact resistivity ρ_c for the charge carrier type the contact should be selective to.
- The recombination current of the other charge carrier type to the metal contact, which can be characterized by J_0 .

To a first order approximation, the (total) contact resistance influences the FF , whereas the recombination current limits the V_{oc} . In Fig. 20, a contour plot of the maximum Si solar cell efficiency is displayed as a function of the ρ_c and J_0 values of the rear contact. This calculation assumes a full area rear contact with no other loss mechanisms (no optical losses, no other recombination anywhere in the cell and no other resistive losses), and thus represents the upper bound of the solar cell efficiency set by the rear contact.

As can be seen from Fig. 20, high efficiency (>25 %) devices require both low ρ_c (<1 $\Omega\cdot\text{cm}^2$) and J_0 (<100 fA/cm^2) values, a region which can be defined as a criterion for being a passivating contact. For comparison, a typical Si/metal contact in a p -type Al-BSF concept has a very low contact resistivity ($\sim 5 \text{ m}\Omega\cdot\text{cm}^2$), but the high J_0 (>500 fA/cm^2) severely limits the conversion efficiency. On the other hand, an Al_2O_3 passivation layer can yield a very low J_0 (<10 fA/cm^2), but is insulating. For this reason, many cell designs (e.g., PERC and PERL) employ a local metal contacting scheme: By making local metal contacts to the silicon, a trade-off is made between passivated regions of low J_0 ($J_{0,pass}$) with contacting regions that have a high J_0 ($J_{0,cont}$) but a low ρ_c . The effective J_0 and ρ_c of a locally contacted rear are determined by the contact area fraction f by the relations $J_{0,eff} = f \cdot J_{0,cont} + (1-f)J_{0,pass}$ and $\rho_{c,eff} = \rho_c / f$. However, local contacting might add to processing complexity and additionally induces resistive FF losses in the bulk of Si due to the required lateral transport of carriers therein, as shown in Fig. 21.[3] Figure 20 also shows literature values for various passivating contact concepts, as well as for various rear sides of cell concepts using partial metallization. The classical SHJ concept based on (doped) a-Si:H layers is probably the best-known example of a passivating contact. The rear contact of the current record solar cell of Kaneka (25.1% efficiency) combines a very low J_0 value of 12 fA/cm^2 with a low contact resistivity of 30 $\text{m}\Omega\cdot\text{cm}^2$. [14] The TOPCon concept and the SiO_2/ITO stack of Young *et al.*, [180] (as will be discussed below) are both

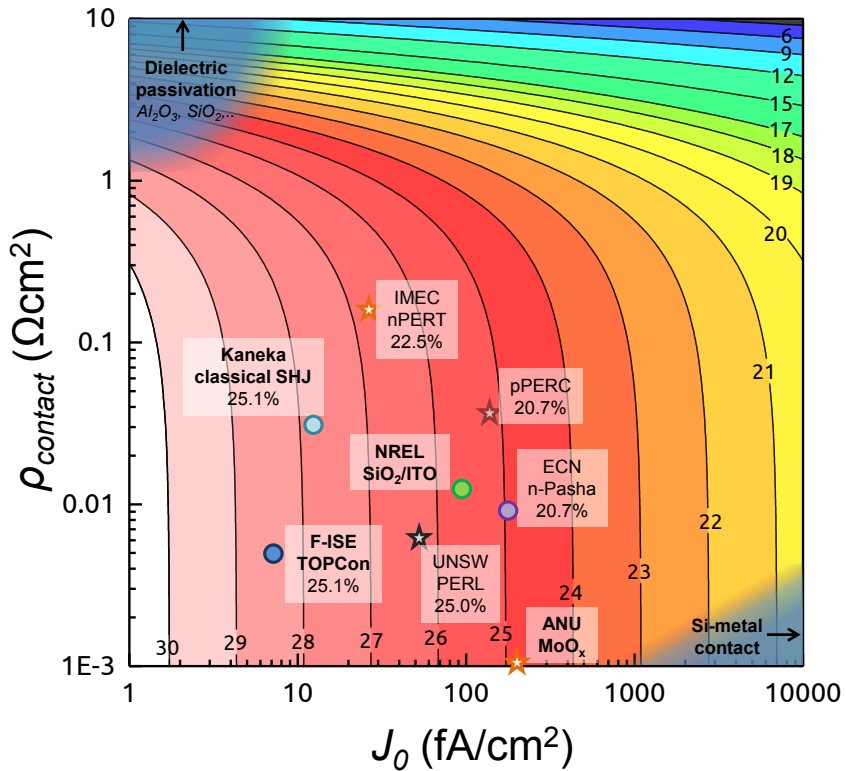


Figure 20 Contour plot of the calculated upper limit of efficiency of a solar cell featuring a full area passivating contact, as a function of J_0 and ρ_c . The calculation is done similarly as in references [180] and [181] and assumes no other recombination channels (surface nor bulk), no shunting and no optical losses (i.e., a J_{sc} of 44 mA/cm^2). For comparison, data points for various reported structures/cells are shown, along with the efficiencies of the full devices. These include a SHJ concept of Kaneka [14],[182], the TOPCon concept of F-ISE [3],[183], the SiO_2/ITO stack of NREL [180], the TiO_2 contact of ANU [108], the UNSW PERL [184], a p -type PERC [184], the IMEC nPERT [185,186], the ECN nPasha [184],[182] and a p -type Si/MoO_x contact [187]. Hole-selective contacts are denoted by star-shaped symbols, whereas electron-selective contacts are denoted by circular symbols. Concepts employing a full area rear contact are noted in bold. For the PERL cell, the J_0 was estimated using the reported surface recombination velocity in reference [184] and case 3 in reference [25]. For cell concepts that use a partial rear contact, the J_0 and ρ_c values have been corrected for the contact area fraction f .

electron-selective contacts that use a tunnel oxide. As can be seen, both concepts have a very low ρ_c , demonstrating that efficient transport can occur through such oxides.

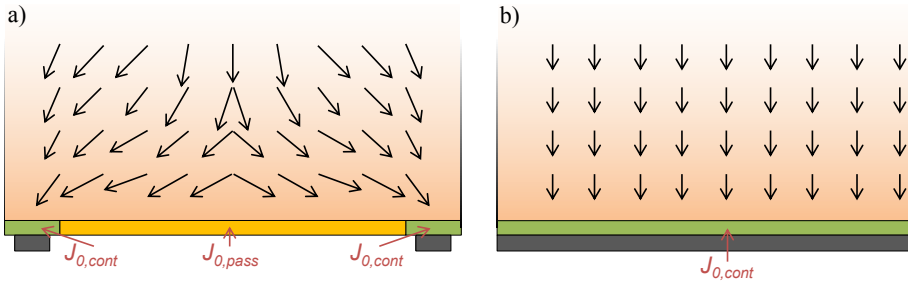


Figure 21 Schematic showing the current flow pattern in (a) a locally contacted cell and (b) a solar cell with a full-area rear contact. Adapted from Glunz *et al.*[3]

Moreover, the TOPCon concept shows that very low J_0 values can be achieved with tunnel oxides.

Due to the excellent properties of such passivating contacts, full area contacts can be employed while still having a low J_0 . This has the benefit of having one-dimensional charge transport in the solar cell, thereby reducing resistive losses due to lateral transport, as well as being very straightforward from a processing point of view. As can be seen, the solar cell concepts employing partial rear metallization are also capable of reaching low ρ_c values, but the local metal contacts inevitably lead to higher J_0 values.

As will be discussed below, other metal oxide films are promising for passivating contact formation as well, such as TiO_2 for electron-selective contacts and MoO_x , WO_x and VO_x for hole-selective contacts. Evaporated MoO_x directly on p -type Si has been reported to have a very low contact resistivity ($1 \text{ m}\Omega\cdot\text{cm}^2$) and an intermediate J_0 of $\sim 200 \text{ fA/cm}^2$, as can be seen in Fig. 20.[187] Because of the low ρ_c and intermediate J_0 , such contacts are best used in a partial rear contacting scheme, as shown by a reported 20.4% efficient solar cell using a 5% rear contact area fraction.[188] Moreover, MoO_x has been used as a replacement of the a-Si:H(p) layer in a conventional SHJ concept. Due to the passivating properties of the a-Si:H layer, an impressive 22.5% efficiency has been reported for a full area front contact.[189] The J_0 and ρ_c values of the a-Si:H/ MoO_x /TCO contact were not reported for this solar cell.

2.4.2 ALD for passivating contacts

As was discussed in the previous section, (stacks of) various thin films are of interest to serve as passivating contact, which in principle can be prepared by ALD. Moreover, the use of ALD may offer distinct advantages, e.g., in terms of processing/doping control and the easy manufacturing of stacks. Nonetheless, this new field has yet to be fully explored.

Therefore, in this section the possible role of ALD in preparing tunneling oxides and carrier-selective oxides is discussed, addressing both the few examples of ALD already shown in this field as well as the future prospects.

ALD for tunneling oxides

For tunnel oxides, the contact resistivity (i.e., ρ_c) and level of surface passivation (i.e., J_0) are extremely dependent on the thickness of the oxide. Therefore, it is expected that the submonolayer thickness control over a large surface area offered by ALD can be a key enabler in this respect. It is worth mentioning that ultrathin ALD Al_2O_3 has also been used in between the metal contacts and the highly doped region of the Si wafer in the PERC concept. Although this is strictly spoken not a passivating contact, it has been shown that only 2 cycles of Al_2O_3 enhances the passivation (12 mV increase in V_{oc}) without a significant increase in contact resistivity.[190]

A tunneling ALD Al_2O_3 film has been successfully used in a $\text{Al}_2\text{O}_3/\text{ZnO}(\text{:Al})$ stack to make a hole-selective contact, fully prepared by ALD.[22,23] Such a stack achieves selectivity towards holes by the negative fixed charge in the Al_2O_3 which leads to accumulation of holes at the Si surface, which is analogous to the use of a high work function metal oxide as in Fig. 18(d). The holes subsequently recombine with the electrons in the conduction band of the $\text{ZnO}(\text{:Al})$. Interestingly, such a stack takes advantage of the fact that the fixed charge in Al_2O_3 has been observed to be *interfacial*, i.e., it resides at the Si- Al_2O_3 interface, and is thus persistent even for ultrathin films.[191] Additionally, the position of the Fermi level in the TCO, which is readily tuned in ALD by control of the doping level, was found to be crucial for the working of such a contact. Nonetheless, although this work nicely demonstrates a proof-of-concept, the high reported J_0 ($>10^4$ fA/cm²) and intermediate ρ_c (>1 Ωcm^2) values hinder a high efficiency.

Besides Al_2O_3 , many passivating contacts employ SiO_2 as tunnel oxide. Young *et al.*, have shown that a stack of thin SiO_2 and sputtered ITO can also make an electron-selective contact through energetic lineup of the Fermi levels of the Si and the heavily degenerate ITO.[180] Promisingly, a low J_0 of 92.5 fA/cm² and a contact resistivity ρ_c of only 11.5 m $\Omega\cdot\text{cm}^2$ were achieved, as indicated in Fig. 20. Remarkably, the optimal SiO_2 thickness prior to ITO sputtering was found to be 4.5 nm, much more than would be expected on the basis of a tunneling process. This has been attributed to intermixing of the SiO_2 /ITO layer by the energetic ions coming from the plasma.[180] In this respect, atomic layer deposition of TCOs ($\text{In}_2\text{O}_3\text{:H}$, ZnO)[4] could be a much better controlled process due to the absence of plasma-related damage.[114]

Finally it is worth noting that the use of ultrathin ALD metal oxides as tunneling layers has already been explored in the field of organic PV.[192,193] Specifically, ALD layers of Ga₂O₃ and Ta₂O₅ have been used successfully in such solar cells. These two materials have recently been shown to provide excellent Si surface passivation, making also these materials highly interesting for passivating contact formation for Si solar cells.[104,105]

ALD for electron-selective contacts

An electron-selective contact has been prepared by an ultrathin (1-4 nm) layer of TiO₂ by Avasthi *et al.*, [20]. The selectivity of this film is achieved through band alignment as shown in Fig. 18(c). Although the work of Avasthi *et al.*, demonstrates the electron selectivity of TiO₂, the rather simple device structure and lack of passivation severely limited the performance of the device.

Promisingly, as discussed earlier, Liao *et al.*, have demonstrated that it is possible to achieve excellent surface passivation using a thermal ALD process using TiCl₄ and H₂O at 100 °C to deposit TiO₂, which suggests that this concept could be optimized further.[106] In other work also a very low surface recombination velocity of 16 cm/s was observed for a carefully prepared TiO₂/Si heterojunction, showing that this interface can be highly passivating.[194] Yang *et al.*, [108] have subsequently demonstrated that 4.5 nm of TiO₂ prepared by ALD (using Ti(OⁱPr)₄ and H₂O at 230 °C) can also yield a relatively low contact resistivity of ~0.25 Ω·cm² and a J_0 of 25 fA/cm². When combining this ALD TiO₂ with a 1.5 nm SiO₂ interlayer, they demonstrated an impressive 20.5% efficiency for their champion cell.

As can be seen from Fig. 19, also Ta₂O₅ and STO have the proper band alignment to serve as an electron-selective contact. As already pointed out in section 2.2.4, ALD Ta₂O₅ can provide excellent surface passivation when capped with SiN_x. [105] Therefore, the use of a dedicated passivation layer in between the Si and Ta₂O₅ can potentially be avoided. Nonetheless, the observed negative fixed charge of ~10¹² cm⁻³ observed might hinder the working as a selective electron contact.

STO is mostly known in the semiconductor industry for its very high dielectric constant. It has been shown experimentally that the conduction band off-set of STO on both *n*- and *p*-type Si is negligible (~0.1 eV) and does not change significantly if a very thin SiO₂ interlayer is applied (<1.2 nm).[195] More importantly, DFT calculations predict that the conduction band offset is highly dependent on the initial layer of the STO thin film: The desired negligible conduction band offset (0.1-0.2 eV) occurs when the initial

layer of the STO film consists of SrO, whereas a higher offset of 1.2–1.3 eV has been predicted when the initial layer consists of TiO₂. [196] Since both the interfacial and bulk composition can be controlled accurately by ALD by choosing the appropriate initial cycle (TiO₂ or SrO) and cycle ratio, [197] respectively, it can be expected that ALD is very well suited for the preparation of such oxides.

Table 8. Selection of ALD processes reported in literature of potential carrier-selective oxides.

Metal Oxide	Metal Precursor	Reactant	T_{dep} (°C)	GPC (Å)	Ref
<i>Electron-selective oxides</i>					
TiO ₂	Ti(O ⁱ Pr) ₄	H ₂ O	150-300	0.2-0.3	[198]
	TiCl ₄	H ₂ O	100	0.6	[106]
	Ti(Cp [*])(OMe) ₃	O ₂ plasma	50-300	0.5	[199]
	Ti(NMe ₂) ₄	H ₂ O	25-325	0.5-1.4	[200]
Ta ₂ O ₅	Ta ₂ (OEt) ₁₀	H ₂ O	250	0.3	[105]
	Ta(NMe ₂) ₅	O ₂ plasma	100-250	0.8-0.9	[199]
	Ta(NMe ₂) ₅	H ₂ O/O ₃	200-300	0.9/1.1	[201]
STO	Cp(Me) ₅ Ti(OMe) ₃ / Sr(ⁱ Pr ₃ Cp) ₂ DME	O ₂ plasma	150-350	2.3-2.6*	[197]
	Ti(O ⁱ Pr) ₄ /Sr(thd) ₂	H ₂ O plasma	250	0.6**	[202]
<i>Hole-selective oxides</i>					
MoO _x	(N ⁱ Bu) ₂ (NMe ₂) ₂ Mo	O ₃	100-300	0.3-2.4	[203]
	(N ⁱ Bu) ₂ (NMe ₂) ₂ Mo	O ₂ plasma	50-350	0.8-1.9	[21,204]
	Mo(CO) ₆	O ₃	152-172	0.8	[205]
WO _x	(N ⁱ Bu) ₂ (NMe ₂) ₂ W	H ₂ O	300-350	0.4-1.0	[206]
	W(CO) ₆	O ₃	195-205	0.2	[207]
	WH ₂ (ⁱ PrCp) ₂	O ₂ plasma	300	0.9	[208]
VO _x	V(NEtMe) ₄	H ₂ O	125-200	0.8	[209]
	VO(OPr) ₃	H ₂ O	170-190	1.0	[210]
	VO(OPr) ₃	O ₂ /H ₂ O plasma	50-200	0.7	[211]
NiO _x	Ni(Et ₂ Cp) ₂	O ₃	150-300	0.4-0.9	[212]
	Ni(thd) ₂	H ₂ O	260	0.4	[213]
	Ni(Cp) ₂	H ₂ O	165	-	[214]
	Ni(dmamp) ₂	H ₂ O	120	0.8	[215]

*The reported GPC is the growth per supercycle for a [SrO]/[TiO₂] cycle ratio of 1:3.

**The reported GPC is the growth per supercycle for a [SrO]/[TiO₂] cycle ratio of 1:1.

ALD for hole-selective contacts

Molybdenum oxide (MoO_x) is well-known in the organic PV literature as a hole transport material. However, it has only very recently been demonstrated that evaporated MoO_x can replace the hole-selective a-Si:H(*p*) layer at the front of a standard SHJ solar cell. [17,187,216] The working principle of such a selective hole contact is thought to be

based on the high work function of MoO_x (~ 6.6 eV), as shown in Fig. 18(d). Promisingly, the reduced optical losses enable a substantial enhancement in photocurrent of 1.9 mA/cm^2 . Currently, the highest reported efficiency for a MoO_x -based SHJ is already 22.5%, which is very promising given the novelty of this approach.[189]

Recently, it has also been shown that MoO_x can be deposited by plasma-enhanced ALD using $(\text{N}^i\text{Bu})_2(\text{NMe}_2)_2\text{Mo}$ and O_2 plasma at temperatures down to 50 °C.[204] Additionally, this ALD MoO_x layer was implemented in an $a\text{-Si:H}/\text{MoO}_x/\text{ALD In}_2\text{O}_3\text{:H}$ stack (Fig. 22), and a high level of passivation in combination with a high optical transparency was demonstrated.[21] In other work, initial solar cell results based on ALD MoO_x have been reported, although the efficiency ($\sim 11\%$) is not yet on par with its evaporated counterpart.[217]

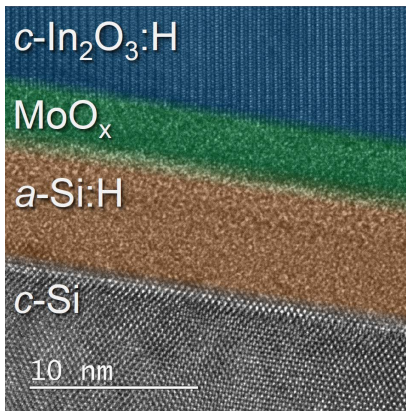


Figure 22 False-colored cross-sectional TEM image of a stack of amorphous silicon, ALD MoO_x and crystallized ALD hydrogen-doped indium oxide ($c\text{-In}_2\text{O}_3\text{:H}$). Adapted from Macco *et al.*[21]

For the other aforementioned hole-selective materials of WO_x , VO_x and NiO_x , there have been no reports yet on the use of ALD to make carrier-selective contacts with these materials. Since all these materials can be made by ALD, it is likely that this will be explored in the near future. The assessment of the passivation quality, possibly in combination with an $a\text{-Si:H}$ layer or a tunnel oxide, and the carrier-selectivity should be the main focus when screening ALD approaches for the fabrication of passivating contacts.

2.5 Conclusions & Outlook

In the field of Si photovoltaics, ALD of Al_2O_3 resulted in a break-through in the passivation of p -type Si surfaces. As a result, it is currently incorporated in solar cells with

high efficiencies over 25% and it enables challenging concepts, such as solar cells with black Si surface textures. Due to these successes, in the last few years, high-throughput reactors based on temporal and spatial ALD have successfully been developed. These reactors can meet the stringent demands of high-volume manufacturing in photovoltaic industries in terms of throughput and cost, and ALD is competitive with other techniques for the deposition of Al_2O_3 . Also other materials prepared by ALD have successfully been explored for the passivation of Si. Examples include HfO_2 , SiO_2 , Ga_2O_3 , Ta_2O_5 and TiO_2 , which altogether can passivate a variety of doped surfaces. The passivation by $\text{SiO}_2/\text{Al}_2\text{O}_3$ stacks has recently even been successfully scaled-up using batch ALD.

Apart from surface passivation, also the potential of ALD to prepare transparent conductive oxides, such as doped ZnO and In_2O_3 films, has been recognized. Key advantages of ALD as deposition method of TCOs include a very precise control in film properties, in particular when using extrinsic dopants, such as for doped ZnO. Moreover, its soft nature does not induce damage on sensitive a-Si:H passivation layers. For In_2O_3 TCOs prepared by ALD, the electron mobility is record high and reaches even the fundamental limit. The latter allows for the best possible trade-off between conductivity and transparency. Altogether, these merits make ALD very promising as deposition method for TCOs in Si solar cell manufacturing, although its potential is yet to be demonstrated on a solar cell level. Moreover, also the industrial viability of ALD to prepare TCOs in solar cell manufacturing remains to be determined, although the deposition of doped ZnO films by high-throughput spatial ALD reactors has recently been achieved.

Finally, an interesting, emerging field of research governs passivating contacts. In this field, very thin films or stacks of metal oxides (i.e., a thickness of 1-80 nm) should meet many requirements in terms of surface passivation, carrier selectivity to Si, a low contact resistivity, etc. Fortunately, ALD is ideally suited to deposit such stacks in a precisely controlled way. Moreover, the knowledge gained from ALD of TCOs and passivating films can be combined in this field. For instance, stacks of $\text{Al}_2\text{O}_3/\text{ZnO}$ are pioneered as a hole-selective contact to Si, whereas $\text{SiO}_2/\text{In}_2\text{O}_3$ stacks are promising as an electron-selective passivating contact. With high-throughput ALD reactors available, it is likely that if such passivating contact schemes have come to full development, they can be prepared in a single deposition run, even on both sides of the cells at once. This could yield a significant process simplification in Si solar cell manufacturing and would underline the potential of ALD in the field of photovoltaics.

References

1. (2015) Photovoltaics Report, Fraunhofer ISE. *Freiburg*, 17 nov.
2. Agostinelli, G., Vitanov, P., Alexieva, Z., *et al.* (2004) Surface passivation of silicon by means of negative charge dielectrics. *19th Eur. Photovolt. Sol. Energy Conf. 7-11 June 2004, Paris, Fr.*, (June), 2529–2532.
3. Glunz, S.W., Feldmann, F., Richter, A., *et al.*, (2015) The Irresistible Charm of a Simple Current Flow Pattern – 25 % With a Solar Cell Featuring a Full-Area Back Contact. *Proc. 31st EU-PVSEC Hambg.*, (September), 259–263.
4. Macco, B., Wu, Y., Vanhemel, D., and Kessels, W.M.M. (2014) High mobility In₂O₃:H transparent conductive oxides prepared by atomic layer deposition and solid phase crystallization. *Phys. status solidi - Rapid Res. Lett.*, **8** (12), 987–990.
5. Green, M.A., Emery, K., Hishikawa, Y., *et al.*, (2014) Solar cell efficiency tables (version 44). *Prog. Photovoltaics Res. Appl.*, **22** (7), 701–710.
6. Cousins, P.J., Smith, D.D., Luan, H.-C., *et al.*, (2010) Generation 3: Improved performance at lower cost. *35th IEEE Photovolt. Spec. Conf.*, 275–278.
7. Yamaguchi, T., Ichihashi, Y., Mishima, T., *et al.*, (2014) Achievement of More Than 25 % Conversion Heterojunction Solar Cell. **4** (6), 1433–1435.
8. Smith, D.D., Cousins, P., Westerberg, S., *et al.*, (2014) Toward the Practical Limits of Silicon Solar Cells. *IEEE J. Photovoltaics*, **4** (6), 1465–1469.
9. Richter, A., Hermle, M., and Glunz, S.W. (2013) Reassessment of the limiting efficiency for crystalline silicon solar cells. *IEEE J. Photovoltaics*, **3** (4), 1184–1191.
10. Benick, J., Hoex, B., van de Sanden, M.C.M., *et al.*, (2008) High efficiency n-type Si solar cells on Al₂O₃-passivated boron emitters. *Appl. Phys. Lett.*, **92** (25), 253504.
11. van de Loo, B.W.H., Knoops, H.C.M., Dingemans, G., *et al.*, (2015) “Zero-charge” SiO₂/Al₂O₃ stacks for the simultaneous passivation of n+ and p+ doped silicon surfaces by atomic layer deposition. *Sol. Energy Mater. Sol. Cells*, **143**, 450–456.
12. Taguchi, M., Yano, A., Tohoda, S., *et al.*, (2014) 24.7% Record Efficiency HIT Solar Cell on Thin Silicon Wafer. *IEEE J. Photovoltaics*, **4** (1), 96–99.
13. Nandakumar, N., Dielissen, B., Garcia-alonso, D., *et al.*, (2014) Spatial atomic layer deposition of intrinsic zinc oxide films for applications in the photovoltaics industry. *Tech. Proc. 6th WCPEC Conf.*
14. Adachi, D., Hernández, J.L., and Yamamoto, K. (2015) Impact of carrier recombination on fill factor for large area heterojunction crystalline silicon solar cell with 25.1% efficiency. *Appl. Phys. Lett.*, **107** (23), 233506.
15. World’s Highest Conversion Efficiency of 26.33% Achieved in a Crystalline Silicon Solar Cell - A World First in a Practical Cell Size -. *New Energy Ind. Technol. Dev. Organ. Kaneka Corp.*, September 14, 2016.
16. Moldovan, A., Feldmann, F., Zimmer, M., *et al.*, (2015) Tunnel oxide passivated carrier-selective contacts based on ultra-thin SiO₂ layers. *Sol. Energy Mater. Sol. Cells*, **142**, 123.
17. Battaglia, C., de Nicolás, S.M., De Wolf, S., *et al.*, (2014) Silicon heterojunction solar cell with passivated hole selective MoO_x contact. *Appl. Phys. Lett.*, **104** (11), 113902.
18. Gerling, L.G., Mahato, S., Morales-vilches, A., *et al.*, (2015) Transition metal oxides as hole-selective contacts in silicon heterojunctions solar cells. *Sol. Energy Mater. Sol. Cells*, **145**, 109–115.
19. Islam, R., and Saraswat, K.C. (2014) Metal/insulator/semiconductor carrier selective contacts for photovoltaic cells. *IEEE 40th Photovolt. Spec. Conf.*, 285–289.
20. Avasthi, S., McClain, W.E., Man, G., *et al.*, (2013) Hole-blocking titanium-oxide/silicon heterojunction and its application to photovoltaics. *Appl. Phys. Lett.*, **102** (20), 203901.

21. Macco, B., Vos, M.F.J., Thissen, N.F.W., *et al.*, (2015) Low-temperature atomic layer deposition of MoO₃ for silicon heterojunction solar cells. *Phys. status solidi - Rapid Res. Lett.*, **9** (7), 393–396.
22. Smit, S., Garcia-Alonso, D., Bordihn, S., *et al.*, (2014) Metal-oxide-based hole-selective tunneling contacts for crystalline silicon solar cells. *Sol. Energy Mater. Sol. Cells*, **120**, 376–382.
23. Garcia-Alonso, D., Smit, S., Bordihn, S., and Kessels, W.M.M. (2013) Silicon passivation and tunneling contact formation by atomic layer deposited Al₂O₃/ZnO stacks. *Semicond. Sci. Technol.*, **28** (8), 82002.
24. del Alamo, J.A., and Swanson, R.M. (1984) The physics and modeling of heavily doped emitters. *IEEE Trans. Electron Devices*, **31** (12), 1878–1888.
25. McIntosh, K.R., and Black, L.E. (2014) On effective surface recombination parameters. *J. Appl. Phys.*, **116** (1), 14503.
26. Hoex, B., Schmidt, J., Pohl, P., *et al.*, (2008) Silicon surface passivation by atomic layer deposited Al₂O₃. *J. Appl. Phys.*, **104** (4), 44903.
27. Agostinelli, G., Delabie, A., Vitanov, P., *et al.*, (2006) Very low surface recombination velocities on *p*-type silicon wafers passivated with a dielectric with fixed negative charge. *Sol. Energy Mater. Sol. Cells*, **90** (18–19), 3438–3443.
28. Cuevas, A., Allen, T., Bullock, J., *et al.*, (2015) Skin care for healthy silicon solar cells. *42nd IEEE Photovolt. Spec. Conf.*
29. Dingemans, G., and Kessels, W.M.M. (2012) Status and prospects of Al₂O₃-based surface passivation schemes for silicon solar cells. *J. Vac. Sci. Technol. A*, **30** (4), 40802.
30. Dauwe, S., Mittelstadt, L., Metz, A., *et al.*, (2002) Experimental evidence of parasitic shunting in silicon nitride rear surface passivated solar cells. *Prog. Photovoltaics Res. Appl.*, **10** (4), 271–278.
31. Dirnstorfer, I., Simon, D.K., Jordan, P.M., and Mikolajick, T. (2014) Near surface inversion layer recombination in Al₂O₃ passivated *n*-type silicon. *J. Appl. Phys.*, **116** (4), 44112.
32. Girisch, R.B.M., Mertens, R., and Keersmaecker, R.F. (1988) Determination of Si-SiO₂ interface recombination parameters using a gate-controlled point-junction diode under illumination. *Electron Devices, IEEE ...*, **35**, (2), 203–222.
33. Altermatt, P.P., Schenk, A., Geelhaar, F., and Heiser, G. (2003) Reassessment of the intrinsic carrier density in crystalline silicon in view of band-gap narrowing. *J. Appl. Phys.*, **93** (3), 1598.
34. Yan, D., and Cuevas, A. (2013) Empirical determination of the energy band gap narrowing in highly doped *n*+ silicon. *J. Appl. Phys.*, **114** (4), 44508.
35. Yan, D., and Cuevas, A. (2014) Empirical determination of the energy band gap narrowing in *p*+ silicon heavily doped with boron. *J. Appl. Phys.*, **116** (19), 194505.
36. Cousins, P.J., and Cotter, J.E. (2006) Minimizing lifetime degradation associated with thermal oxidation of upright randomly textured silicon surfaces. *Sol. Energy Mater. Sol. Cells*, **90** (2), 228–240.
37. Thomson, A.F., and McIntosh, K.R. (2009) Degradation of oxide-passivated boron-diffused silicon. *Appl. Phys. Lett.*, **95** (5), 52101.
38. Grove, A.S., Leistiko, O., and Sah, C.T. (1964) Redistribution of Acceptor and Donor Impurities during Thermal Oxidation of Silicon. *J. Appl. Phys.*, **35** (9), 2695.
39. Jaeger, K., and Hezel, R. (1985) A novel thin silicon solar cell with Al₂O₃ as surface passivation. 18th *IEEE Photov. Spec. Conf.*, 1752–1753.
40. Hezel, R., and Jaeger, K. (1989) Low-Temperature Surface Passivation of Silicon for Solar Cells. *J. Electrochem. Soc.*, **136** (2), 518–523.
41. Hoex, B., Heil, S.B.S., Langereis, E., *et al.*, (2006) Ultralow surface recombination of *c*-Si substrates passivated by plasma-assisted atomic layer deposited Al₂O₃. *Appl. Phys. Lett.*,

- 89 (4), 42112.
42. Higashi, G.S., and Fleming, C.G. (1989) Sequential surface chemical reaction limited growth of high quality Al₂O₃ dielectrics. *Appl. Phys. Lett.*, **55** (19), 1963.
 43. Hoex, B., Schmidt, J., Bock, R., *et al.*, (2007) Excellent passivation of highly doped p-type Si surfaces by the negative-charge-dielectric Al₂O₃. *Appl. Phys. Lett.*, **91** (11), 112107.
 44. Schmidt, J., Merkle, A., Brendel, R., *et al.*, (2008) Surface passivation of high-efficiency silicon solar cells by atomic-layer-deposited Al₂O₃. *Prog. Photovoltaics Res. Appl.*, **16** (6), 461–466.
 45. Knoops, H.C.M., Potts, S.E., Bol, A.A., and Kessels, W.M.M. (2015) Atomic Layer Deposition, in *Handbook of Crystal Growth*, Elsevier, pp. 1101–1134.
 46. Dingemans, G., Terlinden, N.M., Pierreux, D., *et al.*, (2011) Influence of the Oxidant on the Chemical and Field-Effect Passivation of Si by ALD Al₂O₃. *Electrochem. Solid-State Lett.*, **14** (1), H1.
 47. Profijt, H.B., Kudlacek, P., van de Sanden, M.C.M., and Kessels, W.M.M. (2011) Ion and Photon Surface Interaction during Remote Plasma ALD of Metal Oxides. *J. Electrochem. Soc.*, **158** (4), G88.
 48. Dingemans, G., Seguin, R., Engelhart, P., *et al.*, (2010) Silicon surface passivation by ultrathin Al₂O₃ films synthesized by thermal and plasma atomic layer deposition. *Phys. status solidi - Rapid Res. Lett.*, **4** (1–2), 10–12.
 49. Hoex, B., Bosman, M., Nandakumar, N., and Kessels, W.M.M. (2013) Silicon surface passivation by aluminium oxide studied with electron energy loss spectroscopy. *Phys. status solidi - Rapid Res. Lett.*, **7** (11), 937–941.
 50. Dingemans, G., Beyer, W., van de Sanden, M.C.M., and Kessels, W.M.M. (2010) Hydrogen induced passivation of Si interfaces by Al₂O₃ films and SiO₂/Al₂O₃ stacks. *Appl. Phys. Lett.*, **97** (15), 152106.
 51. Richter, A., Benick, J., Hermle, M., and Glunz, S.W. (2014) Reaction kinetics during the thermal activation of the silicon surface passivation with atomic layer deposited Al₂O₃. *Appl. Phys. Lett.*, **104** (6), 61606.
 52. Dingemans, G., Einsele, F., Beyer, W., *et al.*, (2012) Influence of annealing and Al₂O₃ properties on the hydrogen-induced passivation of the Si/SiO₂ interface. *J. Appl. Phys.*, **111** (9), 93713.
 53. Bordihn, S., Mertens, V., Müller, J.W., and Kessels, W.M.M. (2014) Deposition temperature dependence of material and Si surface passivation properties of O₃-based atomic layer deposited Al₂O₃-based films and stacks. *J. Vac. Sci. Technol. A Vacuum, Surfaces, Film.*, **32** (1), 01A128.
 54. Simon, D.K., Jordan, P.M., Dirnstorfer, I., *et al.*, (2014) Symmetrical Al₂O₃-based passivation layers for p- and n-type silicon. *Sol. Energy Mater. Sol. Cells*, **131**, 72–76.
 55. Dingemans, G., van Helvoirt, C.A.A., Pierreux, D., *et al.*, (2012) Plasma-Assisted ALD for the Conformal Deposition of SiO₂: Process, Material and Electronic Properties. *J. Electrochem. Soc.*, **159** (3), H277–H285.
 56. Dingemans, G., van de Sanden, M.C.M., and Kessels, W.M.M. (2011) Excellent Si surface passivation by low temperature SiO₂ using an ultrathin Al₂O₃ capping film. *Phys. status solidi - Rapid Res. Lett.*, **5** (1), 22–24.
 57. Dingemans, G., Terlinden, N.M., Verheijen, M.A., *et al.*, (2011) Controlling the fixed charge and passivation properties of Si(100)/Al₂O₃ interfaces using ultrathin SiO₂ interlayers synthesized by atomic layer deposition. *J. Appl. Phys.*, **110** (9), 93715.
 58. Nemeth, B., Young, D.L., Page, M.R., *et al.*, (2016) Polycrystalline silicon passivated tunneling contacts for high efficiency silicon solar cells. *J. Mater. Res.*, **31** (6), 671–681.
 59. A. Richter, S. Henneck, J. Benick, M. Hörteis, M. Hermle, S.W.G. (2010) Firing Stable Al₂O₃/SiN_x Layer Stack Passivation for the Front Side Boron Emitter of n-Type Silicon

- Solar Cells. *Proc. 25th EU-PVSEC, Val. Spain*, 1453–1459.
60. Hennen, L., Granneman, E.H.A., and Kessels, W.M.M. (2012) Analysis of blister formation in spatial ALD Al₂O₃ for silicon surface passivation. *38th IEEE Photovolt. Spec. Conf.*, (August), 1049–1054.
 61. Vermang, B., Goverde, H., Uruena, A., *et al.*, (2012) Blistering in ALD Al₂O₃ passivation layers as rear contacting for local Al BSF Si solar cells. *Sol. Energy Mater. Sol. Cells*, **101**, 204–209.
 62. Terlinden, N.M., Dingemans, G., van de Sanden, M.C.M., and Kessels, W.M.M. (2010) Role of field-effect on c-Si surface passivation by ultrathin (2–20 nm) atomic layer deposited Al₂O₃. *Appl. Phys. Lett.*, **96** (11), 112101.
 63. Schuldis, D., Richter, A., Benick, J., *et al.*, (2014) Properties of the c-Si/ Al₂O₃ interface of ultrathin atomic layer deposited Al₂O₃ layers capped by SiN_x for c-Si surface passivation. *Appl. Phys. Lett.*, **105** (23), 231601.
 64. Altermatt, P.P., Schumacher, J.O., Cuevas, A., *et al.*, (2002) Numerical modeling of highly doped Si:P emitters based on Fermi-Dirac statistics and self-consistent material parameters. *J. Appl. Phys.*, **92**, 3187–3197.
 65. Baker-Finch, S.C., and McIntosh, K.R. (2011) The Contribution of Planes, Vertices, and Edges to Recombination at Pyramidally Textured Surfaces. *IEEE J. Photovoltaics*, **1** (1), 59–65.
 66. Hoex, B., Schmidt, J., Bock, R., *et al.*, (2007) Excellent passivation of highly doped p-type Si surfaces by the negative-charge-dielectric Al₂O₃. *Appl. Phys. Lett.*, **91** (11), 112107.
 67. Mok, K.R.C., van de Loo, B.W.H., Vlooswijk, A.H.G., *et al.*, (2015) Boron-Doped Silicon Surfaces From B₂H₆ Passivated by ALD Al₂O₃ for Solar Cells. *IEEE J. Photovoltaics*, **5** (5), 1310–1318.
 68. Liao, B., Stangl, R., Ma, F., *et al.*, (2013) Excellent c-Si surface passivation by thermal atomic layer deposited aluminum oxide after industrial firing activation. *J. Phys. D. Appl. Phys.*, **46** (38), 385102.
 69. Black, L.E., Allen, T., McIntosh, K.R., and Cuevas, A. (2014) Effect of boron concentration on recombination at the p-Si– Al₂O₃ interface. *J. Appl. Phys.*, **115** (9), 93707.
 70. Liao, B., Stangl, R., Ma, F., *et al.*, (2013) Deposition temperature independent excellent passivation of highly boron doped silicon emitters by thermal atomic layer deposited Al₂O₃. *J. Appl. Phys.*, **114** (9), 94505.
 71. Liang, W., Weber, K.J., Suh, D., *et al.*, (2013) Surface Passivation of Boron-Diffused p-Type Silicon Surfaces With (100) and (111) Orientations by ALD Al₂O₃. *IEEE J. Photovoltaics*, **3** (2), 678–683.
 72. Phang, S.P., Liang, W., Wolpensinger, B., *et al.*, (2013) Tradeoffs between impurity gettering, bulk degradation, and surface passivation of boron-rich layers on silicon solar cells. *IEEE J. Photovoltaics*, **3** (1), 261–266.
 73. Hoex, B., van de Sanden, M.C.M., Schmidt, J., *et al.*, (2012) Surface passivation of phosphorus-diffused n⁺-type emitters by plasma-assisted atomic-layer deposited Al₂O₃. *Phys. status solidi - Rapid Res. Lett.*, **6** (1), 4–6.
 74. Richter, A., Benick, J., Kimmerle, A., *et al.*, (2014) Passivation of phosphorus diffused silicon surfaces with Al₂O₃: Influence of surface doping concentration and thermal activation treatments. *J. Appl. Phys.*, **116** (24), 243501.
 75. Bordihn, S., Dingemans, G., Mertens, V., and Kessels, W.M.M. (2013) Passivation of n⁺-Type Si Surfaces by Low Temperature Processed SiO₂/Al₂O₃ Stacks. *IEEE J. Photovoltaics*, **3** (3), 925–929.
 76. Bordihn, S., Engelhart, P., Mertens, V., *et al.*, (2011) High surface passivation quality and thermal stability of ALD Al₂O₃ on wet chemical grown ultra-thin SiO₂ on silicon. *Energy Procedia*, **8** (3494), 654–659.

77. Granneman, E.H.A., Kuznetsov, V.I., and Vermont, P. (2014) Spatial ALD, Deposition of Al₂O₃ Films at Throughputs Exceeding 3000 Wafers per Hour. *ECS Trans.*, **61** (3), 3–16.
78. Dingemans, G., and Kessels, W.M.M. (2010) Recent Progress in The Development and Understanding of Silicon Surface Passivation by Aluminum Oxide for Photovoltaics. *25th Eur. Photovolt. Sol. Energy Conf. Exhib. Val. Spain*, (6–10 september), 1083–1090.
79. Nandakumar, N., Lin, F., Dielissen, B., *et al.*, (2013) Silicon Surface Passivation By Al₂O₃ Films Grown By Spatial Atomic Layer Deposition Using Low-Cost Precursors. *28th Eur. Photovolt. Sol. Energy Conf. Exhib.*, 1105–1107.
80. Granneman, E., Fischer, P., Pierreux, D., *et al.*, (2007) Batch ALD: Characteristics, comparison with single wafer ALD, and examples. *Surf. Coatings Technol.*, **201** (22–23 SPEC. ISS.), 8899–8907.
81. van Delft, J.A., Garcia-Alonso, D., and Kessels, W.M.M. (2012) Atomic layer deposition for photovoltaics: applications and prospects for solar cell manufacturing. *Semicond. Sci. Technol.*, **27** (7), 74002.
82. S. Miyajima, J. Irikawa, A. Yamada, M.K. (2008) Hydrogenated Aluminium Oxide Films Deposited by Plasma Enhanced Chemical Vapor Deposition for Passivation of *p*-Type Crystalline Silicon. *Proc. 23rd EU-PVSEC, Val. Spain*, (September), 1029–1032.
83. Black, L.E., Allen, T., Cuevas, A., *et al.*, (2014) Thermal stability of silicon surface passivation by APCVD Al₂O₃. *Sol. Energy Mater. Sol. Cells*, **120**, 339–345.
84. Li, T.-T., and Cuevas, A. (2009) Effective surface passivation of crystalline silicon by rf sputtered aluminum oxide. *Phys. status solidi - Rapid Res. Lett.*, **3** (5), 160–162.
85. Chunduri, S.K., and Schmela, M. (2016) PERC Solar Cell Technology 2016 Background, Status and Outlook. *Taiyang news*.
86. Schmidt, J., Werner, F., Veith, B., *et al.*, (2010) Industrially relevant Al₂O₃ deposition techniques for the surface passivation of Si solar cells, *proc. 24th EU-PVSEC*, Valencia, Spain.
87. Zhang, X., and Cuevas, A. (2013) Plasma hydrogenated, reactively sputtered aluminium oxide for silicon surface passivation. *Phys. status solidi - Rapid Res. Lett.*, **7** (9), 619–622.
88. Duttagupta, S., Lin, F., Shetty, K.D., *et al.*, (2013) Excellent boron emitter passivation for high-efficiency Si wafer solar cells using AlO_x/SiN_x dielectric stacks deposited in an industrial inline plasma reactor. *Prog. Photovoltaics Res. Appl.*, **21** (4), 760–764.
89. Saynova, D.S., Romijn, I.G., Cesar, I., *et al.*, (2013) Dielectric Passivation Schemes for High Efficiency *n*-Type c-Si Solar Cells. *28th EU-PVSEC Proc.*, 1188–1193.
90. Dingemans, G., and Kessels, W.M.M. (2011) Aluminum Oxide and Other ALD Materials for Si Surface Passivation. *ECS Trans.*, **41** (2), 293–301.
91. Duttagupta, S., Ma, F., Lin, S., and Mueller, T. (2013) Progress in Surface Passivation of Heavily Doped *n*-Type and *p*-Type Silicon by Plasma-Deposited AlO_x/SiN_x Dielectric Stacks. 1–7.
92. Terlinden, N.M., Dingemans, G., Vandalon, V., *et al.*, (2014) Influence of the SiO₂ interlayer thickness on the density and polarity of charges in Si/SiO₂/Al₂O₃ stacks as studied by optical second-harmonic generation. *J. Appl. Phys.*, **115** (3), 33708.
93. Simon, D.K., Jordan, P.M., Benner, F., *et al.*, (2014) Universal Al₂O₃ -based passivation layers for *p* - and *n* -type silicon. *Sol. Energy Mater. Sol. Cells*, **131** (72), 8–10.
94. Spinelli, P., Macco, B., Verschuuren, M. a., *et al.*, (2013) Al₂O₃/TiO₂ nano-pattern antireflection coating with ultralow surface recombination. *Appl. Phys. Lett.*, **102** (23), 233902.
95. Ingenito, A., Isabella, O., and Zeman, M. (2014) Experimental Demonstration of $4n^2$ Classical Absorption Limit in Nanotextured Ultrathin Solar Cells with Dielectric Omnidirectional Back Reflector. *ACS Photonics*, **1** (3), 270–278.
96. Wang, W.-C., Lin, C.-W., Chen, H.-J., *et al.*, (2013) Surface passivation of efficient

- nanotextured black silicon solar cells using thermal atomic layer deposition. *ACS Appl. Mater. Interfaces*, **5** (19), 9752–9.
97. Savin, H., Repo, P., von Gastrow, G., *et al.*, (2015) Black silicon solar cells with interdigitated back-contacts achieve 22.1% efficiency. *Nat. Nanotechnol.*, **10** (7), 624–628.
 98. von Gastrow, G., Alcubilla, R., Ortega, P., *et al.*, (2015) Analysis of the Atomic Layer Deposited Al₂O₃ field-effect passivation in black silicon. *Sol. Energy Mater. Sol. Cells*, **142**, 29–33.
 99. Allen, T., Bullock, J., Cuevas, A., *et al.*, (2014) Reactive Ion Etched Black Silicon Texturing : A Comparative Study. *proc. 40th IEEE Photov. Spec. Confer.*, 562–566.
 100. Otto, M., Kroll, M., Käsebier, T., *et al.*, (2012) Extremely low surface recombination velocities in black silicon passivated by atomic layer deposition. *Appl. Phys. Lett.*, **100** (19), 191603.
 101. Repo, P., Haarahiltunen, A., Sainiemi, L., *et al.*, (2013) Effective Passivation of Black Silicon Surfaces by Atomic Layer Deposition. *IEEE J. Photovoltaics*, **3** (1), 90–94.
 102. Repo, P., Benick, J., Gastrow, G. Von, *et al.*, (2013) Passivation of black silicon boron emitters with atomic layer deposited aluminum oxide. *Phys. Status Solidi - Rapid Res. Lett.*, **7** (11), 950–954.
 103. Liu, Y., Das, A., Lin, Z., *et al.*, (2014) Hierarchical robust textured structures for large scale self-cleaning black silicon solar cells. *Nano Energy*, **3**, 127–133.
 104. Allen, T.G., and Cuevas, A. (2014) Electronic passivation of silicon surfaces by thin films of atomic layer deposited gallium oxide. *Appl. Phys. Lett.*, **105** (2014), 31601.
 105. Wan, Y., Bullock, J., and Cuevas, A. (2015) Tantalum oxide/silicon nitride: A negatively charged surface passivation stack for silicon solar cells. *Appl. Phys. Lett.*, **106** (20), 201601.
 106. Liao, B., Hoex, B., Aberle, A.G., *et al.*, (2014) Excellent c-Si surface passivation by low-temperature atomic layer deposited titanium oxide. *Appl. Phys. Lett.*, **104** (25), 253903.
 107. Cui, J., Allen, T., Wan, Y., *et al.*, (2016) Titanium Oxide (TiO₂): A Re-emerging Optical and Passivating Material for Silicon Solar Cells. *Sol. Energy Mater. Sol. Cells*, **158**, 115–121
 108. Yang, X., Zheng, P., Bi, Q., and Weber, K. (2016) Silicon heterojunction solar cells with electron selective TiO_x contact. *Sol. Energy Mater. Sol. Cells*, **150**, 32–38.
 109. Benner, F., Jordan, P.M., Richter, C., *et al.*, (2014) Atomic layer deposited high-κ nanolaminates for silicon surface passivation. *J. Vac. Sci. Technol. B Microelectron. Nanom. Struct.*, **32** (3), 03D110.
 110. Simon, D.K., Jordan, P.M., Knaut, M., *et al.*, (2015) ALD Al₂O₃ based nanolaminates for solar cell applications. *42nd IEEE Photovolt. Spec. Conf.*
 111. Suh, D. (2015) Stacked and nanolaminated Al₂O₃/TiO₂ for surface passivation and encapsulation of silicon. *Phys. status solidi - Rapid Res. Lett.*, **9** (6), 344–347.
 112. Repo, P., Talvitie, H., Li, S., *et al.*, (2011) Silicon surface passivation by Al₂O₃: Effect of ALD reactants. *Energy Procedia*, **8** (April), 681–687.
 113. Wu, Y., Hermkens, P.M., van de Loo, B.W.H., *et al.*, (2013) Electrical transport and Al doping efficiency in nanoscale ZnO films prepared by atomic layer deposition. *J. Appl. Phys.*, **114** (2), 24308.
 114. Macco, B., Deligiannis, D., Smit, S., *et al.*, (2014) Influence of transparent conductive oxides on passivation of a-Si:H/c-Si heterojunctions as studied by atomic layer deposited Al-doped ZnO. *Semicond. Sci. Technol.*, **29** (12), 122001.
 115. De Wolf, S., Descoedres, A., Holman, Z.C., and Ballif, C. (2012) High-efficiency Silicon Heterojunction Solar Cells: A Review. *green*, **2** (1), 7–24.
 116. Pisarkiewicz, T., Zakrzewska, K., and Leja, E. (1989) Scattering of charge carriers in transparent and conducting thin oxide films with a non-parabolic conduction band. *Thin Solid Films*, **174**, 217–223.
 117. Preissler, N., Bierwagen, O., Ramu, A.T., and Speck, J.S. (2013) Electrical transport,

- electrothermal transport, and effective electron mass in single-crystalline In_2O_3 films. *Phys. Rev. B*, **88** (8), 85305.
118. Ellmer, K. (2012) Past achievements and future challenges in the development of optically transparent electrodes. *Nat. Photonics*, **6** (12), 809-817.
 119. McIntosh, K.R., and Baker-Finch, S.C. (2012) OPAL 2: Rapid optical simulation of silicon solar cells. *38th IEEE Photovolt. Spec. Conf.*, 265–271.
 120. Macco, B., Knoops, H.C.M., and Kessels, W.M.M. (2015) Electron Scattering and Doping Mechanisms in Solid-Phase-Crystallized $\text{In}_2\text{O}_3\text{:H}$ Prepared by Atomic Layer Deposition. *ACS Appl. Mater. Interfaces*, **7** (30), 16723–16729.
 121. Masetti, G., Severi, M., and Solmi, S. (1983) Modeling of carrier mobility against carrier concentration in arsenic-, phosphorus-, and boron-doped silicon. *IEEE Trans. Electron Devices*, **30** (7), 764–769.
 122. Ellmer, K., and Mientus, R. (2008) Carrier transport in polycrystalline transparent conductive oxides: A comparative study of zinc oxide and indium oxide. *Thin Solid Films*, **516** (14), 4620–4627.
 123. Sharma, K., Williams, B.L., Mittal, A., *et al.*, (2014) Expanding Thermal Plasma Chemical Vapour Deposition of ZnO:Al Layers for CIGS Solar Cells. *Int. J. Photoenergy*, **2014**, 1–9.
 124. Yoshida, Y., Wood, D.M., Gessert, T. A., and Coutts, T.J. (2004) High-mobility, sputtered films of indium oxide doped with molybdenum. *Appl. Phys. Lett.*, **84** (12), 2097–2099.
 125. Morales-Masis, M., Martin De Nicolas, S., Holovsky, J., *et al.*, (2015) Low-Temperature High-Mobility Amorphous IZO for Silicon Heterojunction Solar Cells. *IEEE J. Photovoltaics*, **5** (5), 1340–1347.
 126. Yu, J., Bian, J., Duan, W., *et al.*, (2016) Tungsten doped indium oxide film: Ready for bifacial copper metallization of silicon heterojunction solar cell. *Sol. Energy Mater. Sol. Cells*, **144**, 359–363.
 127. Newhouse, P.F., Park, C.H., Keszler, D. A., *et al.*, (2005) High electron mobility W-doped In_2O_3 thin films by pulsed laser deposition. *Appl. Phys. Lett.*, **87** (11), 112108.
 128. Macco, B., Knoops, H.C.M., Vos, M.F.J., *et al.*, (2015) $\text{In}_2\text{O}_3\text{:H}$ Transparent Conductive Oxides Prepared by Atomic Layer Deposition for Application in Passivated Contacts. *EU PVSEC 2015 (oral Present.)*.
 129. Knoops, H.C.M., van de Loo, B.W.H., Smit, S., *et al.*, (2015) Optical modeling of plasma-deposited ZnO films: Electron scattering at different length scales. *J. Vac. Sci. Technol. A Vacuum, Surfaces, Film.*, **33** (2), 21509.
 130. Koida, T., Fujiwara, H., and Kondo, M. (2007) Hydrogen-doped In_2O_3 as High-mobility Transparent Conductive Oxide. *Jpn. J. Appl. Phys.*, **46** (No. 28), L685–L687.
 131. Barraud, L., Holman, Z.C., Badel, N., *et al.*, (2013) Hydrogen-doped indium oxide/indium tin oxide bilayers for high-efficiency silicon heterojunction solar cells. *Sol. Energy Mater. Sol. Cells*, **115**, 151–156.
 132. Tohsophon, T., Dabirian, A., De Wolf, S., *et al.*, (2015) Environmental stability of high-mobility indium-oxide based transparent electrodes. *APL Mater.*, **3** (11), 116105.
 133. Demaurex, B., Wolf, S. De, Descoedres, A., *et al.*, (2012) Damage at hydrogenated amorphous/crystalline silicon interfaces by indium tin oxide overlayer sputtering. *Appl. Phys. Lett.*, **101** (17), 171604.
 134. Ritzau, K.-U., Bivour, M., Schröer, S., *et al.*, (2014) TCO work function related transport losses at the a-Si:H/TCO-contact in SHJ solar cells. *Sol. Energy Mater. Sol. Cells*, **131**, 9-13
 135. Rößler, R., Leendertz, C., Korte, L., *et al.*, (2013) Impact of the transparent conductive oxide work function on injection-dependent a-Si:H/c-Si band bending and solar cell parameters. *J. Appl. Phys.*, **113** (14), 144513.
 136. Bivour, M., Schröer, S., and Hermle, M. (2013) Numerical Analysis of Electrical TCO / a-

- Si:H(p) Contact Properties for Silicon Heterojunction Solar Cells. *Energy Procedia*, **38**, 658–669.
137. Tomasi, A., Sahli, F., Fanni, L., *et al.*, (2016) Transparent Electrodes in Silicon Heterojunction Solar Cells : Influence on Carrier Recombination. *IEEE J. Photov.*, **6**, 17
 138. Klein, A., Körber, C., Wachau, A., *et al.*, (2010) Transparent Conducting Oxides for Photovoltaics: Manipulation of Fermi Level, Work Function and Energy Band Alignment. *Materials*, **3** (11), 4892–4914.
 139. P. Carroy, D. Muñoz, F. Ozanne, A. Valla, P. Mur, G.R. (2015) Analysis of Different Front and Back TCO on Heterojunction Solar Cells. *30th EU PVSEC*, 359–364.
 140. Tynell, T., and Karppinen, M. (2014) Atomic layer deposition of ZnO: a review. *Semicond. Sci. Technol.*, **29**, 43001.
 141. Elam, J.W., and George, S.M. (2003) Growth of ZnO/Al₂O₃ Alloy Films Using Atomic Layer Deposition Techniques. *Chem. Mater.*, **15** (19), 1020–1028.
 142. Lee, D.-J., Kim, H.-M., Kwon, J.-Y., *et al.*, (2011) Structural and Electrical Properties of Atomic Layer Deposited Al-Doped ZnO Films. *Adv. Funct. Mater.*, **21** (3), 448–455.
 143. Park, H.K., and Heo, J. (2014) Improved efficiency of aluminum doping in ZnO thin films grown by atomic layer deposition. *Appl. Surf. Sci.*, **309**, 133–137.
 144. Yanguas-Gil, A., Peterson, K.E., and Elam, J.W. (2011) Controlled Dopant Distribution and Higher Doping Efficiencies by Surface-Functionalized Atomic Layer Deposition. *Chem. Mater.*, **23** (19), 4295–4297.
 145. Wu, Y., Potts, S.E., Hermkens, P.M., *et al.*, (2013) Enhanced Doping Efficiency of Al-Doped ZnO by Atomic Layer Deposition Using Dimethylaluminum Isopropoxide as an Alternative Aluminum Precursor. *Chem. Mater.*, **25** (22), 4619–4622.
 146. Garcia-Alonso, D., Potts, S.E., van Helvoirt, C. A. A., *et al.*, (2015) Atomic layer deposition of B-doped ZnO using triisopropyl borate as the boron precursor and comparison with Al-doped ZnO. *J. Mater. Chem. C*, **3** (13), 3095–3107.
 147. Sang, B., Yamada, A., and Konagai, M. (1997) Growth of boron-doped ZnO thin films by atomic layer deposition. *Sol. Energy Mater. Sol. Cells*, **49** (1–4), 19–26.
 148. Lee, D.-J., Kim, K.-J., Kim, S.-H., *et al.*, (2013) Atomic layer deposition of Ti-doped ZnO films with enhanced electron mobility. *J. Mater. Chem. C*, **1** (31), 4761.
 149. Ye, Z.-Y., Lu, H.-L., Geng, Y., *et al.*, (2013) Structural, electrical, and optical properties of Ti-doped ZnO films fabricated by atomic layer deposition. *Nanoscale Res. Lett.*, **8** (1), 108.
 150. Ott, A. W., and Chang, R.P.H. (1999) Atomic layer-controlled growth of transparent conducting ZnO on plastic substrates. *Mater. Chem. Phys.*, **58**, 132–138.
 151. Geng, Y., Xie, Z.-Y., Yang, W., *et al.*, (2013) Structural, optical, and electrical properties of Hf-doped ZnO films deposited by atomic layer deposition. *Surf. Coatings Technol.*, **232**, 41–45.
 152. Thomas, M. a., Armstrong, J.C., and Cui, J. (2013) New approach toward transparent and conductive ZnO by atomic layer deposition: Hydrogen plasma doping. *J. Vac. Sci. Technol. A Vacuum, Surfaces, Film.*, **31**, 01A130.
 153. Na, J.-S., Peng, Q., Scarel, G., and Parsons, G.N. (2009) Role of Gas Doping Sequence in Surface Reactions and Dopant Incorporation during Atomic Layer Deposition of Al-Doped ZnO. *Chem. Mater.*, **21** (23), 5585–5593.
 154. Asikainen, T. (1995) Growth of Indium-Tin-Oxide Thin Films by Atomic Layer Epitaxy. *J. Electrochem. Soc.*, **142** (10), 3538.
 155. Elam, J.W., Martinson, A.B.F., Pellin, M.J., and Hupp, J.T. (2006) Atomic Layer Deposition of In₂O₃ Using Cyclopentadienyl Indium: A New Synthetic Route to Transparent Conducting Oxide Films. *Chem. Mater.*, **18** (23), 3571–3578.
 156. Libera, J.A., Hryn, J.N., and Elam, J.W. (2011) Indium Oxide Atomic Layer Deposition

- Facilitated by the Synergy between Oxygen and Water. *Chem. Mater.*, **23** (8), 2150–2158.
157. Nilsen, O., Balasundaraprabhu, R., Monakhov, E. V., *et al.*, (2009) Thin films of In_2O_3 by atomic layer deposition using $\text{In}(\text{acac})_3$. *Thin Solid Films*, **517** (23), 6320–6322.
158. Gebhard, M., Hellwig, M., Parala, H., *et al.*, (2014) Indium-tris-guanidinate: a promising class of precursors for water assisted atomic layer deposition of In_2O_3 thin films. *Dalton Trans.*, **43**, 937–40.
159. Lee, D.-J., Kwon, J.-Y., Lee, J. Il, and Kim, K.-B. (2011) Self-Limiting Film Growth of Transparent Conducting In_2O_3 by Atomic Layer Deposition using Trimethylindium and Water Vapor. *J. Phys. Chem. C*, **115** (31), 15384–15389.
160. Kim, D., Nam, T., Park, J., *et al.*, (2015) Growth characteristics and properties of indium oxide and indium-doped zinc oxide by atomic layer deposition. *Thin Solid Films*, **587**, 83–87.
161. Ramachandran, R.K., Dendooven, J., Poelman, H., and Detavernier, C. (2015) Low Temperature Atomic Layer Deposition of Crystalline In_2O_3 Films. *J. Phys. Chem. C*, **119** (21), 11786–11791.
162. Elam, J.W., Baker, D.A., Martinson, A.B.F., *et al.*, (2008) Atomic Layer Deposition of Indium Tin Oxide Thin Films Using Nonhalogenated Precursors. *J. Phys. Chem. C*, **112**, 1938–1945.
163. Demaurex, B., Seif, J.P., Smit, S., *et al.*, (2014) Atomic-Layer-Deposited Transparent Electrodes for Silicon Heterojunction Solar Cells. *IEEE J. Photovoltaics*, **4** (6), 1387–1396.
164. Hoye, R.L.Z., Muñoz-Rojas, D., Nelson, S.F., *et al.*, (2015) Research Update: Atmospheric pressure spatial atomic layer deposition of ZnO thin films: Reactors, doping, and devices. *APL Mater.*, **3** (4), 40701.
165. Munoz-Rojas, D., and MacManus-Driscoll, J. (2014) Spatial Atmospheric Atomic Layer Deposition: A new laboratory and industrial tool for low-cost photovoltaics. *Mater. Horizons*, **1** (3), 314–320.
166. Illiberi, A., Poodt, P., Bolt, P.J., and Roozeboom, F. (2014) Recent advances in atmospheric vapor-phase deposition of transparent and conductive zinc oxide. *Chem. Vap. Depos.*, **20** (7–9), 234–242.
167. Illiberi, A., Roozeboom, F., and Poodt, P. (2012) Spatial atomic layer deposition of zinc oxide thin films. *ACS Appl. Mater. Interfaces*, **4** (1), 268–272.
168. Nandakumar, N., Dielissen, B., Garcia-alonso, D., *et al.*, (2015) Resistive Intrinsic ZnO Films Deposited by Ultrafast Spatial ALD for PV Applications. *IEEE J. Photov.* **5** (5), 1462
169. Illiberi, A., Scherpenborg, R., Wu, Y., *et al.*, (2013) Spatial atmospheric atomic layer deposition of $\text{In}_x\text{Zn}_{1-x}\text{O}$. *ACS Appl. Mater. Interfaces*, **5** (24), 13124–13128.
170. Ellinger, C.R., and Nelson, S.F. (2014) Selective area spatial atomic layer deposition of ZnO, Al_2O_3 , and aluminum-doped ZnO using poly(vinyl pyrrolidone). *Chem. Mater.*, **26**, 1514–1522.
171. Illiberi, A., Scherpenborg, R., Roozeboom, F., and Poodt, P. (2014) Atmospheric Spatial Atomic Layer Deposition of In-Doped ZnO. *ECS J. Solid State Sci. Technol.*, **3** (5), P111–P114.
172. Nandakumar, N., Hoex, B., Dielissen, B., *et al.*, (2015) Conductive gallium-doped ZnO films deposited by ultrafast spatial atomic layer deposition for photovoltaic application. *Present. 25th Asia Photovolt. Sol. Energy Conf. Exhib.*
173. Illiberi, A., Cobb, B., Sharma, A., *et al.*, (2015) Spatial atmospheric atomic layer deposition of $\text{In}_x\text{Ga}_y\text{Zn}_z\text{O}$ for thin film transistors. *ACS Appl. Mater. Interfaces*, **7** (6), 3671–3675.
174. Wurfel, U., Cuevas, A., and Wurfel, P. (2015) Charge Carrier Separation in Solar Cells. *IEEE J. Photovoltaics*, **5** (1), 461–469.
175. Islam, R., Shine, G., and Saraswat, K.C. (2014) Schottky barrier height reduction for holes by Fermi level depinning using metal/nickel oxide/silicon contacts. *Appl. Phys. Lett.*, **105**

- (18).
176. Bivour, M., Temmler, J., Steinkemper, H., and Hermle, M. (2015) Molybdenum and tungsten oxide: High work function wide band gap contact materials for hole selective contacts of silicon solar cells. *Sol. Energy Mater. Sol. Cells*, **142**, 34–41.
 177. Robertson, J. (2000) Band offsets of wide-band-gap oxides and implications for future electronic devices. *J. Vac. Sci. Technol. B Microelectron. Nanom. Struct.*, **18** (3), 1785.
 178. Stradins, P., Essig, S., Nemeth, W., *et al.*, (2014) Passivated Tunneling Contacts to n-Type Wafer Silicon and Their Implementation into High Performance Solar Cells, *6th World Conf. Photovolt. Energy Convers.*, (December).
 179. Ng, K.K., and Card, H.C. (1980) Asymmetry in the SiO₂ tunneling barriers to electrons and holes. *J. Appl. Phys.*, **51** (4), 2153.
 180. Young, D.L., Nemeth, W., Grover, S., *et al.*, (2014) Carrier-selective, passivated contacts for high efficiency silicon solar cells based on transparent conducting oxides. *40th IEEE Photovolt. Spec. Conf.*
 181. Khanna, A., Mueller, T., Stangl, R. A., *et al.*, (2013) A Fill Factor Loss Analysis Method for Silicon Wafer Solar Cells. *IEEE J. Photovoltaics*, **3** (4), 1170–1177.
 182. Private communication (2015)
 183. Feldmann, F., Bivour, M., Reichel, C., *et al.*, (2014) Passivated rear contacts for high-efficiency n-type Si solar cells providing high interface passivation quality and excellent transport characteristics. *Sol. Energy Mater. Sol. Cells*, **120**, 270–274.
 184. Fell, A., McIntosh, K.R., Altermatt, P.P., *et al.*, (2015) Input Parameters for the Simulation of Silicon Solar Cells in 2014. *IEEE J. Photovoltaics*, **5** (4), 1250–1263.
 185. Hameln, S., Isfh, E., Ohrberg, A., and Emmerthal, D.- (2010) Passivation of n-type Cz Silicon Substrates. *IEEE J. Photovoltaics*, **5** (5), 1207–1209.
 186. Naguib, N., Ye, H., Gogotsi, Y., *et al.*, (2004) Observation of water confined in nanometer channels of closed carbon nanotubes. *Nano Lett.*, **4** (11), 2237–2243.
 187. Bullock, J., Cuevas, A., Allen, T., and Battaglia, C. (2014) Molybdenum oxide MoO_x: A versatile hole contact for silicon solar cells. *Appl. Phys. Lett.*, **105** (23), 232109.
 188. Bullock, J., Samundsett, C., Cuevas, A., *et al.*, (2015) Proof-of-concept p-type silicon solar cells with molybdenum oxide partial rear contacts. *42nd IEEE PVSC*, **5** (6), 1591–1594.
 189. Geissbühler, J., Werner, J., Martin De Nicolas, S., *et al.*, (2015) 22.5% Efficient Silicon Heterojunction Solar Cell With Molybdenum Oxide Hole Collector. *Appl. Phys. Lett.*, **107** (8), 81601.
 190. Zielke, D., Petermann, J.H., Werner, F., *et al.*, (2011) Contact passivation in silicon solar cells using atomic-layer-deposited aluminum oxide layers. *Phys. status solidi - Rapid Res. Lett.*, **5** (8), 298–300.
 191. Werner, F., Veith, B., Zielke, D., *et al.*, (2011) Electronic and chemical properties of the c-Si/ Al₂O₃ interface. *J. Appl. Phys.*, **109** (11), 113701.
 192. Chandiran, A.K., Nazeeruddin, M.K., and Graetzel, M. (2014) The Role of Insulating Oxides in Blocking the Charge Carrier Recombination in Dye-Sensitized Solar Cells. *Adv. Funct. Mater.*, **24**, 1615–1623.
 193. Chandiran, A.K., Tetreault, N., Humphry-baker, R., *et al.*, (2012) Sub-nanometer Ga₂O₃ tunnelling layer by atomic layer deposition to achieve 1.1V open- circuit potential in dye-sensitized solar cells. *Nano Lett.* **12** (8), 1-12.
 194. Sahasrabudhe, G., Rupich, S.M., Jhaveri, J., *et al.*, (2015) Low Temperature Synthesis of a TiO₂/Si Heterojunction. *J. Am. Chem. Soc.*, **137** (47), 14842-14845.
 195. Chambers, S.A., Liang, Y., Yu, Z., *et al.*, (2001) Band offset and structure of SrTiO₃ /Si(001) heterojunctions. *J. Vac. Sci. Technol. A Vacuum, Surfaces, Film.*, **19** (1), 934–939.
 196. Först, C.J., Ashman, C.R., Schwarz, K., and Blöchl, P.E. (2004) The interface between silicon and a high-k oxide. *Nature*, **427** (6969), 53–56.

197. Longo, V., Leick, N., Roozeboom, F., and Kessels, W.M.M. (2012) Plasma-Assisted Atomic Layer Deposition of SrTiO₃: Stoichiometry and Crystallinity Studied by Spectroscopic Ellipsometry. *ECS J. Solid State Sci. Technol.*, **2** (1), N15–N22.
198. Ritala, M., Leskela, M., Niinisto, L., *et al.*, (1993) Titanium Isopropoxide as a Precursor in Atomic Layer Epitaxy of Titanium Dioxide Thin Films. *Chem. Mater.*, **5** (8), 1174–1181.
199. Potts, S.E., Keuning, W., Langereis, E., *et al.*, (2010) Low Temperature Plasma-Enhanced Atomic Layer Deposition of Metal Oxide Thin Films. *J. Electrochem. Soc.*, **157** (7), P66.
200. Xie, Q., Jiang, Y.-L., Detavernier, C., *et al.*, (2007) Atomic layer deposition of TiO₂ from tetrakis-dimethyl-amido titanium or Ti isopropoxide precursors and H₂O. *J. Appl. Phys.*, **102** (8), 83521.
201. Kim, M.K., Kim, W.H., Lee, T., and Kim, H. (2013) Growth characteristics and electrical properties of Ta₂O₅ grown by thermal and O₃-based atomic layer deposition on TiN substrates for metal-insulator-metal capacitor applications. *Thin Solid Films*, **542**, 71–75.
202. Kwon, O.S., Kim, S.K., Cho, M., *et al.*, (2005) Chemically Conformal ALD of SrTiO₃ Thin Films Using Conventional Metallorganic Precursors. *J. Electrochem. Soc.*, **152**, C229.
203. Bertuch, A., Sundaram, G., Saly, M., *et al.*, (2014) Atomic layer deposition of molybdenum oxide using bis(tert-butylimido)bis(dimethylamido) molybdenum. *J. Vac. Sci. Technol. A Vacuum, Surfaces, Film.*, **32** (1), 01A119.
204. Vos, M.F.J., Macco, B., Thissen, N.F.W., *et al.*, (2016) Atomic layer deposition of molybdenum oxide from (NtBu)₂(NMe₂)₂Mo and O₂ plasma. *J. Vac. Sci. Technol. A Vacuum, Surfaces, Film.*, **34** (1), 01A103.
205. Diskus, M., Nilsen, O., and Fjellvåg, H. (2011) Growth of thin films of molybdenum oxide by atomic layer deposition. *J. Mater. Chem.*, **21** (3), 705.
206. Liu, R., Lin, Y., Chou, L.-Y., *et al.*, (2011) Water Splitting by Tungsten Oxide Prepared by Atomic Layer Deposition and Decorated with an Oxygen-Evolving Catalyst. *Angew. Chemie Int. Ed.*, **50** (2), 499–502.
207. Malm, J., Sajavaara, T., and Karppinen, M. (2012) Atomic Layer Deposition of WO₃ Thin Films using W(CO)₆ and O₃ Precursors. *Chem. Vap. Depos.*, **18** (7–9), 245–248.
208. Song, J., Park, J., Lee, W., *et al.*, (2013) Conformal Synthesis of Tungsten Disulfide Nanosheets Using Atomic Layer Deposition. *ACS Nano*, **7**, 11333–11340.
209. Blanquart, T., Niinistö, J., Gavagnin, M., *et al.*, (2013) Atomic layer deposition and characterization of vanadium oxide thin films. *RSC Adv.*, **3** (4), 1179–1185.
210. Boukhalfa, S., Evanoff, K., and Yushin, G. (2012) Atomic layer deposition of vanadium oxide on carbon nanotubes for high-power supercapacitor electrodes. *Energy Environ. Sci.*, **5** (5), 6872.
211. Musschoot, J., Deduytsche, D., Van Meirhaeghe, R.L., and Detavernier, C. (2009) ALD of Vanadium Oxide. *ECS Trans.*, **25** (4), 29–37.
212. Lu, H.L., Scarel, G., Li, X.L., and Fanciulli, M. (2008) Thin MnO and NiO films grown using atomic layer deposition from ethylcyclopentadienyl type of precursors. *J. Cryst. Growth*, **310** (24), 5464–5468.
213. Lindahl, E., Ottosson, M., and Carlsson, J.-O. (2009) Atomic Layer Deposition of NiO by the Ni(thd)₂/H₂O Precursor Combination. *Chem. Vap. Depos.*, **15** (7–9), 186–191.
214. Chae, J., Park, H.-S., and Kang, S. (2002) Atomic Layer Deposition of Nickel by the Reduction of Preformed Nickel Oxide. *Electrochem. Solid-State Lett.*, **5** (6), C64.
215. Yang, T.S., Cho, W., Kim, M., *et al.*, (2005) Atomic layer deposition of nickel oxide films using Ni(dmamp)₂ and water. *J. Vac. Sci. Technol. A Vacuum, Surfaces, Film.*, **23** (4), 1238.
216. Battaglia, C., Yin, X., Zheng, M., *et al.*, (2014) Molybdenum oxide MoO_x: A versatile hole contact for silicon solar cells. *Nano Lett.*, **14**, 967–971.
217. Ziegler, J., Mews, M., Kaufmann, K., *et al.*, (2015) Plasma-enhanced atomic-layer-deposited MoO_x emitters for silicon heterojunction solar cells. *Appl. Phys. A*, **120**, (3) 811.

CHAPTER 3

Boron-Doped Silicon Surfaces from B_2H_6 Passivated by ALD Al_2O_3 for Solar Cells*

Abstract A p^+ -doping method for silicon solar cells is presented, whereby boron atoms from a pure boron (PureB) layer deposited by chemical vapor deposition using B_2H_6 gas precursors were thermally diffused into silicon. The applicability of this doping process for the doped surfaces of silicon solar cells was evaluated in terms of 1) the surface morphology after thermal diffusion, 2) the boron doping profiles and sheet resistances, and 3) the recombination parameter, J_{0p^+} when the doped layers were passivated by Al_2O_3 films prepared by atomic layer deposition. Adequate surface passivation could be achieved, with the contribution of surface recombination to J_{0p^+} of < 20 fA/cm² for most samples. However, when a boron-rich layer (BRL) was present at the Si surface, a much higher recombination current density was observed, proving that a BRL was detrimental to the high-quality surface passivation of boron-diffused surfaces. It was found that sufficient O_2 in the furnace during the thermal diffusion process could eliminate any potential residual BRL, while excessive O_2 concentration results in boron depletion and a higher sheet resistance. Therefore, in addition to optimizing the initial PureB layer thickness and thermal budget to control the dopant profiles, the O_2 concentration during the diffusion must also be well controlled.

* Published as: K. R. C. Mok,¹ B. W. H. van de Loo,¹ A. H. G. Vlooswijk, W. M. M. Kessels, L. K. Nanver, *IEEE J. Photovoltaics*, 5 (5), 1310–1318. (¹Both authors contributed equally.)

3.1 Introduction

The majority of industrially produced silicon solar cells have a p -type base in combination with an n^+ highly-doped region. However, due to superior electronic properties of n -type Si wafers, which include a high bulk lifetime, no light-induced degradation [1]–[3] and a higher tolerance to metallic impurities [4], there is an increasing focus on n -type cells both in research as well as in industrial production [5], [6].

There are several methods used to manufacture p^+ -regions for n -type silicon solar cells. Methods include diffusion from boron glass formed by gaseous BBr_3 [5]–[9] and BCl_3 [10] precursors, diffusion from spin-on boron source [11], inkjet-printed boron source [12], [13] and atmospheric pressure chemical-vapor-deposited boron-silicate glass (BSG) [14], as well as conventional boron ion implantation [15],[16] and plasma ion implantation [17] followed by thermal activation and diffusion. The various doping methods have their unique advantages and disadvantages. Thermal gas-phase diffusion by BBr_3 using a conventional furnace is an established method, with high throughput and low cost of ownership. In fact, industrial n -type solar cells have achieved >20% efficiency with this method, whereby a boron silicate glass (BSG) layer is first formed before the dopant is driven-in [5], [6]. Generally, this otherwise undesirable layer has to be subsequently removed and replaced by a suitable passivation layer, in order to attain surface passivation.

The spin-on dopant technique offers single-sided diffusion, but it can suffer from contamination by metallic impurities initially present in the spin-on dopant film [11]. The ink-jet printing technique on the other hand, has the added advantage of creating selective emitters. Compared to the aforementioned methods, ion implantation offers improved control, uniformity, and flexibility over the dopant profile, as well as the elimination of wet processing steps. Moreover, localized, one-sided doping can be easily achieved in a single step using a shadow mask. This comparative advantage allows for novel process flows and high-efficiency cell architecture [16]. However, it is well known that ion implantation induces defects that must be completely removed in subsequent annealing, and may additionally induce dopant deactivation, especially for boron [18], [19]. Plasma immersion ion implantation has an advantage in terms of being able to quickly implant very high doses at a lower cost. It has a very low implantation energy suited for the fabrication of ultra-shallow junctions which show optimal behavior in the short wavelength region [17].

For application in standard n -type screen-printed crystalline silicon solar cells, regardless of the dopant source, substantial diffusion is required to achieve the dopant profiles and sheet resistances necessary for a low series resistance through the p -type

region and associated contacts. More critically, a well-passivated surface is required to ensure a low surface recombination rate of charge carriers. Traditionally, thermally grown SiO₂ has been used as high-quality surface passivation for fabricating high-efficiency solar cells due to its low interface defect density. More recently, it was demonstrated that Al₂O₃ is an excellent material to passivate *p*-type crystalline silicon [20]. It offers a relatively high negative fixed charge density in the range of 10¹²–10¹³ cm⁻², as well as a low interface defect density of ≤10¹¹ eV⁻¹cm⁻² [21]. The high negative charge density effectively reduces the electron concentration at the surface and consequently reduces the recombination rate. In this way, Al₂O₃ provided an effective field-effect passivation. In contrast, thermal SiO₂ has a low positive fixed charge density in the range of 10¹⁰–10¹¹ cm⁻² [22].

The compatibility of *p*⁺ doping with high-quality Al₂O₃ surface passivation is important for achieving a low recombination parameter, J_{0p+} . However, it is known that in some cases the boron diffusion process can induce a boron-rich layer (BRL), which prevents the passivation of the surface. In this way, the J_{0p+} of the highly-doped region becomes comparable to an unpassivated doped surface [9]. In other work, it is shown that BRLs thicker than 10 nm lead to degradation of bulk lifetime [8]. The BRL is formed during the diffusion process due to very high concentration of boron at the surface of the wafer, which is effectively transformed into a silicon boride layer. The BRL is hydrophilic and insoluble in HF. Under certain process conditions for BBr₃-based diffusion, a BRL can be formed and is clearly observable from cross-sectional scanning electron microscopy (SEM) [8], [9] extending up to tens of nanometers. A BRL has also been identified as dark agglomerations seen in transmission electron microscopy (TEM) images when using inkjet-printed paste as a source for boron diffusion [13]. Due to its detrimental effects to cell efficiency, BRLs are usually avoided or if formed, removed by oxidation [7], [8], which converts the BRL into BSG that is easily etched away by diluted HF.

In this work, with solar cell application as objective, a further development is presented of a recently demonstrated *p*⁺ doping method by chemical vapor deposition (CVD) of boron layers (PureB) using B₂H₆ precursors [23], [24]. Up until now, the application of PureB deposition has primarily been for the fabrication of photodiodes. Due to the special properties of PureB layers deposited at 700 °C, *p*⁺*n* photodiode detectors have been realized that already are well established as the devices of choice for detection of low-penetration-depth beams such as vacuum-ultraviolet light (VUV) [25] and low-energy electrons [26] where the photosensitive region must lie in the top few nanometer of the silicon. These applications rely on the PureB-to-Si interface properties to achieve low dark current and on the robustness of the PureB layer for high stability [27]. However, the sheet

resistance of as-deposited PureB layers prepared at 700 °C is about 10 k Ω /sq which can be too high for some specific applications. Extra in-situ thermal drive-in has been shown to be an efficient way of lowering the sheet resistance. An additional 850 °C 1-min diffusion reduced the sheet resistance to about 1 k Ω /sq and a 950 °C 20-min diffusion brought it down to about 100 Ω /sq [28]. From studies of the quantum efficiency of VUV photodiodes [25] fabricated with PureB anode regions subjected to various drive-in procedures, it has been found that the high efficiencies are maintained despite the increase in junction depth from a few nanometer to the hundred-nanometer range, particularly if the PureB layer is preserved on the surface [27]. In cases where it was removed the efficiency dropped but still remained much higher than that of junctions produced by implantations [25]. This was attributed to the defect-free nature of the doping process and the lack of roll-off of the resulting dopant profiles. These two features have also been shown in our previous work to be potentially attractive for manufacturing p^+ -doped regions in Si solar cells [23], [24].

For solar cell applications, the PureB layer has to be thermally diffused into the silicon to lower the sheet resistance. At the same time, obtaining a low recombination in the resulting doped layer is critical. In this work, processes are investigated that give increased control of the doping and surface conditions. It will be shown that by adjusting the thickness of the initial PureB layer, which acts as dopant source, as well as the subsequent thermal diffusion conditions, the dopant profiles can be well controlled. In particular, the role of gas composition during the diffusion process was investigated. To evaluate the applicability of this doping process in solar cell manufacturing, several aspects were studied. Firstly, the surface morphology of the layers before and after the thermal diffusion step was analysed. Secondly, boron profiles and sheet resistances were evaluated. Lastly, the recombination parameters of the doped layers passivated by Al₂O₃ were investigated.

3.2 Experimental

A. Deposition of PureB Layers

The CVD of the PureB layers was performed in a commercial ASM single-wafer Epsilon 2000 epitaxial reactor. During deposition, B₂H₆ (0.2%) was used as a source gas and H₂ as the carrier gas. Before deposition, the native oxide was removed from the Si surface by 0.55% HF dip etching and Marangoni drying. PureB was deposited at 700 °C and atmospheric pressure with different deposition times. To form symmetrically doped $p^+/n/p^+$ samples for lifetime measurements, PureB was deposited on one side of a bare

wafer, and then the wafer was manually flipped ex-situ and immediately processed with the same recipe on the other side. The second exposure of the first side to 700 °C gave a very limited drive-in of boron into the Si as set by the corresponding solid solubility of boron of $2 \times 10^{19} \text{ cm}^{-3}$ [29]. This effect was negligible since the final dopant profile was entirely determined by the subsequent thermal diffusion step at 950 °C. A customized batch furnace system for the high-volume manufacturing is currently under development for this process. Preliminary results are promising but are beyond the scope of this work[30].

B. Analysis of the Surface Morphology

The thickness and surface morphology of the deposited and diffused layers was characterized using spectroscopic ellipsometry (SE), high-resolution transmission electron microscopy (HRTEM) and electron energy loss spectroscopy (EELS). The Si substrates used were phosphorus-doped Czochralski (Cz) wafers of (100) orientation and 1-5 $\Omega \cdot \text{cm}$ resistivity. The TEM samples were prepared using in-situ focused ion beam (FIB) lift out technique on a FEI Strata Dual Beam FIB/SEM. The samples were coated with platinum prior to FIB milling. The samples were imaged with a FEI Tecnai TF-20 FEG/TEM. In addition, EELS was used to determine the elemental composition of the surface layers. The EELS analyses were done in scanning transmission electron microscopy (STEM) mode using a nominal 2 nm electron beam and a Gatan Enfina DigiPEELS Spectrometer. For the line scan, the beam was stepped 4 nm apart and acquired for 1.5 s.

C. Boron Diffusion and Dopant Profiles

For application in various *n*-type crystalline silicon solar cells, specific requirements are demanded of the *p*⁺ doped regions in terms of dopant profile, sheet resistance and homogeneity. As the chemical vapor deposited PureB layer from B₂H₆ precursors acts as a dopant source, subsequent thermal diffusion was required to drive in the dopants to achieve the desired profile.

Thermal diffusion was performed with different concentrations of O₂ mixed with N₂ in a Tempress furnace TS 3603 oxidation system at 950 °C for 10 min, in order to investigate the effect of the gas composition on the properties of the boron doped region. It should be noted that this thermal diffusion was done without any capping layer, and the PureB layers acted as dopant source. For measurements of the dopant profiles and sheet

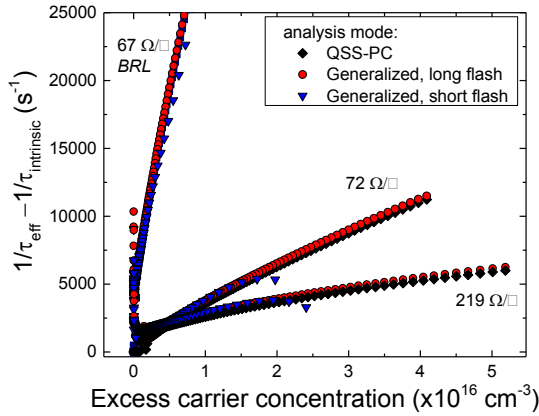


Figure 1 The inverse effective lifetime, corrected for Auger recombination, as obtained from photoconductive lifetime measurements on boron-doped samples with three different sheet resistances and passivated by Al_2O_3 . Straight lines were found for all measured samples in the excess carrier concentrations range Δn ($0.7 - 1.3$) $\times 10^{16} \text{ cm}^{-3}$, indicating that the method of Kane & Swanson to extract J_{0p+} was appropriate.

resistances, n -type monocrystalline Si (100) wafers were used, which were float zone (FZ), 4-inch diameter, double-side polished, 1–5 $\Omega\text{-cm}$ resistivity and 260–300 μm in thickness. The active boron dopant profiles were analysed by electrochemical capacitance voltage (ECV) measurements using a WEP wafer profiler CVP21 table-top unit and sheet resistances were determined from 4-point probe measurements.

D. Surface passivation by Al_2O_3

An important aspect of implementing B_2H_6 boron diffusion in silicon solar cells is the compatibility with high-quality surface passivation. After the doping process, samples were etched in 1% HF to remove any undesirable surface layer, followed by plasma-assisted atomic layer deposition (ALD) of Al_2O_3 as a passivation layer in order to evaluate the recombination parameter of the highly doped region. A 30-nm Al_2O_3 layer was deposited on both sides of the lifetime samples by plasma-assisted ALD in an Oxford instruments OpALTM reactor at 200°C, using $\text{Al}(\text{CH}_3)_3$ (TMA) as precursor and O_2 plasma as reactant. Finally, a post-deposition 400 °C anneal in N_2 was performed for 10 min to activate passivation. The recombination parameter J_{0p+} was evaluated from quasi-steady-state photoconductance decay (QSS-PC), and generalized mode measurements on a Sinton WCT100. It was extracted from the slope of the inverse effective lifetime τ_{eff} at high excess carrier concentrations Δn ($0.7 - 1.3$) $\times 10^{16} \text{ cm}^{-3}$ by the method of Kane and Swanson [31];

$$\frac{1}{\tau_{eff}} - \frac{1}{\tau_{Intrinsic}} = \frac{1}{\tau_{SRH}} + J_0 \cdot \frac{(N_d + \Delta n)\Delta n}{qn_i^2 W} \quad (1)$$

with $\tau_{Intrinsic}$ the intrinsic (bulk) lifetime, τ_{SRH} the Shockley-Read-Hall lifetime, q the elementary charge, W the wafer thickness, N_d the base doping concentration, and n_i the intrinsic carrier concentration (we used $n_i = 9.65 \times 10^9 \text{ cm}^{-3}$, corresponding to a temperature of 300 K [32]). To ensure an accurate extraction of J_{0p+} , we compared the use of QSS-PC mode with generalized mode (Fig. 1). Interestingly, even though the absolute effective lifetime values changed in the different analysis modes, they did not result in significantly different J_{0p+} values. Furthermore, the use of a short flash, typically used for transient measurements, also yielded very similar results to the QSS-PC measurements. To study the influence of surface orientation on the surface passivation quality, some planar Si (111) wafers were additionally included in the analysis.

3.3 Results

A. Surface Morphology of the PureB and BSG layers

The surface morphology of the as-deposited and diffused PureB layers were analyzed with HRTEM. Fig. 2 shows a PureB layer of approximately 3-nm-thick, which was prepared by 9-minutes of CVD. Fig. 3 shows the HRTEM images of the samples after diffusion of PureB source layer into Si (100). The diffusion took place in a furnace at 950 °C for 30 min, in either N₂ ambient (7 slm) or in 14% O₂ in N₂ (1 slm O₂, 6 slm N₂).

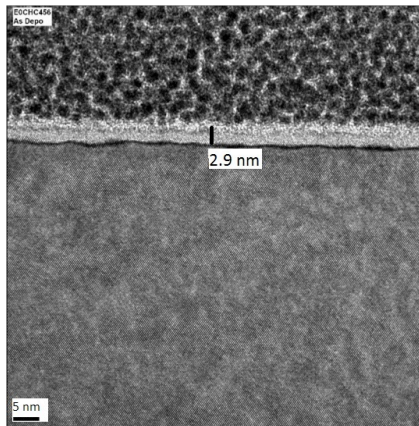


Figure 2 HRTEM image of an as-deposited PureB layer formed by a 9 min deposition on a Si (100) surface, adapted from [23].

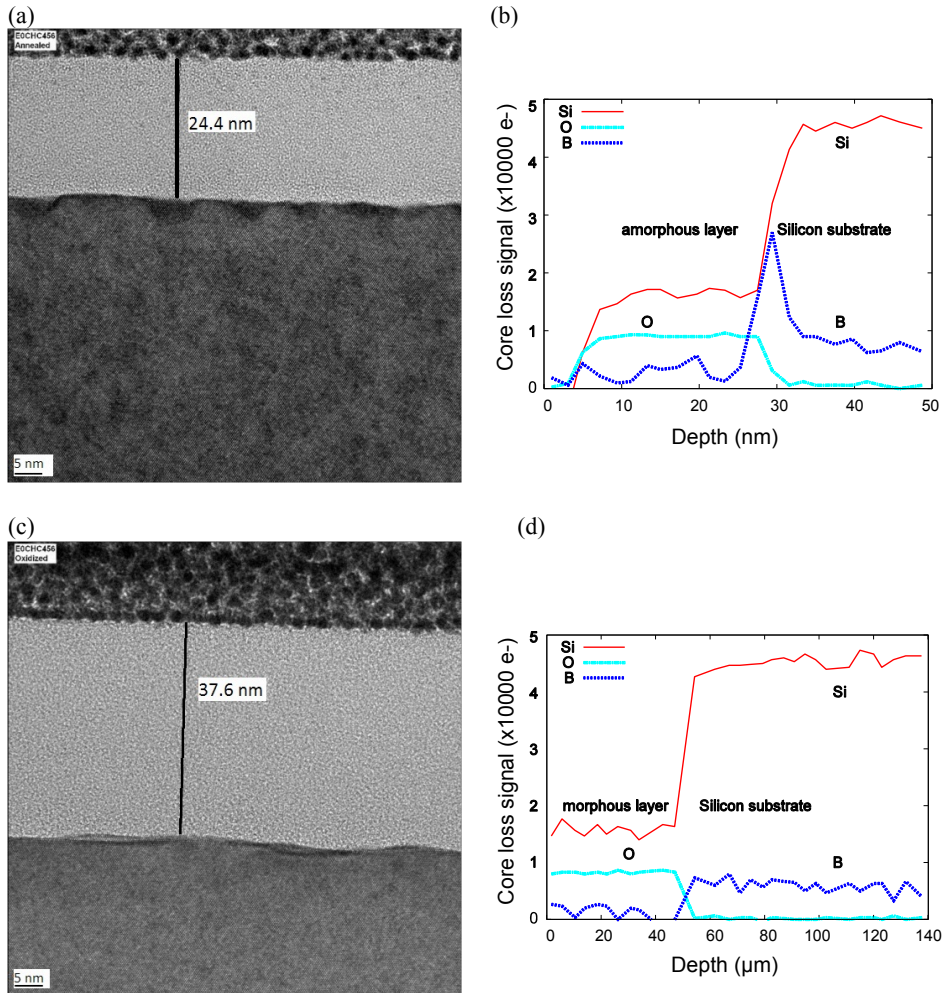


Figure 3 HRTEM images of a BSG layers formed on a Si (100) surface by a 9-min deposition of PureB followed by furnace diffusion at 950 °C for 30 min in (a) a N₂ ambient and (c) a N₂ ambient with 14% O₂ admixed, adapted from reference [23]. In (b) and (d) EELS results from a line scan of the surface layer as shown in (a) and (c) are shown, respectively. The boron peak at the interface of the amorphous layer and Si substrate in (b) indicates the presence of a BRL.

As can be seen, after diffusion, an amorphous layer was formed on the silicon. A PureB layer of 3 nm in thickness resulted in an amorphous layer with a thickness of about 24 nm when diffused in N₂ ambient (Fig. 3a), while diffusion in 14% O₂ resulted in an even thicker layer, measured to be about 40 nm (Fig. 3c). Note that on planar Si (111) surfaces,

the results are very similar [23]. For comparison, a Si (100) control sample without PureB layer was also annealed at the same conditions. In this case, no amorphous layer could be detected by spectroscopic ellipsometry during diffusion in N_2 ambient, while annealing in 14% O_2 concentration resulted in 9 nm of silicon oxide. It can be concluded that the presence of boron significantly increases the rate of oxidation, as is observed more often in literature [33]. Finally, it should be noted that the furnace is likely not completely O_2 -free, even when using a N_2 ambient. Indeed, when the diffusion was carried out *in-situ* in the Epsilon reactor in N_2 ambient instead of the furnace, no oxide layer was detected by SE. This can be explained by the fact that the carrier gases used in the Epsilon reactor pass through a purifier and have impurity levels below 10 ppb, such that the PureB deposition and *in-situ* thermal diffusions take place under practically O_2 -free conditions.

Based on Electron Energy Loss Spectroscopy (EELS) characterization (see Fig. 3b and 3d), the elemental composition of the amorphous layers is predominantly silicon, followed by oxygen, with small amounts of boron. Therefore, the layer can be identified as a BSG. The amorphous layers grown in an oxygen limited ambient showed – in contrast to the sample diffused in oxygen containing environment – a clear peak in the boron signal at the BSG – Si interface, indicating the presence of a BRL. Note that also for the EELS results, no significant difference was found between Si (100) or Si (111) surfaces. For the as-deposited layer, no EELS line scan was performed, as the as-deposited layer was thinner than the beam step-size of 4 nm. However, EELS spot analysis was able to pick up a strong boron signal in the as-deposited layer. Furthermore, SIMS measurements in earlier work showed that for long pureB deposition times, the peak concentration of boron saturated at the equivalent atom density of pure amorphous boron [34].

Next, the influence of the diffusion conditions on the formation of the BSG was investigated. As the thicknesses measured by SE were so far found to be consistent with the layer thicknesses observed in the TEM images, all subsequent layer thicknesses are from here determined by SE measurements. For the determination of the BSG thickness by SE, a pure SiO_2 layer was assumed. Fig. 4 shows the oxide layer thickness as a function of O_2 concentration used during the 10-min diffusion at 950 °C, for various initial PureB thicknesses. It can be seen that the resulting BSG thickness depended strongly on the initial PureB layer thickness. Moreover, there was an appreciable increase in oxide thickness when the O_2 concentration during diffusion was increased from 0% to 14%, although a further increase in O_2 concentration had no effect on the final BSG thickness. This can be explained as the growth is reaction-limited for oxygen concentrations >14%, with the temperature being a determining factor for the final BSG thickness [23].

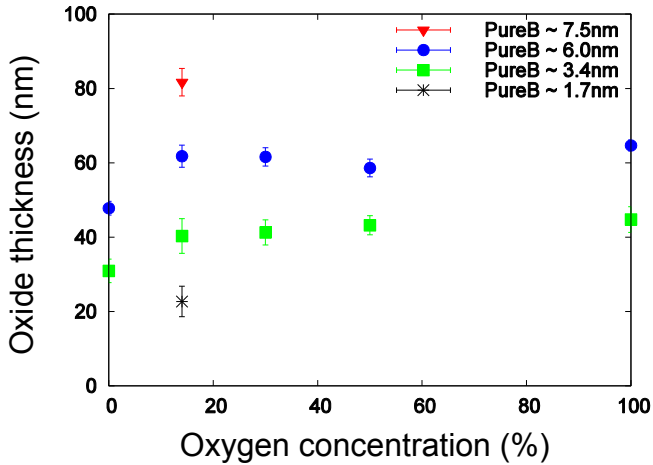


Figure 4 Boron-silicate glass thickness as determined from spectroscopic ellipsometry. The BSG was formed by thermal diffusion (950 °C, 10 min) of PureB layers of various thicknesses in N₂ ambient, with varying concentrations of admixed O₂.

To gain more knowledge on the surface conditions, the samples were subjected to chemical etchants. It is known that BRLs are hydrophilic and resistant to various acidic solutions like H₂SO₄, HF and H₃PO₄ due to the low solubility of the layers [35], [36]. As a chemical etch test, various samples received a dip in diluted HF (1%). The samples which were thermally diffused in N₂ ambient remained hydrophilic after prolonged HF-dipping, although ellipsometry measurement showed that the oxide layer was effectively etched away. This hydrophilic nature indicate the existence of a BRL, which is consistent with the TEM and EELS results in Fig. 3 (the BRL can be seen from the TEM images in Fig. 3 of diffused samples as a distinct dark agglomeration at the interface of oxide/Si). Importantly, all samples that were annealed with various concentrations of O₂, as shown in Fig. 4., became hydrophobic after a 3-4 min 1% HF etch, which indicates that the surface was free of both the BSG and the BRL after etching.

B. Dopant Diffusion and Dopant Profiles

Boron-doped Si surfaces prepared by CVD using B₂H₆ and subsequent thermal diffusion were evaluated in terms of dopant profiles and sheet resistance, for various thicknesses of the PureB layer, diffusion time and temperature, as well as the O₂ concentration in the furnace during diffusion.

Figure 5a shows the active boron profiles for various initial thicknesses of PureB layers, followed by thermal diffusion at 950 °C for 10 min in 14% O₂ in N₂. The corresponding sheet resistances of the various profiles are also indicated in Fig. 5a, showing that sheet resistance decreases with increasing initial PureB layer thickness. The initial PureB layer acts as a source of the boron dopants, which diffuse into silicon up to the solid solubility, which is about $1.3 \times 10^{20} \text{ cm}^{-3}$ at 950 °C [29]. For a thinner initial PureB layer, the amount of dopants for diffusion into silicon was limited, leading to higher sheet resistance and lower peak doping concentration.

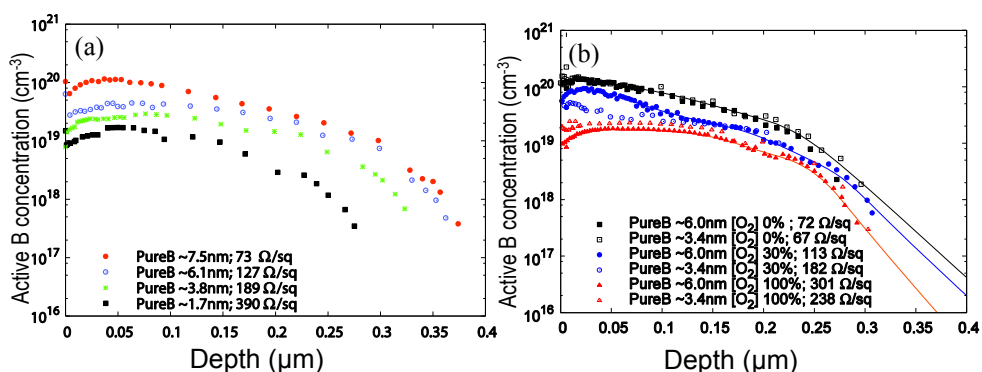


Figure 5 Profiles of the active boron concentration as determined from electrochemical capacitance-voltage measurements for PureB layers of different thickness (a), thermally diffused at 950 °C for 10 min in 14% O₂ in N₂. Sheet resistances of these profiles are given in the legend. In (b) two different (3.4-nm and 6-nm thick) initial PureB layers, were thermally diffused at 950 °C for 10 min with varying concentrations of oxygen (i.e., 0%, 30% and 100%) in N₂. Lines serve as a guide to the eye.

A characteristic dip in surface doping concentration is visible, as is typically observed at the Si/SiO₂ interface due to the higher solubility of boron in silicon oxide than in silicon [37]. A high surface dopant concentration can be desirable to reduce the minority carrier concentration near the surface, especially in the absence of field-effect passivation. Earlier work showed that the removal of this dip (the *boron-depletion region*) resulted in a lower recombination parameter J_{0p+} in case the passivating layer did not contain a high density of negative fixed charges, which translated to an absolute efficiency gain of 0.2% on the cell level [6].

The effect of the O₂ concentration in the diffusion ambient on the resulting boron dopant profiles and sheet resistances is investigated in Fig. 5b. The sheet resistances of the dopant profiles varies from ~70 Ω/sq when diffusing from a 6-nm PureB source layer in

N_2 ambient (0% O_2) to $\sim 240\text{-}300 \text{ } \Omega/\text{sq}$ when using an O_2 ambient (100% O_2). When diffused in N_2 ambient (0% O_2), initial PureB layer thicknesses of 3.4 nm as well as of 6 nm result in similar dopant profiles and sheet resistances. Therefore, it can be concluded that both cases provide a virtually unlimited source of boron dopants. Hence, the thickness and thereby the uniformity of the initial PureB layers is not critical when diffusing in N_2 ambient and the final dopant profile and sheet resistance are only dependent on diffusion conditions. In contrast, in case of an intentional O_2 flow during diffusion, the sheet resistance decreases with increasing initial PureB layer thickness (see Fig. 5a). Therefore, for such conditions, the uniformity of the initial PureB layer becomes a prerequisite for achieving homogeneous diffusion and uniform sheet resistance. In fact, an increase of O_2 concentration decreases the surface and peak dopant concentrations significantly, although the BSG thicknesses as shown in Fig. 4 is relatively insensitive to higher oxygen concentrations.

In summary, the dopant profile and peak concentration are not only determined by the initial PureB layer thickness and diffusion temperature, but also by the O_2 concentration during diffusion. The latter can accordingly be used as a parameter to optimize the doping profile.

C. Surface Passivation by Al_2O_3

One of the important prerequisites for high-efficiency silicon solar cells is a high minority carrier lifetime, which requires well-passivated interfaces and surfaces. Al_2O_3 prepared by plasma-enhanced ALD is known to provide excellent passivation for p^+ Si surfaces,[20] and is used here to compare the recombination parameter J_{0p^+} obtained for the different dopant profiles in Fig. 6. The uniformity of the p^+ Si surfaces over the wafer is indicated as the standard deviation of the sheet resistance.

It was found that the measured J_{0p^+} increases with decreasing sheet resistance, which can be expected from considering Auger recombination. The latter is illustrated by calculating the theoretical contribution of Auger recombination using the dopant profiles as input to the freeware program EDNA2 [38]. The ECV dopant profiles of the samples were scaled by a factor close to 1, in order to match the sheet resistance obtained by four-point probe measurements and to compensate for systematic measurement errors. Note that the EDNA2 evaluation revealed that the contribution of Auger recombination to J_{0p^+} was very sensitive to the choice of band gap narrowing model and the use of Fermi-Dirac statistics rather than Boltzmann statistics. In the simulations, the most up-to-date empirical models were used for Auger recombination [39] and band gap narrowing [40], which are

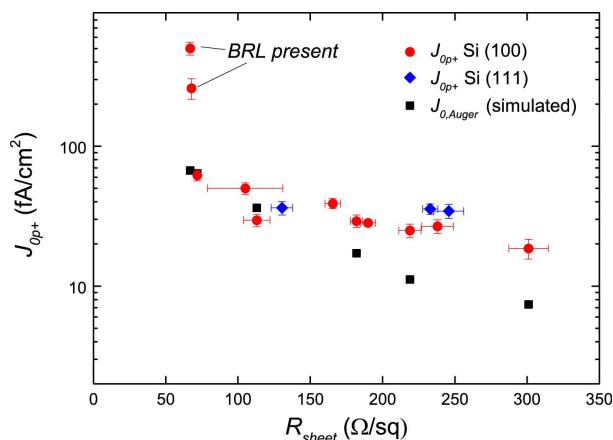


Figure 6 Recombination parameter J_{0p^+} of symmetrical $p^+/n/p^+$ lifetime samples fabricated by thermal diffusion of PureB on Si (100) and Si (111) at 950 °C for 10 min with various O_2 concentrations, passivated by 30-nm thick Al_2O_3 films prepared by plasma-enhanced ALD. For comparison, also the expected contributions from Auger recombination are included, as was determined from EDNA modeling.

consistent with Fermi-Dirac statistics. It can be seen from Fig. 6 that the results from both planar Si (100)- and (111)-oriented wafers are not significantly different and are close to the Auger limit. Acceptable surface passivation was achieved for most samples, with the contribution of surface recombination to the total J_{0p^+} being well below < 20 fA/cm².

Interestingly, some of the samples having sheet resistance of ~ 70 Ω/sq, exhibited a very high J_{0p^+} of ~ 260 – 502 fA/cm². As these samples were thermally diffused in N_2 ambient and remained hydrophilic after prolonged HF-dipping, the poor passivation results can be explained by the presence of a BRL. Such a BRL has previously also been associated with a degradation in Si bulk lifetime [8]. Note that the measured J_{0p^+} however only accounts for the recombination in the highly-doped region and at its surface. Therefore, it can be concluded that a BRL is detrimental for surface recombination. These results therefore seem to be in line to those of Phang *et al.* [9], who recently found in the presence of BRL, J_{0p^+} was comparable to an unpassivated doped surface. Nonetheless, before HF-dipping and Al_2O_3 passivation, we found J_{0p^+} of ~ 602 fA/cm² for the samples containing a BRL. Therefore, apparently, the Al_2O_3 layer improved the passivation slightly in case of a BRL. In literature, the BRL is sometimes etched to achieve good surface passivation which might be a way to also make these surfaces suitable for application in solar cells. [13]

3.4 Conclusions

In this work, a p^+ -doping method was demonstrated, in which a PureB layer was deposited by CVD using B_2H_6 as precursor, followed by thermal diffusion. In addition to optimizing the initial PureB layer thickness and thermal budget to control the dopant profiles, the oxygen concentration during diffusion is key in the resulting doping profiles. On the one hand, oxygen forms thicker BSG layers, but on the other hand results in doped regions with higher sheet resistances and the incorporation of less boron in the Si.

By using Al_2O_3 as surface passivation layer, it was found that for most p^+ Si surfaces the J_{0p^+} values were found to be close to the fundamental Auger limit, with similar results from planar Si (100) and (111) oriented surfaces. However, when a BRL is present after diffusion, a much higher J_{0p^+} was observed of $\sim 260\text{--}502$ fA/cm². The presence of a BRL clearly impedes the high-quality surface passivation of boron-diffused surfaces, which is essential for high-efficiency n -type solar cells, and a BRL should therefore be avoided or removed. The experiments in this work demonstrate that with correct tuning of the O_2 concentration during diffusion, no additional processing step is needed to etch away the BRL, and promising parameters for solar cells in terms of J_{0p^+} and sheet resistance can be achieved. For the high-volume manufacturing in Si solar cell industry, a customized batch furnace system is currently under development for the B_2H_6 doping process.

Acknowledgements

The authors would like to thank the staff of the NanoLab@TU/e and the former DIMES IC-processing cleanroom for their support, especially Alex van den Bogaard and Cassan Visser for help with the furnace recipes and with spectroscopic ellipsometry.

References

1. J.Schmidt, A.G. Aberle and R. Hezel, Investigation of carrier lifetime instabilities in Cz-grown silicon, Proc. 26th IEEE Photovoltaic Specialist Conference (1997) 13-18.
2. S.W. Glunz, S. Rein, J.Y. Lee, W. Warta, Minority carrier lifetime degradation in boron-doped Czochralski silicon, J. Appl. Phys. 90 (2001) 2397-2404.
3. T. Saitoh, H. Hashigami, *et al.*, Suppression of light-induced degradation of minority carrier lifetimes in low-resistivity Cz-silicon wafers and solar cells, 16th EU PV Solar Energy Conf. (2000) 1206-1209.
4. Macdonald, L.J. Geerlings, Recombination activity of interstitial iron and other transition metal point defects in p and n -type crystalline silicon, Appl. Phys. Lett. 85 (2004) 4061-4063.
5. Romijn, L. Fang, A. Vlooswijk, Industrial n -type solar cells: Towards 20% efficiency, Photovoltaics International 15 (2012) 63-69.

6. B.W.H. van de Loo, G. Dingemans, E.H.A. Granneman, *et al.*, Advanced front-surface passivation schemes for industrial *n*-type silicon solar cells, *Photovoltaics International* 24 (2014) 1-7.
7. J. Libal, R. Petres, R. Kopecek, G. Hahn, K. Wambach, P. Fath, *N*-type multicrystalline silicon solar cells with BBr₃-diffused front junction, 31st IEEE Photovoltaic Specialist Conference (2005) 1209-1212.
8. M.A. Kessler, T. Ohrdes, B. Wolpensinger, R. Bock, N.-P. Harder, Charge carrier lifetime degradation in Cz silicon through the formation of a boron-rich layer during BBr₃ diffusion processes, *Semicond. Sci. Technol.* 25 (2010) 055001.
9. S.P. Phang, W. Liang, B. Wolpensinger, M. A. Kessler, D. Macdonald, Tradeoffs between impurity gettering, bulk degradation and surface passivation of boron-rich layers on silicon solar cells, *IEEE J. Photovoltaics* 3 (2013) 261-266.
10. Y. Veschetti, R. Cabel, P. Brand, V. Sanzone, G. Raymond, A. Bettinelli, High efficiency on boron emitter *n*-type Cz silicon solar cells with industrial process, *IEEE J. Photovoltaics* 1 (2011) 118-122.
11. J. Jourdan, Y. Veschetti, S. Dubois, T. Desrues, R. Monna, Formation of boron-doped region using spin-on dopant: Investigation on the impact of metallic impurities, *Prog. Photovolt: Res. Appl.* 16 (2008) 379-387.
12. K. Ryu, A. Upadhyaya, Y. -W. Ok, M.K. Kang, V. Upadhyaya, L. Metin, H. Xu, A. Bhanap, A. Rohatgi, High-efficiency *n*-type Si solar cells with novel ink-jet printed boron emitters, *IEEE Electron. Dev. Lett.* 33 (2012) 854-856.
13. K. Ryu, A. Upadhyaya, H. -J. Song, C. -J. Choi, A. Rohatgi, Y. -W. Ok, Chemical etching of boron-rich layer and its impact on high-efficiency *n*-type silicon solar cells, *Appl. Phys. Lett.* 101 (2012) 073902-4.
14. Kurachi, K. Yoshioka, Investigation of boron solid-phase diffusion from BSG film deposited by AP-CVD for solar cell application, 27th EU PVSEC (2012) 1873-1876.
15. J. Benick, N. Bateman, M. Hermle, Very low emitter saturation current densities on ion implanted boron emitters, 25th EU PV Solar Energy Conf. (2010) 1169-1173.
16. N. Bateman, P. Sullivan, C. Reichel, J. Benick, M. Hermle, High quality ion implanted boron emitters in an interdigitated back contact solar cell with 20% efficiency, *Energy Procedia* 8 (2011) 509-514.
17. Torregrosa, C. Laviron, H. Faik, D. Barakel, F. Milesi, S. Beccaccia, Realization of ultra shallow junctions by PIII: application to solar cells, *Surface & Coatings Technology* 186 (2004) 93-98.
18. B. J. Pawlak, T. Janssens, S. Singh, *et al.*, Studies of implanted boron emitters for solar cell applications, *Prog. Photovolt: Res. Appl.* 20 (2012) 106-110.
19. K.R.C. Mok, R.C.G. Naber, L.K. Nanver, Insights to emitter saturation current densities of boron implanted samples based on defects simulations, 19th International Conference on Ion Implantation (2012) 245-248.
20. B. Hoex, J. Schmidt, R. Bock, P.P. Altermatt, M.C.M. van de Sanden, W.M.M. Kessels, Excellent passivation of highly doped *p*-type Si surfaces by the negative -charge-dielectric Al₂O₃, *Appl. Phys. Lett.* 91 (2007) 112107.
21. G. Dingemans and W. M. M. Kessels, Status and prospects of Al₂O₃ based surface passivation schemes for silicon solar cells, *J. Vac. Sci. Technol. A Vacuum, Surfaces, Film.*, 30, 4, (2012) 040802.
22. G. Aberle, *Crystalline Silicon Solar Cells: Advanced Surface Passivation and Analysis*, University of New South Wales, Sydney (1999) 77-78.
23. K.R.C. Mok, A.H.G. Vlooswijk, V. Mohammadi, L.K. Nanver, Effects of annealing on chemical-vapor deposited PureB layers, *ECS J. Solid State Science and Technology* 2 (2013) 413-417.

24. K.R.C. Mok, A.H.G. Vlooswijk, J. Derakhshandeh, L.K. Nanver, Chemical vapor deposition of PureB layers for solar cell application, Proc. 39th IEEE Photovoltaic Specialist Conference (2013) 2234-2238.
25. L. Shi, S. Nihtianov, L. Haspelslagh, F. Scholze, A. Gottwald, L.K. Nanver, Surface-charge-collection-enhanced high-sensitivity high-stability silicon photodiodes for DUV and VUV spectral ranges. IEEE Trans. Electron Devices 59 (2012) 2888-2894.
26. Sakic, G. van Veen, K. Kooijman, P. Vogelsang, *et al.*, High-efficiency silicon photodiode detector for sub-keV electron microscopy, IEEE Trans. Electron Devices 59, (2012) 2707-2714.
27. L.K. Nanver, L. Qi, V. Mohammadi, K.R.C. Mok, *et al.*, Robust UV/VUV/EUV PureB Photodiode Detector Technology With High CMOS Compatibility, IEEE J. of Selected Topic in Quantum Electronics 20 (2014) 3801711.
28. Sarubbi, L.K. Nanver, T.L.M. Scholtes, High effective Gummel number of CVD Boron layers in ultrashallow p^+n diode configurations, IEEE Trans. Electron Devices 57 (2010) 1269-1278
29. L. Vick, K.M. Whittle, Solid Solubility and Diffusion Coefficients of Boron in Silicon, J. Electrochem. Soc. 116 (1969) 1142-1144.
30. K.R.C. Mok, A.H.G. Vlooswijk, B.W.H. van de Loo, *et al.*, Furnace deposition of PureB layers from B_2H_6 for solar cell applications, 29th EU PV Solar Energy Conf., Amsterdam, The Netherlands, Sep. 22-26, 2014.
31. D. E. Kane, R. M. Swanson, Measurement of the Emitter Saturation Current by a Contactless Photoconductivity Decay Method, Proc. 18th IEEE Photovoltaic Specialists Conference (1985) 578-583.
32. P.P. Altermatt, A. Schenk, F. Geelhaar and G. Heiser, Reassessment of the intrinsic carrier density in crystalline silicon in view of band-gap narrowing, J. Appl. Phys. 93, (2003) 1598.
33. B.E. Deal, M. Sklar, Thermal oxidation of heavily doped silicon, J. Electrochem. Soc. 112 (1965) 430-435.
34. Sarubbi, T.L.M. Scholes, L.K. Nanver, Chemical Vapor Deposition of α -Boron Layers on Silicon for Controlled Nanometer-Deep p^+n Junction Formation, J. Electronic Materials 39 (2010) 162-173.
35. K.M. Busen, W.A. FitzGibbons, W.K. Tsang, Ellipsometric Investigations of Boron-Rich Layers on Silicon, J. Electrochem. Soc.: Solid State Science 115 (1968) 291-294.
36. N. Saitoh, T. Akamine, K. Aoki, Y. Kojima, Composition and growth mechanism of a boron layer formed using the molecular layer doping process, Jpn J. Appl. Phys. 32 (1993) 4404.
37. S. Grove, O. Leistiko, C.T. Sah, Redistribution of acceptor and donor impurities during thermal oxidation of silicon, J. Appl. Phys. 35 (1964) 2695-2701.
38. K.R. McIntosh, P.P. Altermatt, A freeware 1D emitter model for silicon solar cells, Proceedings of the 35th IEEE Photovoltaics Specialist Conference, Honolulu, 2010.
39. Richter, S.W. Glunz, F. Werner, J. Schmidt, A. Cuevas, Improved quantitative description of Auger recombination in crystalline silicon, Phys. Rev. B 86 (2012) 165202.
40. D. Yan and A. Cuevas, Empirical determination of the energy band gap narrowing in p^+ silicon heavily doped with boron, J. Appl. Phys. 116, 194505 (2014).

CHAPTER 4

'Zero-charge' SiO₂/Al₂O₃ Stacks for the Simultaneous Passivation of n^+ - and p^+ -Doped Silicon Surfaces by Atomic Layer Deposition*

Abstract To achieve high conversion efficiencies, advanced silicon solar cell architectures such as interdigitated back contact solar cells demand that defects at both the n^+ and p^+ doped Si surfaces are passivated simultaneously by a single passivation scheme. In this work, corona charging experiments show that the fixed charge density Q_f is a key parameter governing the passivation of both surface types. In solar cells, this Q_f can be controlled from strongly negative to even positive values by carefully tuning the SiO₂ interlayer thickness in SiO₂/Al₂O₃ stacks prepared by atomic layer deposition (ALD). The control in Q_f allows for a superior passivation of n^+ Si surfaces by SiO₂/Al₂O₃ stacks compared to a single layer Al₂O₃. For instance, for SiO₂ interlayer thicknesses of ~3–14 nm, the recombination parameter of an n^+ Si surface having a high surface doping concentration N_s of $2 \times 10^{20} \text{ cm}^{-3}$ was reduced from $J_{0n^+} = 81 \text{ fA/cm}^2$ to $J_{0n^+} = 50 \text{ fA/cm}^2$. Simulations predict that the SiO₂/Al₂O₃ stacks outperform Al₂O₃ passivation layers particularly on n^+ Si surfaces having a moderate N_s in the range of $10^{18} - 10^{20} \text{ cm}^{-3}$. On p^+ Si surfaces, $J_{0p^+} \leq 54 \text{ fA/cm}^2$ was achieved for all ALD SiO₂ interlayer thicknesses investigated (i.e., 1–14 nm). The SiO₂/Al₂O₃ stacks presented in this work are compatible with SiN_x capping and subsequent high-temperature firing steps, which are typically used in solar cell processing. Furthermore, the results were successfully reproduced in an industrial ALD batch reactor using a low-temperature process. This makes ALD SiO₂/Al₂O₃ stacks a promising candidate for the simultaneous passivation of n^+ and p^+ Si surfaces in solar cells.

* Published as: B. W. H. van de Loo, H. C. M. Knoops, G. Dingemans, G. J. M. Janssen, M. W. P. E. Lamers, I. G. Romijn, A. W. Weeber, W. M. M. Kessels, *Sol. Energy Mater. Sol. Cells*, 143 (2015), 450–456.

4.1 Introduction

A high level of surface passivation is a prerequisite to achieve crystalline silicon solar cells with high conversion efficiencies. Less than a decade ago, it was reported that Al_2O_3 films prepared by atomic layer deposition (ALD) provides superior passivation of p and p^+ -type Si surfaces, which was technologically challenging at that time.[1–3] The excellent passivation by Al_2O_3 can be related to a very low interface defect density D_{it} ($<10^{11} \text{ cm}^{-2}$) on Si, which is essential for *chemical* passivation. Furthermore, a high *negative* (fixed) charge density Q_f in of the order of $10^{12} - 10^{13} \text{ cm}^{-2}$ (depending on synthesis method) is present at the interface,[4] which reduces the minority carrier (i.e., electron) concentration near the Si surface, providing *field-effect* passivation. Even an ultrathin film of Al_2O_3 of less than 2 nm was found to be sufficient to passivate the Si surface, when combined with a-SiN_x:H (in short SiN_x) as anti-reflection coating (ARC) and/or capping layer.[5,6] The high levels of surface passivation provided by Al_2O_3 have led to significantly enhanced conversion efficiencies for diffused-junction solar cells, in particular for n -type Si solar cells (e.g., PERL)[7] and p -type cells such as PERC,[8] which is an Al local back surface field cell concept.[9] Due to superior uniformity and passivation performance, ALD of Al_2O_3 is currently piloted in industry.[10]

Despite the excellent results on p -type Si, on heavily doped n^+ Si surfaces the passivation of Al_2O_3 is compromised, as the minority carrier (i.e., hole) concentration at the surface is *increased* by the negative Q_f of the Al_2O_3 . [11,12] On lowly doped n -type Si, Al_2O_3 generally passivates the surface well, as it induces strong near-surface inversion. However, inversion layers are associated with a lifetime reduction at low injection levels ($\Delta n < 10^{15} \text{ cm}^{-3}$), which is within the operating regime of solar cells.[13–15] Secondly, inversion layers potentially act as undesired conduction pathway to metal contacts, resulting in parasitic shunting.[16] Note that parasitic shunting does not directly affect the surface passivation, but is predominantly affecting the performance of solar cells via a reduced fill factor and short-circuit current.[16] All of these unfavorable effects occur when an n or n^+ -type Si surface is passivated by a dielectric with a negative Q_f such as Al_2O_3 , and when the p or p^+ type Si surface is passivated by a dielectric containing a *positive* charge density, such as SiN_x.

In conventional diffused-junction Si solar cells, the n^+ and p^+ doped surfaces are located at each side of the cell, and hence can be passivated independently by a dielectric having the right charge polarity. However, in more advanced solar cell architectures such as interdigitated back-contact (IBC) cells, or in even more advanced axial Si nanowire cells,[17] the n^+ and p^+ doped Si surfaces are adjacent and preferably passivated

simultaneously by one film or film stack. To this end, we propose the use of a passivation scheme without significant Q_f , while providing very low D_{it} . Rather than relying on a fixed charge density to reduce one of the two charge carrier types at the surface, such a “zero-charge” passivation approach could rely on high surface doping concentration of the n^+ - and p^+ Si regions, which locally the minority carrier concentration at the surface and suppresses surface recombination. Besides for IBC cells, this approach can also be useful for conventional solar cells as both sides can then be passivated using a single production step in an industrial ALD reactor. Hence, the aim of this work is to achieve the passivation of both n^+ and p^+ Si surfaces and in a single deposition run, via a low-temperature and industrially viable process.

Although the simultaneous passivation of n^+ and p^+ Si has been addressed before using a variety of film stacks,[18–21] other very promising candidates are stacks of SiO₂/Al₂O₃ prepared by ALD. It is shown that these stacks exhibit excellent chemical passivation (e.g., D_{it} values $<10^{11}$ eV⁻¹cm⁻² at mid gap [22]), while their Q_f can effectively be tuned to virtually zero by carefully tuning the ALD SiO₂ thickness as shown by Dingemans *et al.*,[13] and Terlinden *et al.*,[23]. It is hypothesized that the SiO₂ interlayer in these stacks acts as a (trap-assisted) electron tunnel barrier, preventing charge-injection from the c-Si base into the electron trap sites in the Al₂O₃. [13,23] The Al₂O₃ plays a key role in the reduction of Si/SiO₂ interface defect states, which are effectively passivated by the diffusion of hydrogen from the Al₂O₃ film to the Si/SiO₂ interface during annealing.[24] It should be noted that also some positive charge formation in the SiO₂ film occurs (this is a “bulk” charge, instead of “interface charge” in Al₂O₃). However, this charge density is relatively low ($\sim 10^{11}$ cm⁻²) for ALD SiO₂ films and is therefore only partly contributing to the nullification of Q_f of the total SiO₂/Al₂O₃ system. Due to the positive charges in the SiO₂ film, the overall charge polarity of the SiO₂/Al₂O₃ becomes slightly *positive* for increasing ALD SiO₂ thicknesses (i.e., Q_f changes from $-5 \cdot 10^{12}$ cm⁻² for Al₂O₃ only to $Q_f = (4 \pm 2) \times 10^{11}$ cm⁻² for SiO₂/Al₂O₃ stacks with 12–16 nm thick SiO₂ interlayer [23]).

In previous work, the influence of the fixed charge density and the role of surface doping concentration on the passivation of n^+ and p^+ Si surfaces is not fully addressed yet. In this work, first the influence of the charge density on the passivation these surfaces is systematically investigated via corona charging experiments. The results serve as a benchmark for the next part of this Chapter, where we will carefully tune the SiO₂ interlayer thickness to control of the fixed-charge density of ALD SiO₂/Al₂O₃ stacks to passivate both surface types. Next, the role of surface doping concentration on the passivation properties will be discussed. Finally, we will study the compatibility of ALD

SiO₂/Al₂O₃ films as “zero-charge” passivation scheme with typical Si solar cell processing steps, such as the compatibility with SiN_x capping layers and high-temperature steps.

4.2 Experimental

Symmetrical $n^+/p/n^+$ lifetime samples were made by POCl₃ diffusions in an industry-scale tube furnace process (Tempress systems TS81003) on double-side chemically polished, p -type Czochralski-grown (Cz) Si (100) wafers. In another tube of the furnace, symmetrical $p^+/n/p^+$ lifetime samples were fabricated using BBr₃ as precursor, on Cz n -type wafers with a random-pyramid textured surface. After diffusion, the surface doping concentration of the $p^+/n/p^+$ sample was increased by a short wet etch.[25] The resulting (active) doping profiles were determined from electrochemical capacitance-voltage (ECV) profiling (see Fig. 1) using a WEP wafer profiler CVP21 table-top unit. Note, that the doping profile of the boron-doped samples can be affected by the texture of the surface, and a heavier doping level can be expected at the pyramid tips.[26] The sheet resistance R_s and the homogeneity of the doped regions were measured using a Signatone four-point probe, in combination with a Keithley 2400 Source Measurement Unit.

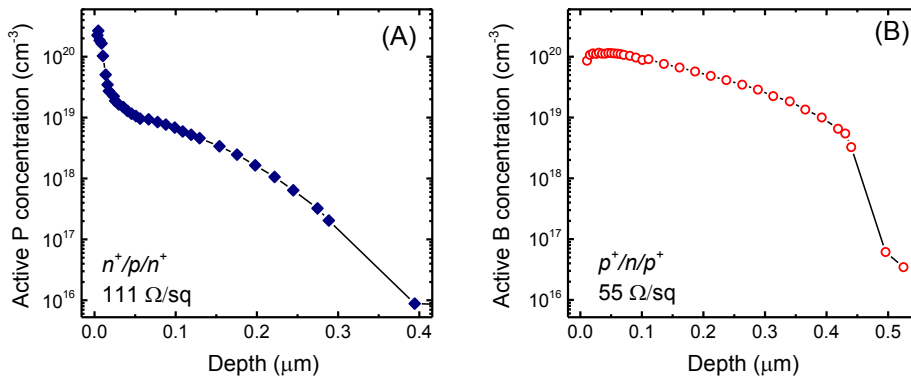
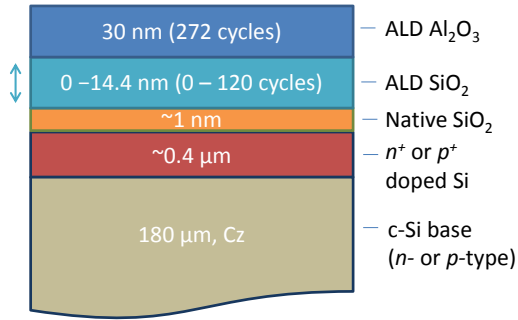


Figure 1 Doping profiles as determined by electrochemical capacitance-voltage (ECV) profiling of (a) $n^+/p/n^+$ samples of $R_s = 111 \pm 2 \Omega/\text{sq}$, and (b) $p^+/n/p^+$ lifetime samples, having $R_s = 55 \pm 2 \Omega/\text{sq}$. Note, that with ECV only the active dopant concentration is measured. The sheet resistance was measured by four-point probe measurements.

After glass removal, the samples received a short dip in diluted HF (1%, 1 min). Subsequently, SiO₂/Al₂O₃ stacks and Al₂O₃ films were deposited on both sides of the samples by plasma-enhanced ALD in an Oxford Instruments OpALTM reactor at 200 °C in a *single* deposition run. H₂Si(N(C₂H₅)₂)₂ and Al(CH₃)₃ were used as metal-organic

precursors and O₂ plasma as oxidant. More details on the ALD processes can be found elsewhere.[27] In principle, also other interlayers can be used to control the Q_f of Al₂O₃, including SiO₂ layers grown by plasma-enhanced chemical vapor deposition (PE-CVD), thermally-grown SiO₂, or ALD HfO₂ films.[11,20,28,29] Note that the latter material does not offer apparent benefits in terms of passivation of or industrial applicability. A schematic display of the passivated lifetime samples is given in Fig. 2. To activate the passivation, the stacks were either annealed for 10 minutes at 400 °C in N₂, or capped with 70 nm SiN_x followed by an industrial firing step (~800°C for 1s). The SiN_x was prepared by in-line PE-CVD reactor (MAiA, Roth & Rau), equipped with a microwave plasma source. As-deposited, the SiN_x has a refractive index of $n=2.05$ at 633nm.



Symmetric lifetime samples

Figure 2 Schematic representation of the passivated $n^+/p/n^+$ and $p^+/n/p^+$ lifetime samples used in this work.

A lifetime tester (Sinton WCT 100) was used for quasi-steady state photoconductance decay (QSS-PC) and transient-PC measurements. Using QSS-PC the recombination parameter J_0 was derived at high injection levels of $\Delta n \sim (0.4 - 6.2) \times 10^{16} \text{ cm}^{-3}$ using the method of Kane and Swanson,[30] which allows the extraction of J_0 from lifetime measurements via

$$\frac{1}{\tau_{\text{eff}}} - \frac{1}{\tau_{\text{Auger}}} = \frac{1}{\tau_{\text{SRH}}} + J_0 \cdot \frac{(N_d + \Delta n)\Delta n}{qn_i^2 W} \quad (1)$$

with τ_{eff} the effective lifetime, τ_{Auger} the (bulk) Auger lifetime, τ_{SRH} the Shockley-Read-Hall (SRH) lifetime of the bulk, n_i the intrinsic carrier concentration, q the elementary charge, W the wafer thickness and N_d the base doping concentration. Importantly, it was verified that the method of Kane & Swanson could be used for all samples in this work, as straight lines were observed for the Auger-corrected inverse lifetime plots. Note, that J_0 values of

the $p^+/n/p^+$ doped samples were divided by a factor of 1.7 to account for the increase in surface area due to the surface texture of these samples.

Corona charging measurements were carried out by depositing (positive) corona charges on both sides of the lifetime samples which were passivated by Al_2O_3 . The charges were deposited by applying a DC-bias (+/- 11kV) between a tungsten needle and a grounded plate to ionize air molecules. After charge deposition step lifetime measurements were performed. Additionally, the deposited density of corona-charges Q_{corona} was derived from Kelvin probe potential measurements, using a Trek electrostatic voltmeter. Note that the deposited charge density on the Al_2O_3 surface was found to be stable for days, even when placing the charged surfaces directly onto a grounded metal.

4.3 Results

4.3.1 The influence of fixed charges on the passivation of n^+ and p^+ Si

Before investigating the passivation quality of $\text{SiO}_2/\text{Al}_2\text{O}_3$ stacks, it is illustrative to demonstrate the effect of fixed charges on the passivation of both n^+ and p^+ doped Si surfaces. To this end, the symmetrically doped lifetime samples were passivated by a single-layer of Al_2O_3 , after which lifetime measurements and positive corona charging on both sides were carried out in a step-wise fashion. In this way, the net charge density Q_{net} was varied from being strongly negative (i.e., $Q_{net} = -5 \cdot 10^{12} \text{ cm}^{-2}$, which corresponds to Q_f of the (ALD) Al_2O_3 films [31]) to positive values of $+5 \cdot 10^{12} \text{ cm}^{-2}$.

In Fig. 3a, the results of $n^+/p/n^+$ samples are given. Prior to deposition, the level of surface passivation provided by the Al_2O_3 results in $J_{0n^+} = 79 \text{ fA/cm}^2$. When changing the net charge density via corona charging towards a more positive Q_f , J_{0n^+} decreases. The decrease in J_{0n^+} can be understood as the more positive fixed charge will reduce the minority carrier (i.e., hole) concentration at the surface. A similar trend was observed in reference [11] for corona charging experiments on highly n -doped surfaces passivated by Al_2O_3 . However, note that also opposite trends are observed in case of lowly doped n -type Si surfaces passivated by Al_2O_3 . [31] There, positive corona charging first results in an *increase* of surface recombination. For such lowly doped surfaces, an inversion layer is formed near the Si surface by the negative Q_f of Al_2O_3 , after which the surface is gradually moved to depletion and consequently accumulation by positive corona charging. Therefore, we can conclude that the highly-doped n^+ Si surfaces used in this work were not in inversion, not even for the highest negative fixed charge densities. For high positive $Q_{net} = 4.9 \times 10^{12} \text{ cm}^{-2}$, the reduction of J_{0n^+} saturated at $J_{0n^+} = 50 \text{ fA/cm}^2$, behavior which is

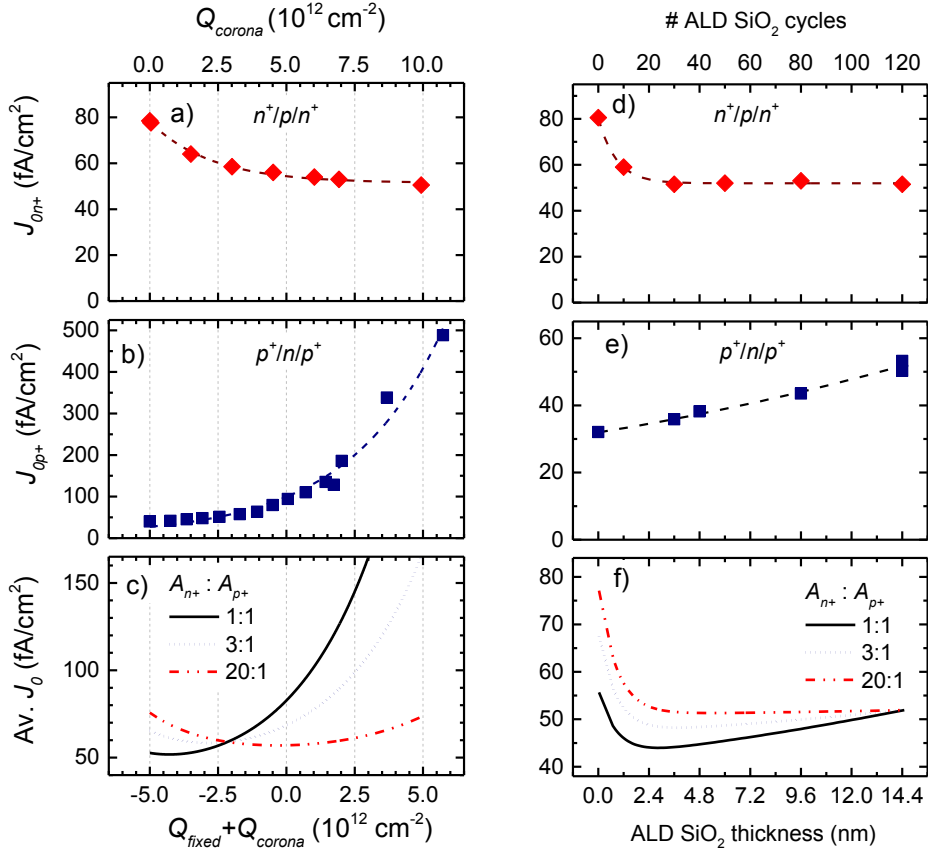


Figure 3 Recombination parameter of n^+ and p^+ Si lifetime samples passivated by ALD Al₂O₃ where the total charge was changed by corona charging from $Q_f = -5 \cdot 10^{12} \text{ cm}^{-2}$ (a)-(b) and for samples passivated by SiO₂/Al₂O₃ stacks with varying SiO₂ thickness (d)-(e) (note the difference in scale of the y-axes). The J_0 values were determined by QSS-PC, where J_{0p^+} was corrected for the increased surface area due to surface texture. Lines serve as guide to the eye. In (c) and (f), the average J_0 for both the n^+ and p^+ regions are calculated for several different area fractions $A_{n^+}:A_{p^+}$.

observed more often for such high charge doses.[11,32] Simulations using the free-ware program EDNA,[33] using Fermi-Dirac statistics, the Auger parameterization from Richter *et al.*,[34] and the band-gap narrowing model of Schenk,[35] indicate that the Auger limit of the n^+ region is $J_{0n^+,Auger} = 16 \text{ fA/cm}^2$. This significant difference ΔJ_0 of 34 fA/cm^2 can indicate the presence of other recombination processes in the n^+ doped region, potentially due to SRH recombination via inactive phosphorus precipitates.[36,37]

On the $p^+/n/p^+$ doped samples in Fig. 3b, the opposite behavior to Fig. 3a is obtained when depositing positive corona charges, and an strong increase in J_{0p^+} can be observed. On the p^+ Si surface a negative Q_f provides strong field-effect passivation, enabling very low $J_{0p^+}=32$ fA/cm² for Al₂O₃. EDNA simulations indicate that this value is within the error equal to the (lower) limit set by Auger recombination, i.e., $J_{0p^+,Auger}=35$ fA/cm².

Interestingly, the recombination parameter of the $p^+/n/p^+$ sample is much more sensitive to the total fixed charge density than the $n^+/p/n^+$ sample, as is evident from the drastic increase in J_{0p^+} to ~ 490 fA/cm² at $Q_{net} = 5.7 \cdot 10^{12}$ cm⁻². This higher sensitivity to Q_f of J_{0p^+} compared to J_{0n^+} can be explained by two possible effects. First, the defects at the Si/Al₂O₃ interface (which essentially is a Si/SiO₂/Al₂O₃ interface, as interfacial SiO₂ is always present for ALD Al₂O₃ films on Si [4,13,38,39]) can have higher capture cross-section for electrons than for holes (e.g., $\sigma_n \approx 10^2 \times \sigma_h$ [40,41]). As the capturing of holes is limiting the recombination at n^+ Si surfaces, a lower capture cross-section aids in lower surface recombination for n^+ Si than for p^+ Si. Secondly, the doping profiles used (see Fig. 1) have an influence on the surface recombination, which has not been discussed so far. Nonetheless, we can state here that the relatively low (active) surface doping concentration of the boron-doped regions as compared to the phosphorus doped surfaces (i.e., $N_s=9 \cdot 10^{19}$ cm⁻³ versus $\sim 2 \cdot 10^{20}$ cm⁻³, respectively) plays a key role in the increased sensitivity of J_{0p^+} to surface passivation and charges. A route to further reduce the recombination at p^+ Si surfaces in a case without fixed charges is therefore to increase the (boron-) surface doping concentration, as will be discussed in section 3C. For instance, the boron surface doping concentration could be increased by etching of the boron-depletion region (BDR) which is typically present near the surface.[25]

Finally, it is interesting to look at a case where n^+ and p^+ Si surfaces should be passivated by a single passivation scheme. Considering the fact that in an actual solar cell, the surface recombination also scales with the surface areas of the n^+ and p^+ region, i.e., A_{p^+} and A_{n^+} respectively, we have evaluated several different cases using the interpolation of the corona-charging results of Figs. 3a and 3b. In case of equal area fractions $A_{n^+}=A_{p^+}$ (1:1), which, for instance, would be the case when both front and back-side of a bifacial solar cell are passivated at once, a value of $Q_{net}=-4 \cdot 10^{12}$ cm⁻² would result in the lowest average J_0 . For p -type based IBC cells, it is common that $A_{n^+} \gg A_{p^+}$ at the back side to prevent electrical shading, (or conversely, $A_{p^+} \gg A_{n^+}$ for n -type Si based IBC cells [42]). As can be seen from Fig. 3c, the optimum charge density in terms of J_0 shifts from $Q_{net}=-4 \cdot 10^{12}$ cm⁻² for $A_{n^+}=A_{p^+}$ (1:1), towards $Q_{net}=0$ for the fraction $A_{n^+}=20 \times A_{p^+}$ (1:20).

To summarize, it can be concluded that the fixed charge density is an important parameter when optimizing the simultaneous passivation of n^+ and p^+ doped Si surfaces. The optimum charge density will in practice vary from case to case, and is dependent on the doping profile and the area fractions of the n^+ and p^+ doped regions. In particular on p^+ Si surfaces, the passivation shows a strong dependence on the charge density, most likely due to a moderate level of chemical passivation and a relative low surface doping concentration (i.e., below $<10^{20}$ cm⁻³).

4.3.2 Passivation of n^+ and p^+ Si surfaces by ALD SiO₂/Al₂O₃ stacks

It is clear that the control in fixed charge density and polarity provides an additional parameter to optimize the passivation of both n^+ and p^+ Si surfaces. Next, we will investigate the possibility to optimize this passivation by precisely tuning the ALD SiO₂ interlayer thickness of the SiO₂/Al₂O₃ stack between 0 and 14.4 nm. It has been hypothesized, that an ALD SiO₂ interlayer of 2–4 nm thickness prevents the charge-injection from the Si into trap sites in the Al₂O₃ layers.[23] Therefore, the negative Q_f of SiO₂/Al₂O₃ stacks rapidly decreases towards virtually zero for these SiO₂ thicknesses. For thicker SiO₂ layers, the net charge density of the SiO₂/Al₂O₃ stacks becomes slightly positive (i.e., $\sim 10^{11}$ cm⁻² for ~ 14 nm ALD SiO₂) due to the positive bulk charge in the SiO₂ films.

In Fig. 3d, J_{0n^+} of the $n^+/p/n^+$ samples passivated by single layer Al₂O₃ or SiO₂/Al₂O₃ stacks are shown for varying SiO₂ interlayer thickness. For all cases where ALD SiO₂ was present, the recombination parameter J_{0n^+} was reduced when compared to single-layer Al₂O₃ films. For instance, SiO₂/Al₂O₃ stacks having an ultrathin ALD SiO₂ interlayer of 3.6 nm thickness, results in the significant improvement in J_{0n^+} as compared to single layer Al₂O₃ from 81 to 50 fA/cm². This improvement is in line with the expected transition from negative to positive charges, as a negative Q_f was undesirable for the passivation of n^+ Si surfaces, as also the corona charging experiments have pointed out. Interestingly, no further decrease in J_{0n^+} was observed for SiO₂ films with thicknesses >3.6 nm. The lowest values of J_{0n^+} correspond well to the final J_{0n^+} values after positive corona charging of 50 fA/cm². This further supports the hypothesis that recombination in the n^+ doped region itself is limiting J_{0n^+} under these circumstances.

On $p^+/n/p^+$ samples, J_{0p^+} gradually increases with increasing ALD SiO₂ thickness from 32 fA/cm² for single-layer Al₂O₃ to 52 fA/cm² for 14.4 nm ALD SiO₂ (Fig. 3e). This increase in J_{0p^+} can be explained by the reduction in negative Q_f , and accompanying loss in field-effect passivation. It is notable that the maximal J_{0p^+} values obtained for

SiO₂/Al₂O₃ stacks (i.e., ($J_{0p+} \leq 54$ fA/cm² for all ALD SiO₂ thicknesses investigated) are significantly lower than the charged samples passivated by Al₂O₃, having $J_{0p+}=95$ fA/cm² for $Q_{net} \sim 0$ cm⁻². This could indicate that the introduction of ALD SiO₂ stacks also improves the chemical passivation compared to single-layer Al₂O₃, as is also observed in literature by a slight decrease in D_{it} . [27]

To simulate the (average) recombination parameter in case both surface types would be passivated by SiO₂/Al₂O₃ stacks, the results of n^+ and p^+ Si are combined in Fig. 3f. The results show an optimal ALD SiO₂ thickness of 2–5 nm in case $A_{n+} = A_{p+}$ (1:1), having a significantly lower average J_0 as compared to single layer Al₂O₃ film ($J_0 = 44$ versus 55 fA/cm², respectively). For $A_{n+} > A_{p+}$, the optimal SiO₂ thickness becomes less critical and ~3–12 nm SiO₂ is preferred.

4.3.3 Role of surface doping concentration

Besides being dependent upon the relative areas of both regions, the optimal SiO₂ thickness in ALD SiO₂/Al₂O₃ stacks to passivate both n^+ and p^+ surfaces is also dependent upon the doping concentrations at both surfaces. Note that in this work, corona charging indicated that the n^+ doped surfaces are depleted. Apparently, the high negative Q_f of the Al₂O₃ is insufficient to induce inversion on these highly doped surfaces, having a phosphorus surface concentration of $N_s \sim 2 \cdot 10^{20}$ cm⁻³. Using the device simulation package Atlas, [43] the J_{0n+} values belonging to Gaussian-shaped n^+ doping profiles having different surface doping concentrations and a fixed depth of 0.1 μm were calculated. Note that the commonly reported effective surface recombination velocity S_{eff} principally varies with surface doping concentration. [44] However, S_{eff} was not required as input parameter for the Atlas simulations. Instead, the simulations are based on the assumption that the interface input parameters Q_f , S_{n0} and S_{p0} (being the fundamental surface recombination velocities for electrons and holes respectively) are independent of the surface doping concentration.

For the S_{n0} and Q_f of ALD Al₂O₃ films this was recently experimentally proven for boron-doped surfaces having N_s in the range of $9 \cdot 10^{15} - 3 \cdot 10^{19}$ cm⁻³. [45] The simulations allow for the identification of the different contributions to the total recombination of the highly-doped region J_{0n+} , that is the contributions of Auger, surface, defect and radiative recombination:

$$J_{0n+} = J_{0,Auger} + J_{0,surface} + J_{0,SRH} + J_{0,rad} \quad (2)$$

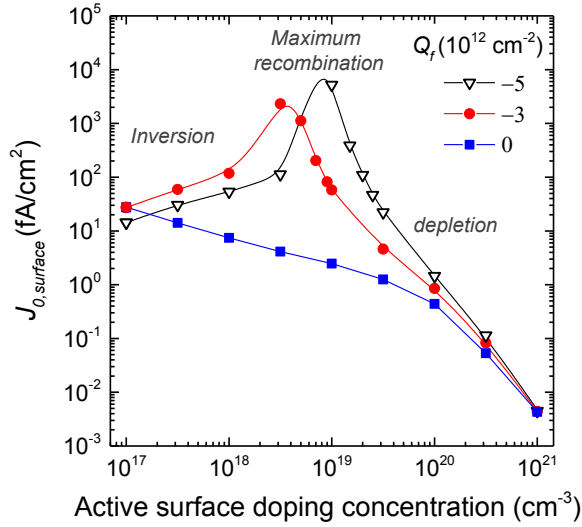


Figure 4 Results from Atlas simulations for Gaussian n^+ doping profiles, having the peak doping at the surface and having a depth of 0.1 μm . Values for $J_{0,\text{surface}}$ are given for three different fixed charge densities in the dielectric. As input for the simulations, the fundamental surface recombination velocities for electrons and holes were $S_{n0}=6500$ cm/s and $S_{p0}=65$ cm/s, respectively. In the simulations, Fermi-Dirac statistics were used, in combination with the band-gap narrowing model of Schenk,[35] the Auger model of Dzewior and Schmid,[47] and the Klaassen mobility model.[48] The bulk SRH lifetimes were $\tau_{p0}=\tau_{n0}=1$ ms.

The results for $J_{0,\text{surface}}$ are presented in Fig. 4. It can be seen that for moderate surface doping concentrations ($N_s \sim 10^{17}$ cm^{-3}), low $J_{0,\text{surface}}$ values are obtained for all Q_f values investigated. However, in case of a negative Q_f , the near surface region is strongly inverted which is why Al₂O₃ single layers will likely passivate very well. Nevertheless, as was mentioned in the introduction, inversion conditions are undesirable in solar cells due to inversion layer recombination and potential parasitic shunting.[15]

For higher n^+ Si surface doping concentrations within the range of 10^{18} – 10^{20} cm^{-3} , $J_{0,\text{surface}}$ is severely increased for dielectrics having a strong negative Q_f (such as for Al₂O₃), which is in line with the experimental observations by others [11,12,21]. This strong surface recombination occurs when the n^+ surface transitions from depletion to inversion, and the concentrations of electrons and holes at the surface (n_s and p_s , respectively) satisfy the condition $\sigma_p p_s \approx \sigma_n n_s$. [46] Interestingly, the simulations predict that for this particular surface doping range excellent passivation can be maintained in case of $Q_f=0$. Therefore, a strong gain in passivation for SiO₂/Al₂O₃ stacks compared to single layer Al₂O₃ can be expected in the range of surface doping 10^{18} – 10^{20} cm^{-3} . This may be very relevant when

SiO₂/Al₂O₃ stacks are used to passivate a lightly doped n^+ Si front surface of e.g., an IBC cell.

Although moderate doping concentrations are often desirable to ensure a low Auger recombination (i.e., a low $J_{0,Auger}$), it is insightful to consider the effects of very high surface doping concentrations $N_s > 10^{20}$ cm⁻³ on $J_{0,surface}$. Interestingly, the Atlas simulations show a strongly reduced $J_{0,surface}$ for all fixed charge densities investigated. This effect can be understood as the high surface doping levels reduce the minority carrier (i.e., hole) concentration at the surface. For these very low $J_{0,surfaces}$ values, it can be expected from Eq.(2) that surface recombination will become negligible compared to the other recombination mechanisms in the highly doped region, such as Auger and SRH recombination. The results from the simulations can explain the excellent passivation results on highly-doped n^+ Si surfaces by PE-CVD Al₂O₃/SiN_x stacks, which are obtained despite of their negative Q_f of $(1-2) \times 10^{12}$ cm⁻², [18] which now can (partly) be attributed to the very high phosphorus surface doping concentration which was used ($N_s \sim (4-6) \times 10^{20}$ cm⁻³).

Overall, it can be expected that SiO₂/Al₂O₃ stacks will outperform Al₂O₃ passivation schemes in a wide range of phosphorus surface doping concentrations from $\sim 5 \cdot 10^{17}$ to $\sim 10^{20}$ cm⁻³ due to the absence of a negative Q_f , which is the range of practical interest for most solar cell applications.

4.3.4 Aspects related to application of SiO₂/Al₂O₃ stacks in solar cells

In solar cells, typically thin ($\sim 2-5$ nm) Al₂O₃ passivation layers are combined with SiN_x capping layers, which serve as anti-reflection coating when on the front side or as dielectric mirror when on the rear side of the solar cell. Furthermore, to “fire” the (printed) metal contacts through the passivation layers, a very short (~ 1 s) high temperature anneal at 800°C (firing step) is typically performed. To study the compatibility of the ALD passivation layers of this work with SiN_x capping and subsequent firing, various passivation schemes are compared on $n^+/p/n^+$ lifetime samples in Fig. 5. The passivation schemes include single layer Al₂O₃ and SiO₂/Al₂O₃ stacks with or without SiN_x capping, and in addition to this, also results from a batch ALD reactor are shown.

Interestingly, the passivation of n^+ Si surfaces by thin Al₂O₃ films capped by SiN_x in combination with a firing step (Fig. 5b) leads to a reduced J_{0n^+} compared to the thicker reference Al₂O₃ films without SiN_x capping and firing (Fig. 5a). This can possibly be

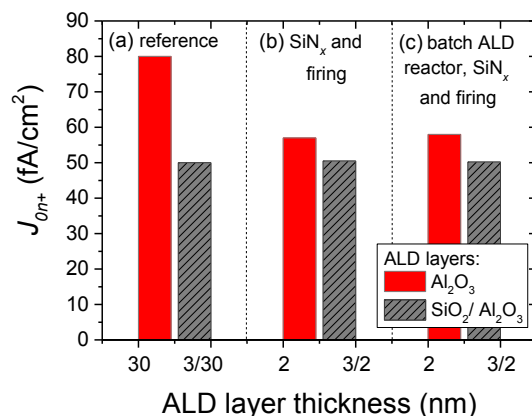


Figure 5 The recombination parameter of $n^+/p/n^+$ lifetime samples. In (a), SiO₂/Al₂O₃ passivation stacks are prepared in a single-wafer reactor and annealed at 400 °C. In (b) the ALD based passivation layers are capped by 70 nm of SiN_x, which was deposited in an in-line PE-CVD reactor. These stacks are subsequently fired at ~800 °C for ~1 second. In (c), the results of (b) were reproduced by depositing the SiO₂ and Al₂O₃ layers in a batch ALD reactor for high-volume manufacturing, before capping with SiN_x and subsequent firing. The horizontal axis displays the thickness of the individual ALD layers.

explained by a reduction in terms of D_{it} in combination with a reduction of negative Q_f , as was observed by Richter *et al.*, for similar passivation schemes after firing.[21] Here, we show that even though Al₂O₃ films capped by SiN_x can provide excellent passivation of the n^+ Si surfaces, its passivation could be even further improved by having a thin (3 nm) ALD SiO₂ interlayer. Moreover, the ALD SiO₂/Al₂O₃ films capped by SiN_x of Fig. 5b yield similar results compared to their reference samples of Fig. 5a. Hence, these initial findings indicate that the application of a SiN_x capping layer and a high temperature firing step do not significantly affect the passivation level offered by the SiO₂/Al₂O₃ stacks.

The results of Fig. 5b, which were obtained using a single-wafer ALD reactor, could be successfully reproduced by depositing the Al₂O₃ and SiO₂ layers by a batch ALD reactor in Fig. 5c. This reactor was designed specifically for high-volume manufacturing. Note that in the batch ALD reactor, the passivation layers were deposited on both sides of the lifetime samples at the same time. Moreover, the SiO₂/Al₂O₃ stacks were deposited in a single deposition run without unloading the samples in between. In the batch ALD reactor, O₃ was used as oxidant in the ALD processes, whereas O₂ plasma was used in the single wafer reactor. Despite the differences in reactor geometry and oxidants, both reactor types yielded very similar passivation results as can be seen when comparing Fig. 5b with Fig. 5c. This demonstrates the robustness and scalability of the ALD processes.

4.4 Conclusions

In this work, the simultaneous passivation of n^+ and p^+ Si surfaces has been investigated. Corona charging experiments on lifetime samples clearly demonstrated that the fixed charge density is a key parameter controlling the passivation of both surface types. It was shown, that by controlling the Q_f in $\text{SiO}_2/\text{Al}_2\text{O}_3$ stacks via tuning the amount of ALD SiO_2 cycles, a strongly improved passivation on highly-doped n^+ Si compared to single layer Al_2O_3 films could be achieved. Simultaneously, due to a high level of chemical passivation, a low J_{0p^+} on p^+ Si could be maintained. Simulations predict that $\text{SiO}_2/\text{Al}_2\text{O}_3$ stacks have the potential to outperform Al_2O_3 in a wide range of phosphorus surface doping concentrations, most prominently in the range of $10^{18} - 10^{20} \text{ cm}^{-3}$. In general, at highly-doped surfaces the condition for maximal surface recombination (i.e., $\sigma_n n_s \approx p_s \sigma_h$) is less likely to be met for ‘zero-charge’ passivation schemes.

Initial feasibility studies on the compatibility of the $\text{SiO}_2/\text{Al}_2\text{O}_3$ stacks with conventional Si solar cell steps such as capping by a SiN_x layer and a subsequent high temperature (firing) step, yielded similar results in terms of J_{0n^+} . Moreover, after successful upscaling of the ALD process from a single-wafer ALD reactor to an industrial batch ALD reactor, similar passivation results were achieved.

In conclusion, this work reveals the opportunities for ALD based passivation schemes to passivate e.g., n^+ and p^+ Si surfaces either separately or even simultaneously in a single deposition run. These results are particular relevant for the passivation of the back side of IBC solar cells, but are also of interest for the passivation of both sides of a diffused-junction solar cell at once. Further research is currently ongoing to demonstrate the concept of a “zero-charge” passivation scheme on solar cell level.

Acknowledgements

The authors would like to thank D. Saynova (ECN) and C.A.A. van Helvoirt, Dr. J. Melskens, T.L.I. Frankort and R.J. van Gils (TU/e) for their valuable contributions to this work. We are grateful for financial support from the Dutch Ministry of Economic Affairs, via the Top-consortia Knowledge and Innovation (TKI) programs “Advanced Nanolayers” and “DutchNess”.

References

1. Hoex, B., Heil, S.B.S., Langereis, E., *et al.*, (2006) Ultralow surface recombination of c-Si substrates passivated by plasma-assisted atomic layer deposited Al₂O₃. *Appl. Phys. Lett.*, **89** (4), 42112.
2. Hoex, B., Schmidt, J., Bock, R., *et al.*, (2007) Excellent passivation of highly doped *p*-type Si surfaces by the negative-charge-dielectric Al₂O₃. *Appl. Phys. Lett.*, **91** (11), 112107.
3. Agostinelli, G., Delabie, A., Vitanov, P., *et al.*, (2006) Very low surface recombination velocities on *p*-type silicon wafers passivated with a dielectric with fixed negative charge. *Sol. Energy Mater. Sol. Cells*, **90** (18–19), 3438–3443.
4. Dingemans, G., and Kessels, W.M.M. (2012) Status and prospects of Al₂O₃-based surface passivation schemes for silicon solar cells. *J. Vac. Sci. Technol. A*, **30** (4), 40802.
5. Liang, W., Weber, K.J., and Thomson, A.F. (2014) Effective SiN_x:H Capping Layers on 1-nm Al₂O₃ for *p*+ Surface Passivation. *IEEE J. Photovoltaics*, **4** (6), 1405–1412.
6. Richter, A., Benick, J., and Hermle, M. (2013) Boron Emitter Passivation With Al₂O₃ and Al₂O₃/SiN_x Stacks Using ALD Al₂O₃. *Photovoltaics, IEEE J.*, **3** (1), 236–245.
7. Benick, J., Hoex, B., van de Sanden, M.C.M., *et al.*, (2008) High efficiency *n*-type Si solar cells on Al₂O₃-passivated boron emitters. *Appl. Phys. Lett.*, **92** (25), 253504.
8. Schmidt, J., Merkle, A., Brendel, R., *et al.*, (2008) Surface passivation of high-efficiency silicon solar cells by atomic-layer-deposited Al₂O₃. *Prog. Photovoltaics Res. Appl.*, **16** (6), 461–466.
9. J. Knobloch, A. G. Aberle, and B.V. (1989) Cost effective processes for silicon solar cells with high performance. *Proc. 9th EU-PVSEC*, 777–780.
10. van Delft, J.A., Garcia-Alonso, D., and Kessels, W.M.M. (2012) Atomic layer deposition for photovoltaics: applications and prospects for solar cell manufacturing. *Semicond. Sci. Technol.*, **27** (7), 74002.
11. Bordihn, S., Dingemans, G., Mertens, V., and Kessels, W.M.M. (2013) Passivation of *n*+ -Type Si Surfaces by Low Temperature Processed SiO₂/Al₂O₃ Stacks. *IEEE J. Photovoltaics*, **3** (3), 925–929.
12. Hoex, B., van de Sanden, M.C.M., Schmidt, J., *et al.*, (2012) Surface passivation of phosphorus-diffused *n*+ -type emitters by plasma-assisted atomic-layer deposited Al₂O₃. *Phys. status solidi - Rapid Res. Lett.*, **6** (1), 4–6.
13. Dingemans, G., Terlinden, N.M., Verheijen, M.A., *et al.*, (2011) Controlling the fixed charge and passivation properties of Si(100)/Al₂O₃ interfaces using ultrathin SiO₂ interlayers synthesized by atomic layer deposition. *J. Appl. Phys.*, **110** (9), 93715.
14. Dingemans, G., Mandoc, M.M., Bordihn, S., *et al.*, (2011) Effective passivation of Si surfaces by plasma deposited SiO_x/a-SiN_x:H stacks. *Appl. Phys. Lett.*, **98** (22), 222102.
15. Dirnstorfer, I., Simon, D.K., Jordan, P.M., and Mikolajick, T. (2014) Near surface inversion layer recombination in Al₂O₃ passivated *n*-type silicon. *J. Appl. Phys.*, **116** (4), 44112.
16. Dauwe, S., Mittelstadt, L., Metz, A., *et al.*, (2002) Experimental evidence of parasitic shunting in silicon nitride rear surface passivated solar cells. *Prog. Photovoltaics Res. Appl.*, **10** (4), 271–278.
17. T. Shoji, K. Kakushima, Y. Kataoka, A. Nishiyama, N. Sugii, H. Wakabayashi, K. Tsutsui, K. Natori, H.I. (2014) Effect of Surface Potential Control and Interface States for Silicon Nanowire Solar Cells. *Proc. 29th EU-PVSEC*, 844–847.
18. Duttagupta, S., Ma, F.J., Lin, S.F., *et al.*, (2013) Progress in surface passivation of heavily doped *n*-type and *p*-type silicon by plasma-deposited AlO_x/SiN_x dielectric stacks. *IEEE J. Photovoltaics*, **3** (4), 1163–1169.
19. Duttagupta, S., Hoex, B., and Aberle, A.G. (2013) Progress with industrially-feasible excellent surface passivation of heavily-doped *p*-type and *n*-type crystalline silicon by

- PECVD SiO_x/SiN_x with optimised anti-reflective performance. *28th Eur. PVSEC*, 993–996.
20. Lin, F., Duttagupta, S., Aberle, A.G., and Hoex, B. (2012) Excellent passivation of *n*+ and *p*+ silicon by PECVD SiO_x/AlO_x stacks. *27th Eur. Photovolt. Sol. Energy Conf. Exhib.*, 1251–1254.
 21. Richter, A., Benick, J., Kimmerle, A., *et al.*, (2014) Passivation of phosphorus diffused silicon surfaces with Al₂O₃: Influence of surface doping concentration and thermal activation treatments. *J. Appl. Phys.*, **116** (24), 243501.
 22. Dingemans, G., Terlinden, N.M., Pierreux, D., *et al.*, (2011) Influence of the Oxidant on the Chemical and Field-Effect Passivation of Si by ALD Al₂O₃. *Electrochem. Solid-State Lett.*, **14** (1), H1.
 23. Terlinden, N.M., Dingemans, G., Vandalon, V., *et al.*, (2014) Influence of the SiO₂ interlayer thickness on the density and polarity of charges in Si/SiO₂/Al₂O₃ stacks as studied by optical second-harmonic generation. *J. Appl. Phys.*, **115** (3), 33708.
 24. Dingemans, G., Beyer, W., van de Sanden, M.C.M., and Kessels, W.M.M. (2010) Hydrogen induced passivation of Si interfaces by Al₂O₃ films and SiO₂/Al₂O₃ stacks. *Appl. Phys. Lett.*, **97** (15), 152106.
 25. van de Loo, B.W.H., Dingemans, G., Granneman, E.H.A., *et al.*, (2014) Advanced front-surface passivation schemes for industrial *n*-type silicon solar cells. *Photovoltaics Int.*, **24**, 43–50.
 26. Ma, F.-J., Duttagupta, S., Shetty, K.D., *et al.*, (2014) Two-dimensional numerical simulation of boron diffusion for pyramidally textured silicon. *J. Appl. Phys.*, **116**, (18) 184103.
 27. Dingemans, G., van Helvoirt, C.A.A., Pierreux, D., *et al.*, (2012) Plasma-Assisted ALD for the Conformal Deposition of SiO₂: Process, Material and Electronic Properties. *J. Electrochem. Soc.*, **159** (3), H277–H285.
 28. Simon, D.K., Jordan, P.M., Dirnstorfer, I., *et al.*, (2014) Symmetrical Al₂O₃-based passivation layers for *p*- and *n*-type silicon. *Sol. Energy Mater. Sol. Cells*, **131**, 72–76.
 29. Mack, S., Wolf, A., Brosinsky, C., *et al.*, (2011) Silicon Surface Passivation by Thin Thermal Oxide/PECVD Layer Stack Systems. *IEEE J. Photovoltaics*, **1** (2), 135–145.
 30. Kane, D.E., and Swanson, R.M. (1985) Measurement of the emitter saturation current by a contactless photoconductivity decay method. *IEEE Photovolt. Spec. Conf.* **18**, **69**, 578–583.
 31. Dingemans, G., van de Sanden, M.C.M., and Kessels, W.M.M. (2010) Influence of the Deposition Temperature on the *c*-Si Surface Passivation by Al₂O₃ Films Synthesized by ALD and PECVD. *Electrochem. Solid-State Lett.*, **13** (3), H76.
 32. Weber, K.J., Jin, H., Zhang, C., *et al.*, (2009) Surface Passivation Using Dielectric Films: How Much Charge is Enough? *Proc. 24th EU-PVSEC*, (September), 534–537.
 33. McIntosh, K.R., Altermate, P.P., Altermatt, P.P., *et al.*, (2010) A freeware 1D emitter model for silicon solar cells. *Conf. Rec. IEEE 35th Photovolt. Spec. Conf.*, 2188–2193.
 34. Richter, A., Werner, F., Cuevas, A., *et al.*, (2012) Improved Parameterization of Auger Recombination in Silicon. *Energy Procedia*, **27**, 88–94.
 35. Schenk, A. (1998) Finite-temperature full random-phase approximation model of band gap narrowing for silicon device simulation. *J. Appl. Phys.*, **84** (7), 3684.
 36. Ostoja, P., Guerri, S., Negrini, P., and Solmi, S. (1984) The effects of phosphorus precipitation on the open-circuit voltage in *N*+/*P* silicon solar cells. *Sol. Cells*, **11** (1), 1–12.
 37. Min, B., Wagner, H., Dastgheib-Shirazi, A., *et al.*, (2014) Heavily doped Si: P emitters of crystalline Si solar cells: Recombination due to phosphorus precipitation. *Phys. Status Solidi - Rapid Res. Lett.*, **8** (8), 680–684.
 38. Hoex, B., Bosman, M., Nandakumar, N., and Kessels, W.M.M. (2013) Silicon surface

- passivation by aluminium oxide studied with electron energy loss spectroscopy. *Phys. status solidi - Rapid Res. Lett.*, **7** (11), 937–941.
39. Stesmans, A., and Afanas'ev, V. V. (2002) Si dangling-bond-type defects at the interface of (100)Si with ultrathin layers of SiO_x, Al₂O₃, and ZrO₂. *Appl. Phys. Lett.*, **80** (11), 1957.
 40. Saint-Cast, P., Heo, Y.-H., Billot, E., *et al.*, (2011) Variation of the layer thickness to study the electrical property of PECVD Al₂O₃ / c-Si interface. *Energy Procedia*, **8**, 642–647.
 41. Aberle, A.G., Glunz, S., and Warta, W. (1992) Impact of illumination level and oxide parameters on Shockley–Read–Hall recombination at the Si-SiO₂ interface. *J. Appl. Phys.*, **71** (9), 4422.
 42. Reichel, C., Granek, F., Hermle, M., and Glunz, S.W. (2011) Investigation of electrical shading effects in back-contacted back-junction silicon solar cells using the two-dimensional charge collection probability and the reciprocity theorem. *J. Appl. Phys.*, **109** (2), 24507.
 43. Silvaco Inc. Atlas Device Simulation Framework. *St. Clara, CA, USA*.
 44. McIntosh, K.R., and Black, L.E. (2014) On effective surface recombination parameters. *J. Appl. Phys.*, **116** (1), 14503.
 45. Black, L.E., Allen, T., McIntosh, K.R., and Cuevas, A. (2014) Effect of boron concentration on recombination at the *p*-Si–Al₂O₃ interface. *J. Appl. Phys.*, **115** (9), 93707.
 46. Aberle, A.G., Glunz, S., and Warta, W. (1993) Field effect passivation of high efficiency silicon solar cells. *Sol. Energy Mater. Sol. Cells*, **29** (2), 175–182.
 47. Dzierwior, J., and Schmid, W. (1977) Auger coefficients for highly doped and highly excited silicon. *Appl. Phys. Lett.*, **31** (5), 346–348.
 48. Klaassen, D.B.M. (1992) A unified mobility model for device simulation—I. Model equations and concentration dependence. *Solid. State. Electron.*, **35** (7), 953–959.

Addendum: integration of ALD SiO₂/Al₂O₃ stacks in industrial solar cells

The ALD SiO₂/Al₂O₃ stacks presented in this chapter have been explored for the simultaneous passivation of n^+ and p^+ Si surfaces of full-area (6-inch) n -type Si bifacial and IBC solar cells, see Fig. A1.

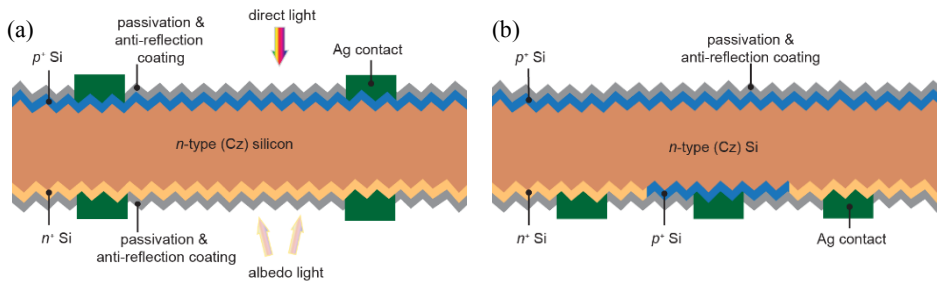


Figure A1 Schematics layout of (a) a n -type bifacial solar cell and (b) an interdigitated-back contact (IBC) cell concept, which are based on high-quality, Czochralski-grown n -type Si. The highly doped p^+ and n^+ Si regions are formed through diffusion of boron and phosphorus atoms in a horizontal tube furnace, respectively. Both sides of the cells comprise a random-pyramid texture and an anti-reflection and passivating coating.

For the bifacial solar cells, the random-pyramid (RP) textured, uniform p^+ Si front and n^+ Si rear surfaces were either simultaneously passivated by nitric acid oxidation (NAOS) or by an ALD SiO₂/Al₂O₃ stack (3nm SiO₂, 2 nm Al₂O₃). In both cases, a PE-CVD SiN_x layer was subsequently deposited on the two sides of the cells. The solar cells were finalized through the screen printing of silver paste, followed by a high temperature firing step. In addition, selected samples without silver paste were fired, which served as reference for minority carrier lifetime measurements. The resulting solar cell parameters are given in Table A1.

Table A1 The influence of the passivation scheme on the solar cell parameters of 6" bifacial n -type Si solar cells, measured under standard test conditions (25 °C, 1000 W/m², AM1.5g).

Passivation scheme	J_0 (fA/cm ²)	iV_{oc} (mV)	V_{oc} (mV)	J_{sc} (mA/cm ²)	FF (%)	η (%)
NAOS of both sides	189	664	650	38.9	76.7	19.4
ALD SiO ₂ /Al ₂ O ₃ on both sides	132	668	650	38.6	76.7	19.2

The ALD SiO₂/Al₂O₃ passivation scheme results in a conversion efficiency of 19.2%, demonstrating the feasibility of the passivation scheme. However, the achieved efficiency is 0.2% absolute lower than when using the NAOS reference. This loss can be attributed to a reduced J_{sc} , as the thickness of the SiN_x anti-reflection layer was not optimized. Lifetime measurements showed an improvement in iV_{oc} and J_0 for the ALD SiO₂/Al₂O₃ stacks compared to the NAOS reference passivation. Nevertheless, this gain did not result in a higher V_{oc} on finalized solar cells. The V_{oc} values are 14–18 mV lower than the iV_{oc} levels, which can be explained by a significant recombination channel associated with the contacting. Presumably this recombination is obscuring the gains from the improved surface passivation.

Additionally, on 6" diffused-junction IBC solar cells the SiO₂/Al₂O₃ passivation scheme has been investigated. The IBC cells comprise a RP textured p^+ Si front surface, and an RP-textured rear surface where n^+ and p^+ Si regions are interdigitated. Particularly, the following interface layers were compared;

1. NAOS of both sides
2. ALD SiO₂/Al₂O₃ on both sides
3. ALD Al₂O₃ on the front surface, NAOS of the rear surface.
4. ALD Al₂O₃ on both sides

After preparation, the interface layers were capped by PE-CVD SiN_x.

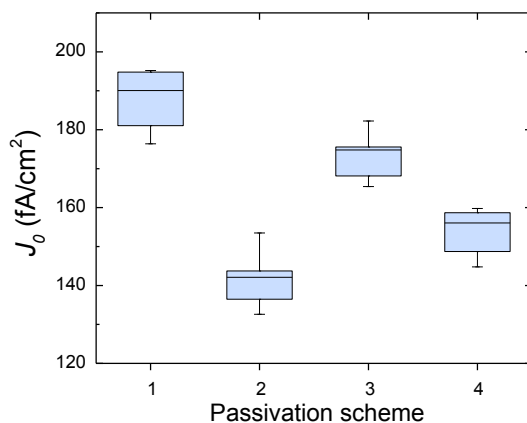


Figure A2 The total recombination in terms of J_0 at the front and rear side of the IBC lifetime samples for various interface layers.

Figure A2 shows the J_0 of fired, lifetime samples without metallization. The ALD $\text{SiO}_2/\text{Al}_2\text{O}_3$ stacks show the lowest J_0 values, indicating the highest levels of surface passivation. Nevertheless, as can be seen in Table A2, also for the IBC solar cells, nearly identical solar cell efficiencies of 18.6 – 18.8% were measured for all passivation schemes. Particularly, the obtained V_{oc} values of 624 – 626 mV are significantly lower than expected (i.e., ~680 mV) on the bases of the measured J_0 values for lifetime samples without metallization. Additionally, the fill factor of ~75 % is considerably lower than the pseudo fill factor of 79%. Therefore, it is expected that contact recombination and recombination at the pn -junction have to be addressed first to improve the efficiency, as will also be discussed in Chapter 7. Note however that the reduced J_0 values achieved for surface passivation by ALD $\text{SiO}_2/\text{Al}_2\text{O}_3$ imply an increased efficiency potential for the ALD $\text{SiO}_2/\text{Al}_2\text{O}_3$ stacks.

Table A2 Solar cell parameters of 6" diffused-junction n -type IBC solar cells for various passivation schemes, as measured under standard test conditions. The results of each data set are the average values of 4 - 6 cells.

Passivation scheme	V_{oc} (mV)	J_{sc} (mA/cm ²)	pFF (%)	FF (%)	η (%)
NAOS of both sides	624	39.8	78.9	74.9	18.6
ALD $\text{SiO}_2/\text{Al}_2\text{O}_3$ on both sides	626	40.0	79.2	75.1	18.8
ALD Al_2O_3 front, NAOS rear	626	39.8	79.0	75.1	18.7
ALD Al_2O_3 on both sides	626	39.8	78.8	75.1	18.7

CHAPTER 5

Understanding and Reducing Charge-Carrier Recombination at Highly Doped Crystalline Silicon Surfaces

Abstract Many crystalline silicon (c-Si) solar cell architectures rely on the surface passivation of their highly doped n - or p -type doped regions by dielectrics such as SiN_x and Al_2O_3 . In this work, the influence of the doping concentration near the c-Si surface on surface recombination is investigated for various passivation schemes which are relevant to homojunction solar cells. It was found that for passivation layers which provide field-effect passivation through a negative fixed interface charge, such as Al_2O_3 , the surface doping concentration of p^+ Si has a negligible influence on the surface saturation current density J_{0s} . However, in case this negative fixed charge is absent, surface recombination can be suppressed by a high p^+ Si surface doping concentration, provided that the high doping levels do not cause a deterioration of the interface properties. This finding was subsequently used to improve recombination at boron doped Si surfaces passivated by SiN_x or $\text{SiO}_2/\text{Al}_2\text{O}_3$ stacks. By removal of the boron-depletion region near the surface through a short wet-chemical etch, the concentration of boron dopants at the surface could be increased. This resulted in a reduced surface recombination for passivation schemes which do not provide field-effect passivation on p^+ Si through a negative Q_f , such as for $\text{SiO}_2/\text{Al}_2\text{O}_3$ stacks and SiN_x films.

5.1 Introduction

Homojunction silicon solar cells, such as passivated emitter and rear cell (PERC), and passivated emitter, rear totally diffused (PERT) solar cells, but also more novel concepts such as TOPCon[1], rely on the outstanding passivation of defect states at the surface of the highly doped p^+ or n^+ Si regions, which are conventionally termed “emitter” or “back-surface field”. However, the optimization of the doped regions and their surfaces is not straightforward, as highly doped regions fulfil several functions. Specifically, the highly doped Si regions make the contacting metal grid selective for the extraction of either electrons or holes, and ensures a low contact resistance. In between the metal contacts, the doped-regions serve as lateral conduction pathway for charge carriers, albeit at the expense of Auger recombination and free-carrier absorption which are both induced by a high doping concentration. The diffusion processes used to prepare the highly doped regions also result in gettering of impurities from the c-Si bulk. On top of that, the highly doped regions influence charge-carrier recombination at the passivated surface, as will be discussed below.

Due to the many different requirements the highly doped regions have to fulfil, and due the strong influence of these regions on the conversion efficiency, there is an ongoing trend to use tailored highly doped regions in c-Si solar cells. However, when precisely tuning the dopant concentration and profiles of highly doped regions through e.g., an etch back of the doped regions,[2] through the creation of ‘(area-) selective emitters’,[1] or by epitaxially-grown base materials,[3] it is imperative to understand how charge-carrier recombination at the passivated doped surface is affected by the local dopant concentration.

The influence of the doping level on surface passivation has been subject of research already for a long time in the photovoltaic community.[4–12] The charge-carrier recombination which takes place within the highly doped region and at its passivated surface is often described by reporting the recombination parameter of the highly doped region J_0 , or implied open-circuit voltage iV_{oc} , which both are experimentally accessible through e.g., photoconductance decay (PCD) measurements. However, neither of these two parameters solely relate to surface recombination, as they also account for recombination pathways within the highly doped region itself. Additionally, also the transport of minority carriers through the highly doped region affects the surface recombination. Therefore, to isolate the effects of the surface-doping concentration N_s on

the surface recombination, the effective surface recombination velocity S_{eff} is often extracted from the measured J_0 or iV_{oc} values by numerical simulations.[4–9,12] From such analysis, it is typically observed that S_{eff} strongly increases as a function of N_s for phosphorus-doped surfaces passivated by SiN_x or SiO_2 , [6–8] and for boron-doped surfaces passivated by Al_2O_3 . [9,12] This increase in S_{eff} with N_s seems to suggest that the quality of surface passivation deteriorates at higher surface doping concentrations. However, in recent publications by Black and McIntosh *et al.*, [9,13] the increase in S_{eff} with N_s could be fully attributed to ‘an artefact of its derivation’ for Al_2O_3 on p^+ Si. In their publications, it was shown that S_{eff} by definition depends on N_s or the excess carrier concentration Δn , even when the surface passivation quality (e.g., in terms of interface parameters such as interface defect density N_{it} and fixed charge density Q_f) remains unchanged. Specifically, they showed that the surface passivation quality in terms of Q_f and S_{n0} (the latter being the fundamental surface recombination velocity for electrons) provided by Al_2O_3 films are *independent* of the boron doping concentration at the surface, at least for $N_s \leq 3 \cdot 10^{19} \text{ cm}^{-3}$. Even though the interface quality provided by the surface passivation scheme (such as expressed in terms of Q_f and S_{n0} etc.) is thus not necessarily dependent on N_s , it is important to note that the charge-carrier rate at the surface, which can be expressed by the parameter surface saturation current density J_{0s} , still depends on N_s , [13] as is the topic of this work.

In this Chapter, it is evaluated how charge-carrier recombination at the surface is affected by the surface doping concentration for phosphorus and boron doped surfaces for various passivation schemes. The structure of this work is as follows: First, the recombination rate at highly doped surfaces is theoretically evaluated for various fixed-charge densities Q_f and surface doping concentrations N_s . Next, the recombination at p^+ and n^+ Si surfaces is experimentally addressed for several passivation schemes (including results from literature), such as plasma-enhanced atomic layer deposited (PE-ALD) Al_2O_3 , PE-ALD $\text{SiO}_2/\text{Al}_2\text{O}_3$ stacks, plasma-enhanced chemical vapor deposited (PE-CVD) SiN_x and thermally-grown SiO_2 . Finally, it will be shown that the recombination at p^+ Si surfaces can be reduced for some passivation schemes by increasing the surface doping concentration.

5.2 Theoretical evaluation of recombination at the highly doped surface

The recombination parameter of the highly doped region, J_0 , can be expressed as the sum of the parameters related to recombination at the surface and to recombination within the highly doped region, i.e., Auger, radiative, and Shockley-Read-Hall (SRH) recombination;

$$J_0 = J_{0,surface} + J_{0,Auger} + J_{0,radiative} + J_{0,SRH} \quad (1)$$

Note that the different recombination pathways are in first order independent of each other. In practice, for many passivated highly doped regions, transport of minority carriers through the highly doped region does not limit the surface recombination, and the doped region is called ‘transparent’ [14]. Then, the quasi-Fermi levels are approximately flat throughout the highly doped region, and $J_{0,surface}$ equals the so-called surface saturation current density $J_{0,surface} \approx J_{0s}$. In Appendix A, it is discussed in more detail when this approximation holds and what the consequences are in case it does not hold. In the remaining of this section, for simplicity first p^+ Si surfaces are discussed. For passivated highly p -type doped surfaces (e.g., with $N_s > 10^{17} \text{ cm}^{-3}$), J_{0s} can be approximated using the Shockley-Read-Hall equation for a single defect level as [13]

$$J_{0s} = qS_{n0} \frac{n_{i,eff}^2}{p_s} \quad (2)$$

In this expression, q is the elementary charge, p_s the hole concentration at the surface and $n_{i,eff}$ the effective intrinsic carrier concentration at the surface. Note that the last term is labelled ‘effective’ as it accounts for the effects of band gap narrowing and Fermi-Dirac statistics on the density of charge carriers.

From equation (2), it can be seen that two strategies can be used to minimize J_{0s} : First of all, S_{n0} can be lowered, e.g., by reducing the interface defect density, which is referred to as *chemical* passivation. Secondly, the majority carrier (i.e., hole) concentration at the surface, p_s can be increased, for instance by a negative fixed-charge density in the passivation scheme, which provides *field-effect* passivation.

To evaluate the influence of the doping density on J_{0s} , in the remaining of this section it is assumed that S_{n0} and Q_f are independent of the doping concentration (as has been verified for Al_2O_3 on p^+ Si [9]). $n_{i,eff}^2$ is calculated as a function of doping density using Fermi-Dirac statistics, using the intrinsic carrier density of $n_i = 9.65 \times 10^9 \text{ cm}^{-3}$ at

300 K,[15] and the empirical band gap narrowing (BGN) model from Yan and Cuevas,[16] that is determined for boron-doped Si and which is consistent with Fermi-Dirac statistics. p_s is numerically evaluated for various Q_f values using the approach of Girisch,[17] with Fermi-Dirac statistics and under the assumption that the quasi-Fermi levels and the doping concentration are constant throughout the space-charge region. It was verified that p_s was for the investigated range of fixed charge densities independent of the minority carrier density in the c-Si bulk $<10^{16} \text{ cm}^{-3}$, for a bulk doping density (whether n - or p -type) $<10^{16} \text{ cm}^{-3}$.

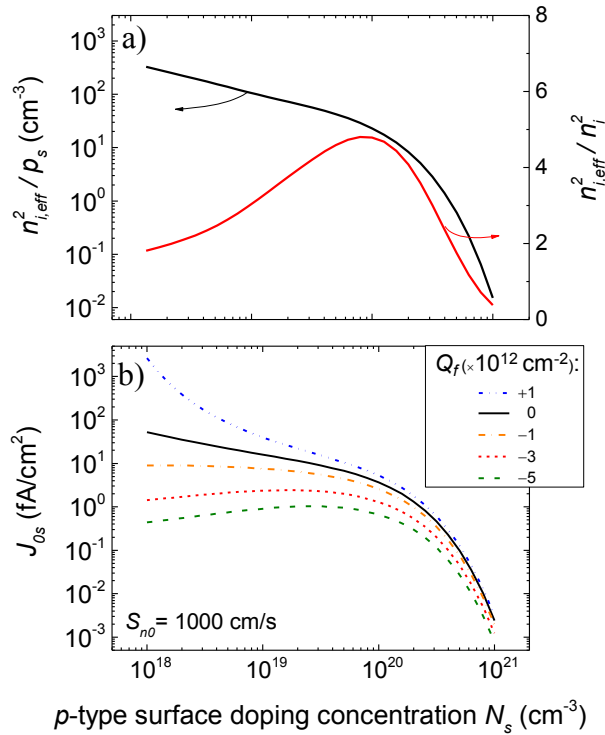


Figure 1 (a) The normalized effective intrinsic carrier density $n_{i,eff}^2 / n_i^2$ as function of the active p -type doping concentration at the c-Si surface. $n_{i,eff}$ is derived by taking into account Fermi-Dirac statistics, $n_i = 9.65 \times 10^9 \text{ cm}^{-3}$ at 300 K,[15] and the band gap narrowing model of Ref.[16]. Also the last term of Eq. (2), i.e., $n_{i,eff}^2 / p_s$, is indicated for the case that $Q_f = 0$. (b) J_{0s} for $-5 \times 10^{12} \leq Q_f \leq 1 \times 10^{12} \text{ cm}^{-2}$, as evaluated from Eq. 2 for a fixed level of $S_{n0} = 1000 \text{ cm/s}$.

First, the case is considered that the passivation layer has no fixed charge density; $Q_f = 0$. In this case, p_s is approximately given by the active p -type doping concentration at the surface: $p_s \approx N_s$. As can be seen in Fig. 1a, the normalized effective intrinsic carrier density $n_{i,eff}^2 / n_i^2$ first increases with N_s , which can be attributed to band gap narrowing (BGN). For $N_s > 9 \times 10^{20} \text{ cm}^{-3}$ however (doping levels which in practice might be hard to achieve for p -type Si), $n_{i,eff}^2 / n_i^2$ is strongly reduced –despite of the increasing BGN– as a consequence of Fermi-Dirac statistics. The last term of Eq. 2, i.e., $n_{i,eff}^2 / p_s$, in case of $Q_f = 0$ reduces however monotonically with increasing N_s , most prominently for degenerate doping $N_s > 10^{20} \text{ cm}^{-3}$. Therefore, as can be seen in Fig. 1b, it can be concluded that a high N_s reduces the surface recombination prefactor J_{0s} for $Q_f = 0$ and a constant level of S_{n0} . Even though a high surface doping concentration thus can be beneficial to reduce surface recombination, this effect is often not observed throughout literature as Auger recombination typically increases with higher doping levels. Nonetheless, for ‘tuned’ highly doped regions, there are regimes where the surface doping concentration can be increased without inducing additional Auger recombination, as will for instance be demonstrated in Section 5.4. Note, that the degeneracy effects which are observed for $N_s > 10^{20} \text{ cm}^{-3}$ also have large implications for the recombination parameter of highly doped regions which are contacted by metal, as is discussed in Appendix B.

Next, more practical cases, where a fixed charge is present in the passivation scheme (i.e., $Q_f \neq 0$), are discussed. As can be seen in Fig. 1b, for p -type doped surfaces, a negative Q_f reduces J_{0s} due to field-effect passivation. For negative Q_f values of -5 to $-1 \cdot 10^{12} \text{ cm}^{-2}$, J_{0s} shows only a limited dependence on the surface doping concentration for $N_s < 10^{20} \text{ cm}^{-3}$. For $N_s > 10^{20} \text{ cm}^{-3}$ however, J_{0s} also in these cases sharply decreases due to the strong decrease in $n_{i,eff}$. The effect of either positive or negative fixed charges becomes less pronounced at higher N_s . For positive Q_f values, J_{0s} monotonically decreases with N_s , indicating that also in that case a high surface doping concentration reduces surface recombination. Finally, note that for high J_{0s} values, surface recombination can become limited by the diffusion of minority carriers towards the surface, and $J_{0s} > J_{0,surface}$ (see Appendix A).

For highly doped n^+ Si surfaces, similar results are obtained as for p^+ Si surfaces, with as key difference that on n -type Si, a passivation scheme with a *positive* Q_f provides field-effect passivation. Moreover, in practice generally higher surface doping concentrations

can be obtained for n^+ Si than for p^+ Si. This difference in surface doping can be attributed to a higher solubility of phosphorus than of boron dopants in c-Si, i.e., $\sim 1 \cdot 10^{21} \text{ cm}^{-3}$ for phosphorus,[18] compared to $\sim 2 \cdot 10^{20} \text{ cm}^{-3}$ for boron,[19] (the exact numbers depend on the diffusion temperature). In addition, the diffusion of phosphorus generally results in a relatively high concentration of dopants near the c-Si surface, whereas boron diffusions result in a characteristic dip in concentration of dopants near the surface,[20] due different redistribution of B and P dopants at the advancing Si/SiO₂ interface during oxidation.[20] In Section 5.4, we show how the actual surface doping concentration of B can be increased.

5.3 Empirical evaluation of recombination at the highly doped surface

The results in the previous section were derived under the assumptions that the fixed charge density and chemical passivation levels provided by the passivation scheme are independent of the surface doping concentration. Nonetheless, in practice, these two assumptions are not necessarily valid for all surface passivation schemes. Therefore, in Fig. 2, J_{0s} is evaluated for boron- and phosphorus-doped surfaces which are passivated by commonly used thin films. Specifically, in Fig. 2a, J_{0s} is extracted from measured J_0 values reported Ref.[21] for planar boron-doped Si (100) surfaces passivated by PE-ALD Al₂O₃. J_{0s} was extracted from simulations of the dopant profiles by EDNA2,[22] taking into account ECV dopant profiles, Fermi-Dirac statistics, the BGN model for p^+ Si of Yan and Cuevas,[16] the Auger parameterization of Richter,[23] and the Klaassen mobility model[24] (Note that some samples resulted in negative J_{0s} values and were therefore discarded). Additionally, for comparison, in this work textured p^+ Si samples were passivated by PE-ALD SiO₂/Al₂O₃ stacks (comprising $\sim 4 \text{ nm}$ SiO₂ and 30 nm Al₂O₃), which provide a high level of chemical passivation but which do not entail a negative fixed charge density.[25–28] In Fig. 2b, J_{0s} was derived for phosphorus doped surfaces passivated by thermally-grown SiO₂ or plasma-enhanced chemical vapor deposited SiN_x from the parameterizations of $S_{p0}(N_s)$ derived by Altermatt *et al.*,[7]. These parameterizations in Ref.[7] were obtained from careful modeling of experimentally obtained J_0 values from Refs. [5,6], using the theoretical BGN model of Schenk,[29] and Fermi-Dirac statistics.

The results in Fig. 2a are in qualitative agreements with J_{0s} values derived from Eq. 2 for $Q_f = -5 \cdot 10^{12} \text{ cm}^{-2}$ and $S_{n0} = 12000 \text{ cm/s}$ for PE-ALD Al₂O₃ and $Q_f = 0$ and $S_{n0} = 6500 \text{ cm/s}$ for SiO₂/Al₂O₃ stacks. The results for SiO₂/Al₂O₃ stacks indicate that for

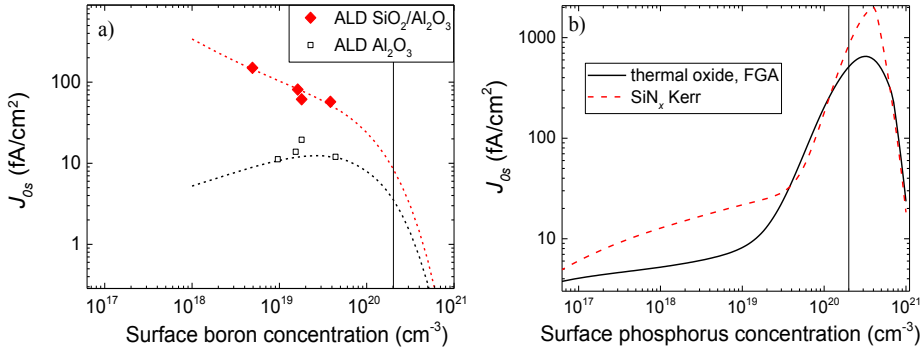


Figure 1 a) J_{0s} for planar, boron-doped p^+ Si passivated by PE-ALD Al_2O_3 and PE-ALD $\text{SiO}_2/\text{Al}_2\text{O}_3$ passivation stacks. The vertical line depicts the solid solubility of boron in Si. The dashed lines are evaluations of Eq. 2 for $Q_f = -5 \cdot 10^{12} \text{ cm}^{-2}$ and $S_{n0} = 12000 \text{ cm/s}$ for PE-ALD Al_2O_3 and $Q_f = 0$, $S_{n0} = 6500 \text{ cm/s}$ for $\text{SiO}_2/\text{Al}_2\text{O}_3$ stacks. b) J_{0s} derived from the parameterizations of S_{p0} from Altermatt *et al.*, [7]. The S_{p0} parameterizations were derived from experimental results of PE-CVD SiN_x from Kerr *et al.*, [6] and thermal SiO_2 after forming gas anneal (FGA) from Refs. [4–6] on planar phosphorus doped n^+ Si. The n -type equivalent of Eq. (2) was used for the derivation of J_{0s} , where the electron density at the surface was calculated while taking the fixed charge of SiO_2 ($Q_f = 7 \times 10^{10} \text{ cm}^{-3}$) and SiN_x ($Q_f = 2 \times 10^{11} \text{ cm}^{-3}$) into account. Note that the S_{p0} parameterizations was fitted to experimental results for $N_s < 2 \times 10^{20} \text{ cm}^{-3}$, as is indicated by the vertical line. The extrapolated S_{p0} values for $N_s > 2 \times 10^{20} \text{ cm}^{-3}$ on the rights side of the vertical line were limited to the thermal velocity of electrons and holes.

boron-doped surfaces, a high doping concentration at the surface helps in minimizing surface recombination in case of no (significant) negative Q_f is present, such as for passivation by $\text{SiO}_2/\text{Al}_2\text{O}_3$ passivation.

The results of Fig. 2b show a completely different trend, which is attributed to the strongly increasing S_{p0} for increasing surface doping levels. Note, that the mechanisms for this change in S_{p0} are beyond the scope of this work. For the SiN_x as well as the SiO_2 , the J_{0s} is only slightly dependent on the surface doping level for $N_s < 10^{19} \text{ cm}^{-3}$. For higher surface doping concentrations $\sim 10^{19} < N_s < 4 \cdot 10^{20} \text{ cm}^{-3}$ however, J_{0s} increases strongly with N_s due to the increasing S_{p0} . For these high J_{0s} values, the surface recombination will be diffusion limited (see Appendix A). When extrapolating the parameterizations of Altermatt *et al.*, for $N_s > 4 \cdot 10^{20} \text{ cm}^{-3}$, it is expected that J_{0s} will again strongly reduce, even though S_{p0} is at its maximum value and equals the thermal velocity of holes, $S_{p0} \sim 1.5 \times 10^7 \text{ cm/s}$. Note however that no measurements are available yet which support this hypothesis.

5.4 Reducing recombination at boron-doped surfaces

In previous sections, it was shown that a high concentration of boron at the surface can in some cases be beneficial to reduce surface recombination, such as for passivation layers which do not provide field-effect passivation through a negative fixed charge density. In this section, this insight will be used to reduce charge carrier recombination at boron doped surfaces.

Most boron doped regions typically have a rather low concentration of boron near the surface,[10,30–32] i.e., a concentration which is much lower than the (maximum) solid solubility limit of B in Si of $\sim 2 \times 10^{20} \text{ cm}^{-3}$. [19] This near-surface region of low doping concentration we term the ‘boron-depletion region’ (BDR). An example of a BDR of a typical boron-dopant profile prepared by diffusion of boron from a boron silicate glass is given in Fig. 3. The BDR is formed by a redistribution of boron atoms at the advancing Si/SiO₂ interface during thermal oxidation of c-Si.[20] This oxidation is required to avoid or (when formed) to remove the boron-rich layer (BRL) at the surface. This BRL prevents the passivation of the surface,[21,33] and can reduce the lifetime of the Si bulk.[34]

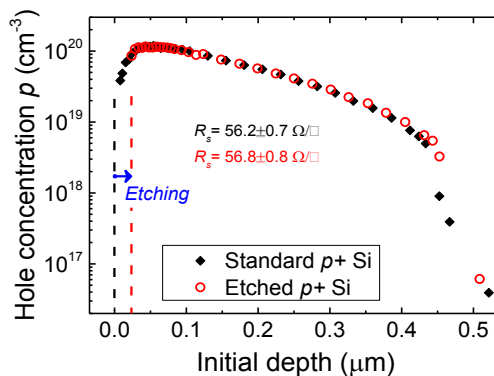


Figure 3 Electrochemical capacitance-voltage (ECV) measurements of the (equilibrium) hole concentration in the highly doped regions before and after wet-chemical etch. In a standard p^+ Si region, a characteristic decrease in hole-concentration near the surface is observed, the *boron-depletion region*. The corresponding sheet resistances of boron-diffused textured wafers are measured by four point probe.

In Fig. 3, the BDR of a p^+ Si surface is (partly-) removed through a well-controlled wet chemical etch of the doped surface, to increase the surface doping concentration, as was also previously reported in Refs.[2,35]. As a result of the etch, the equilibrium hole density near the surface of the textured p^+ Si samples is increased from $\sim 3.8 \times 10^{19}$ to

$8.6 \times 10^{19} \text{ cm}^{-3}$. Note that the sheet resistance is virtually not affected by the etch and only increases from 56.2 to 56.8 Ω/\square . This therefore implies that most of the functions of the highly doped region, such as lateral conduction of holes, and the contact screening, are virtually not affected by the etch.

Table 1 Overview of the interface defect density D_{it} and the fixed charge density Q_f of several passivation schemes as obtained on planar n -type c -Si (100) surfaces (3 Ohmcm, undiffused), as measured by COCOS (Corona Oxide Characterization of Semiconductors).

<i>Passivation scheme</i>	$Q_f (\cdot 10^{12} \text{ cm}^{-2})$	$D_{it} (\cdot 10^{11} \text{ eV}^{-1} \text{ cm}^{-2})$
PE-ALD Al_2O_3	-5.0	4.5
Thermal ALD Al_2O_3	-2.3	1.6
PE-ALD $\text{SiO}_2/\text{Al}_2\text{O}_3$	-0.5	3.0
PE-CVD SiN_x	3.1	17

Next, the p^+ Si regions, which were present on both sides of symmetrical, textured lifetime samples, were passivated by plasma-enhanced ALD (PE-ALD) Al_2O_3 , thermal ALD Al_2O_3 , PE-ALD $\text{SiO}_2/\text{Al}_2\text{O}_3$ stacks or PE-CVD SiN_x . An overview of the interface properties of these passivation materials, as measured on planar undiffused n -type Si (100) wafers, is given in Table 1. The J_0 of the p^+ Si regions was measured from quasi-steady state photoconductance decay measurements using the method of Kane and Swanson.[36] J_0 was divided by a factor 1.7 to account for the increase in surface area after random pyramid texturing. Note that the values of Fig. 4 are slightly higher than previously reported values on similar surfaces (see e.g., Chapter 4) due to a difference in quality of hydrofluoric acid dip, which was carried out before employing the passivation scheme.

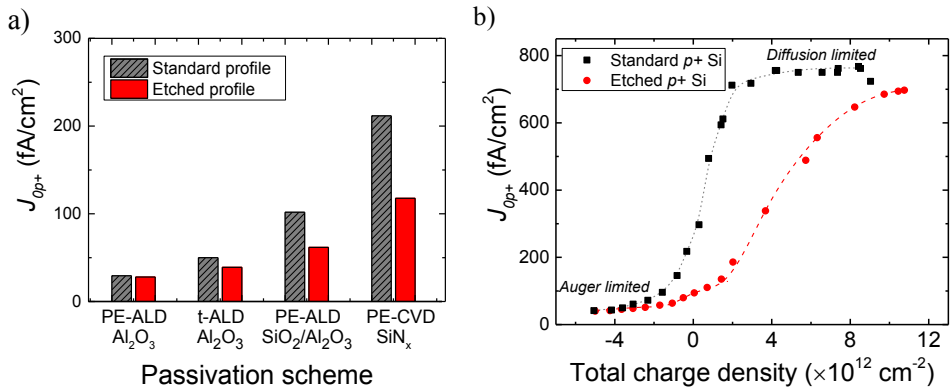


Figure 4 (a) The recombination parameter J_{0p^+} for the textured, boron doped regions of Fig. 3 passivated by PE-ALD Al₂O₃, thermal-ALD Al₂O₃, PE-ALD SiO₂/Al₂O₃, and PE-CVD SiN_x with and without removal of the boron-depletion region. (b) The net charge density p^+ Si region with and without BDR etch and passivated by PE-ALD Al₂O₃ was varied by corona charging for p^+ Si, starting from a negative Q_f which was present in the Al₂O₃ layer of -5×10^{12} cm⁻³. The J_0 values in (a) and (b) are divided by a factor 1.7 to account for the increase in surface area due to the random-pyramid texture.

In Fig. 4a, the passivation results are given for p^+ Si surfaces with or without etch of the BDR. As can be seen, J_0 decreases in particular significantly after etch of the BDR for the SiO₂/Al₂O₃ and the SiN_x passivation schemes, whereas the J_0 is only slightly reduced for thermal Al₂O₃. For PE-ALD, virtually no change in J_0 is visible. This is consistent with the expectations of Fig. 1b, where a high doping density was proven to be beneficial for passivation schemes which do not exhibit a large negative Q_f . Note that no significant difference in Auger, bulk SRH or radiative recombination is expected between the two doping profiles of Fig. 3. Therefore, etching the BDR shows to be an effective way to reduce surface recombination for passivation schemes which do not entail a negative fixed charge density.

To gain even deeper insights in the change in passivation between the two doped regions of Fig. 3, positive corona charging was employed on both sides of the p^+ Si samples that were passivated by PE-ALD Al₂O₃. As a result, the total charge density of the stack was varied from strongly negative ($Q_f \sim -5 \cdot 10^{12}$ cm⁻²) to highly positive, as is depicted in Fig. 4b. It can be seen that the surface recombination for the passivation scheme that does not entail a strong negative fixed charge density is strongly reduced after etching the BDR. This once again confirms that having a high boron doping concentration at the surface can in some cases be beneficial to reduce surface recombination.

5.5 Conclusions

Charge-carrier recombination at the surface of highly doped silicon regions depends, besides on the level of chemical passivation, also on the local electron and hole densities. By isolating surface recombination from other recombination pathways in the highly doped region, the influence of surface doping concentration on surface recombination parameter J_{0s} is examined for passivation schemes with various fixed charge densities.

For p^+ Si, the J_{0s} results for ALD Al_2O_3 and $\text{SiO}_2/\text{Al}_2\text{O}_3$ stacks are in line with theoretical expectations based on SRH statistics for fixed levels of S_{n0} and Q_f , as has been observed previously for Al_2O_3 [9]. For passivation layers which provide field-effect passivation on p^+ Si, such as Al_2O_3 , the boron doping concentration at the surface is found to be of negligible influence on J_{0s} . However, in case such field-effect passivation provided by a fixed charge in the passivation scheme is absent, such as for $\text{SiO}_2/\text{Al}_2\text{O}_3$ stacks, a high surface doping concentration can be beneficial to suppress surface recombination. It was demonstrated that the concentration of boron dopants at the surface can be increased by the removal of a boron-depletion region near the surface through a short wet-chemical etch. This reduces surface recombination for passivation schemes without negative Q_f , such as $\text{SiO}_2/\text{Al}_2\text{O}_3$ stacks and SiN_x films. For n^+ Si, increasing the surface doping concentration does not reduce J_{0s} for PE-CVD SiN_x and thermal SiO_2 , as the chemical passivation (i.e., S_{p0}) was found in Ref.[7] and references therein to deteriorate significantly at higher surface doping levels.

The method described in this work provides more insight into how the surface doping concentration affects the recombination at the passivated surfaces. This is particularly useful for the optimization of passivated highly doped regions for c-Si solar cells. The great level of control in dopant distribution, as enabled in emerging technologies such as epitaxially-grown Si, are expected to be of great advantage in such further optimization of highly doped regions.

Acknowledgements

Dr. G. J. M. Janssen, dr. I. G. Romijn, M. Koppes and J. Liu, from ECN Solar Energy, N. Nandakumar from SERIS and C. A. A. van Helvoirt, R. J. van Gils, dr. S. Smit from the Eindhoven University of Technology are gratefully acknowledged for experimental support and fruitful discussions. We are grateful for financial support from the Dutch Ministry of Economic Affairs, via the Top Sector Alliance for Knowledge and Innovation (TKI) programs *Antilope* and *Advanced Nanolayers*.

References

1. Glunz, S.W., Feldmann, F., Richter, A., *et al.*, (2015) The Irresistible Charm of a Simple Current Flow Pattern – 25 % With a Solar Cell Featuring a Full-Area Back Contact. *Proc. 31st EU-PVSEC Hambg.*, 259–263.
2. van de Loo, B. W. H., Dingemans, G., Granneman, E.H.A., *et al.*, (2014) Advanced front-surface passivation schemes for industrial *n*-type silicon solar cells. *Photovoltaics Int.*, **24**, 43–50.
3. Hao, R., Ravi, T.S., Siva, V., *et al.*, (2016) Kerfless Epitaxial Mono Crystalline Si Wafers With Built-in Junction And From Reused Substrates For High Efficiency PERx Cells. *Proc. 43rd IEEE Photovoltaics Spec. Conf.*, 6–8.
4. Cuevas, A., Basore, P.A., Giroult-Matlakowski, G., and Dubois, C. (1996) Surface recombination velocity of highly doped *n*-type silicon. *J. Appl. Phys.*, **80** (6), 3370–3375.
5. King, R.R., Sinton, R.A., and Swanson, R.M. (1990) Studies of diffused phosphorus emitters: saturation current, surface recombination velocity, and quantum efficiency. *IEEE Trans. Electron Devices*, **37** (2), 365–371.
6. Kerr, M.J., Schmidt, J., Cuevas, A., and Bultman, J.H. (2001) Surface recombination velocity of phosphorus-diffused silicon solar cell emitters passivated with plasma enhanced chemical vapor deposited silicon nitride and thermal silicon oxide. *J. Appl. Phys.*, **89** (7), 3821.
7. Altermatt, P.P., Schumacher, J.O., Cuevas, A., *et al.*, (2002) Numerical modeling of highly doped Si:P emitters based on Fermi-Dirac statistics and self-consistent material parameters. *J. Appl. Phys.*, **92** (2002), 3187–3197.
8. Min, B., Wagner, H., Dastgheib-Shirazi, A., *et al.*, (2014) Heavily doped Si: P emitters of crystalline Si solar cells: Recombination due to phosphorus precipitation. *Phys. Status Solidi - Rapid Res. Lett.*, **8** (8), 680–684.
9. Black, L.E., Allen, T., McIntosh, K.R., and Cuevas, A. (2014) Effect of boron concentration on recombination at the *p*-Si–Al₂O₃ interface. *J. Appl. Phys.*, **115** (9), 93707.
10. Richter, A., Benick, J., and Hermle, M. (2013) Boron Emitter Passivation With Al₂O₃ and Al₂O₃/SiN_x Stacks Using ALD Al₂O₃. *Photovoltaics, IEEE J.*, **3** (1), 236–245.
11. Richter, A., Benick, J., Kimmerle, A., *et al.*, (2014) Passivation of phosphorus diffused silicon surfaces with Al₂O₃: Influence of surface doping concentration and thermal activation treatments. *J. Appl. Phys.*, **116** (24), 243501.
12. Hoex, B., Schmidt, J., Bock, R., *et al.*, (2007) Excellent passivation of highly doped *p*-type Si surfaces by the negative-charge-dielectric Al₂O₃. *Appl. Phys. Lett.*, **91** (11), 112107.
13. McIntosh, K.R., and Black, L.E. (2014) On effective surface recombination parameters. *J. Appl. Phys.*, **116** (1), 14503.
14. del Alamo, J.A., and Swanson, R.M. (1984) The physics and modeling of heavily doped emitters. *IEEE Trans. Electron Devices*, **31** (12), 1878–1888.
15. Altermatt, P.P., Schenk, A., Geelhaar, F., and Heiser, G. (2003) Reassessment of the intrinsic carrier density in crystalline silicon in view of band-gap narrowing. *J. Appl. Phys.*, **93** (3), 1598.
16. Yan, D., and Cuevas, A. (2014) Empirical determination of the energy band gap narrowing in *p+* silicon heavily doped with boron. *J. Appl. Phys.*, **116** (19), 194505.
17. Girisch, R.B.M., Mertens, R., and Keersmaecker, R.F. (1988) Determination of Si-SiO₂ interface recombination parameters using a gate-controlled point-junction diode under illumination. *IEEE Electron Devices*, **35** (2), 203-222
18. Kooi, E. (1964) Formation and Composition of Surface Layers and Solubility Limits of Phosphorus During Diffusion in Silicon. *J. Electrochem. Soc.*, **111** (12), 1383.
19. Vick, G.L., and Whittle, K.M. (1969) Solid Solubility and Diffusion Coefficients of Boron

- in Silicon. *J. Electrochem. Soc.*, **116** (8), 1142.
20. Grove, A.S., Leistikio, O., and Sah, C.T. (1964) Redistribution of Acceptor and Donor Impurities during Thermal Oxidation of Silicon. *J. Appl. Phys.*, **35** (9), 2695.
 21. Mok, K.R.C., van de Loo, B.W.H., Vlooswijk, A.H.G., *et al.*, (2015) Boron-Doped Silicon Surfaces From B₂H₆ Passivated by ALD Al₂O₃ for Solar Cells. *IEEE J. Photovoltaics*, **5** (5), 1310–1318.
 22. McIntosh, K.R., Altermate, P.P., Altermatt, P.P., *et al.*, (2010) A freeware 1D emitter model for silicon solar cells. *Conf. Rec. IEEE 35th Photovolt. Spec. Conf.*, 2188–2193.
 23. Richter, A., Glunz, S.W., Werner, F., *et al.*, (2012) Improved quantitative description of Auger recombination in crystalline silicon. *Phys. Rev. B*, **86** (16), 165202.
 24. Klaassen, D.B.M. (1992) A unified mobility model for device simulation—I. Model equations and concentration dependence. *Solid. State. Electron.*, **35** (7), 953–959.
 25. Dingemans, G., van Helvoirt, C.A.A., Pierreux, D., *et al.*, (2012) Plasma-Assisted ALD for the Conformal Deposition of SiO₂. *J. Electrochem. Soc.*, **159** (3), H277–H285.
 26. van de Loo, B.W.H., Knoops, H.C.M., Dingemans, G., *et al.*, (2015) “Zero-charge” SiO₂/Al₂O₃ stacks for the simultaneous passivation of *n*+ and *p*+ doped silicon surfaces by atomic layer deposition. *Sol. Energy Mater. Sol. Cells*, **143**, 450–456.
 27. Dingemans, G., Terlinden, N.M., Verheijen, M.A., *et al.*, (2011) Controlling the fixed charge and passivation properties of Si(100)/Al₂O₃ interfaces using ultrathin SiO₂ interlayers synthesized by atomic layer deposition. *J. Appl. Phys.*, **110** (9), 93715.
 28. Terlinden, N.M., Dingemans, G., Vandalon, V., *et al.*, (2014) Influence of the SiO₂ interlayer thickness on the density and polarity of charges in Si/SiO₂/Al₂O₃ stacks as studied by optical second-harmonic generation. *J. Appl. Phys.*, **115** (3), 33708.
 29. Schenk, A. (1998) Finite-temperature full random-phase approximation model of band gap narrowing for silicon device simulation. *J. Appl. Phys.*, **84** (7), 3684.
 30. Saint-Cast, P., Richter, A., Billot, E., *et al.*, (2012) Very low surface recombination velocity of boron doped emitter passivated with plasma-enhanced chemical-vapor-deposited AlO_x layers. *Thin Solid Films*, **522**, 336–339.
 31. Lin, F., and Duttagupta, S. (2012) Excellent Passivation of *p*+ Silicon Surfaces by Inline Plasma Enhanced Chemical Vapor Deposited SiO_x/AlO_x Stacks. *Japanese J. ...*, **51**, 17–19.
 32. Nursam, N.M., Ren, Y., and Weber, K.J. (2010) PECVD Silicon Nitride Passivation on Boron Emitter: The Analysis of Electrostatic Charge on the Interface Properties. *Adv. Optoelectron.*, **2010**, 1–8.
 33. Phang, S.P., Liang, W., Wolpensinger, B., *et al.*, (2013) Tradeoffs between impurity gettering, bulk degradation, and surface passivation of boron-rich layers on silicon solar cells. *IEEE J. Photovoltaics*, **3** (1), 261–266.
 34. Kessler, M.A., Ohrdes, T., Wolpensinger, B., and Harder, N.-P. (2010) Charge carrier lifetime degradation in Cz silicon through the formation of a boron-rich layer during BBr₃ diffusion processes. *Semicond. Sci. Technol.*, **25** (5), 55001.
 35. Janssen, G.J.M., Koppes, M., Komatsu, Y., *et al.*, (2014) Front Side Improvements for *n*-Pasha Solar Cells. *29th Eur. Photovolt. Sol. Energy Conf. Exhib.*, 812-815
 36. Kane, D.E., and Swanson, R.M. (1985) Measurement of the emitter saturation current by a contactless photoconductivity decay method. *IEEE Photovolt. Spec. Conf. 18*, **69**, 578–583.
 37. Cuevas, A., and Yan, D. (2013) Misconceptions and misnomers in solar cells. *IEEE J. Photovoltaics*, **3** (2), 916–923.
 38. Feldmann, F., Simon, M., Bivour, M., *et al.*, (2014) Efficient carrier-selective *p*- and *n*-contacts for Si solar cells. *Sol. Energy Mater. Sol. Cells*, **131**, 100–104.

Appendix A. The relation of surface recombination and J_0

The parameter $J_{0,surface}$ represents the contribution of surface recombination to the recombination parameter of the highly doped region J_0 , as can be seen in Eq. 1. Specifically, $J_{0,surface}$ relates the charge-carrier recombination rate at the surface, $U_{surface}$, to the charge-carrier densities at the base side of the highly doped region (at position $x=W^-$)

$$qU_{surface} = J_{0,surface} \left(\frac{p(x)n(x)}{P_0(x)n_0(x)} - 1 \right)_{x=W^-} \quad (A1)$$

Nonetheless, this expression is of not much practical use as $U_{surface}$ depends on the charge-carrier densities at the surface. Therefore, the *surface* saturation current density J_{0s} can be introduced,[13] which relates the surface recombination rate to the charge-carrier densities at the surface, at position $x = s$;

$$qU_{surface} = J_{0s} \left(\frac{p(x)n(x)}{P_0(x)n_0(x)} - 1 \right)_{x=s} \quad (A2)$$

From Eqs. A1 and A2, it follows that when the quasi-Fermi levels are flat through the highly doped region, which is the case for low levels of recombination, $J_{0s} = J_{0,surface}$, as is shown in Fig. A1. Nonetheless, in case of strong charge-carrier recombination in either the highly doped region or at its surface, the quasi-Fermi level splitting is locally reduced. Then, $J_{0s} < J_{0,surface}$, and the recombination at the surface is limited by the diffusion of minority carriers from the bulk towards the surface through the highly doped region. The ratio $J_{0s} / J_{0,surface}$ depends on the dopant and illumination profiles and the recombination pathways in the highly doped region. It can be numerically evaluated using e.g., the free online tool EDNA2 [22].

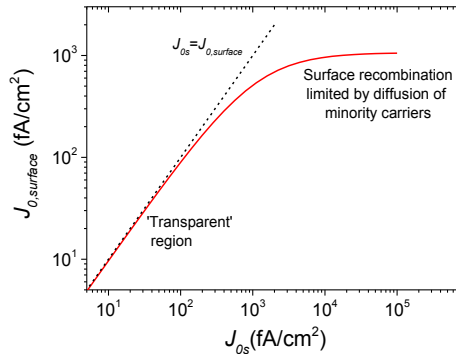


Figure A1 The relation of J_{0s} to $J_{0,surface}$ simulated using EDNA2,[22] for the boron-doped region of Fig. 3 with a sheet resistance of $56.2 \Omega/\square$.

Appendix B. Reduction of contact recombination by degenerately doped regions

In Section 5.2 it was shown that degenerate doping levels can strongly reduce surface recombination. In this appendix, it will be demonstrated that degeneracy can also be used to reduce recombination at highly doped regions which are contacted by metal. This recombination is, due to high recombination at the metal, always limited by the diffusion of minority charge carriers through the highly doped region. The recombination parameter for a uniformly doped n -type Si region with an active doping density N_{D-} and width W , which is contacted by metal can be approximated (e.g., by assuming no recombination in the highly doped region itself) by [37];

$$J_0 \approx q \frac{n_{i,eff}^2 D_p}{N_{D-} W} \quad (B1)$$

With D_p the diffusion coefficient for holes. As was discussed in Section 5.2, the term $n_{i,eff}^2 / N_{D-}$ strongly decreases for $N_{D-} > 10^{20} \text{ cm}^{-3}$. Therefore, according to Eq. B1, a degenerate doping level can also be beneficial to reduce J_0 for the doped regions contacted by metal.

To further illustrate how degeneracy effects could be used to strongly reduce recombination at the contacted doped regions, as example two distinct cases are considered;

- 1) A uniformly doped n^+ Si region with high doping density $N_{D-} = 8 \times 10^{20} \text{ cm}^{-3}$ and width of 20 nm.
- 2) A uniformly doped n^+ Si region with moderate doping density $N_{D-} = 1 \times 10^{20} \text{ cm}^{-3}$ and width of 160 nm.

Note that both dopant profiles have an identical number of active doping atoms within the highly doped region. The recombination for both doping profiles has been evaluated with $S_{eff} = 10^7 \text{ cm/s}$ (the thermal velocity of free carriers) in EDNA2, which includes Auger and radiative recombination in the highly doped region itself. The numerical modeling results in $J_0 = 4 \text{ fA/cm}^2$ for case 1 compared to $J_0 = 416 \text{ fA/cm}^2$ for case 2. This confirms that having a degenerate doped region can be a very effective way to reduce contact recombination. Note that the doping profile of case 1 is similar to the TOPCon passivating contact which exhibits very low recombination.[38] In TOPCon, highly doped polycrystalline silicon (poly-Si) is used, which is deposited on a $\sim 1.5 \text{ nm SiO}_2$ layer at the interface between the c-Si bulk and the highly doped poly-Si region. Therefore, the benefits of a degenerate doping levels are already used in present-day c-Si solar cells.

Surface Passivation of Phosphorus-Doped Black Si by Atomic Layer Deposited SiO₂/Al₂O₃ Stacks

Abstract In this work, lowly- and highly- *n*-type doped black silicon textures (b-Si) were studied as front surface for crystalline silicon solar cells. For lowly-doped b-Si, a low total surface recombination pre-factor $J_0 = 47$ fA/cm² was achieved after surface passivation by atomic layer deposited (ALD) Al₂O₃. Using a short wet-etch, charge-carrier recombination could be reduced further to $J_0 = 16$ fA/cm², while preserving the excellent light trapping properties of b-Si. Transmission electron microscopy studies revealed that the wet-etch largely removed a defect-rich region below the b-Si surface. For highly doped *n*⁺-type b-Si, considerable improvements in passivation compared to ALD Al₂O₃ single layers was achieved by using ALD SiO₂/Al₂O₃ stacks that do not possess strong negative fixed charge in combination with the aforementioned defect removal etch.

6.1 Introduction

Black silicon (b-Si) nanotextures are of interest in the field of crystalline silicon (c-Si) solar cells due to their excellent light trapping capabilities. Specifically, b-Si nanotextures induce a high absorption over a wide wavelength range without the need for an anti-reflection coating (ARC),[1–4] even for light entering under wide range of angles.[2,5] The latter can increase the energy yield of solar cells operating under realistic, non-ideal conditions. Moreover, the light absorption in b-Si can (when the b-Si is combined with a back reflector) approach the fundamental classical absorption limit, even for thin c-Si wafers with a thickness $<35 \mu\text{m}$.[5] Despite these excellent optical properties, numerous challenges still have to be overcome for realizing a large-scale breakthrough of b-Si in the field of photovoltaics. For instance, b-Si should be compatible with a heavily n -type doped Si front surface (n^+ -type Si, conventionally termed the “emitter”), screen printing of the front metal grid and module encapsulation, while low solar cell manufacturing costs should be maintained. Most importantly however, is a further reduction in charge-carrier recombination at b-Si surfaces, as the large surface area and high roughness of b-Si surfaces render its passivation challenging.

In the last decade, considerable progress has been made in the passivation of b-Si surfaces,[2,6–8] largely enabled by Al_2O_3 prepared by atomic layer deposition (ALD).[9,10] As ALD is based on self-limiting surface reactions, conformal deposition of thin films over high-aspect ratio structures – such as b-Si – can be achieved. Moreover, Al_2O_3 provides a very low interface defect density $D_{it} < 10^{11} \text{ eV}^{-1}\text{cm}^{-2}$ in combination with a distinctively high *negative* fixed-charge density Q_f in the range of $\sim 10^{12} - 10^{13} \text{ cm}^{-2}$.[11] This large negative fixed charge is especially for lowly n - or p -type doped b-Si beneficial, as it can bring the ‘needles’ of b-Si in depletion or accumulation, respectively.[8] Due to this strong field-effect, low surface recombination rates have been reported for lowly-doped b-Si, much lower than could be expected on the basis of the large b-Si surface area.[6–8,12] By passivation of a lowly p -type doped b-Si front surface by ALD Al_2O_3 , interdigitated back contact (IBC) solar cells with a conversion efficiency of 22.1% have recently been demonstrated.[2]

Even though Al_2O_3 provides excellent passivation of lowly-doped b-Si, the most commonly used solar cell architectures, such as the aluminum back surface field (Al-BSF) cell and passivated emitter and rear cell (PERC), fundamentally rely on a heavily n -type doped Si front surface. Unfortunately, Al_2O_3 is not well suited for the passivation of these

n^+ Si surfaces, as its high negative Q_f increases the minority charge carrier density at these surfaces which increases surface recombination.[13] Therefore, SiO₂/Al₂O₃ stacks have recently emerged as an alternative ALD-based passivation scheme for n^+ Si.[14] The Q_f of the stacks can be tailored from strongly negative to slightly positive by carefully tuning the SiO₂ thickness. Moreover, ALD SiO₂/Al₂O₃ stacks provide excellent levels of chemical passivation with $D_{it} < 10^{11}$ eV⁻¹cm⁻² and can be deposited conformally throughout trenches.[15] Therefore, the ALD SiO₂/Al₂O₃ stack are an interesting candidate for the passivation of n^+ -type b-Si surfaces.

In addition to the surface passivation scheme, also the preparation method of b-Si has an important influence on the charge-carrier recombination. For instance, it has been shown in previous work that carrier recombination could be strongly reduced for b-Si prepared by reactive ion etching (RIE) by applying a short alkaline etch, termed “defect removal etching” (DRE).[16]

In this work, carrier-recombination at lowly- and highly-doped n -type b-Si is addressed through a combination of DRE and surface passivation by ALD Al₂O₃ or SiO₂/Al₂O₃ stacks. The work is structured as follows: first, the optical and morphological properties of b-Si surfaces are studied for various DRE times. Next, the surface passivation of lowly n -type doped b-Si textures is studied. Finally, the passivation of highly n -type doped b-Si surfaces is addressed, and the potential of n^+ -type b-Si as front texture in c-Si solar cells is explored through corona-charging experiments.

6.2 Experimental details

Lifetime samples with a b-Si front surface were created by RIE of planar 280- μ m thick floatzone Si (100) wafers (n -type, 2.8 Ω cm) using a SF₆ and O₂ plasma in a Drytek Triode 384T Plasma Etcher at room temperature. The samples were subjected to 0, 15, or 30 seconds of DRE by diluted TMAH (1%), as developed by Ingenito *et al.*,[16]. Subsequently, two groups of b-Si front surfaces were heavily n -type doped using phosphorus ion implantation with constant energy (20 keV) and variable doses of 5×10^{14} cm⁻² (“low dose”) and 1×10^{15} cm⁻² (“high dose”). This was followed by annealing at 850 °C for 90 min in O₂ ambient and a buffered hydrofluoric acid (BHF) etch. The polished rear sides of the lifetime samples were passivated by 30-nm thick Al₂O₃ layers. The b-Si front surfaces were passivated by either a single Al₂O₃ layer or by SiO₂/Al₂O₃ stacks. The Al₂O₃ was prepared by 272 ALD cycles using Al(CH₃)₃ and O₂

plasma in an Oxford Instruments OpAL™ reactor at 200 °C. The SiO₂/Al₂O₃ stacks were deposited at the same temperature in the abovementioned reactor using 33 ALD cycles with H₂Si(N(C₂H₅)₂)₂ and O₂ plasma. Immediately afterwards, the Al₂O₃ was deposited without vacuum break. Next, the samples received a post deposition anneal at 400 °C in N₂ ambient for 10 minutes.

The absorption of the samples was derived from $1-R-T$, where the wavelength-dependent reflectance (R) and transmittance (T) were measured with an integrating-sphere PerkinElmer Lambda 950 spectrophotometer. The minority carrier lifetime was assessed by transient and quasi-steady-state photoconductance (QSSPC) measurements in a Sinton WCT100. The recombination parameter J_0 was derived from QSSPC using the method of Kane & Swanson,[17] while illuminating the polished rear side. The iV_{oc} was determined for 1-sun illumination of the b-Si side, to in this way represent the actual situation where b-Si is applied in a solar cell. The J_0 could not in all cases reliably be extracted, as not for all samples the method of Kane & Swanson could be used. In these cases, J_0 was therefore determined from the iV_{oc} . On selected samples, corona charges were deposited on the b-Si by applying a voltage of 11 kV between the sample and a tungsten needle for 25 minutes.

6.3 Results and discussion

6.3.1 Optical properties of b-Si

In Fig. 1a, the absorbance for b-Si textures is compared to a random-pyramid (RP) texture capped by 75-nm thick SiN_x ARC, which is the standard front surface of monocrystalline Si solar cells. Especially in the ultra-violet region, b-Si strongly enhances the absorption of light compared to the RP-texture. The sharp features of the b-Si texture gradually change the refractive index of air into that of Si, and in this way minimize front reflection. However, because of the small size of the nanotextured features, the scattering of long wavelength light is weaker than for a RP texture. To increase the absorption in this range, b-Si can therefore be combined with a micro-sized textured rear surface,[5] or b-Si can be superimposed on a RP-textured front surface.[16] Note that the light absorption of both samples will change under encapsulation in PV modules, which is however beyond the scope of this study. In Fig. 1b, the impact of the DRE time on the optical properties of the b-Si surfaces is shown. As the figure depicts, for DRE times of 30 seconds or longer, the absorbance of b-Si is reduced.

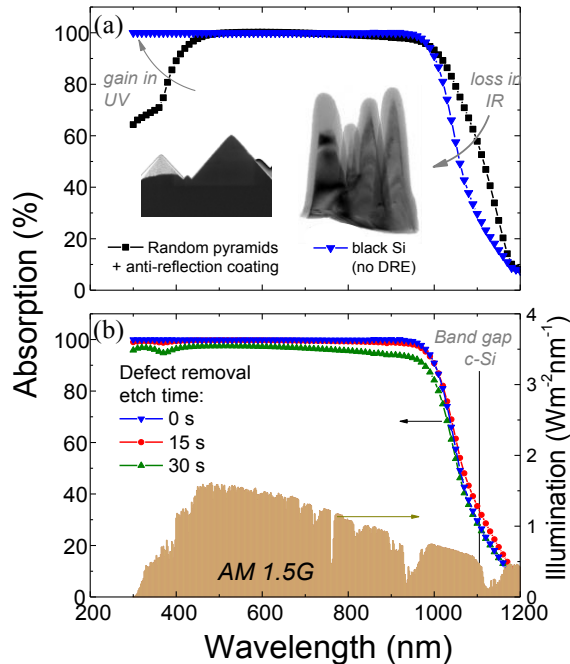


Figure 1 (a) Absorption of c-Si which comprises a b-Si front surface texture, passivated by 30-nm of ALD Al₂O₃, compared to c-Si with on both sides a random-pyramid texture and a 75-nm SiN_x anti-reflection coating. The inset shows scanning and transmission electron microscopy images of the textures. (b) Absorption of b-Si, passivated by 30-nm of Al₂O₃, for various defect removal etching (DRE) times. Additionally, the AM1.5 spectrum is displayed for reference.

6.3.2 Structural analysis of black Si

Figure 2 shows the scanning- and high-resolution transmission electron microscopy (SEM and TEM, respectively) images of the passivated b-Si surfaces. As can be seen, the b-Si needles are conformally coated by ALD Al_2O_3 or $\text{SiO}_2/\text{Al}_2\text{O}_3$ stacks.

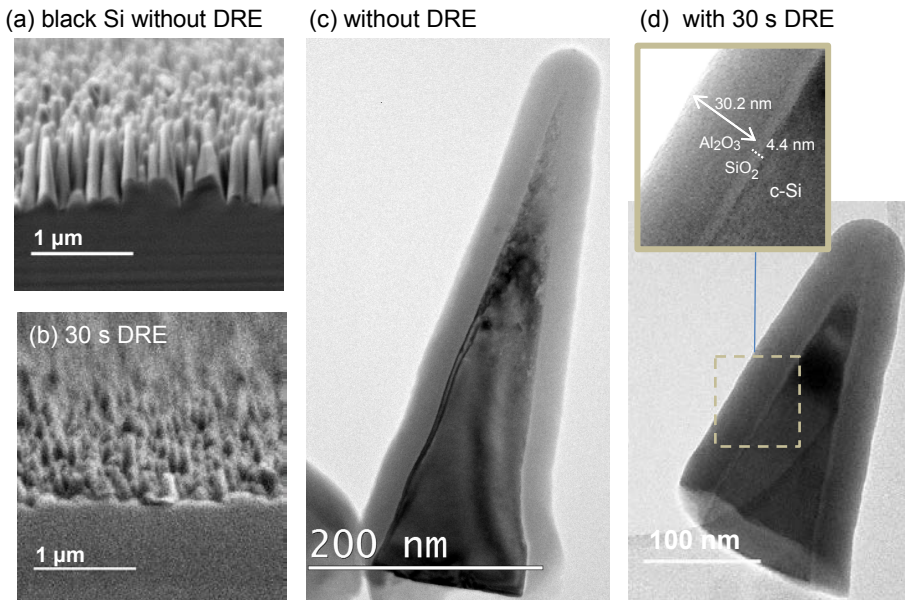


Figure 2 Cross-sectional scanning electron microscopy (SEM) images of b-Si surfaces (a) without or (b) with 30 seconds of defect removal etching (DRE). (c) Transmission electron microscopy (TEM) image of a b-Si needle without DRE passivated by 30-nm thick ALD Al_2O_3 . (d) TEM of a b-Si needle with 30 seconds of DRE passivated by ALD $\text{SiO}_2/\text{Al}_2\text{O}_3$. In the inset, the film thicknesses are indicated.

Moreover, TEM reveals in Fig. 2c the presence of defect clusters in case of no DRE, predominantly at the tips of the needles. The presence of these defects can be attributed to ion bombardment during the room-temperature RIE process. In some other studies addressing the preparation of b-Si by RIE, such defects were not reported, potentially due to the more gentle structuring of the b-Si surface by RIE at cryogenic temperatures.[8] Fig. 2d shows a b-Si needle which was exposed to 30 seconds of DRE. As can be seen, most of the defect clusters are etched away, indicating that they were apparently confined to a sub-surface region. With increasing DRE time, the roughness of the texture decreases (see Fig. 2a and Fig. 2d), which explains why, as is shown in previous section, the optical properties of b-Si texture are compromised for prolonged etch times ≥ 30 s.

6.3.3 Surface passivation of lowly-doped black Si

In Table 1, lifetime results are given for various b-Si and polished lifetime samples. Mirror-polished wafers passivated by ALD Al₂O₃ resulted in a $J_0 = 4 \text{ fA/cm}^2$, underlining the high quality of the surface passivation layer. The samples comprising a b-Si front surface without DRE and polished rear surface could also be passivated well by Al₂O₃, as is illustrated by $J_0 = 47 \text{ fA/cm}^2$, despite the presence of defects (Fig. 2). Presumably, passivation can still be achieved due to the strong field-effect passivation on such lowly-doped samples provided by the strong negative Q_f of Al₂O₃. [6,8] Indeed, for SiO₂/Al₂O₃ stacks, which do not exhibit the strong negative Q_f and accompanied field-effect passivation, the charge-carrier recombination is considerably higher, as can be seen from the low iV_{oc} of 589 mV for SiO₂/Al₂O₃ compared to 685 mV for Al₂O₃.

Table 1 Lifetime results of b-Si samples etched with various defect removal etching times and with several phosphorus ion implantation doses. The b-Si textured surface was passivated either by ALD Al₂O₃ or by ALD SiO₂/Al₂O₃ stacks, whereas the polished rear surface was passivated by ALD Al₂O₃ in all cases.

Ion implantation dose	DRE time (s)	R_{sheet} (Ω /sq)	Al ₂ O ₃ passivation		SiO ₂ /Al ₂ O ₃ passivation	
			iV_{oc} (mV)	J_0 (fA/cm ²)	iV_{oc} (mV)	J_0 (fA/cm ²)
no	0	> 100	685	47	589	2530
	15	> 100	695	24	590	1850
	30	> 100	692	16	603	1580
low	0	86 ± 3	589	700	625	639
	15	80 ± 1	599	628	629	524
	30	81 ± 2	600	750	639	338
high	0	71 ± 2	596	541	620	843
	15	64 ± 2	611	644	641*	312
	30	62 ± 2	609	719	640	300

* = value before corona charging.

By carrying out a short DRE before ion implantation and surface passivation, the outer part of the b-Si needles is removed. This reduction of sub-surface defects and surface area decreases the total J_0 from 47 to 24 and 16 fA/cm² for 0, 15 and 30 seconds of etching, respectively (see Table 1), resulting in iV_{oc} values higher than 690 mV when using DRE. Note that for short etch times in the range of 15 seconds, the recombination is reduced without compromising the optical properties (see Fig. 1).

6.3.4 Surface passivation of ion-implanted black Si

As a next step, highly n -type doped b-Si surface textures are studied. The sheet resistance of the b-Si samples which were ion-implanted (i.e., above >80 Ohm/sq for the low dose, >62 Ohm/sq for the high dose) are significantly higher than for planar surfaces which received the same ion implantation (i.e., 57 Ohm/sq for the low dose and 38 Ohm/sq for the high dose). This can be explained as phosphorus dopants within the tip of the needles do not contribute to the lateral conduction of charge carriers. Therefore, significant ion-implantation doses were required on b-Si to achieve a relatively low sheet resistance.

As is shown in in Table 1, the surface passivation of the n^+ -type b-Si surfaces (whether formed by a low or high ion implantation dose) by Al_2O_3 results in iV_{oc} values below 611 mV for all DRE times used. As was stated in the introduction, the poor passivation of n^+ Si by Al_2O_3 was expected on the bases of the large negative Q_f . Considerably higher iV_{oc} values were achieved for surface passivation by $\text{SiO}_2/\text{Al}_2\text{O}_3$ stacks, which do not contain the negative Q_f . Moreover, the passivation by $\text{SiO}_2/\text{Al}_2\text{O}_3$ improved significantly for n^+ -type black Si which received a DRE. The highest iV_{oc} value obtained for n^+ -type b-Si is 641 mV for 15 seconds of DRE.

The question arises whether the passivation of the n^+ -type black-Si front surface can be further improved. Therefore, positive corona charging was carried out on the front side of the b-Si texture passivated by the $\text{SiO}_2/\text{Al}_2\text{O}_3$ stack which gave the highest passivation results. Due to the positive charges deposited on the stack, the field-effect passivation improved, leading to a maximum $iV_{oc} = 652$ mV after prolonged (25 minutes) of charging. This value is marginally (i.e., $\Delta iV_{oc} = +11$ mV) higher than before corona charging. Presumably, the heavy phosphorus doping which was required to achieve low sheet resistances, results in significant Auger recombination in doped b-Si needles. The Auger recombination cannot be reduced by improvements in surface passivation by corona charging. In future studies, deeper and lower doped regions could therefore be promising, as dopants which are not within the b-Si needles can contribute to the lateral conduction of charge carriers, whereas lower doping concentrations will induce less Auger recombination.

6.4 Conclusions

The effects of defect removal etching on the optical, structural and electronic properties of b-Si surfaces prepared by RIE at room temperature has been investigated. It was demonstrated DRE can remove defects which are present below the b-Si surface, without significantly effecting the excellent light coupling properties of b-Si. DRE effectively reduced charge-carrier recombination for lowly-doped b-Si, which after passivation by ALD Al₂O₃ results in low J_0 values of ~ 16 fA/cm² and $iV_{oc} = 695$ mV. For n^+ -type b-Si, a combination of the DRE and the use of ALD SiO₂/Al₂O₃ passivation stacks significantly reduced surface recombination, and an iV_{oc} of 641 mV was achieved. A reduction in Auger recombination is expected to be required as a next step towards optimized n^+ -type b-Si front surface textures for c-Si solar cells.

Acknowledgements

The authors gratefully acknowledge A. Ingenito, O. Isabella, M. Zeman, R.H.J. Vervuurt, G. Limodio, and C.A.A. van Helvoirt for experimental assistance. This work was supported by the Dutch Ministry of Economic Affairs via the Top Consortia for Knowledge and Innovation (TKI) programs *Advanced Nanolayers* and *IBChampion*. The Solliance consortium and the Dutch province of Noord-Brabant are acknowledged for funding the TEM facility.

References

1. Wang, W.-C., Lin, C.-W., Chen, H.-J., *et al.*, (2013) Surface passivation of efficient nanotextured black silicon solar cells using thermal atomic layer deposition. *ACS Appl. Mater. Interfaces*, **5** (19), 9752–9759.
2. Savin, H., Repo, P., von Gastrow, G., *et al.*, (2015) Black silicon solar cells with interdigitated back-contacts achieve 22.1% efficiency. *Nat. Nanotechnol.*, **10** (7), 624–628.
3. Gaudig, M., Hirsch, J., Schneider, T., *et al.*, (2015) Properties of black silicon obtained at room-temperature by different plasma modes. *J. Vac. Sci. Technol. A Vacuum, Surfaces, Film.*, **33** (5), 05E132.
4. Liu, X., Coxon, P.R., Peters, M., *et al.*, (2014) Black silicon: fabrication methods, properties and solar energy applications. *Energy Environ. Sci.*, **7**, (10), 3223–3263.
5. Ingenito, A., Isabella, O., and Zeman, M. (2014) Experimental Demonstration of $4n^2$ Classical Absorption Limit in Nanotextured Ultrathin Solar Cells with Dielectric Omnidirectional Back Reflector. *ACS Photonics*, **1** (3), 270–278.
6. Repo, P., Haarahluntunen, A., Sainiemi, L., *et al.*, (2013) Effective Passivation of Black Silicon Surfaces by Atomic Layer Deposition. *IEEE J. Photovoltaics*, **3** (1), 90–94.
7. Otto, M., Kroll, M., Käsebier, T., *et al.*, (2012) Extremely low surface recombination velocities in black silicon passivated by atomic layer deposition. *Appl. Phys. Lett.*, **100** (19), 191603.
8. von Gastrow, G., Alcubilla, R., Ortega, P., *et al.*, (2015) Analysis of the Atomic Layer

- Deposited Al₂O₃ field-effect passivation in black silicon. *Sol. Energy Mater. Sol. Cells*, **142**, 29–33.
9. Agostinelli, G., Delabie, A., Vitanov, P., *et al.*, (2006) Very low surface recombination velocities on *p*-type silicon wafers passivated with a dielectric with fixed negative charge. *Sol. Energy Mater. Sol. Cells*, **90**, 3438–3443.
 10. Hoex, B., Heil, S.B.S., Langereis, E., *et al.*, (2006) Ultralow surface recombination of c-Si substrates passivated by plasma-assisted atomic layer deposited Al₂O₃. *Appl. Phys. Lett.*, **89** (4), 42112.
 11. Dingemans, G., and Kessels, W.M.M. (2012) Status and prospects of Al₂O₃-based surface passivation schemes for silicon solar cells. *J. Vac. Sci. Technol. A*, **30** (4), 40802.
 12. Allen, T., Bullock, J., Cuevas, A., *et al.*, (2014) Reactive Ion Etched Black Silicon Texturing : A Comparative Study. *Proc. 40th IEEE Photovolt. Spec. Conf.* 562–566.
 13. Hoex, B., van de Sanden, M.C.M., Schmidt, J., *et al.*, (2012) Surface passivation of phosphorus-diffused *n*⁺-type emitters by plasma-assisted atomic-layer deposited Al₂O₃. *Phys. status solidi - Rapid Res. Lett.*, **6** (1), 4–6.
 14. van de Loo, B.W.H., Knoops, H.C.M., Dingemans, G., *et al.*, (2015) “Zero-charge” SiO₂/Al₂O₃ stacks for the simultaneous passivation of *n*⁺ and *p*⁺ doped silicon surfaces by atomic layer deposition. *Sol. Energy Mater. Sol. Cells*, **143**, 450–456.
 15. Dingemans, G., van Helvoirt, C.A.A., Pierreux, D., *et al.*, (2012) Plasma-Assisted ALD for the Conformal Deposition of SiO₂: Process, Material and Electronic Properties. *J. Electrochem. Soc.*, **159** (3), H277–H285.
 16. Ingenito, A., Isabella, O., and Zeman, M. (2015) Nano-cones on micro-pyramids: modulated surface textures for maximal spectral response and high-efficiency solar cells. *Prog. Photovoltaics Res. Appl.*, **23** (11), 1649–1659.
 17. Kane, D.E., and Swanson, R.M. (1985) Measurement of the emitter saturation current by a contactless photoconductivity decay method. *Proc. 18th IEEE Photovolt. Spec. Conf.* 578–583.

CHAPTER 7

Quantification of pn -junction Recombination in Interdigitated-Back Contact Crystalline Silicon Solar Cells

Abstract Interdigitated back-contact (IBC) solar cells based on diffused crystalline silicon comprise a series of pn -junctions which border at the rear surface of the wafer. In this work, it was established that the presence of these pn -junctions in some cases induced significant additional charge-carrier recombination, which affected the conversion efficiency of IBC cells through a reduction in fill factor and open-circuit voltage. Using specialized test structures with varying length of pn -junctions per area of solar cell (i.e., with varying junction density), the magnitude of the recombination at the pn -junction was determined. For non-passivated rear surfaces, a second-diode recombination current density per unit of junction density J_{02} of $\sim 61 \text{ nA}\cdot\text{junction}^{-1}\text{cm}^{-1}$ was measured, whereas for surfaces which were passivated by either SiN_x or $\text{Al}_2\text{O}_3/\text{SiN}_x$, J_{02} was reduced to $\sim 0.4 \text{ nA}\cdot\text{junction}^{-1}\text{cm}^{-1}$. Therefore, passivation of defects at the rear surface was proven to be vital in reducing this characteristic recombination current. Finally, by optimizing the p - and n -type dopant diffusion recipes, the J_{02} recombination could be suppressed to negligible values of $\sim 0.02 \text{ nA}\cdot\text{junction}^{-1}\text{cm}^{-1}$. The improved doping recipes lead to an increase in conversion efficiency of industrially relevant ‘Mercury’ IBC solar cells by $\sim 1\%$ absolute.

7.1 Introduction

In interdigitated back-contact (IBC) solar cells, both the positive and negative contacts are located at the rear side, to avoid parasitic absorption and reflection by front side metallization. Despite this advantage, the performance of IBC solar cells can be significantly reduced by a low short-circuit current density (J_{sc}), for instance due to lateral transport losses of charge carriers towards the rear contacts, an effect known as “electrical shading”.[1] To reduce such losses, crystalline silicon (c-Si) solar cells with a diffused “front floating emitter” (FFE) have been developed (see Fig. 1), in which the lateral conduction of minority carriers takes place via a highly doped region near the front surface.[2][3] In this way, a high J_{sc} can be achieved with minimal constraints to rear side patterning. ECN’s IBC concept *Mercury*, based on a FFE, has so far reached conversion efficiencies up to 21.1%.[4,5] Although the problems of electrical shading thus can be minimized, in this work it will be shown that another mechanism can induce a significant loss in performance for diffused-junction IBC solar cells. Specifically, it will be shown that a distinctive charge-carrier recombination current can be associated with the presence of the pn -junctions which border the at the rear surface of the solar cell.

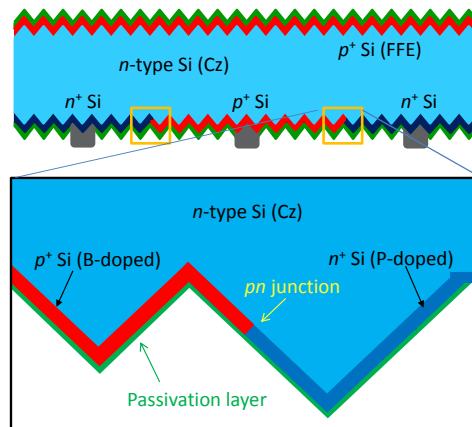


Figure 1 Schematic of the ECN IBC cell *Mercury*, which comprises a front-floating emitter.

In semiconductor physics, it is known that additional charge-carrier recombination can occur when a pn -junction borders a surface. First of all, it follows from the Shockley-Read-Hall (SRH) theory that defect states within the band gap are most effective when electrons and holes are captured with equal rates. This is when the condition $n \cdot \sigma_n = p \cdot \sigma_p$

(1) is satisfied, with n and p the electron and hole carrier densities, σ_n and σ_p the electron and hole capture cross sections of the defects, respectively.[6,7] Under such conditions, the recombination current J_{rec} is given by $J_{rec} = J_{02} (\exp(V/m \cdot V_t) - 1)$, with m the ideality factor (in this case $m=2$), V the voltage, V_t the thermal voltage and J_{02} the second-diode recombination parameter. As the electron and hole densities change sharply across the *pn*-junction, condition (1) is typically satisfied somewhere across the junction, such as in its depletion region.[8,9] The so-called “depletion region recombination” which occurs as a result, is particularly pronounced where the *pn*-junction borders a surface, as at a surface often a high density of defect states is present. In fact, any depleted surface near the bordering *pn*-junction can lead to severe J_{02} -type recombination, due to efficient transport of charge-carriers through the highly doped *p*- and *n*-type regions towards this recombination active region.

Secondly, adjacent highly doped *n*- and *p*-type Si regions can induce a tunneling recombination current between the conduction band of n^+ Si and the valence band of p^+ Si. Such tunneling recombination current occurs in particular for abrupt, highly-doped *pn*-junctions and is aided by defect states that are present within the band gap (such as at the c-Si surface) which facilitate trap-assisted tunneling.[10]

Although the above-mentioned recombination mechanisms have a different physical nature, in practice it can be hard to discern amongst them. Therefore, we will simply refer to them together as ‘*pn*-junction recombination’ pathways.

Also for c-Si solar cells in specific, signs of a significant J_{02} -recombination pathway of charge carriers have been observed when a *pn*-junction terminates at a surface (or at the perimeter of the cell) that is poorly or not passivated.[11–14] For monocrystalline front-contacted solar cells, surface bordering of the *pn*-junction occurs only at the edge of the wafer. Hence, its detrimental effects on the performance of the solar cells, such as a reduced fill factor FF and reduced V_{oc} at low light intensities, are in general minimal. In IBC cells however, the length of *pn*-junction which borders at the surface is significantly larger per unit area. Therefore, the question arises whether for IBC solar cells the above-mentioned J_{02} -type recombination channels might still induce a significant loss mechanism.

Recent publications provide indications that *pn*-junction recombination can indeed significantly affect the conversion efficiency of IBC solar cells. For instance Müller *et al.*[3] found a reduction in efficiency of diffused-junction IBC cells by 2% absolute after

placing the cell under reverse bias. The reduction in efficiency was in part attributed to an increase in J_{02} from 12 to 82 nA/cm². A plausible explanation for the increase in J_{02} was the degradation of the rear surface passivation layer, which would affect the recombination at the bordering pn -junction. Yet, the presence of this recombination mechanism could not be verified.

Additionally, Dong *et al.*, [15] found by simulating the tunneling recombination current between the n^+ and p^+ Si in IBC solar cells, that tunneling can be significant for solar cells under forward bias, and that the profile of boron dopants had a pronounced influence on the tunneling recombination.

Finally, indications for a recombination channel at or near the pn -junction have also been found for novel IBC solar cell concepts which are not based on diffused junctions, but which comprise n^+ and p^+ -type doped polycrystalline Si (poly-Si) passivating contacts. For instance, for lifetime samples with interdigitated p - and n -type doped poly-Si contacts, minority carrier lifetime data could only be fitted using a diode with local ideality factor $n > 1$, whereas for samples without rear interdigitated junctions such non-ideal recombination current was absent. [16] Interestingly, by creating a gap between the n^+ and p^+ poly-Si regions, the open-circuit voltage V_{oc} as well as the pseudo fill factor pFF of the IBC solar cell increased significantly. [17] Nonetheless, the creation of a gap between the p and n -type poly-Si regions imposes additional and complex process steps (as it also does for IBC solar cells based on diffused c-Si junctions) and is therefore undesirable from an industrial point of view.

Despite the potential detrimental effects of pn -junction recombination on IBC solar cells, a systematic study or quantification of this recombination mechanism is still lacking. Therefore, in this work, the charge-carrier recombination at the pn -junction was systematically investigated by using dedicated test structures, in which the density of pn -junctions was varied. The recombination at the pn -junction was examined for unpassivated rear surfaces, as well as for surfaces which were passivated by industrially-relevant passivation schemes, i.e., nitric acid oxidation of Si (NAOS) in combination with SiN_x or for Al₂O₃/SiN_x stacks. Finally, the influence of the boron and phosphorus diffusion recipe on recombination at the pn -junction was studied on test structures as well as on completed IBC solar cells. It will be shown that by careful tuning of the diffusion recipe, the conversion efficiency of IBC Mercury cells could be improved by ~1 % absolute, which relates to a reduction of pn -junction recombination.

7.2 Experimental details

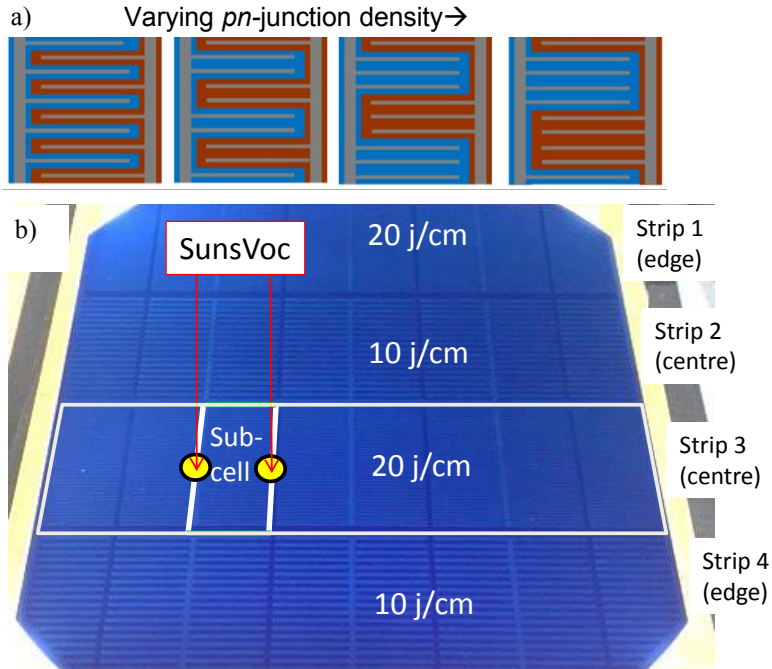


Figure 2 (a) Schematic of the sub-cells present in the test wafers which were used to monitor pn -junction recombination. The sub-cells have a varying pn -junction density, ranging from 5 to 30 junctions/cm. The red and blue lines represent the p^+ and n^+ Si regions, respectively, whereas the grey areas represent the metal contacts, which are applied by screen printing and a high-temperature “firing” step. (b) Photograph of a 6” test wafer comprising 4 rows (“strip 1 to 4”) which contain eight identical sub-cells of $1.9 \times 3.8 \text{ cm}^2$, with in this case either 10 or 20 junctions/cm. To account for potential non-uniformities across the wafer, identical rows were used in the center and near the edge of the wafer. The position of where the electrodes of the Suns- V_{oc} set-up contact the sub-cell is indicated. For the purpose of this photograph, the highly doped regions were not contacted by metal.

To assess recombination at the pn -junction, specialized test wafers were made. Figure 2 shows a schematic of the test structures (a) and a photograph of a test wafer (b). The test wafers were fabricated by the same process steps as used for the Mercury solar cells (see Fig. 1),[2] with the exception of the patterning design of the p and n -type doped regions at the rear surface. As a base material, 6-inch, Czochralski-grown, n -type Si wafers with a resistivity of $\sim 5 \text{ Ohm-cm}$ were used. After random pyramid texturing by alkaline (KOH) etching, boron and phosphorus diffusions were carried out in a horizontal tube furnace

(Tempress Systems) to form the heavily doped *p*- and *n*-type regions, respectively. The interdigitated pattern at the rear surface was obtained using a screen-printed resist in combination with subsequent wet-chemical removal of the highly doped Si, before carrying out the next diffusion step. In this work, three different boron and phosphorus (co-)diffusion recipes were studied, labelled A, B and C. Figure 3 shows the doping concentration profiles as determined by electrochemical capacitance-voltage (ECV) measurements, before they are simultaneously etched back to obtain tailored R_{sheet} values for the boron doped regions with $72 \Omega/\square$ for recipe A, and $85 \Omega/\square$ for recipe B and C.

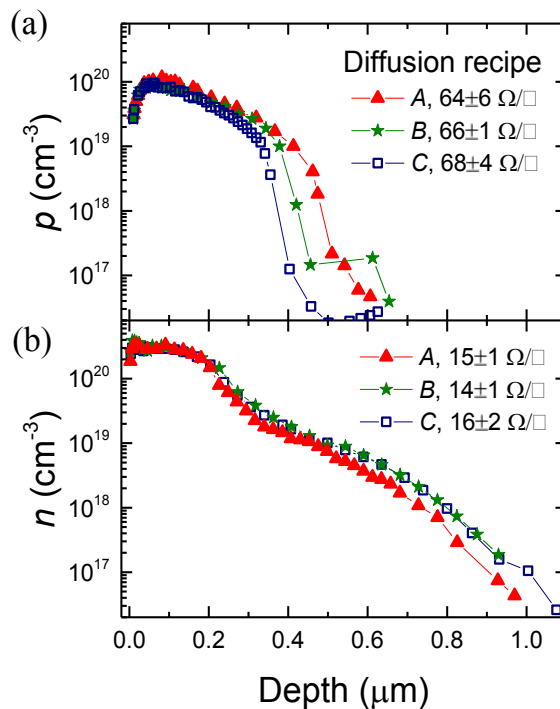


Figure 3 Electrochemical capacitance-voltage (ECV) measurements of the dopant profiles of (a) the boron- and (b) the phosphorus-doped regions for the three different (co-)diffusion recipes A, B, and C. The sheet resistance was determined by four-point probe measurements for each doped region.

After the diffusion steps, the phosphorus and boron containing glass was removed. Subsequently, the front and rear Si surfaces were oxidized simultaneously using a nitric acid dip at room temperature (NAOS). Next, Al_2O_3 was deposited on the front surface

using spatial atomic layer deposition (*Levitrack*, Levitech), after which it was capped by plasma-enhanced chemical vapor deposited SiN_x (*Maia*, Meyer Burger). The rear surface (where the *pn*-junctions border) was either passivated by a single layer of SiN_x, a stack of Al₂O₃/SiN_x, or was not passivated at all. Note, that the passivation performance of the SiN_x single layers significantly changes by the used nitric-acid oxidation of the Si.[18] Finally, the passivated and doped Si regions at the rear were contacted by screen-printed Ag paste and a high-temperature ‘firing’ step.

At the front surfaces of the test structures as well as of the IBC Mercury solar cells, a homogeneously doped *p*⁺ Si front floating emitter was present. At the rear surface of the test structures, the length of the *pn*-junction was varied by changing the ‘linear’ *pn*-junction density from 5 to 20 junctions per centimeter (see Fig. 2a). Specifically, the (equal) widths of both the *n*⁺ and *p*⁺ Si regions on the test structures were varied from 500 to 1000, 1500 and 2000 μm, whereas the total area of *n*⁺ Si or *p*⁺ Si was identical for each test structure. In contrast, in actual IBC Mercury cells, a typical junction density of 15 cm⁻¹ is used with unequal widths of the *n*⁺ and *p*⁺ Si region. Also the metal contact area was kept equal between all test structures, and was similar to the metal coverage used in IBC Mercury solar cells. After metallization, each sub-cell was measured in a Suns-*V*_{oc} setup (Sinton Instruments) by contacting the adjacent positive and negative busbars by electrodes. By fitting the Suns-*V*_{oc} measurements to a two-diode model, the *J*₀₁, *J*₀₂, pseudo fill factor (*pFF*), and shunt resistance *R*_{Shunt} were extracted. It was verified by laser cutting of the individual sub-cells that there was no cross correlation between them.

7.3 Results

7.3.1 Influence of surface passivation on *pn*-junction recombination

First, the test structures with unpassivated rear surfaced were examined. The structures were prepared using diffusion recipe *B*. The homogeneously doped *p*⁺ Si front surfaces were passivated by a stack of Al₂O₃/SiN_x. For this specific experiment without rear-surface passivation, no screen-printed metal contacts were applied to prevent shunting, although a firing step was carried out. Therefore, in this case the electrodes of the Suns-*V*_{oc} setup were put in direct contact with the *n*⁺ and *p*⁺ Si regions. The results of the Suns-*V*_{oc} data, fitted to a two-diode model, are shown in Fig. 4a-c.

As can be seen in Fig. 4a, *J*₀₁ is approximately constant with the junction density, and has relatively high values of 2540±400 fA/cm², which are typical for doped surfaces that are not passivated. In contrast, *J*₀₂ shows a linear increase with the junction density at a

rate of $61 \pm 5 \text{ nA} \cdot \text{junction}^{-1} \cdot \text{cm}^{-1}$ and thus reveals *pn*-junction recombination (see Fig. 4b). Moreover, the *pFF* (see Fig. 4c) and the V_{oc} at 1-sun illumination (not shown here) decrease significantly with the density of junctions, the latter from 583 mV at a junction density of 5 cm^{-1} to 553 mV at a density 20 cm^{-1} .

For comparison, also the FFJ_{01} , which is the fill-factor in case it is only limited by J_{01} -type recombination is shown in Fig. 4c. FFJ_{01} was evaluated from the V_{oc} at 1-sun using the exact analytical solution of reference [19]. The difference between FFJ_{01} and the *pFF* can for a two diode model in principle only be attributed to losses due to the parasitic shunting, ΔFF_{Rsh} , or J_{02} -type recombination, ΔFFJ_{02} :

$$pFF = FFJ_{01} - \Delta FF_{Rsh} - \Delta FFJ_{02}$$

The shunt resistance R_{shunt} for all test structures was too high to be determined via the Suns- V_{oc} measurements. Considering the strong increase in J_{02} with the junction density, it is likely that the observed decrease in *pFF* with increasing junction density therefore predominantly originates from J_{02} -type recombination (ΔFFJ_{02}).

In the case of a passivated rear-surface of the test structures (see Fig.4d-f), J_{01} is significantly reduced compared to the unpassivated case, with lower J_{01} values for $\text{Al}_2\text{O}_3/\text{SiN}_x$ than for SiN_x passivation. For both passivation schemes, J_{01} is independent of the junction density. Also the J_{02} values are significantly reduced when the surface is passivated for all junction densities, with overall higher J_{02} values for $\text{Al}_2\text{O}_3/\text{SiN}_x$ than for SiN_x . Despite the significantly reduced J_{02} values after passivation, an increase in J_{02} with junction density of $\sim 0.37 \text{ nA} \cdot \text{junction}^{-1} \cdot \text{cm}^{-1}$ for $\text{Al}_2\text{O}_3/\text{SiN}_x$ and $\sim 0.43 \text{ nA} \cdot \text{junction}^{-1} \cdot \text{cm}^{-1}$ for SiN_x can still be observed. Note that J_{02} for the passivated case is extrapolated to 0 junctions/cm, still a J_{02} current of 6-8 fA/cm² is found, which is related to recombination in other parts of the cell.

The *pFF* for the case that the test structures are passivated decreases with increasing junction density, albeit to a much lesser extent than in the case of an unpassivated rear surface. Also when the rear surface is passivated, the shunt resistance values are too high to be determined by fitting a two-diode model to the Suns- V_{oc} data. The decrease in *pFF* with junction density (and the highest *pFF* values for SiN_x) can qualitatively be explained well by the trends in J_{02} with junction density, where high J_{02} values reduce the *pFF*.

Despite the significant lower J_{02} recombination per density of junction for the passivated surface compared to the unpassed surface, it is important to note that for the passivated surfaces still a J_{02} -type recombination pathway can be associated with the density of *pn*-junctions.

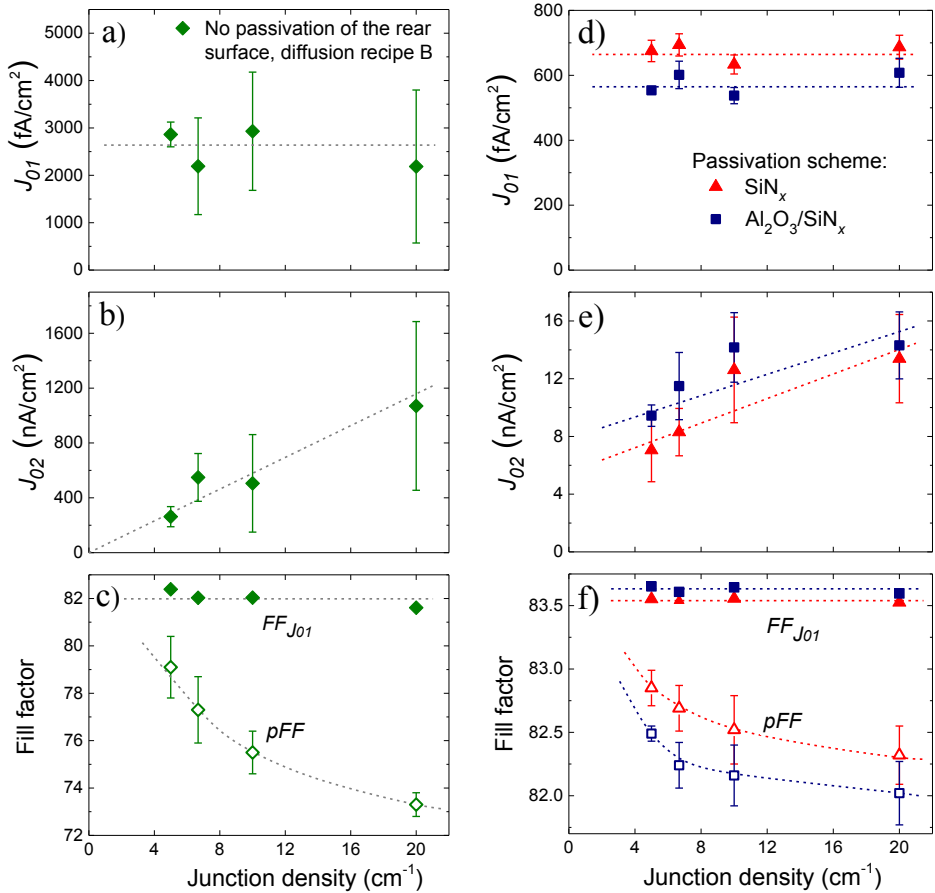


Figure 4 Results from fitting Suns- V_{oc} measurements to a two-diode model, for test structures prepared by diffusion recipe *B* for (a)-(c) samples without rear-surface passivation and (d)-(f) samples where the rear surface is passivated by either Al₂O₃/SiN_x or SiN_x. The upper limit of the fill factor, FF_{J01} shown in (c) and (f) is derived from the open-circuit voltage at one sun using the (exact) analytical method described in Ref. [19]. Lines are guides for the eye.

7.3.2. Influence of the diffusion recipe on pn -junction recombination

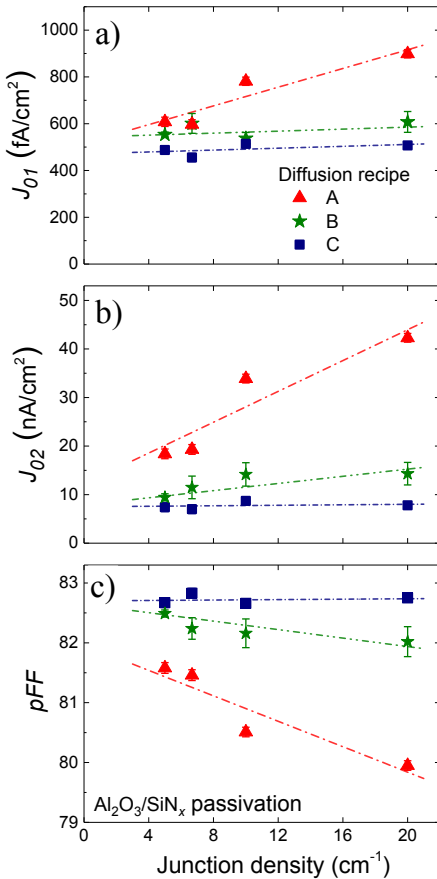


Figure 5 J_{01} , J_{02} and pFF are extracted from Suns- V_{oc} measurements on test structures, which are prepared using three different diffusion recipes. A stack of Al₂O₃/SiN_x was used for the passivation of the rear-side, where the pn -junctions were present. Lines are linear fits to the data.

Results on test structures

Next, the influence of the diffusion recipe on pn -junction recombination was evaluated. To this end, the Suns- V_{oc} data obtained from test structures with three different diffusion recipes were again fitted by the two-diode model. The rear surfaces of the test structures (where the pn -junctions border) were passivated by Al₂O₃/SiN_x, which yielded the lowest J_{01} values in the previous section.

As can be seen in Fig. 5, diffusion recipe A, shows a clear increase in J_{02} recombination with increasing junction density at a rate of $\sim 1.6 \text{ nA} \cdot \text{junction}^{-1} \cdot \text{cm}^{-1}$. Note that this increase in J_{02} is even more significant for diffusion recipe A than for recipe B, which was used in the previous section. Remarkably, for diffusion recipe A, even the J_{01} -type recombination increases with $\sim 20 \text{ fA} \cdot \text{junction}^{-1} \cdot \text{cm}^{-1}$. As a result of the increase in J_{01} and J_{02} , a decrease in V_{oc} of about 10 mV is observed when the junction density is increased from 5 to 20 $\text{junction}^{-1} \cdot \text{cm}^{-1}$. [20] Moreover, the results show a very strong decrease in pFF with increasing junction density. Interestingly, for recipe C, which has shallowest boron doped region, virtually no additional J_{01} and J_{02} recombination is observed with increasing junction densities, nor is a decrease in pFF

observed. Therefore, this experiment demonstrates that by tuning the diffusion recipe any significant *pn*-junction recombination can practically be avoided, even in case of a gap-less *pn*-junction. The latter is particularly important for a cost-effective processing of IBC solar cells.

Results on Mercury solar cells

Next, the influence of the different diffusion recipes on IBC solar cells was studied. To this end, full-area (6-inch) IBC Mercury solar cells were fabricated using diffusion recipe *C* and recipe *A*. The solar cell parameters for both groups were evaluated from light *J-V* measurements as shown in Table 1. Note that the cell efficiencies obtained here are about ~1.8% absolute lower than the current record efficiencies for Mercury cells of 21.1% [5]. Nonetheless, both groups of solar cells are, apart from the diffusion step, fabricated in the same process run and therefore allow for a close comparison to discriminate the effect of the diffusion step on the solar cell performance.

The largest relative differences between the two diffusion recipes occur between the J_{01} and J_{02} parameters, where doping recipe *C* shows significantly improved values over recipe *A*. As a result, the efficiency of the IBC cells improves by 1% absolute from 18.3 to 19.3% when going from recipe *A* to recipe *C*. By looking at the *J-V* parameters, it can be seen that the V_{oc} has the largest influence on the cell efficiency difference. The improvement in the V_{oc} of Recipe *C* with respect to Recipe *A* stems from a reduction of both J_{01} and J_{02} which is in qualitative accordance with the results from previous section. The results were additionally corroborated by dark *J-V* measurements (as is discussed in the Supplementary Info S1).

Table 1 Solar cell parameters for Mercury IBC cells which were fabricated by diffusion recipes *A* and *C*. The rear surface was passivated by a stack of $\text{Al}_2\text{O}_3/\text{SiN}_x$. The results were obtained from *J-V* measurements under standard test conditions (25 °C, 1000 W/m², AM1.5g), and represent the average of 7 solar cells. The area of each solar cell was 239 cm².

Mercury cell with diffusion	J_{sc} (mA/cm ²)	V_{oc} (mV)	FF (%)	pFF (%)	J_{01} (fA/cm ²)	J_{02} (nA/cm ²)	R_{shunt} (Ω)	η (%)
Recipe A	39.6	627	73.8	79.2	609	74.1	9.4	18.3
Recipe C	40.1	643	75.0	80.7	330	50.2	8.9	19.3
Relative change (%)	1.2	2.7	1.6	1.9	-45.8	-32.3	-5.3	5.5

7.4 Discussion: mechanisms of *pn*-junction recombination

In the previous section, it was shown that the J_{02} recombination, which is associated with the density of *pn*-junctions, can be reduced considerably from $\sim 61 \text{ nA}\cdot\text{junction}^{-1}\text{cm}^{-1}$ without surface passivation to values below $<1.6 \text{ nA}\cdot\text{junction}^{-1}\text{cm}^{-1}$ after surface passivation. Surface passivation is therefore of key importance in the reduction of J_{02} recombination in IBC solar cells. This importance of surface passivation can, as was discussed in the introduction, for a part be attributed to a very efficient charge transport of minority carriers to the surface near the *pn*-junction. As a consequence of this transport, surface recombination will not become limited by the diffusion of minority charge carriers. Note that this also holds for IBC cells which comprise a gap between the *p*- and *n*- type highly doped regions, as has also been found by simulations of IBC cells [21]. Furthermore, efficient carrier transport can also take place through the space-charge region induced by the fixed charge in the passivation scheme, as has been observed in, e.g., Ref. [22].

Even though passivation of the rear surface of IBC solar cells is thus of high importance, the passivation of interdigitated n^+ and p^+ Si surfaces can especially near the *pn*-junction be challenging. For instance, as the net doping level along the surface where the *pn*-junction borders changes from *n*- to *p*-type, the fixed charge density of the passivation scheme will at some point not provide field-effect passivation any more. For example for surface passivation by Al_2O_3 , it is experimentally and theoretically demonstrated that the negative fixed charge (of typically $-5\cdot 10^{12} \text{ cm}^{-2}$) does not provide field-effect passivation for n^+ Si surfaces having a (net) local *n*-type doping concentration around $\sim 10^{19} \text{ cm}^{-3}$. [23,24] Therefore, in particular chemical passivation of the rear surface of IBC cells is of high importance to avoid surface recombination at these regions near the *pn*-junction. In this work, no significant *pn*-recombination for the $\text{Al}_2\text{O}_3/\text{SiN}_x$ passivation scheme was found.

Apart from surface passivation, it was found in Section 7.3.2 that the *pn*-junction recombination was also dependent on the diffusion recipe employed. Specifically, for the surfaces which were passivated by $\text{Al}_2\text{O}_3/\text{SiN}_x$, the highest J_{02} -recombination current per junction was observed for the diffusion recipes that also resulted in the highest J_{01} values on interdigitated and uniformly doped surfaces (the passivation results of uniformly boron doped surfaces are shown in the Supplementary Info, Fig. S2). As surface passivation also manifests itself as J_{01} -type recombination pathway, changes in surface passivation quality

are a plausible cause for the observed differences in J_{01} and J_{02} per junction between the three diffusion recipes. Processing related differences between the diffusion recipes, such as differences in BSG may cause the observed variation in passivation quality.

Besides surface recombination, also an increased defect density in the c-Si bulk could in principle be responsible for the difference in *pn*-junction recombination for the three diffusion recipes, as bulk defects can also induce additional depletion region recombination and tunneling recombination at the *pn*-junction. To investigate this possibility, the influence of the diffusion recipes on the c-Si bulk material quality has been monitored. After diffusion of boron and phosphorus, the highly-doped regions were removed through wet-chemical etching, after which the c-Si surfaces were passivated by a-Si:H. For all three diffusion recipes, minority carrier lifetimes above 2 ms were measured, without revealing a significant difference between the recipes. Therefore, it can be concluded that an increased level of bulk defects is an unlikely cause for the observed differences in *pn*-junction recombination between the diffusion recipes.

Finally, the tunneling current between p^+ and n^+ Si could also depend on the doping distribution which slightly varies for the various diffusion recipes. In literature, simulations on IBC cells show that boron-doped regions with higher doping concentrations increase the tunneling recombination and reduce the shunt resistance.[15] In this work, the boron doping profile with the highest concentrations ($N_d > 1.1 \times 10^{20} \text{ cm}^{-3}$ for recipe A compared to $9.6 \times 10^{20} \text{ cm}^{-3}$ for recipe C) shows the highest *pn*-junction recombination. Nonetheless, in this work, a reduction in shunt resistance has not been observed (i.e., see Table 1), making a significant change in tunnel recombination unlikely. Therefore, on the basis of the discussion, it seems likely that the observed changes in *pn*-junction recombination for different diffusion recipes are mainly related to differences in surface passivation quality. Nonetheless, more research would be required to corroborate this hypothesis.

7.5 Conclusions

In this work, a method was presented to quantify charge-carrier recombination induced by the *pn*-junctions at the rear surface for IBC solar cells. The results underline that passivation of the c-Si surface where *pn*-junctions border is vital to reduce J_{02} recombination, which is in accordance with previous reports in the literature. Moreover, on the basis of this work, it can be concluded that even after passivation of this surface, recombination at *pn*-junction can still be significant for IBC solar cells, resulting in V_{oc} losses of up to 10 mV. Therefore, it can be concluded that increasing the junction density –by e.g., reducing the pitch– will not necessarily improve the performance of IBC solar cells.

Besides surface passivation, the diffusion recipe for boron and phosphorus also had a strong impact on the presence of recombination at the *pn*-junction. In fact, by proper tuning of the dopant profiles, losses due to *pn*-junction recombination could be virtually eliminated, even in case of a *gapless pn*-junction. As a result of the improved diffusion recipe, the efficiency of industrially relevant ‘Mercury’ IBC solar cells could be improved by 1% absolute.

Finally, we would like to stress that the methods described in this work could be used for the evaluation of *pn*-junction recombination in other types of IBC solar cells as well, such as IBC cells which are based on doped a-Si:H or poly-Si carrier-selective contacts. Moreover, the results presented in this work are also relevant to other solar cell architectures which might suffer from *pn*-junction recombination, such as multicrystalline or small area (cleaved) c-Si solar cells, where respectively the grain-boundaries or the cell perimeter are crossing the *pn*-junction.

Acknowledgements

The authors would like to thank Dr. P. Spinelli, Dr. I. Cesar, Dr. A. Mewe, Dr. L.J. Geerligs and G. J. M. Janssen from ECN, A.H.G. Vlooswijk from Tempres Systems and Dr. J. Melskens and Dr. L.E. Black from the Eindhoven University of Technology and for their valuable contributions to this work. We are grateful for financial support from the Dutch Ministry of Economic Affairs, via the Top Sector Alliance for Knowledge and Innovation (TKI) program *IBCChampion*.

References

1. Reichel, C., Granek, F., Hermle, M., and Glunz, S.W. (2011) Investigation of electrical shading effects in back-contacted back-junction silicon solar cells using the two-dimensional charge collection probability and the reciprocity theorem. *J. Appl. Phys.*, **109** (2), 24507.
2. Cesar, I., Guillevin, N., Burgers, A.R., *et al.*, (2014) Mercury: a back junction back contact cell with novel design for high efficiency and simplified processing. *29th Eur. Photovolt. Sol. Energy Conf. Exhib.*, 681–688.
3. Müller, R., Reichel, C., Schrof, J., *et al.*, (2015) Analysis of *n*-type IBC solar cells with diffused boron emitter locally blocked by implanted phosphorus. *Sol. Energy Mater. Sol. Cells*, **142**, 54–59.
4. Mewe, A., Spinelli, P., Burgers, A., *et al.*, (2015) Mercury: Industrial IBC cell with front floating emitter for 20.9% and higher efficiency. *IEEE 42nd Photovolt. Spec. Conf.*
5. Spinelli, P., Danzl, P., Guillevin, N., *et al.*, (2016) High resolution sheet resistance mapping to unveil edge effects in industrial IBC solar cells. *Energy Procedia*, **92**, 218-224
6. Shockley, W., and Read, W.T.J. (1952) Statistics of the recombinations of holes and electrons. *Phys. Rev.*, **87** (5), 835–842.
7. Hall (1952) Electron-hole recombination in germanium. *Phys. Rev.*, **87**, 387
8. Sah, C.T., Noyce, R.N., and Shockley, W. (1957) Carrier Generation and Recombination in P-N Junctions and P-N Junction Characteristics. *Proc. IRE*, **45** (9), 1228–1243.
9. McIntosh, K., Altermatt, P., and Heiser, G. (2000) Depletion-region recombination in silicon solar cells: when does mDR=2. *Proc. 16th Eur. Photovolt. Sol. energy Conf.*, 251–254.
10. Hurkx, G.A.M., Klaassen, D.B.M., and Knuvers, M.P.G. (1992) A new recombination model for device simulation including tunneling. *IEEE Trans. Electron Devices*, **39** (2), 331–338.
11. Schönecker, A., Weeber, A.W., Sinke, W.C., *et al.*, (1998) Attacking limiting factors in 10x10 cm² multicrystalline silicon, emitter wrap-through solar cell design and processing. *Proc. 2nd World Conf. Photovolt. Sol. Energy Conversion, Vienna*.
12. Kuhn, R., Boueke, A., Wibrat, M., *et al.*, (1998) 11% semitransparent bifacially active power crystalline silicon solar cells. *2nd world Conf. Exhib. Photovolt. Sol. Energy Conversion, Vienna*, 1415–1417.
13. Altermatt, P.P., Aberle, A.G., Zhao, J., *et al.*, (2002) A numerical model of *p-n* junctions bordering on surfaces. *Sol. Energy Mater. Sol. Cells*, **74** 165–174.
14. McIntosh, K.R. (2001) Lumps, Humps and Bumps: Three Detrimental Effects in the Current-Voltage Curve of Silicon Solar Cells. *PhD thesis Univ. New South Wales*.
15. Dong, J., Tao, L., Zhu, Y., *et al.*, (2014) High-Efficiency Full Back Contacted Cells Using Industrial Processes. *IEEE J. Photovoltaics*, **4** (1), 130–133.
16. Römer, U., Peibst, R., Ohrdes, T., *et al.*, (2014) Ion Implantation for Poly-Si Passivated Back-Junction Back-Contacted Solar Cells. *IEEE J. Photovoltaics*, **5** (2), 507–514.
17. Römer, U., Peibst, R., Ohrdes, T., *et al.* (2014) Recombination behavior and contact resistance of *n+* and *p+* poly-crystalline Si/mono-crystalline Si junctions. *Sol. Energy Mater. Sol. Cells*, **131**, 85–91.
18. Mihăilețchi, V.D., Komatsu, Y., and Geerligs, L.J. (2008) Nitric acid pretreatment for the passivation of boron emitters for *n*-type base silicon solar cells. *Appl. Phys. Lett.*, **92** (6), 63510.

19. Khanna, A., Mueller, T., Stangl, R. A., *et al.*, (2013) A Fill Factor Loss Analysis Method for Silicon Wafer Solar Cells. *IEEE J. Photovoltaics*, **3** (4), 1170–1177.
20. Guillevin, N., Mewe, A., Spinelli, P., *et al.*, (2015) Mercury: Industrial IBC Cell with Front Floating Emitter for 20.9% and Higher Efficiency. *Proc. 31st EU-PVSEC Hambg.*
21. Zanucoli, M., Magnone, P., Sangiorgi, E., and Fiegna, C. (2015) Analysis of the impact of geometrical and technological parameters on recombination losses in interdigitated back-contact solar cells. *Sol. Energy*, **116**, 37–44.
22. Ruhle, K., Juhl, M.K., Abbott, M.D., *et al.*, (2015) Impact of Edge Recombination in Small-Area Solar Cells with Emitter Windows. *IEEE J. Photovoltaics*, **5** (4), 1067–1073.
23. Richter, A., Benick, J., Kimmerle, A., *et al.*, (2014) Passivation of phosphorus diffused silicon surfaces with Al₂O₃: Influence of surface doping concentration and thermal activation treatments. *J. Appl. Phys.*, **116** (24), 243501.
24. van de Loo, B.W.H., Knoops, H.C.M., Dingemans, G., *et al.*, (2015) “Zero-charge” SiO₂/Al₂O₃ stacks for the simultaneous passivation of *n*+ and *p*+ doped silicon surfaces by atomic layer deposition. *Sol. Energy Mater. Sol. Cells*, **143**, 450–456.
25. Kane, D.E., and Swanson, R.M. (1985) Measurement of the emitter saturation current by a contactless photoconductivity decay method. *Proc. 18th IEEE Photovolt. Spec. Conf.* 578–583.

Supplementary information

S1. Dark *J-V* measurements

In addition to the *J-V* measurements under illumination, of which the results were presented in Table I, dark *J-V* measurements were carried out on the same solar cells. The results for the dark *J-V* are shown in the upper panel of Figure S1, together with the local ideality factor which was calculated from the dark *J-V* data (lower panel).

The dark *J-V* curves show ideality factors deviating from 1, particularly at low to moderate bias (0-0.5 V). Note that voltage over the *pn*-junction is lower in dark *J-V* than in illuminated *J-V* measurements, due to the voltage drop induced by series resistance in both cases. [14] The dark *J-V* data were fitted using a 2-diode model. The results are shown in Table 2 below. A strong reduction in J_{01} and J_{02} for recipe C was found compared to recipe A in Table 2 which is in qualitative agreement with the *J-V* results obtained under 1-sun illumination (Table 1). The absolute values of Table 2 deviate from Table 1. Lower J_{01} and J_{02} values for the dark *J-V* measurements compared to the illuminated measurements are anticipated as the actual voltage over the *pn*-junction is lower for dark *J-V* than for illuminated *J-V* measurements due to the aforementioned voltage drop induced by series resistance.[14]

Table S1 Two-diode parameters for Mercury IBC cells which were fabricated by diffusion recipes A and C. The rear surface was passivated by a stack of $\text{Al}_2\text{O}_3/\text{SiN}_x$. The results are obtained from *J-V* measurements in the dark at room temperature. The area of each solar cell was 239 cm^2 .

dopant recipe	J_{01} (fA/cm ²)	J_{02} (nA/cm ²)	R_{shunt} (Ω)	R_{se} (m Ω)
Recipe A	569	122	103	7.1
Recipe C	206	39	143	4.3

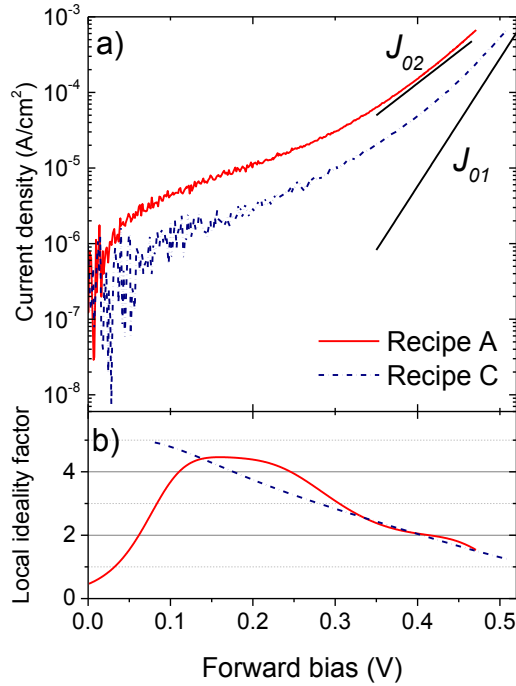


Figure S1 a) Dark J - V measurements in forward bias of Mercury solar cells for the two different doping recipes A and C. As reference, the slopes for J_{01} and J_{02} recombination channels are indicated. The current density was fitted by a polynomial function, which is used to extract the local ideality factor shown in b).

S2. Surface passivation quality and bulk lifetime

The recombination parameter J_{01} for uniformly doped p^+ Si passivated by $\text{Al}_2\text{O}_3/\text{SiN}_x$ was studied on wafers which were diffused by boron on both sides by recipes A and C. Figure S2a shows J_{01} as evaluated by the method of Kane & Swanson for both recipes.[25] Recipe C has a lower J_{01} than recipe A, indicating lower recombination in the highly-doped region and at its passivated surface.

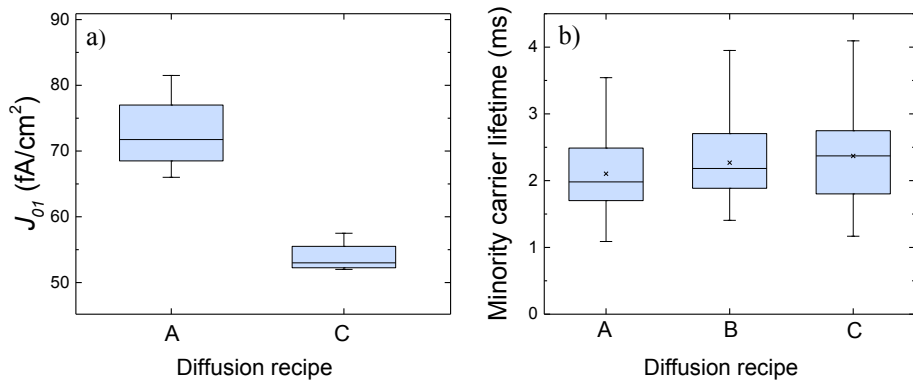


Figure S2 (a) The recombination parameter at symmetrical textured $p^+/n/p^+$ lifetime samples fabricated by diffusion recipe A and C and passivated by $\text{Al}_2\text{O}_3/\text{SiN}_x$. (b) The minority carrier lifetime of c-Si wafers passivated by a-Si:H, which were previously subjected to diffusion recipe A, B or C.

In addition, the bulk lifetime of the test samples of Section 7.4 was determined. To this end, the highly phosphorus and boron-doped regions were completely removed by wet-chemical etching, after which the wafers were passivated by a-Si:H prepared by plasma-enhanced chemical vapor deposition. Subsequently, the minority carrier lifetime was determined by photoconductance decay measurements. Figure S3 shows the minority carrier lifetime of the c-Si for diffusion recipes A, B and C. As can be seen, the average lifetime for all recipes is above 2 ms, with no significant difference between the different recipes.

CHAPTER 8

Silicon Surface Passivation by by Transparent Conductive Zinc Oxide

Abstract Excellent passivation of *n*- and *p*-type crystalline silicon (c-Si) surfaces was achieved for doped ZnO films prepared by atomic layer deposition (ALD). A high implied open-circuit voltage of 735 mV at 1-sun illumination was obtained by *i*) the optimization of an ultrathin (~1.5 nm) SiO₂ interface layer between the ZnO and the c-Si, *ii*) the use of an Al₂O₃ capping layer on top of the ZnO during forming gas annealing and *iii*) the incorporation of *n*-type dopants B or Al in the ZnO film. The Al₂O₃ capping is required to ensure hydrogenation of interface defects during annealing, whereas the dopants lower the work function of the ZnO, resulting in field-effect passivation through downward band bending near the c-Si surface. The role of hydrogen in the passivation mechanism is revealed by isotope labeling and secondary ion mass spectroscopy measurements. The high levels of surface passivation make conductive ZnO films of particular interest as transparent passivating electron contact for c-Si solar cells.

8.1 Introduction

Heterojunctions based on hydrogenated amorphous silicon (a-Si:H) have led to the world's highest reported conversion efficiencies for crystalline silicon (c-Si) photovoltaics thus far.[1] In recent years however, it has been recognized that also many other materials, referred to as 'passivation contacts', can be used to fabricate c-Si solar cells.[2–4] These passivating contacts offer high conversion efficiencies in combination to a fairly straight forward processing. The two primary functions of passivating contacts are the passivation of defects at the c-Si surface and the formation of a contact which is selective for the extraction of either electrons or holes from the c-Si absorber. Together, these properties should for a full-area passivating contact result in a recombination parameter $J_0 < 8 \text{ fA/cm}^2$, and a contact resistivity $\rho_c < 1 \text{ } \Omega\text{-cm}^2$ to enable an conversion efficiency of 26%.[5,6] The most prominent example of a recently emerged passivating contact material is doped polycrystalline silicon (poly-Si), which has now been used in solar cells with conversion efficiencies $>25\%$.[7] In addition to poly-Si, passivating contacts based on metal oxides have regained considerable interest in the last few years, as their wide band gap makes them very transparent and thus optically more suitable than a-Si:H or poly-Si as front contact.[3,8–11] Additionally, metal oxides will induce considerably less parasitic absorption losses as rear contact compared to e.g., doped poly-Si.

Concerning hole-selective passivating contacts based on metal oxides, among others $\text{Al}_2\text{O}_3/\text{ZnO}$ stacks,[11] MoO_x , [8,12] WO_x , [13] VO_x and NiO_x [14] have recently been investigated. As electron-selective materials, particularly metal oxides with an electron affinity close to that of c-Si (4.05 eV) have been the center of interest. The most prominent example of such a passivating electron contact is TiO_2 prepared by atomic layer deposition (ALD). In 2014, Liao *et al.*, reported that excellent surface passivation of c-Si could be achieved by ALD TiO_2 . [15] Shortly after this discovery, Yang *et al.*, reported that for a precisely tuned film thickness of $\sim 4.5 \text{ nm}$ and after forming gas annealing (FGA), TiO_2 also yield a sufficiently low contact resistivity with c-Si (i.e., $\rho_c = 0.25 \text{ } \Omega\text{-cm}^2$) besides providing surface passivation (resulting in a high implied open-circuit voltage $iV_{oc} = 703 \text{ mV}$). [16] Combined, these two properties make ALD TiO_2 feasible as passivating electron contact. Moreover, both properties improve when using a thin, 1.2-nm thick SiO_2 interlayer between the Si and the TiO_2 . [9,16] So far, ALD TiO_2 has been used as full-area passivating electron contact in c-Si solar cells with a conversion efficiency of 21.6%. [9]

Besides aforementioned results, in publications by Young, Stradins and co-workers, ZnO, SnO₂, and Sn-doped In₂O₃ have been studied as electron-selective materials.[17,18] These materials were prepared by sputter deposition on thermally grown SiO₂ interlayers. In general, the stacks result in a lower ρ_c in comparison to poly-Si, but also yield a higher J_0 , which is attributed to a relatively poor surface passivation. The best passivating contact properties were found after FGA for In₂O₃:Sn, with the In₂O₃:Sn being deposited on a relatively thick (4 nm) SiO₂ tunnel oxide.[17] The passivating contact properties in terms of $J_0 = 93.5 \text{ fA/cm}^2$ and $\rho_c = 11.5 \text{ m}\Omega\text{-cm}^2$ are promising for application in solar cells.

Despite these recent advances in the field of electron contacts, it is not straightforward to attain good passivating contact properties using metal oxides, predominantly due to a lack of passivation quality and a lack of control over the work function of unintentionally doped materials. In this work, we investigate doped ZnO films which are prepared by atomic layer deposition. ZnO is a well-known material in the field of photovoltaics, for instance as window layer in CIGS and in silicon heterojunction solar cells. ZnO is an abundant and transparent material, is suitable as anti-reflection coating (ARC), and is conductive. Importantly, the electron affinity of $\sim 4.4 \text{ eV}$ makes ZnO potentially feasible as electron contact. The carrier density, and hence the work function of ALD ZnO can be accurately controlled via the incorporation of *n*-type dopants, such as Al, B or Ga.[19–22] Additionally, highly doped ZnO films have already been deposited in *spatial* ALD reactors dedicated for high throughput.[22] To conclude, ZnO could potentially fulfil the functions of ARC, lateral transport layer, passivation material, and selective contact, and could therefore lead to strong simplifications in solar cell manufacturing. Nonetheless, effective passivation of defects at the c-Si surface by ZnO has thus far not yet been reported, which will be the topic of this work.

In this Chapter, it will first be demonstrated that ZnO films prepared by ALD can provide excellent passivation to the c-Si surface. Subsequently, the underlying mechanisms governing this passivation, such as optimized interface pretreatments, interface hydrogenation, and field-effect passivation by band-bending, will be scrutinized.

8.2 Experimental details

As substrates for lifetime measurements, 280- μm thick *n*- and *p*-type floatzone c-Si (100) wafers with a base resistivity of 3 $\Omega\text{-cm}$ were used. Prior to the deposition of ZnO, the wafers received different pretreatments: *i*) the standard Radio Corporation of America (RCA) cleans 1 and 2, *ii*) the RCA cleans followed by a dip in diluted hydrofluoric acid

(HF, 1%), or *iii*) RCA cleans, an HF dip and a subsequent nitric acid oxidation step (NAOS) in an azeotropic solution for 15 minutes at room temperature. In addition, on some HF-dipped wafers, a thin (2.5 nm) TiO₂ layer was prepared on both sides by ALD using titanium tetra-isopropoxide (TTIP) and H₂O as precursors in an Oxford Instruments FlexAL™ at 200 °C.

After these pretreatments, the lifetime samples were exposed to an inductively coupled plasma (200 W) with oxygen for 4 seconds, which was immediately followed by atomic layer deposition of 50-nm thick Al-doped ZnO films (ZnO:Al) or 75-nm thick B-doped ZnO (ZnO:B) on both sides of the samples in an Oxford Instruments OpAL™ reactor at 200 °C. The ALD ZnO process uses diethylzinc (DEZ) and H₂O as precursors. To incorporate Al dopants in ZnO:Al, ALD “supercycles” with a *cycle ratio* $m = 15$ were used, meaning that every sequence of 15 ALD cycles of ZnO was followed by 1 cycle of Al₂O₃ using trimethylaluminum (TMA) and H₂O.[19] The ZnO:B films were deposited with a varying dopant cycle ratio m , using TIB and H₂O as precursors during the dopant cycle.[20] Additionally, as reference, the ZnO:Al was also prepared by sputter deposition at 155 °C using targets with 2 wt% Al, and a plasma power of 0.56 W/cm² on *n*-type c-Si substrates which received the RCA cleans. Next, on selected samples, the ZnO films were capped by 30 nm of Al₂O₃, which was deposited by ALD on both sides of the substrates at 200 °C using TMA and H₂O. After deposition, samples were annealed in a Jipelec rapid thermal anneal furnace in forming gas or nitrogen ambient.

The thickness and optical properties of the ZnO films were determined by spectroscopic ellipsometry (SE). The SE data were modelled using Tauc-Lorentz and Drude oscillators, following the approach of Knoops *et al.*,[23]. Hall measurements were carried out on as-deposited ZnO films in the van der Pauw configuration to derive the electron density N_e and electron mobility μ_e . The minority carrier lifetime τ was determined by quasi-steady state (QSS) and transient photoconductance (PC) decay measurements using a Sinton Instruments WCT120. The iV_{oc} was determined from QSS-PC at 1-sun illumination. Note that the recombination parameter J_0 could not in all cases be directly determined from QSS-PC measurements, *i.e.* when no straight lines were observed from $1/\tau$ plots, rendering the method of Kane and Swanson [24] inapplicable. Therefore, in those cases, the upper limits of J_0 were derived by assuming no recombination in the c-Si bulk, $J_{0,bulk}=0$, from the following equation;

$$iV_{oc} = \frac{kT}{q} \ln \left(\frac{J_{ph}}{2 \cdot J_0 + J_{0,bulk}} + 1 \right)$$

with T the temperature, q the elementary charge and J_{ph} the light generated current density. On the samples used for secondary ion mass spectroscopy (SIMS) analysis, ZnO:B films were capped by deuterated ALD Al_2O_3 layers which were prepared using D_2O and deuterated TMA ($\text{Al}(\text{CD}_3)_3$) as precursors. SIMS analysis was carried out by Philips Innovation Services. The H concentration in the ZnO is calibrated from elastic recoil detection measurements on references samples.

8.3 Results

8.3.1 Surface passivation by ALD ZnO

In Fig. 1, the injection-dependent lifetime of various lifetime samples passivated by ALD ZnO:B is given. As can be seen, for c-Si surfaces that received the RCA treatments, no surface passivation by as-deposited ZnO:B is achieved (sample 1). Also after FGA for 30 minutes at 450°C , no passivation is achieved (sample 2). However, after capping the ZnO:B by Al_2O_3 and after conducting FGA at 450°C for 30 minutes, excellent passivation could be obtained on the RCA-cleaned n -type c-Si (sample 3), with $\tau \leq 1.55$ ms and

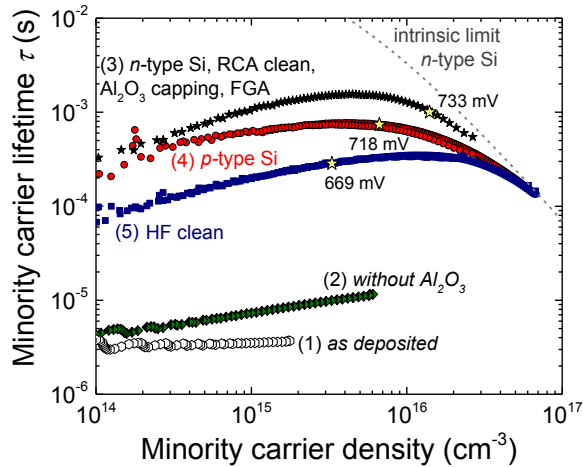


Figure 1 Injection-level dependent minority carrier lifetime for samples passivated by ALD ZnO:B. Sample (1) is n -type c-Si which received RCA cleans, and was passivated by as-deposited ZnO:B. Sample (2) is the same structure after forming gas annealing for 30 minutes at 450°C . For sample (3), the ZnO:B was capped by ALD Al_2O_3 prior to FGA. Sample (4) is based on p -type c-Si which received RCA cleans, Al_2O_3 capping and FGA. Sample (5) is n -type Si, which received RCA cleans, HF-dip, ZnO:B, Al_2O_3 capping and FGA. Stars indicate the implied open-circuit voltage under 1-sun illumination. The upper limit of the lifetime is calculated using the parameterization of intrinsic recombination by Richter *et al.*, [36].

$iV_{oc} = 733$ mV. This iV_{oc} corresponds to an upper limit (assuming no bulk recombination) of $J_0 \leq 7$ fA/cm². Also for p -type c-Si, high levels of surface passivation were achieved under the same conditions (sample 4), with $\tau \leq 770$ μ s, $iV_{oc} = 718$ mV and $J_0 = 2.5$ fA/cm².

To demonstrate that the optimization of the surface pretreatment is essential, the ZnO is deposited on an n -type c-Si surface which received a HF dip after the RCA cleans, prior to ZnO:B/Al₂O₃ deposition and FGA (sample 5). A significantly lower level of surface passivation with $iV_{oc} = 669$ mV was obtained. Note that doping the ZnO by Al resulted in similar levels of surface passivation compared to B-doped ZnO. More specifically, an $iV_{oc} = 733$ mV was also found for ZnO:Al on n -type c-Si which received RCA pretreatment after capping by Al₂O₃ and FGA. Also the thickness of the ZnO is not critical. For instance, for ZnO:Al films of 12.6 nm thickness, lifetime values of ≤ 1.2 ms could still be achieved (not shown).

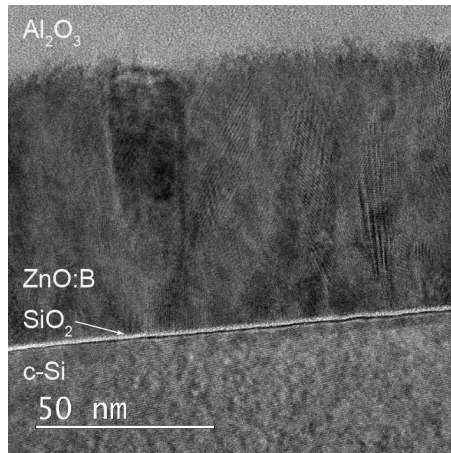


Figure 2 High-resolution transmission electron microscopy image of the ZnO:B passivation layer ($m = 15$), which was deposited on a c-Si (100) surface which received the RCA cleans. The sample received a forming gas anneal at 450 °C for 30 minutes.

In Fig. 2, a high-resolution cross-sectional transmission electron microscopy (TEM) image of the passivating stack. As can be seen, the ~ 73 nm thick ZnO:B is polycrystalline and forms a sharp interface with a uniform and continuous 1.5 ± 0.1 nm thick SiO₂ tunnel oxide, which was formed during the RCA cleans. On top of the ZnO:B, an amorphous Al₂O₃ capping layer is present. In Table I, a summary of the optical and electrical properties of the ZnO:B film of Fig. 2 is provided. The maximum J_{sc} for solar cells was calculated from OPAL2 for the AM1.5G spectrum,[6] for the case that the ZnO:B serves as anti-reflection coating on random-pyramid textured c-Si (180 μ m in thickness) without

considering encapsulation by EVA or glass or any rear contact. The high $J_{sc} = 41.7 \text{ mA/cm}^2$ and low (bulk) resistivity of $\rho < 10^{-3} \text{ } \Omega\cdot\text{cm}$ demonstrate that ZnO:B could be very well suited for application as front contact in c-Si solar cells, provided it can also form a low contact resistivity with c-Si.

Table I Overview of physical properties of as-deposited ALD ZnO:B films prepared with $m = 15$.

Physical property	Value
Thickness	73.1 nm
Resistivity ρ	$9.87 \times 10^{-4} \text{ } \Omega\cdot\text{cm}$
Carrier density N_e	$4.05 \times 10^{20} \text{ cm}^{-3}$
Electron mobility μ_e	$15.6 \text{ cm}^2/\text{Vs}$
Tauc optical bandgap E_g	3.73 eV
Refractive index n (at 2.0 eV)	1.84
$J_{sc, \text{max}}$ (simulated)[25]	41.7 mA/cm^2
iV_{oc} at 1-sun*	735 mV

*After capping by Al_2O_3 and FGA

8.3.2 Aspects ruling the surface passivation by ZnO

A. The influence of the interface treatments and annealing

As was discussed in the introduction, the performance of various passivating layers or passivating contacts critically depends on the quality and presence of a thin SiO₂ interlayer.[9,17,26] Therefore, the passivation quality provided by ZnO:Al is compared for four different surface pretreatments as a function of the annealing temperature, see Fig. 3. Besides various chemical pretreatments, also a thin (2.5 nm) ALD TiO₂ interlayer was examined, as TiO₂ lately receives significant attention due to its passivating (contact) properties.[15][9]

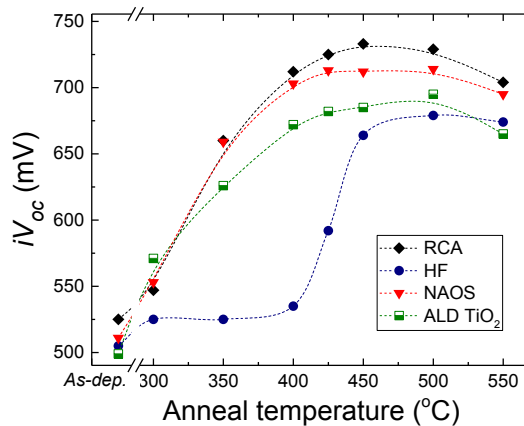


Figure 3 The implied open-circuit voltage at 1-sun illumination of *n*-type c-Si lifetime samples, for cumulative annealing steps of 5 minutes in forming gas. The c-Si wafers received four different pretreatments prior to ALD of 50 nm ZnO:Al (doping cycle ratio $m = 15$) and ALD of 30 nm Al₂O₃; *i*) RCA standard cleans 1 and 2, *ii*) the RCA cleans and a dip in HF, *iii*) RCA and HF treatments and NAOS, *iv*) RCA and HF treatments followed by the deposition of 2.5 nm of TiO₂ prepared by thermal ALD at 200 °C.

The best passivation is observed after FGA at ~450–500 °C. Moreover, it is clear that the presence of a thin tunnel oxide, as is for instance formed by the RCA or NAOS treatments, is crucial to obtain surface passivation, as significantly lower iV_{oc} values are found for HF-dipped surfaces. The ALD TiO₂ interface shows a similar trend as the NAOS or RCA samples, although a slightly lower iV_{oc} is ultimately achieved.

Naturally, it can be expected that it is also important that the tunnel oxide is not negatively affected during deposition of the ZnO to provide surface passivation. According to the TEM image of Fig. 2, the ALD ZnO layer forms a sharp interface with

the underlying SiO₂ tunnel oxide. This can be explained by the fact that ALD is a ‘soft’ deposition technique,[21,27] as opposed to for instance sputter deposition.[27,28] In fact, a thin ALD ZnO layer is sometimes used to protect underlying passivation materials, such as a-Si:H or poly-Si, from damage before thickening the TCO by sputter deposition.[21,27,29] To further investigate the role of the deposition method, 70-nm thick ZnO:Al films were deposited by sputtering on both sides of *n*-type c-Si having a RCA oxide. In analogy with previous experiments, the ZnO:Al was capped by 30-nm of ALD Al₂O₃ before carrying out the FGA. As a result, minority carrier lifetimes of ~30 μs were achieved for sputtered ZnO:Al, indicating poor surface passivation. Therefore, it is expected that the ‘soft deposition’ nature of ALD also plays a crucial role in achieving passivation by ZnO films.

B. Hydrogenation of the interface defects by ALD Al₂O₃

As was observed in Fig. 1, poor surface passivation was obtained without Al₂O₃ capping layer. In fact, stains were observed on the ZnO:B films after 30 minutes of annealing in forming gas without Al₂O₃ capping, as the ZnO:B is etched in forming gas at the anneal temperatures used (i.e., 450 °C). Note that these stains were not observed for ZnO:B/Al₂O₃ stacks or for ZnO:B films which were annealed in nitrogen ambient and can thus be attributed to the FGA. Nonetheless, also after prolonged annealing in nitrogen ambient, no surface passivation was achieved without Al₂O₃ capping layer.

The benefit of an Al₂O₃ capping layer to improve surface passivation has been observed for other materials as well in literature. For instance, for thermally-grown SiO₂,[30,31] ALD SiO₂,[32] as well as for poly-Si,[33] it has been observed that the capping by Al₂O₃ assists in further reducing surface recombination after annealing. In particular, for SiO₂ the defect density at the c-Si/SiO₂ interface is reduced by an anneal through the hydrogenation.[31] After hydrogenation, the Al₂O₃ could even be removed from the SiO₂ while preserving the surface passivation of c-Si.[31]

To gain further understanding of the role of the Al₂O₃ capping layer, also in this work the Al₂O₃ was removed after annealing the ZnO:B/Al₂O₃ passivation stacks using a carefully timed etch in highly diluted HF. No significant change in minority carrier lifetime was observed after removal of the Al₂O₃ capping layer. Therefore, it can be expected that the Al₂O₃ capping layer mainly contributes to surface passivation *during* FGA by hydrogenation of interface defects, improving the so-called *chemical* passivation.

To test this hypothesis, deuterated Al₂O₃ films (Al₂O₃:D), were deposited on ZnO:B by ALD. In this way, transport of deuterium from the Al₂O₃ film to the c-Si – SiO₂

interface could be traced. Figure 4 shows SIMS depth profiles of hydrogen, boron and deuterium throughout the c-Si/SiO₂/ZnO:B/Al₂O₃:D stacks before and after FGA. As can be seen, prior to FGA, the Al₂O₃:D contains high concentrations of deuterium. In addition, hydrogen and deuterium are piled-up at the interface between the Al₂O₃:D/ZnO:B, whereas also a relatively high hydrogen concentration is present at the SiO₂ – c-Si interface. After FGA, hydrogen and deuterium have redistributed throughout the entire film stack and follow similar distribution profiles. Indeed, deuterium (which originates from the Al₂O₃:D) can be found at the SiO₂ – c-Si surface after FGA, which supports the aforementioned hypothesis.

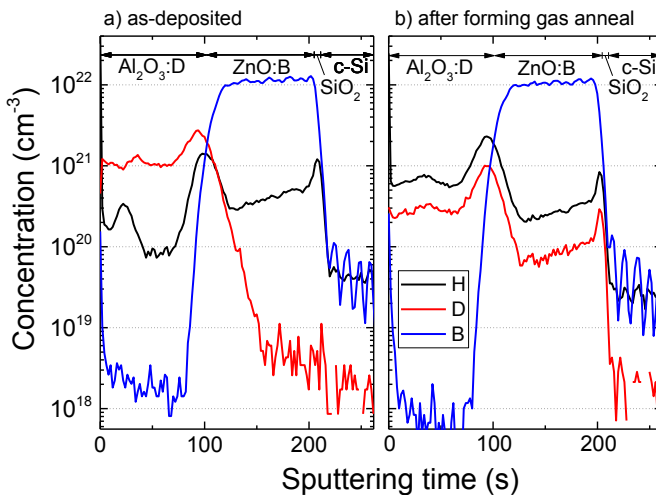


Figure 4 Depth profiles of hydrogen, deuterium and boron measured by SIMS for Al₂O₃:D/ZnO:B stacks on c-Si with an RCA oxide, a) as-deposited b) after FGA at 450 °C (30 min). The absolute uncertainty for [H] in ZnO is $\pm 30\%$, for [D] and [B] $\sim 200\%$.

The question remains however why ZnO:B films cannot provide interface hydrogenation without capping by ALD Al₂O₃, as according to Fig. 4 the ZnO:B also contains hydrogen. Integration of hydrogen concentrations in Fig. 4 reveals that the total [H] in the entire film stack (i.e., SiO₂/ZnO:B/Al₂O₃:D) increases by 18% after FGA. Nonetheless, the cumulative [H] and [D] in the stack *decreases* by 26% after FGA. This effect can be explained as deuterium in the Al₂O₃ film is exchanged with hydrogen from the FGA, with as net result an effusion of deuterium. Strikingly, also in the underlying ZnO:B and SiO₂ layers, the total amount of [H] and [D] have reduced to $\sim 90\%$ of its original value after FGA. Therefore, it can be concluded that no net hydrogenation of these layers took place

during FGA. Apparently, the remaining amount of hydrogen is sufficient to ensure chemical passivation. It is hypothesized that the dense, amorphous and hydrogen/deuterium rich Al_2O_3 capping layers prevent a very significant effusion of hydrogen from the polycrystalline ZnO:B and the underlying c-Si – SiO_2 interface during FGA. Potentially, also other dense and amorphous materials could be used as capping layer, such as SiN_x or transparent and conductive TiO_2 and In_2O_3 layers, although this requires further research,

C. Field-effect passivation by extrinsic doping of the ZnO films

The work function of passivation materials plays an important role in band-alignment with c-Si and hence in amount of field-effect passivation. To investigate this, the electron density in the ZnO was varied using intrinsic ZnO, and B-doped ZnO films with various cycle ratio m . As can be seen in Fig. 5, the lifetime increases significantly for increased electron densities in the ZnO.

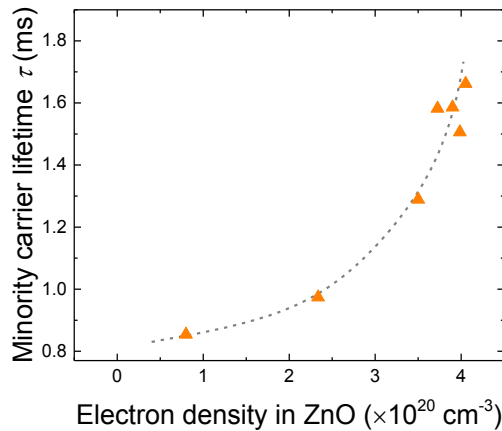


Figure 5 Minority carrier lifetime at $\Delta n = 5 \cdot 10^{15} \text{ cm}^{-3}$ of n -type c-Si ($3 \Omega\text{-cm}$, RCA cleaned), passivated by ZnO/ Al_2O_3 or ZnO:B/ Al_2O_3 stacks after FGA at 450°C , for 30 minutes. Line serves as a guide to the eye.

This effect can be understood by looking at the band alignment of the ZnO with the c-Si. Figure 6 shows the effect of the doping level in the ZnO on this band alignment, as derived by *COMSOL* simulations. As can be seen, a higher n -type doping level in the ZnO result in stronger downward band bending of the c-Si near the interface. The higher doping levels raise the Fermi level into the conduction band of ZnO. Evaluation of the Tauc optical gap shows an increase from $E_g = 3.25 \text{ eV}$ for the lowest electron density, i.e.,

$N_e=8.0\cdot 10^{19}\text{ cm}^{-3}$, to $E_g=3.73\text{ eV}$ for the highest electron density $N_e=4.05\cdot 10^{20}\text{ cm}^{-3}$. This increase in optical band gap of $\sim 0.5\text{ eV}$ is due to the so-called Burstein-Moss shift, which arises when the Fermi level moves further into the conduction band in of the degenerately doped ZnO.[34,35] Therefore, the addition of extrinsic *n*-type dopants, such as boron or aluminum in the ZnO lowers its work function by approximately $\sim 0.5\text{ eV}$, which is the underlying mechanism for the increased downward band bending in the c-Si. As the maximal attainable effective doping density in ZnO is $\sim 1\cdot 10^{21}\text{ cm}^{-3}$, there is in principle considerable room left for further improvements in field-effect passivation.

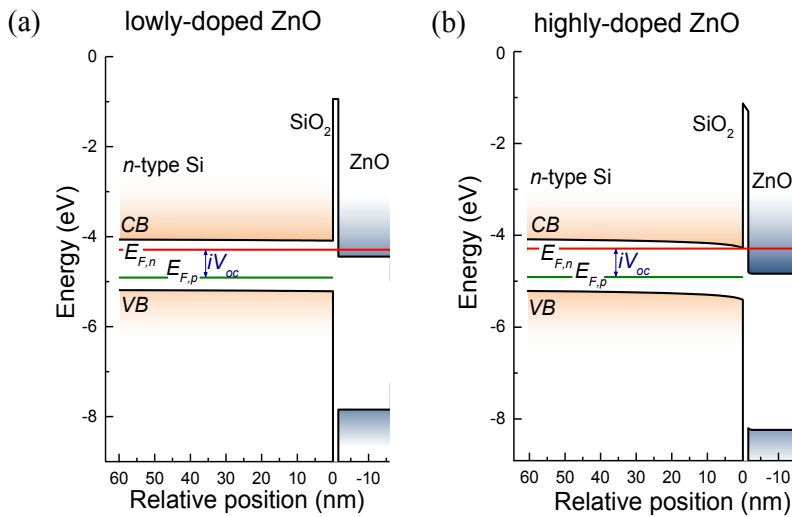


Figure 6 The band alignment of c-Si/SiO₂/ZnO:B, as calculated using COMSOL Multiphysics by solving the Poisson-Boltzmann equation. As input, *n*-type Si ($3\ \Omega\cdot\text{cm}$) with a base injection level of $\Delta n=10^{15}\text{ cm}^{-3}$ and an electron affinity of 4.05 eV was used. For ZnO, an electron affinity of 4.4 eV and electron density of (a) $N_e=1.0\times 10^{20}\text{ cm}^{-3}$ and (b) $N_e=6.5\times 10^{20}\text{ cm}^{-3}$ were used. The thickness of the SiO₂ interlayer was 1.5 nm. The conduction band *CB*, valence band *VB*, and the quasi-Fermi levels for electrons $E_{F,n}$ and holes $E_{F,p}$ are indicated.

8.4 Conclusions

It is shown that ALD ZnO films can provide excellent passivation of *n*- as well as *p*-type crystalline silicon surfaces. To achieve surface passivation, the presence of a high quality SiO₂ interface layer with a thickness of ~1.5 nm between the c-Si and the ZnO has proven to be key. Moreover, it is found that capping the ZnO by Al₂O₃ and subsequent forming gas annealing are required to achieve passivation. The Al₂O₃ layer can be removed afterwards and only assists in providing chemical passivation during FGA. Isotope labeling and SIMS measurements have proven that hydrogen is transported from the Al₂O₃ layer to the c-Si – SiO₂ interface during FGA. Finally, it is demonstrated that the incorporation of extrinsic *n*-type dopants such as boron or aluminum in the ZnO improve the passivation quality. Particularly, the dopants reduce the work function of ZnO and in this way induce field-effect passivation through downward band bending of the c-Si.

As the doped ALD ZnO films are transparent, suitable as anti-reflection coating, conductive and moreover provide surface passivation, promising opportunities for crystalline silicon solar cells are enabled. For instance, in case the contact resistivity of ZnO with c-Si is sufficiently low, the ZnO films are expected to be suitable as a full-area, transparent, passivating electron contact. Finally, the insights gained in this work on the passivation of ZnO are of considerable interest to other passivation layers and passivating contacts based on metal oxides.

Acknowledgements

The authors gratefully acknowledge Dr. G. Yang from Delft University of Technology and Dr. B. Macco, Dr. J. Melskens, Dr. M.A. Verheijen, Dr. B. Barcones Campo, R.H.J. Vervuurt, Dr. S. Smit and R.W.H.S. Scheerder from the Eindhoven University of Technology for experimental support. Dr. J. van Berkum from Philips Innovation Services is acknowledged for SIMS analysis. We thank Air Liquide for providing us with deuterated TMA. This work was funded by the Dutch ministry of Economic Affairs, through the Topconsortia for Knowledge and Innovation program “Compass”. The Solliance Solar Research consortium and the Dutch province of Noord-Brabant are acknowledged for funding the TEM facility.

References

1. World's Highest Conversion Efficiency of 26.33% Achieved in a Crystalline Silicon Solar Cell - A World First in a Practical Cell Size -. *New Energy Ind. Technol. Dev. Organ. Kaneka Corp.*, September 14, 2016.
2. Feldmann, F., Simon, M., Bivour, M., *et al.*, (2014) Carrier-selective contacts for Si solar cells. *Appl. Phys. Lett.*, **104** (18), 181105.
3. Melskens, J., van de Loo, B.W.H., Macco, B., *et al.*, (2015) Concepts and prospects of passivating contacts for crystalline silicon solar cells. *Proc. 42nd IEEE Photovolt. Spec. Conf.*, 1–6.
4. Smit, S. (2015) Passivating selective contacts for silicon photovoltaics: Solar cells designed by physics. PhD thesis, Eindhoven University of Technology.
5. Macco, B., van de Loo, B.W.H., and Kessels, W.M.M. "Atomic Layer Deposition for High Efficiency Crystalline Silicon Solar Cells", in "Atomic Layer Deposition in Energy Conversion Applications" edited by J. Bachmann, Wiley, (in press).
6. Melskens, J., van de Loo, B.W.H., Macco, B., *et al.*, Passivating Contacts for Crystalline Silicon Solar Cells: from Concepts and Materials to Prospects. (Submitted to *IEEE JPV*).
7. Glunz, S.W., Feldmann, F., Richter, A., *et al.*, (2015) The Irresistible Charm of a Simple Current Flow Pattern – 25 % With a Solar Cell Featuring a Full-Area Back Contact. *Proc. 31st EU-PVSEC Hambg.*, 259–263.
8. Geissbühler, J., Werner, J., Martin De Nicolas, S., *et al.*, (2015) 22.5% Efficient Silicon Heterojunction Solar Cell With Molybdenum Oxide Hole Collector. *Appl. Phys. Lett.*, **107** (8), 81601.
9. Yang, X., Bi, Q., Ali, H., *et al.*, (2016) High-Performance TiO₂ -Based Electron-Selective Contacts for Crystalline Silicon Solar Cells. *Adv. Mater.*, **28** (28), 5891–5897.
10. Avasthi, S., McClain, W.E., Man, G., *et al.*, (2013) Hole-blocking titanium-oxide/silicon heterojunction and its application to photovoltaics. *Appl. Phys. Lett.*, **102** (20), 203901.
11. Smit, S., Garcia-Alonso, D., Bordihn, S., *et al.*, (2014) Metal-oxide-based hole-selective tunneling contacts for crystalline silicon solar cells. *Sol. Energy Mater. Sol. Cells*, **120**, 376–382.
12. Macco, B., Vos, M.F.J., Thissen, N.F.W., *et al.*, (2015) Low-temperature atomic layer deposition of MoO_x for silicon heterojunction solar cells. *Phys. status solidi - Rapid Res. Lett.*, **9** (7), 393–396.
13. Bivour, M., Temmler, J., Steinkemper, H., and Hermle, M. (2015) Molybdenum and tungsten oxide: High work function wide band gap contact materials for hole selective contacts of silicon solar cells. *Sol. Energy Mater. Sol. Cells*, **142**, 34–41.
14. Islam, R., Shine, G., and Saraswat, K.C. (2014) Schottky barrier height reduction for holes by Fermi level depinning using metal/nickel oxide/silicon contacts. *Appl. Phys. Lett.*, **105** (18), 182103.
15. Liao, B., Hoex, B., Aberle, A.G., *et al.*, (2014) Excellent c-Si surface passivation by low-temperature atomic layer deposited titanium oxide. *Appl. Phys. Lett.*, **104** (25), 253903.
16. Yang, X., Zheng, P., Bi, Q., and Weber, K. (2016) Silicon heterojunction solar cells with electron selective TiO_x contact. *Sol. Energy Mater. Sol. Cells*, **150**, 32–38.
17. Young, D.L., Nemeth, W., Grover, S., *et al.*, (2014) Carrier-selective, passivated contacts for high efficiency silicon solar cells based on transparent conducting oxides. *Proc. 40th IEEE Photovolt. Spec. Conf.*
18. Stradins, P., Essig, S., Nemeth, W., *et al.*, (2014) Passivated Tunneling Contacts to *n*-Type Wafer Silicon and Their Implementation into High Performance Solar Cells Preprint. *6th World Conf. Photovolt. Energy Convers.* .
19. Wu, Y., Hermkens, P.M., van de Loo, B.W.H., *et al.*, (2013) Electrical transport and Al

- doping efficiency in nanoscale ZnO films prepared by atomic layer deposition. *J. Appl. Phys.*, **114** (2), 24308.
20. Garcia-Alonso, D., Potts, S.E., van Helvoirt, C.A.A., *et al.*, (2015) Atomic layer deposition of B-doped ZnO using triisopropyl borate as the boron precursor and comparison with Al-doped ZnO. *J. Mater. Chem. C*, **3** (13), 3095–3107.
 21. Macco, B., Deligiannis, D., Smit, S., *et al.*, (2014) Influence of transparent conductive oxides on passivation of a-Si:H/c-Si heterojunctions as studied by atomic layer deposited Al-doped ZnO. *Semicond. Sci. Technol.*, **29** (12), 122001.
 22. Nandakumar, N., Hoex, B., Dielissen, B., *et al.*, (2015) Conductive gallium-doped ZnO films deposited by ultrafast spatial atomic layer deposition for photovoltaic application. *Present. 25th Asia Photovolt. Sol. Energy Conf. Exhib.*
 23. Knoops, H.C.M., van de Loo, B.W.H., Smit, S., *et al.*, (2015) Optical modeling of plasma-deposited ZnO films: Electron scattering at different length scales. *J. Vac. Sci. Technol. A Vacuum, Surfaces, Film.*, **33** (2), 21509.
 24. Kane, D.E., and Swanson, R.M. (1985) Measurement of the emitter saturation current by a contactless photoconductivity decay method. *Proc. 18th IEEE Photovolt. Spec. Conf.* 578–583.
 25. McIntosh, K.R., and Baker-Finch, S.C. (2012) OPAL2: Rapid optical simulation of silicon solar cells. *2012 38th IEEE Photovolt. Spec. Conf.*, 265–271.
 26. Moldovan, A., Feldmann, F., Zimmer, M., *et al.*, (2015) Tunnel oxide passivated carrier-selective contacts based on ultra-thin SiO₂ layers. *Sol. Energy Mater. Sol. Cells*, **142**, 123–117
 27. Demaurex, B., Seif, J.P., Smit, S., *et al.*, (2014) Atomic-Layer-Deposited Transparent Electrodes for Silicon Heterojunction Solar Cells. *IEEE J. Photovoltaics*, **4** (6), 1387–1396.
 28. Demaurex, B., Wolf, S. De, Descoeurdes, A., *et al.*, (2012) Damage at hydrogenated amorphous/crystalline silicon interfaces by indium tin oxide overlayer sputtering. *Appl. Phys. Lett.*, **101** (17), 171604.
 29. Feldmann, F., Ritzau, K.U., Bivour, M., *et al.*, (2015) High and Low Work Function Materials for Passivated Contacts. *Energy Procedia*, **77**, 263–270.
 30. Dingemans, G., Einsele, F., Beyer, W., *et al.*, (2012) Influence of annealing and Al₂O₃ properties on the hydrogen-induced passivation of the Si/SiO₂ interface. *J. Appl. Phys.*, **111** (9), 93713.
 31. Dingemans, G., Beyer, W., van de Sanden, M.C.M., and Kessels, W.M.M. (2010) Hydrogen induced passivation of Si interfaces by Al₂O₃ films and SiO₂/Al₂O₃ stacks. *Appl. Phys. Lett.*, **97** (15), 152106.
 32. Dingemans, G., van Helvoirt, C.A.A., Pierreux, D., *et al.*, (2012) Plasma-Assisted ALD for the Conformal Deposition of SiO₂: Process, Material and Electronic Properties. *J. Electrochem. Soc.*, **159** (3), H277–H285.
 33. Nemeth, B., Young, D.L., Page, M.R., *et al.*, (2016) Polycrystalline silicon passivated tunneling contacts for high efficiency silicon solar cells. *J. Mater. Res.*, **31** (6), 671–681.
 34. Burstein, E. (1954) Anomalous Optical Absorption Limit in InSb. *Phys. Rev.*, **93** (3), 632.
 35. Moss, T.S. (1954) The Interpretation of the Properties of Indium Antimonide. *Proc. Phys. Soc. Sect. B*, **67** (10), 775–782.
 36. Richter, A., Glunz, S.W., Werner, F., *et al.*, (2012) Improved quantitative description of Auger recombination in crystalline silicon. *Phys. Rev. B*, **86** (16), 165202.

Conclusions & Outlook

9.1 Conclusions

The demand for higher conversion efficiencies and associated emerging solar cells designs impose increasingly stringent demands on surface passivation of crystalline silicon (c-Si) solar cells. At the start of this research, it was well-known that thin films of Al_2O_3 prepared by ALD could provide excellent levels of passivation to the c-Si surface. Nonetheless, surface recombination can strongly depend on the c-Si surface conditions. Upcoming high-efficiency homojunction solar cell architectures typically demand the passivation of textured, highly doped p - and n -type Si surfaces, sometimes even simultaneously by a single passivation scheme. Additionally, surface passivation schemes should withstand subsequent solar cell processing. A major part of dissertation therefore aimed at the fundamental understanding of the passivation of such intricate surfaces.

First of all, due to the negative fixed charge density, Al_2O_3 is no ideal match for the passivation of n^+ Si surfaces, as was e.g., established in Chapters 4 and 6. Part of the research therefore aimed at the development of an alternative passivation scheme for such surfaces by atomic layer deposition. Particularly $\text{SiO}_2/\text{Al}_2\text{O}_3$ stacks prepared by ALD have extensively been studied in this work as passivation scheme for various n^+ Si surfaces. A key feature of the $\text{SiO}_2/\text{Al}_2\text{O}_3$ stack compared to Al_2O_3 single layer is that the total fixed charge density in the passivation stack can be tuned by precisely controlling the SiO_2 interlayer thickness by ALD. As a result, in Chapter 4, the simultaneous passivation of n^+ and p^+ Si surfaces could be optimized by varying the SiO_2 interface thickness. In Chapter 6, the $\text{SiO}_2/\text{Al}_2\text{O}_3$ stacks has proven to be a promising alternative to Al_2O_3 single layers for the passivation of n^+ -type black Si surfaces. In Chapters 4 and 5, it was discussed that in particular high surface doping concentrations could be helpful to further improve the passivation by the film stacks when their fixed charge density is close to zero.

Ultimately, the $\text{SiO}_2/\text{Al}_2\text{O}_3$ stacks could be scaled-up in batch ALD reactors. Moreover, they were found to be compatible with other solar cell processing steps such as

screen printing and firing, and were found to be suitable for the passivation of the front and rear surface of c-Si solar cells in a single deposition run. Specifically, the simultaneous passivation of both sides of full-area (6-inch) bifacial and IBC n -type Si solar cells by $\text{SiO}_2/\text{Al}_2\text{O}_3$ based stacks has resulted in low levels of surface recombination, particularly compared with other passivation schemes, e.g., Al_2O_3 or SiN_x . However, even though the stacks provide excellent surface passivation, no considerable gains have been observed in terms of solar cell efficiency yet. This can be attributed to the presence of other strong recombination pathways in the solar cells investigated. Nonetheless, the working principle of the $\text{SiO}_2/\text{Al}_2\text{O}_3$ passivation stacks has been demonstrated on bifacial and IBC cells with conversion efficiencies of 19.2% and 18.8%, respectively.

Besides the research on the passivation of n^+ Si surfaces by ALD, also the passivation of other surfaces that are present in upcoming solar cell architectures has been studied, using a variety of surface passivation schemes. Generally, it has been found that the surface conditions, such as the doping level or the surface texture, can significantly affect the surface passivation quality:

- In Chapter 3, a new boron doping method was evaluated for c-Si solar cells. This method was based on the diffusion of dopants from a pure boron source layer, which could be deposited on the c-Si surface by chemical vapor deposition. It was found that during the diffusion, a boron-rich layer can be formed at the c-Si surface, which prevents surface passivation by ALD Al_2O_3 . Yet, when the diffusion of dopants is carried out in an oxygen containing ambient, the presence of a boron-rich layer is avoided. In that case, the pure boron layer can be suitable as diffusion source to form the p^+ Si region for c-Si solar cells.
- In Chapter 5, the influence of the doping level near the surface was scrutinized. It was found that for p^+ Si, a high surface dopant concentration is generally beneficial to reduce surface recombination for passivation layers which do not contain a high negative fixed charge density. For boron-doped surfaces, it was shown that this doping surface concentration can for instance be increased by wet-chemical etching of the boron-depletion region near the surface. In particular *degenerate* doping levels are expected to be useful to suppress charge-carrier recombination at passivated surfaces as well as at doped regions contacted by metal, as degeneracy strongly reduces the (local) minority carrier density even more strongly. For passivation schemes which provide field-effect passivation on p^+ Si, such as ALD Al_2O_3 , the surface doping concentration has relatively small influence on the

surface recombination. The presence of a fixed charge in the passivation layer is most advantageous to suppress recombination at moderately or lowly-doped surfaces.

- Chapter 6 addresses the passivation of black Si surface textures, which is specifically challenging due to the large roughness of the surface. Direct evidence for the presence of sub-surface defects was provided for black Si surfaces prepared by reactive ion etching at room temperatures. It was established that a wet-chemical etch at least partly removes these defects. Therefore, the etching can in addition to surface passivation by e.g., ALD Al_2O_3 , be a valuable approach to tackle charge-carrier recombination. Importantly, the defect removal etch can reduce recombination without significantly compromising the excellent optical properties of black Si.
- For upcoming interdigitated back contact solar cells, the passivation of the rear surface is an intricate task as pn -junctions are bordering at this surface. In Chapter 7 it was demonstrated that these pn -junction can give rise to a considerable J_{02} -type recombination current in IBC cells in case the rear surface is not properly passivated. It was shown that for gapless IBC cells, significant recombination of charge-carriers at the pn -junction can be prevented when the rear surface is passivated by a stack of $\text{Al}_2\text{O}_3/\text{SiN}_x$.

The abovementioned insights underline that, even for outstanding surface passivation schemes such as ALD Al_2O_3 , a detailed understanding of the surface conditions is important to further reduce surface recombination in Si homojunction solar cells.

Ultimately, the need for higher conversion efficiencies and further process simplification will be demanding an alternative for the highly doped regions used in Si homojunction solar cells. To this end, passivating contacts based on heterojunctions are emerging.

Therefore in Chapter 2, along with an overview of ALD as deposition method for surface passivation and transparent conductive oxides, the key figures of merits for passivating contacts, such as ρ_c and J_0 were identified. Moreover, a brief literature review of upcoming passivating contact concepts based on metal oxides was presented. It was outlined that metal oxides are (re-)emerging as passivating contact materials for c-Si solar cells, as their relatively high band gap makes them more transparent than e.g., doped poly-Si and a-Si:H. This transparency could enable the use of passivating contacts at the front side of the solar cell, or at the rear surface of bifacial solar cells. Nonetheless, many issues for passivating contacts based on metal oxides have to be addressed to enable a successful

implementation in Si solar cells and their high-volume manufacturing. These include achieving high levels of surface passivation and a low contact resistivity at the same time, a reproducible process flow, the integration in solar cells, etc. Moreover, little is known yet about their fundamental working principles.

The knowledge gained in this dissertation work on passivation of Si homojunction cells was used to enable surface passivation by ZnO, which is now of interest as transparent passivating electron contact. For instance, it was shown in Chapter 8 that, in analogy to the SiO₂/Al₂O₃ stacks, also for ZnO films surface passivation can be achieved through the use of an Al₂O₃ capping layer during post-deposition annealing. Moreover, fundamental aspects governing this passivation, such as the influence of the doping level of the metal oxide and the role of a SiO₂ tunnel oxide layer have been investigated. By a careful optimization of the tunnel oxide, interface hydrogenation, and the doping level of the ZnO, ultimately very high levels of surface passivation to *n*- and *p*-type c-Si were achieved. It is expected that the insights gained on ZnO can be used in the development of other passivating contacts as well.

As a final point, it is stressed that throughout this dissertation work, the use of ALD as deposition technique proved to be very beneficial to study the fundamentals of surface passivation. For example, the Al₂O₃ surface passivation layers could be prepared with a high reproducibility, which therefore allowed for a careful examination of the boron doping process, the doping levels, and the surface texture on the surface recombination rate in Chapters 3, 5, 6 and 7. For ALD SiO₂/Al₂O₃ stacks, the thickness of SiO₂/Al₂O₃ stacks could be precisely tuned by changing the amount of ALD SiO₂ cycles in Chapter 4, which allowed for the detailed study on the simultaneous passivation of *n*⁺ and *p*⁺ Si surfaces. Additionally, the ALD Al₂O₃ layers and ALD SiO₂/Al₂O₃ stacks could be deposited in a conformal way over structures with high roughness, such as black Si in Chapter 6. Finally, it was discussed in Chapter 2 and Chapter 8 that ALD offers the benefit of being a ‘soft’ deposition technique. This is of particular importance as emerging passivating contacts can rely on a thin SiO₂ tunnel oxide (~1.5 nm) to achieve surface passivation. It was shown in Chapter 8 that excellent surface passivation can be achieved through extrinsically-doped ZnO when it is prepared by ALD on the ultrathin SiO₂ interface, whereas this level of passivation was for instance not achieved when this material was prepared by sputter deposition.

9.2 Outlook: further opportunities for c-Si photovoltaics

9.2.1 Opportunities for Si solar cell processing

Ideally, the manufacturing of high-efficiency solar cells is robust and cost-effective. In this respect, passivating contacts based on metal oxides could play an important role in future solar cell processing. To illustrate this, in Fig. 1 an envisaged process flow for high-efficiency bifacial solar cells based on full-area, transparent passivating contacts is shown. As first step, c-Si wafers receive wet-chemical steps to create the random-pyramid texture and to form a high-quality, ultrathin SiO₂ tunnel oxide. After these steps, metal oxide films or film stacks could be deposited at low temperatures, perhaps even simultaneously on both sides of the cell. To finalize the solar cell, the metal oxides need to be contacted by metal, e.g., through screen-printing and curing of metal paste. As this process flow consist of few steps, such solar cell processing can in potential be very cost-effective.

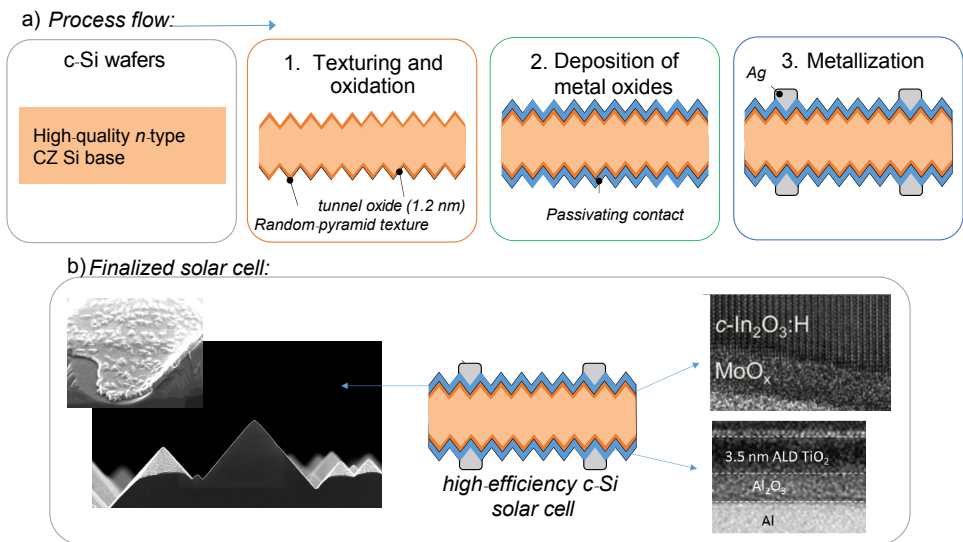


Figure 1 (a) Schematic process flow for envisaged high-efficiency bifacial solar cells based on metal oxides as passivating contacts. The number of projected main process steps is limited to ensure cost-effective cell manufacturing. The main process steps are (1) wet-chemical treatments (2) the deposition of metal oxides on both cell sides, and (3) contacting the passivating contacts by e.g., screen printing and curing of silver paste. (b) An example of an envisioned bifacial solar cell obtained by such a process, consisting of hydrogenated In₂O₃ as TCO, a thin (~5 nm) MoO_x layer as passivating hole contact, and ~3.5 nm of TiO₂ as passivating electron contact. High-resolution transmission electron microscopy images are adapted from Refs. [1,2]

Although this vision in terms of solar cell manufacturing has not been realized yet, it becomes clear that in recent years significant progress has been made;

- Hydrogen-doped In_2O_3 prepared by ALD has an electron mobility at the fundamental upper limit of $\sim 138 \text{ cm}^2/\text{Vs}$, making it a highly transparent and conductive oxide. $\text{In}_2\text{O}_3:\text{H}$ is suitable as ARC and can be prepared by ALD without inducing sputter damage or inducing intermixing with underlying thin films.[1,3]
- MoO_x , WO_x , VO_x and NiO_x are used as hole-selective materials in the field of organic PV, and are nowadays being investigated in the field of c-Si PV as well.[1,4,5] Using evaporated MoO_x as hole-selective layer, a conversion efficiency of 22.5% has already been demonstrated, albeit with the aid of a-Si:H which was used to achieve surface passivation.[6] Potentially, also a tunnel oxide can be used instead of a-Si:H to achieve passivation (see e.g., Chapter 8).
- Using ALD TiO_2 as full-area electron-selective contact, a conversion efficiency of 21.6% was demonstrated by Yang *et al.*,[2]. The TiO_2 layer had a thickness of only 3.5 nm. For TiO_2 films $>5 \text{ nm}$, the contact resistivity increases by almost an order of magnitude, whereas for thinner TiO_2 films ($\leq 3 \text{ nm}$) the passivation or electron-selectivity deteriorated. The extreme thickness control which is required for these TiO_2 electron-selective contacts probably makes the use of ALD a necessity.

Despite these recent promising results, some aspects need further attention for the successful implementation of metal oxides as passivating contacts in high-efficiency c-Si solar cells. For instance, surface passivation and carrier selectivity can be hard to achieve by some of the abovementioned materials as their intrinsic doping levels, which dictate these properties, are very susceptible to the deposition conditions and the post-deposition processing. Through incorporation of extrinsic dopants in the metal oxides, field-effect passivation as well as charge-carrier selectivity can likely be better controlled (see e.g., Chapter 8). It is therefore anticipated that the incorporation of extrinsic dopants will widen the processing window and will significantly increase the stability of metal-oxide based passivating contacts.

9.2.2 Opportunities for ALD

ALD is now a proven deposition technique for the preparation of a variety of passivation materials, including Al_2O_3 , SiO_2 , HfO_2 , Ta_2O_5 , Ga_2O_3 , TiO_2 and ZnO . With the high levels of surface passivation offered by such passivation schemes, charge-carrier recombination at the highly doped surfaces is not necessarily a dominant loss mechanism in diffused-junction solar cells. Nevertheless, there are several other opportunities for ALD to further contribute to the development and production of c-Si photovoltaics. As was already discussed in Chapter 2, most of these opportunities lie in the field of passivating contacts. For instance, ALD Al_2O_3 films can be used for the hydrogenation of poly-Si passivating contacts.[7] Moreover, the use of metal oxides as passivating contacts offer new opportunities for ALD in respect to solar cell processing. Particularly the examples outlined in previous section indicate that some of the advantages of ALD, such as a soft deposition, the formation of sharp interfaces and a precise thickness control can become crucial when preparing passivating contacts. Moreover, the self-limiting surface reactions on which ALD is based could make the manufacturing of c-Si solar cells based on metal oxides robust and reproducible.

Finally, it is stressed that the surface reactions on which ALD is based could also offer some other distinct merits to solar cell processing, which so far only marginally have been explored. For example, *area-selective* ALD (AS-ALD) could be explored for the preparation of self-aligned contacts in IBC solar cells. In AS-ALD, functional materials are only locally grown on specific surfaces, while on other surface types no film growth takes place.

As an example of AS-ALD, in Fig. 2 the rear surface of an IBC solar cell structure is shown. At this random-textured rear surface, ~ 75 nm of $\text{In}_2\text{O}_3\text{:H}$ is deposited on p^+ Si but not on n^+ Si through a mask-less ALD process. Although the exact working mechanisms of this area-selective deposition process of $\text{In}_2\text{O}_3\text{:H}$ are not fully understood yet, the results further underline the potential of ALD in solar cell manufacturing.

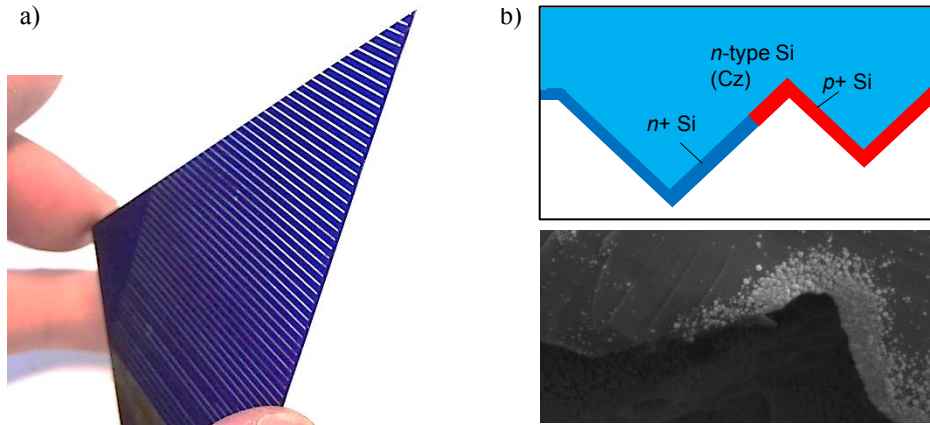


Figure 2 (a) A photograph of an IBC solar cell structure where ~ 75 nm of $\text{In}_2\text{O}_3\text{:H}$ has selectively been deposited by ALD on p^+ Si (the blue stripes), whereas no $\text{In}_2\text{O}_3\text{:H}$ has been deposited on n^+ Si (white stripes). (b) Cross-sectional scanning electron microscopy image of the pn -junction at the rear side of the textured IBC solar cells. The cross section was exposed to the ALD of $\text{In}_2\text{O}_3\text{:H}$. In this way, the diffused p^+ Si highly doped region, (which is approximately ~ 0.4 μm wide) is visible in the cross-section SEM image, as only on top of this p^+ Si region the polycrystalline/amorphous In_2O_3 layer was locally grown. In (a) and (b), the $\text{In}_2\text{O}_3\text{:H}$ was deposited using InCp , H_2O and O_2 at 100 $^\circ\text{C}$. Prior to deposition, the native oxide was fully removed from the n^+ Si as well as the p^+ Si surfaces (as was validated by X-ray photoelectron spectroscopy) using a dip in diluted HF (1%, 10 min). While the n^+ Si became hydrophobic after the HF dip, the p^+ Si remained hydrophilic.

References

1. Macco, B., Vos, M.F.J., Thissen, N.F.W., *et al.*, (2015) Low-temperature atomic layer deposition of MoO_3 for silicon heterojunction solar cells. *Phys. status solidi - Rapid Res. Lett.*, **9** (7), 393–396.
2. Yang, X., Bi, Q., Ali, H., *et al.*, (2016) High-Performance TiO_2 -Based Electron-Selective Contacts for Crystalline Silicon Solar Cells. *Adv. Mater.*, **28** (28), 5891–5897.
3. Macco, B., Knoops, H.C.M., and Kessels, W.M.M. (2015) Electron Scattering and Doping Mechanisms in Solid-Phase-Crystallized $\text{In}_2\text{O}_3\text{:H}$ Prepared by Atomic Layer Deposition. *ACS Appl. Mater. Interfaces*, **7** (30), 16723–16729.
4. Islam, R., and Saraswat, K.C. (2014) Metal/insulator/semiconductor carrier selective contacts for photovoltaic cells. *2014 IEEE 40th Photovolt. Spec. Conf. PVSC 2014*, 285–289.
5. Gerling, L.G., Mahato, S., Morales-vilches, A., *et al.*, (2015) Transition metal oxides as hole-selective contacts in silicon heterojunctions solar cells. *Sol. Energy Mater. Sol. Cells*, **114**, 109–115.
6. Geissbühler, J., Werner, J., Martin De Nicolas, S., *et al.*, (2015) 22.5% Efficient Silicon Heterojunction Solar Cell With Molybdenum Oxide Hole Collector. *Appl. Phys. Lett.*, **107** (8), 81601.
7. Nemeth, B., Young, D.L., Page, M.R., *et al.*, (2016) Polycrystalline silicon passivated tunneling contacts for high efficiency silicon solar cells. *J. Mater. Res.*, **31** (6), 671–681.

SUMMARY

Atomic-Layer-Deposited Surface Passivation Schemes for Silicon Solar Cells

To achieve crystalline silicon (c-Si) solar cells with high energy conversion efficiencies, it is vital to suppress recombination of electrons and holes at the c-Si surface. In upcoming crystalline silicon solar cell concepts, a wide variety of textured and doped surfaces, including highly doped n^+ - and p^+ -type Si surfaces, is present. The conditions of these surfaces strongly influence surface recombination. This dissertation aims at the fundamental understanding and the improvement of the passivation of such surfaces by thin films that are prepared by atomic layer deposition (ALD).

First, a literature review on the use of ALD in c-Si photovoltaics is presented. Besides discussing the physical principles and current status of surface passivation materials which are prepared by ALD, it is outlined that ALD is suitable for the preparation of other functional layers for c-Si photovoltaics as well, such as transparent conductive oxides and novel carrier-selective contacts.

Secondly, $\text{SiO}_2/\text{Al}_2\text{O}_3$ stacks prepared by ALD are investigated for the passivation of n^+ as well as p^+ Si surfaces. The stacks provide high levels of chemical passivation, whereas the density and polarity of fixed charges in the passivation stack can be varied by carefully tuning the SiO_2 thickness. As a result, simultaneous passivation of n^+ as well as p^+ Si surfaces can be achieved. The working principles of the stacks are demonstrated in bifacial and interdigitated-back contact (IBC) solar cells, which have conversion efficiencies of 19.2% and 18.8%, respectively. Moreover, it is shown that the deposition of the $\text{SiO}_2/\text{Al}_2\text{O}_3$ stacks can be scaled up in high-throughput batch ALD reactors, which makes the passivation scheme also of industrial interest.

Next, a p -type doping process for c-Si solar cells is evaluated, which is based on the chemical vapor deposition of a (pure) boron source layer. It is found that low recombination rates could be realized by passivation of the surface by ALD Al_2O_3 . Importantly, the drive-in of dopants has to be carried out in an oxygen containing ambient, to prevent the formation of a boron-rich layer which impedes surface passivation. In addition, the influence of the doping level on the surface recombination rate is scrutinized. It is found that for p^+ Si, a high doping concentration ($\sim 10^{20} \text{ cm}^{-3}$) is beneficial to further suppress surface recombination when field-effect passivation by a negative fixed charge

density is absent. By wet chemical etching of the near-surface depletion region of p^+ Si, the surface doping concentration is increased and charge-carrier recombination is reduced.

Nanotextures, such as black Si, are of interest for c-Si photovoltaics due to their outstanding optical properties, although the passivation of surface defects is challenging due to the high surface roughness and the consequently enlarged surface area. In this work, it is established that for the nanotextures additional charge carrier recombination can take place through defects which reside underneath the surface. By wet chemical removal of this defective region and by using the earlier developed ALD $\text{SiO}_2/\text{Al}_2\text{O}_3$ stacks, passivation of n^+ -type black Si surfaces is ultimately achieved without compromising the optical properties.

In IBC solar cells, the p^+ and n^+ Si regions are adjacent, and pn -junctions are bordering at the rear surface. Charge carrier recombination near these pn -junctions is quantified by e.g., Suns- V_{oc} measurements on specialized test structures that entail a varying junction density. It is demonstrated that a significant J_{02} -recombination current at the pn -junction can be avoided when the surface is passivated by $\text{Al}_2\text{O}_3/\text{SiN}_x$.

Finally, passivation materials which can also function as carrier-selective contact are emerging, as they offer the potential of higher conversion efficiencies in combination with a straight-forward processing. The insights on surface passivation of c-Si surfaces gained throughout this dissertation are used to achieve surface passivation by transparent and conductive ZnO films. Excellent levels of passivation of lowly doped n - and p -type c-Si surfaces, with implied open-circuit voltages of 735 mV at 1-sun illumination, are realized by doped ZnO films prepared by ALD. Specifically, surface passivation is enabled by the use of an ultrathin (~ 1.5 nm) SiO_2 tunnel oxide, the use of an Al_2O_3 capping layer during post-deposition annealing, and the incorporation of extrinsic n -type dopants (i.e., Al and B) in the ZnO. Additionally, the role of hydrogen in the passivation mechanism is revealed by isotope labeling and secondary ion mass spectroscopy. As the passivating ZnO films are also conductive and suitable as anti-reflection coating, the films are of high interest as transparent passivating electron contact.

To conclude, it is underlined that key virtues of ALD, such as the soft deposition of e.g., ZnO on the underlying tunnel oxide, the accurate control over the doping level, the possibility to make complex film stacks, and the high conformality of thin films on nanotextures, make ALD a very versatile technique for the preparation of surface passivation layers for silicon solar cells.

CONTRIBUTIONS OF THE AUTHOR

As was stated in the introduction, some of the work presented in this dissertation was carried out together with our project partners, and consequently several chapters have two first authors who contributed equally. Therefore, the contributions of the main author of this dissertation, B. W. H. van de Loo, to these chapters is discussed in more detail below.

Chapter 2, which was published as a book chapter was co-written by Dr. B. Macco from the Eindhoven University of Technology. Dr. B. Macco focused on ALD of TCOs and passivating contacts in sections 3 and 4, whereas the contributions of the author lie predominantly in sections 1, 2 and 5, dealing with surface passivation.

The work of Chapter 3 was carried out with Dr. C. Mok from Delft University of Technology, who previously studied the doping process based on a CVD boron layer, (e.g., Mok *et al.*, *ECS J. Solid State Sci. Technol.*, **2** (9), P413–P417), albeit not for application in c-Si solar cells. The scientific contributions of the author lie in field of surface passivation and recombination analysis.

The results described in Chapter 6 are obtained in collaboration with the Delft University of Technology. Dr. A. Ingenito was responsible for the preparation of the black-Si textures and the optical characterizations, whereas the author was responsible for surface passivation, structural and lifetime analysis of black Si.

Chapter 7 was carried out in collaboration with Dr. P. Spinelli and co-workers from ECN. The contributions of the author lie in the definition of the research topic and the analysis and physical interpretation of the results.

LIST OF PUBLICATIONS

Peer reviewed

- B. W. H. van de Loo, H. C. M. Knoop, G. Dingemans, G. J. M. Janssen, M. W. P. E. Lamers, I. G. Romijn, A. W. Weeber, and W. M. M. Kessels, “ ‘Zero-charge’ SiO₂/Al₂O₃ stacks for the simultaneous passivation of n^+ and p^+ doped silicon surfaces by atomic layer deposition,” Sol. Energy Mater. Sol. Cells, vol. 143, pp. 450–456, (2015).
- K. R. C. Mok*, B. W. H. van de Loo*, A. H. G. Vlooswijk, W. M. M. Kessels and L. K. Nanver “Boron-doped silicon surfaces from B₂H₆ passivated by ALD Al₂O₃ for solar cells.”, IEEE J. Photovoltaics, vol. 5, no. 5, pp. 1310–1318, (2015).
- H. C. M. Knoop, B. W. H. van de Loo, S. Smit, M. V. Ponomarev, J.-W. Weber, K. Sharma, W. M. M. Kessels, and M. Creatore, “Optical modeling of plasma-deposited ZnO films: Electron scattering at different length scales,” J. Vac. Sci. Technol. A Vacuum, Surfaces, Film., vol. 33, no. 2, p. 021509, (2015).
- S. V. Andersen, V. Vandalon, R. H. E. C. Bosch, B. W. H. van de Loo, K. Pedersen, and W. M. M. Kessels, “Interaction between O₂ and ZnO films probed by time-dependent second-harmonic generation,” Appl. Phys. Lett., vol. 104, no. 5, p. 051602, (2014).
- Y. Wu, P. M. Hermkens, B. W. H. van de Loo, H. C. M. Knoop, S. E. Potts, M. A. Verheijen, F. Roozeboom, and W. M. M. Kessels, “Electrical transport and Al doping efficiency in nanoscale ZnO films prepared by atomic layer deposition,” J. Appl. Phys., vol. 114, no. 2, p. 024308, (2013).

Book Chapter

- B. Macco*, B. W. H. van de Loo*, W. M. M. Kessels, “Atomic layer deposition for high-efficiency c-Si solar cells,” a chapter in “Atomic layer deposition in energy conversion applications,” edited by J. Bachmann, Wiley, (2017).

* The authors contibuted equally

Other publications and conference proceedings

- B. W. H. van de Loo, B. Macco, J. Melskens, M. A. Verheijen, W. M. M. Kessels, “Atomic-Layer Deposited Passivation Schemes for c-Si Solar Cells,” Proc. of 43rd IEEE Photovoltaic Specialist Conference (PVSC), Portland, (2016).
- B. Macco, B. W. H. van de Loo, J. Melskens, S. Smit, W. M. M. Kessels, “Status and Prospects for Atomic Layer Deposited Metal Oxide Thin Films in Passivating Contacts for c-Si Photovoltaics,” Proc. of 43rd IEEE Photovoltaic Specialist Conference (PVSC), Portland, (2016).
- P. Spinelli, P. Danzl, N. Guillevin, A. A. Mewe, S. Sawallich, A. Vlooswijk, B. W. H. van de Loo, W. M. M. Kessels, and I. Cesar, “High resolution sheet resistance mapping to unveil edge effects in industrial IBC solar cells,” in Energy Procedia, 6th International Conference on Silicon Photovoltaics, (2016).
- J. Melskens, B. W. H. van de Loo, B. Macco, M. F. J. Vos, J. Palmans, S. Smit, W. M. M. Kessels, “Concepts and prospects of passivating contacts for crystalline Silicon solar cells,” Proc. of 42th IEEE Photovoltaic Specialist Conference (PVSC), New Orleans, (2015).
- A. A. Mewe, P. Spinelli, A. R. Burgers, G. J. M. Janssen, N. Guillevin, B. W. H. van de Loo, W. M. M. Kessels, A. H. G. Vlooswijk, L. J. Geerligs, I. Cesar, “Mercury: Industrial IBC cell with front floating emitter for 20. 9% and higher efficiency”, Proc. of 42th IEEE Photovoltaic Specialist Conference (PVSC), New Orleans (2015).
- N. Guillevin, A. A. Mewe, P. Spinelli, A. R. Burgers, G. J. M. Janssen, B. W. H. van de Loo, W. M. M. Kessels, A. H. G. Vlooswijk, L. J. Geerligs, and I. Cesar, “Mercury: Industrial IBC cell with front floating emitter for 20. 9% and higher efficiency,” Proc. of the 31st EU-PVSEC, Hamburg, (2015), pp. 976 - 982.
- K. R. C. Mok, A. H. G. Vlooswijk, B. W. H. van de Loo, H. C. M. Knoops, W. M. M. Kessels, J. Derakhshandeh, L. K. Nanver, “Furnace deposition of PureB layers from B₂H₆ for solar cell applications”, Proc. of the 29th EU-PVSEC, Amsterdam, (2014), pp. 863 – 866.
- G. J. M. Janssen, M. Koppes, Y. Komatsu, J. Anker, J. Liu, A. Gutjahr, A. A. Mewe, C. J. J. Tool, I. G. Romijn, O. Siarheyeva, M. Ernst, B. W. H. van de Loo, W. M. M. Kessels, “Front side improvements for *n*-Pasha solar cells”, Proc. of the 29th EU-PVSEC, Amsterdam, (2014), pp. 812 – 815.

- B. W. H. van de Loo, G. Dingemans, E. H. A. Granneman, I. G. Romijn, G. J. M. Janssen and W. M. M. Kessels, “Advanced front-surface passivation schemes for industrial n -type silicon solar cells.” *Photovoltaics International: the Technology Resource for PV Professionals*, (24), pp. 43-50, (2014).
- D. S. Saynova, I. G. Romijn, I. Cesar, M. W. P. E. Lamers, A. Gutjahr, G. Dingemans, H. C. M. Knoop, B. W. H. van de Loo, W. M. M. Kessels, O. Siarheyeva, E. Granneman, L. Gautero, D. M. Borsa, P. R. Venema, A. H. G. Vlooswijk, “Dielectric passivation schemes for high efficiency n -type c-Si solar cells,” *Proc. of the 28th EU-PVSEC*, Paris, (2013), pp. 1188 – 1193.
- B. W. H. van de Loo, H.C.M. Knoop, M. Ponomarev, W.M.M. Kessels, & M. Creatore, “De relatie tussen de elektrische en optische eigenschappen van plasma-gedeponeerd zinkoxide,” *Novac Blad*, 51(2), pp. 14-18, (2013).

Contributions at international conferences

- 43rd IEEE Photovoltaic Specialist Conference, Portland, OR, USA, 2016 (oral)
- Novel High k Application Workshop, Dresden, Germany, 2015 (oral, invited)
- 5th Silicon PV Conference, Konstanz, Germany, 2015 (oral)
- 62nd American Vacuum Society Symposium, San Jose, CA, USA, 2015 (oral)
- 31st EU-PVSEC Hamburg, Germany, 2015 (poster)
- 6th Silicon PV Conference, Chambéry, France, 2015 (poster)
- 61st American Vacuum Society Symposium, Baltimore, MD, USA, 2014 (oral)
- 29th EU-PVSEC, Amsterdam, The Netherlands, 2014 (poster)
- 4th Silicon PV Conference, ‘s-Hertogenbosch, The Netherlands, 2014 (oral)

ACKNOWLEDGEMENTS

Ik heb een **geweldige** tijd gehad de afgelopen jaren binnen de PMP groep. Een enorm goede sfeer, uitstekende labfaciliteiten, experimentele vrijheid, vele interessante congressen en ook goede koffie ;) maakten het tot een bijzonder goede tijd. Daartoe zou ik graag als eerst **Erwin** enorm bedanken, die voor deze geweldige groep verantwoordelijk is. Bedankt voor de grote mate van vertrouwen en experimentele vrijheid die je mij sinds de aanvang van dit project gegund hebt. De snelheid van correcties op artikelen en de gedrevenheid daarachter zijn echt bewonderingswaardig. Ik heb dan ook enorm veel van je geleerd de afgelopen jaren. Ook wil ik graag **Arthur** bedanken. Tot in de laatste uurtjes mocht ik van jou suggesties ontvangen, die dit proefschrift zeker naar een hoger niveau hebben gebracht. Bedankt voor je betrokkenheid.

Bij aanvang van dit project leek het er op dat al het wetenschappelijk werk voldaan was. Atoomlaagdepositie van Al_2O_3 , mijn onderwerp bij aanvang, was industrieel opgeschaald en de belangrijkste wetenschappelijke vraagstukken leken opgelost. Ik had echter het geluk te werken binnen een nieuw consortium in Nederland wat plaatsvond onder de TKI vlag. Hierdoor waren er zeer korte lijntjes tussen onderzoeksinstituten (waaronder de TU/e) en de PV industrie. De wetenschappelijke vragen en technologische uitdagingen die binnen het consortium naar voren kwamen, vormden voor mij de belangrijke inspiratiebron en gaven een flinke stimulans zaken snel uit te zoeken. Vele hoofdstukken, (namelijk 3, 5, 6 en 7) zijn door deze samenwerking tot stand gekomen. Het was fijn om met jullie te discussiëren in een prettige en open verstandhouding. In het bijzonder wil ik daarom **Andrea, Agnes, Ard, Desislava, Erik, Ernst, Gaby, Gijs, Guangtao, Ilkay, Ingrid, Jan-Marc, Jiu, John, Joost Machteld, Miro, Nicolas, Olindo, Olga, Paula, Peter** en **Piero** bedanken. Ik ben benieuwd wat voor mooie cellen we nog gaan ontwikkelen.

De PMP staf, waaronder **Adriana** en **Marcel** wil ik graag bedanken voor hun inzet en prettige samenwerking. Ook de technische staf is een uitzonderlijke luxe, die achter (en voor) de schermen PMP draaiend houdt. Met name **Cristian** en later ook **Jeroen** wil ik bedanken voor hun snelle (en immer gezellige) steun bij de ALD depositiesystemen. Gelukkig werden onze grappen altijd gewaardeerd. In mijn hele carrière binnen PMP ben ik ook zeker **Janneke, Bernadette, Casper, Joris, Ries** en **Wytze** mijn dank verschuldigd. **Jeanne** en **Lianne**, ik kon altijd binnen lopen voor de zeer gedegen administratieve support, hartelijk dank!

Enorm van belang tijdens dit project waren ook de zogenoemde **passivisten**; **Sjoerd, Bart, Jimmy, Lachlan, Harm, en Remco**: Bedankt voor de gezelligheid tijdens SiPV's, voor het vele proeflezen en bovenal de leuke discussies. Wetenschappelijk is het van grote waarde om een sterk team te hebben met mensen die elkaar motiveren en waarbij het bovendien gezellig is. De nieuwe verworven projecten en doorbraken zijn daar echt aan te danken. De passivating contacts zijn een once in a τ opportunity. **Timmo** en **Roderick**, corona charging was soms een moeilijk beheersbare en tijdrovende klus. Toch zijn mede dankzij jullie doorzettingsvermogen een aantal figuren in deze thesis gekomen, waarvoor mijn dank.

De '**Colorado 4+1**', ik hoop dat we snel weer op skivakantie of autoreis gaan. De reizen door heel Amerika waren legendarisch. De roadtrip-cd met daarop klassiekers van Barry Manilow ligt klaar... **René** en **Nick**, bedankt voor de gezelligheid en hulp vanaf het begin van de studietijd. **RAuger**, ondanks dat je een van de grootste verliesfactoren van een zonnecel bent, toch ook bedankt! En **Bart**, bedankt.

Verder wil ik nog heel veel mensen van de PMP groep die nu nog niet genoemd zijn bedanken voor de goede sfeer, de leuke reizen, het voetballen en de inhoudelijke hulp. **Vincent, Yinghuan, R. L. G., Adrie, Ilker, Bart K., Jurgen, Pim, Yizhi, Martijn, J.W., Chai, Ben, Alberto, Valerio**, en met hen vele andere (oud) **PMP'ers**; hopelijk tot snel op donderdagmiddag, 4 uur.

Wim en **Hans**, die misschien wel niet toevallig mijn respectievelijk tweede en derde naam dragen, wil ik graag bedanken voor de gezelligheid in de trein. Dankzij jullie wachten mensen in de coupé nu vast altijd vol spanning af over hoe het verder zal gaan met high-end audio en zonnepanelen.

Vrienden en Familie, met jullie kan ik het altijd voortreffelijk vinden! Bedankt voor de zeer trouwe vriendschappen, en fijn dat jullie allemaal bij de verdediging aanwezig zijn. Jullie hebben een feestje meer dan verdiend, en ik hoop straks meer tijd over te hebben om (meer) leuke dingen te gaan doen.

Pa, Ma, Rob, Kim, Marten, Koen, Stef, Jet, Willem, Peter, Maarten, Christy, Stefan en **Scott**; bedankt voor alle hulp, interesse en onvoorwaardelijke steun, en dat geldt zeker niet alleen voor het tot stand komen van dit proefschrift. Ik heb het getroffen met jullie!

Natascha, of we nu carnavallen, kamperen in vreemde landen, of gewoon thuis zijn, samen maken wij het meeste plezier! Dit zal vast niet minder worden nu mijn thesis af is.
Bedankt voor alles.

CURRICULUM VITAE

7th November 1988

Born in 's-Hertogenbosch,
The Netherlands.

2007

Gymnasium diploma,
Maurick College, Vught.

2010

Bachelor degree Applied Physics,
Eindhoven University of Technology.

Spring 2011

Research internship in the group of prof. C. A. Wolden,
Colorado School of Mines, Golden, CO, USA.

2012

Master degree Applied Physics,
Eindhoven University of Technology.

2012 – 2017

Ph.D. Student in the Plasma & Materials Processing group,
Department of Applied Physics,
Eindhoven University of Technology.

